Title

Stochastic Dynamic Analysis of Bridges Subjected to Spatially Varying Ground Motions

Author

Konakli, Aikaterini

Publication Date

2011

Stochastic Dynamic Analysis of Bridges Subjected to Spatially Varying Ground Motions

By

Aikaterini Konakli

A dissertation submitted in partial satisfaction of the

requirements for the degree of

Doctor of Philosophy

in

Engineering – Civil and Environmental Engineering

in the

Graduate Division

of the

University of California, Berkeley

Committee in charge:

Professor Armen Der Kiureghian, Chair
Professor Filip Filippou
Professor Douglas Dreger

Spring 2011

Stochastic Dynamic Analysis of Bridges
Subjected to Spatially Varying Ground Motions

by

Aikaterini Konakli

Abstract

Stochastic Dynamic Analysis of Bridges Subjected to Spatially Varying Ground Motions

by

Aikaterini Konakli

Doctor of Philosophy in Engineering – Civil and Environmental Engineering

University of California, Berkeley

Professor Armen Der Kiureghian, Chair

Using response spectrum and time-history analysis methods, a thorough investigation of the response of bridges subjected to spatially varying support motions is performed. Three main causes of spatial variability are considered: the *incoherence effect*, which represents random differences in the amplitudes and phases of seismic waves due to reflections and refractions that occur during wave propagation in the heterogeneous medium of the ground and due to differential superposition of waves arriving from different parts of an extended source; the *wave-passage effect*, which describes the differences in the arrival times of waves at separate locations; and the *site-response effect*, which accounts for differences in the intensities and frequency contents of surface motions due to variable soil profiles underneath the supports.

The multiple-support response spectrum (MSRS) method originally developed by Der Kiureghian and Neuenhofer (1992) is generalized to allow consideration of response quantities that depend on the support degrees of freedom, and extended to account for quasi-static contributions of truncated modes. Efficient algorithms and a computer code are developed for the implementation of the generalized and extended MSRS method. The code is used for comprehensive parametric analyses of four real bridge models with vastly different characteristics. The analyses identify cases of ground motion spatial variability and types of bridges for which the effects of spatial variability are significant.

Methods for simulation of spatially varying ground motion arrays incorporating the effects of incoherence, wave passage and differential site response are developed. The simulated motions inherit statistical characteristics of a specified acceleration record at a reference site. The *conditional* simulation approach preserves time-history characteristics of the specified record; however, the array of motions exhibits increasing variability with distance from the reference site. The *unconditional* simulation method generates an array of motions that preserve the overall temporal and spectral characteristics of the specified record and exhibit uniform variability at all locations. The simulated motions are validated by examining their physical compliance and by comparing their response spectra, coherency characteristics and power spectral densities with corresponding target models.

Sets of simulated support motions are used to investigate the effect of spatial variability on linear and non-linear bridge response by time-history analyses. Comparisons between linear and non-linear pier drifts are performed to assess the accuracy of the “equal displacement” rule (Veletsos and Newmark, 1960) for spatially varying ground motions. Comparisons between mean peak responses obtained from linear time-history and MSRS analyses provide information on the range of errors induced by the approximations involved in the latter method.

Finally, coherency analysis of a recorded array of near-fault ground motions is performed. The ability of commonly used models to describe the incoherence component of this array is assessed.

To my brother and parents

To my “Berkeley family”

Contents

CHAPTER 5 - LINEAR AND NON-LINEAR TIME-HISTORY ANALYSIS USING SIMULATED DIFFERENTIAL SUPPORT MOTIONS AND COMPARISON WITH MSRS ESTIMATES 152

CHAPTER 6 - COHERENCY ANALYSIS OF ACCELERATIONS RECORDED BY THE UPSAR ARRAY 202

List of Figures

List of Tables

ACKNOWLEDGEMENTS

I would like to express my infinite gratitude to my research advisor, Professor Armen Der Kiureghian. Being his student has been a great honor and pleasure. I wholeheartedly thank him for all the knowledge and insight he helped me gain, his encouragement in my growth as an independent thinker, the academic values he transmitted to me, his generous support in the pursuit of my every academic and professional goal. I have the utmost appreciation for his academic and humane qualities and he will always be for me an inspirational role model.

I am very honored with the participation of Professor Filip Filippou and Professor Douglas Dreger in my qualifying-exam and dissertation committees. Throughout my graduate studies, Professor Filippou provided me with invaluable academic and personal support, for which I am deeply grateful. I am also grateful for the opportunity I had to work as a teaching assistant for his courses; his excellent guidance has been fundamental in my development as an instructor. Professor Dreger was co-principal investigator in one of the projects that constitute my doctoral research. I sincerely thank him for the insightful discussions and his constructive feedback in our meetings throughout the conduct of this research.

I would like to thank Professor David Brillinger for enhancing my interest in the field of time-series analysis and for providing useful feedback on the subject of coherency analysis. I appreciate the participation of Professor Anil Chopra and Professor Sourav Chatterjee in my qualifying exam committee. I am thankful to all my Professors in UC Berkeley for the precious knowledge I gained in their courses.

I would like to thank Frank McKenna for valuable assistance in use of the OpenSees code and for always being available to address my questions. I would also like to thank Paul Chung from the California Department of Transportation for his guidance in the development of the bridge models I used in this research.

During my doctoral studies, I have been most lucky to work in the same office with Michelle Bensi, Mayssa Dabaghi, Smitha Koduru, Sanaz Rezaeian and Daniel Straub. I would like to thank them not only for our academic collaborations, but also for their friendship and the emotional support I always had in “510 Davis Hall.” Many thanks to all the fellow students and researchers I interacted with during my graduate studies.

I wish to acknowledge assistance from the SEMM administration, and especially Shelley Okimoto.

I am extremely thankful to my friends who filled my “Berkeley years” with most beautiful moments. The love, support and encouragement I found in them made it all possible in the challenging “PhD path.” Special thanks to the Greek communities in Berkeley and in San Francisco, who warmly embraced me and made the Bay Area a “home” for me.

I deeply thank my family, who, despite the geographical distance, were always “next to me” to share my moments of joy and my concerns. I will forever cherish their encouragement to go in the direction of my dreams.

My research has been financially supported by the California Department of Transportation under Contract No. 59A0580 and Contract No. 59A0582, by the Onassis Foundation in Greece, by the UC Berkeley Department of Civil and Environmental Engineering, and by the Taisei Chair in Civil Engineering. These sources of financial support are gratefully acknowledged.

Chapter 1 - Introduction

1.1 MOTIVATION AND BACKGROUND

Seismic design of extended structures, such as bridges, requires accounting for the spatial variability of the earthquake motion. Spatial variability of ground motions is mainly caused by three phenomena (Der Kiureghian 1996): (a) The incoherence effect, which arises from random differences in the amplitudes and phases of seismic waves due to reflections and refractions that occur during their propagation in the heterogeneous medium of the ground and also due to the super-positioning of waves arriving from different parts of an extended source; (b) The wave-passage effect, which arises due to the differences in the arrival times of seismic waves at separate stations; and (c) The differential site-response effect, which arises from differences in the intensity and frequency content of the surface motions due to propagation of seismic waves from the bedrock level to the ground surface through soil layers with different dynamic properties. We note that, under uniform soil conditions, spatial variations in earthquake ground motions are only due to the incoherence and wave-passage effects, and in this case, ground motions at separate surface locations are realizations of random processes characterized by the same intensity and frequency content.

Under spatially varying support excitations, the response of a bridge can be expressed as the sum of two components: a pseudo-static component and a dynamic component. Similarly to the case of uniform support excitations, the dynamic component is the response of the bridge to the dynamic inertia forces induced by the support motions. At each time instant, the pseudo-static component is the static response of the bridge (neglecting inertia and damping forces) to the differential support displacements prescribed by the spatially varying ground motions. This component is zero in the case of uniform support excitations.

Under uniform soil conditions, the effects of incoherence and wave passage tend to decrease the dynamic response due to random cancellations. However, by inducing a pseudo-static response component, these effects may increase or decrease the total bridge response, depending on the structural characteristics and the ground motion field. Thus, even in the case of uniform soil conditions, accounting for the spatial variability of ground motion is important. The additional consideration of the differential site-response effect tends to increase the pseudo-static component, whereas the influence on the dynamic component depends on the types of soils considered. In all cases, neglecting the spatial variability of ground motion may or may not be on the safe side. Thus, incorporating all three effects of incoherence, wave passage and site response in the earthquake response analysis of bridges is necessary.

The response of extended structures to differential support motions has been studied by various researchers using linear time-history analyses (e.g. Price and Eberhard, 1998; Lou and Zerva, 2005), non-linear time-history analysis (e.g. Saxena et al., 2000, Zanardo et al., 2002; Kim and Feng, 2003; Sextos et al., 2004; Lou and Zerva, 2005; Lupoi et al., 2005), the methods of random vibration (e.g. Zerva, 1990; Heredia-Zavoni and Vanmarcke, 1994; Hao, 1998; Dumanogluid and Soyluk, 2003; Zembaty and Rutenberg, 2004; Zhang et al., 2009) or response spectrum methods (e.g. Berrah and Kausel, 1992; Der Kiureghian and Neuenhofer, 1992).

The random vibration approach is based on a statistical characterization of the support excitations. Typically, the set of support motions is assumed to be jointly stationary and specified in terms of a matrix of auto- and cross-power spectral density (PSD) functions. The cross-PSDs are obtained in terms of the respective auto-PSDs and a coherency function that models the spatial variability of the ground motion random field in the frequency domain. The main advantage of this approach is that it provides a statistical measure of the response, which is not controlled by a particular set of selected ground motions. However, it remains rather uncommon in engineering practice, which typically defines earthquake input in terms of response spectra or ground motion time histories. Furthermore, the random vibration approach used in previous studies is based on the strict assumption of stationarity.

Response spectrum methods are based on the random vibration approach, but have the additional advantage of using a response spectrum characterization of the ground motion, which is particularly appealing from a design standpoint. Furthermore, response spectra inherently include the non-stationarity of the ground motion. The multiple-support response spectrum (MSRS) method, developed by Der Kiureghian and Neuenhofer (1992), obtains the mean of the peak structural response in terms of the response spectra and peak ground displacements at the support points of the structure and the coherency function characterizing the spatial variability of the ground motion. This method properly accounts for cross-correlations that occur between the support motions and between modal responses. The MSRS rule has been used by a growing number of researchers to investigate seismic responses of bridges and other multiply-supported structures: Nakamura et al. (1993) used the MSRS method for the analysis of the Golden Gate Bridge; Kahan et al.

(1996) used the MSRS framework to perform sensitivity analysis of the bridge response and develop mode truncation criteria; Der Kiureghian et al. (1997) performed parametric studies of example bridge models incorporating the site-response effect; Soyluk (2004) compared results from MSRS analysis with results from conventional random vibration analysis; Loh and Ku (1995) and Wang and Chen (2005) developed approximations of the correlation coefficient terms in the MSRS rule; and Yu and Zhou (2008) extended the MSRS method for analysis of non-classically damped structures. As a method employing modal superposition, the MSRS method is necessarily limited to linear analysis. However, under severe earthquake loading, bridges, as well as other extended structures, are expected to experience inelastic response.

One way to account for non-linear behavior is to conduct response history analysis (RHA) for specified time histories of ground motions at support points of the structure. Since recordings of closely spaced earthquake ground motions are rare, non-linear response history analysis of multiply supported structures must rely on synthetic ground motions. Simulation methods have been developed that use the coherency function in conjunction with theoretical target PSD functions. The resulting simulated stationary motions are then modulated in time to provide temporal non-stationarity (e.g. Hao et al. 1989, Saxena et al. 2000). However, this approach cannot account for spectral non-stationarity of the ground motion, which can be critical in analysis of hysteretic structures. An earlier work by Deodatis (1996) incorporates spectral non-stationarity, but requires specification of an evolutionary PSD. No investigation of the physical compliance of the synthetic motions was carried out. An alternative approach to simulation of an array of synthetic ground motions with specified coherency function is to use probabilistic conditioning with a seed recorded or simulated motion at a reference site (Vanmarcke and Fenton, 1991; Kameda and Morikawa, 1992; Liao and Zerva, 2006). Applying this approach on segmented records, Vanmarcke and Fenton (1991) and Liao and Zerva (2006) generated motions with temporal and spectral non-stationarities. One disadvantage of generating ground motions by conditioning on a seed accelerogram is that the variance of the array of simulated motions increases with increasing distance from the site of the target motion. This is clearly an undesirable property when performing statistical analysis of bridge response, say, by Monte Carlo simulation. This issue can be addressed by conditioning the simulated array of motions on the PSDs of the segmented seed accelerogram rather than its specific realization. Vanmarcke and Fenton (1991) used this approach to simulate accelerograms, but did not examine the physical compliance of the simulated motions in terms of displacement time histories and response spectra. Furthermore, all previous studies using probabilistic conditioning are limited to the case of uniform soil conditions.

Another way to account for non-linear behavior by avoiding the computationally costly non-linear time-history analysis is to relate non-linear displacement demands to corresponding linear responses. In the so-called "displacement-based" design approach (Moehle, 1992), elements of the structure are designed for a prescribed ductility ratio using seismic demands that are specified in terms of maximum displacement. One can show that, under certain conditions, the displacement computed for the linear structure provides a good approximation of the inelastic displacement demand (Veletsos and Newmark, 1960). This finding, commonly known as the “equal displacement” rule, has been examined for the case of uniform excitations by a number of investigators, including Rahnama and Krawinkler (1993), Miranda and Bertero (1994), Vidic et al. (1994), Gupta and Krawinkler (2000) and Miranda (2000). However, to the author’s knowledge, the validity of the “equal displacement” rule under varying support motions has not been investigated.

In all analysis approaches discussed above, a coherency function is typically employed to describe the spatial variability of support motions. Because of the random nature of the incoherence component of this function, it is not possible to develop a theoretical model of this phenomenon solely based on physics. One approach to characterize the incoherence component is to use a probabilistic model employing parameters that can be determined through statistical inference. A general form for such a theoretical model has been derived by Der Kiureghian (1996) based on elementary principles, and a special case is the well-known model by Luco and Wong (1986). Another approach to model the incoherence component is to develop empirical models using data from recorded acceleration arrays (e.g. Harichandran and Vanmarcke, 1986; Abrahamson et al., 1991). Empirical models account for the complex phenomena that occur during wave propagation and are not captured by simplified mathematical models, but characterize only the specific rupture mechanisms and soil topographies present in the data. It is noted that the incoherence component for near-fault ground motions has not been properly examined.

1.2 OBJECTIVES AND SCOPE

In this study, we develop accurate and practical tools for the analysis of bridges subjected to spatially varying support motions considering both the response spectrum and the RHA approaches. These analysis tools are used for the investigation of the effects of several cases of spatial variability on the responses of real bridge models with vastly different structural characteristics. In the RHA approach, both linear and non-linear responses are investigated with the aim of assessing the accuracy of the “equal displacement” rule. Comparisons of the responses obtained with the response spectrum and the RHA analysis approaches are performed. To make RHA possible, a method to generate synthetic arrays of ground motions is developed. An additional objective is the investigation of existing coherency models, commonly used to describe the spatial variability of ground motion, through comparisons with coherency estimates from an array of near-fault records. These objectives are further described in the following subsections.

Development of analysis tools

Response spectrum approach

Since its development in 1992, the MSRS rule has become popular as a method of analysis of extended structures under differential support motions. As in response spectrum analysis under uniform excitation, use of the MSRS rule in practice involves truncation of modes beyond a number usually far smaller than the total number of modes of the structure. In this study, we present a generalized and extended formulation of the original MSRS method. The original MSRS formulation only considered response quantities that could be expressed as linear combinations of the displacements at the unconstrained degrees of freedom (DOF) of the structure. The generalized formulation presented here also allows consideration of response quantities that involve one or more support DOFs, e.g., drifts of bridge piers. The extended version of the MSRS rule accounts for the quasi-static contribution of the truncated modes. Furthermore, a computer algorithm for the implementation of the generalized and extended MSRS method is developed. In this algorithm, the evaluation of the cross-model, cross-support correlation coefficients is performed with a numerical integration method that accounts for the behavior of the integrand for specific modal quantities. The computational efficiency achieved with this integration method is particularly important due to the large number of correlation coefficients involved in the MSRS analysis of typical bridge models. It is noted that computation of these coefficients with a general-purpose integration algorithm quickly becomes impractical for a structure with a large number of modes and many support points. This problem, which has been noted by a number of investigators (see, e.g., Loh and Ku, 1995; Wang and Chen 2005), is now resolved with the specialized integration algorithm. Another advantage of the implemented algorithm is the ability to evaluate the required response coefficients with a method that can be applied with any "black-box" structural analysis software with restricted access to the source code.

Synthetic motions for RHA

As discussed earlier, the main challenge in the time-history analysis of bridges under differential support motions is the simulation of the input support motions. In this study, we develop methods for simulation of non-stationary spatially varying support motions accounting for the effects of incoherence, wave passage and differential site response. Efficient computer algorithms developed for the implementation of the simulation methods are described in detail. We consider two approaches: the unconditional approach, which generates support motion arrays consistent with the PSDs of a segmented accelerogram, and the conditional approach, which generates support motions by conditioning on the specific realization of the record. The simulation methods are validated by examining the physical compliance of the motions, by comparing the statistical properties of a sample of realizations, i.e., coherency characteristics and PSDs, with the corresponding target models and, also, by examining the corresponding response spectra. By incorporating the differential site-response effect, the present work provides an important enhancement of the previously developed methods of conditional simulation. Another contribution of this study is that it provides detailed discussions on the selection of various parameters involved in the process and their effects on the characteristics of the generated motions.

Parametric analyses of real bridge models

Comparative response analyses of four real bridges allow insightful observations on the influence of differential support motions on the structural response for several cases of ground motion spatial variability. The bridges have been designed by the California Department of Transportation (Caltrans) and the respective models are developed here based on the Caltrans blueprints and following Caltrans specifications. Analyses of the bridge models are performed using both the MSRS and the RHA approaches. When performing MSRS analyses, we also examine the effect of spatial variability of ground motion on modal contributions and assess the effectiveness of the extended rule to approximately account for the contributions of truncated modes. In the RHA approach, of special interest is the effect of spatial variability on the ratios of pier drifts obtained from non-linear and linear analyses. According to the "equal displacement" rule, for sufficiently flexible systems, these ratios are expected to be close to unity. In this study, we investigate the validity of this rule for several cases of varying support motions. Furthermore, we perform comparisons of the MSRS and RHA results for linear structures in order to assess the level of accuracy achieved by the MSRS method.

Investigation of coherency models

As described earlier, several models have been developed to describe the incoherence component of the coherency function. These are mostly based on far-field recordings. In this study, we perform a detailed coherency analysis of the near-fault recordings of the UPSAR array from the 2004 Parkfield (California) earthquake and determine if there is a substantial difference in the coherency characteristics of these near-fault records relative to the existing models.

1.3 ORGANIZATION OF THE REPORT

This dissertation is organized into 7 chapters. Chapter 2 discusses the derivation and implementation of the generalized and extended MSRS method, which is used for the MSRS analysis of real bridge models in Chapter 3. Chapter 4 describes methods for simulation of spatially varying ground motions, which are used in Chapter 5 to investigate linear and non-linear RHA of bridge models under differential support motions. Chapter 6 develops models for the incoherence component of the coherency function using the UPSAR array of recordings. More details on the specific subjects covered in each chapter are presented below.

In Chapter 2, we first introduce a generalization of the original formulation of the MSRS method, which allows consideration of response quantities that involve the support DOFs. An example is drifts of bridge piers. This condition also applies to most response quantities of interest when the structural model has rotational DOFs that are condensed out. Following an investigation of mode truncation criteria for the case of differential support motions, the extended version of the MSRS rule is developed, which accounts for the quasi-static contributions of the truncated modes. A parametric study of additional cross-correlation coefficients introduced in the extended MSRS method is performed to gain insight into their behavior and identify cases of ground motion variability for which these terms are significant. Finally, an overview of the computer program developed for the implementation of the generalized and extended MSRS method is presented and the main computational issues are addressed.

In Chapter 3, we apply the theory presented in Chapter 2 to investigate the effect of ground motion spatial variability on models of four real bridges designed by the California Department of Transportation. The selected bridges have vastly different characteristics, e.g. length, number of spans, number of piers per bent, fundamental period. We perform a comprehensive response analysis of the four bridge models using the MSRS rule and investigate the total, pseudo-static and dynamic responses for three cases of excitation: uniform support motions, varying support motions due only to wave passage and incoherence, and varying support motions due to wave passage, incoherence and differential site effect. The response quantities examined are element forces along the deck and pier drifts. Finally, we compare the accuracies of the extended versus the original MSRS rules when only the first few modes are included and investigate conditions under which the extended rule provides improved approximations.

In Chapter 4, we develop methods for simulation of non-stationary spatially varying support motions accounting for the effects of incoherence, wave passage and differential site response. Using the unconditional approach, we simulate arrays of support motions characterized by similar variability at all sites. Using the conditional approach, we simulate arrays of motions for which the variance increases with increasing distance from the reference site with a specified motion. (The increase levels off after sufficient distance). In the latter approach, we investigate a method that preserves the low-frequency content and, thus, the waveform of the displacement time history of the seed record. In an example application, we simulate support motions for an existing bridge in California considering both simulation approaches and for both cases of uniform and variable soil conditions. The simulation methods are validated by (i) examining the physical compliance of example simulated time histories (e.g., zero acceleration, velocity and displacement residuals), (ii) comparing statistical characteristics of an ensemble of realizations with the corresponding target theoretical models, and (iii) examining the response spectra of the simulated motions. The selection of various parameters involved in the simulation methods and their effect on the characteristics of the generated motions are also investigated.

In Chapter 5, we use arrays of motions simulated with the unconditional approach developed in Chapter 4 to investigate responses of bridge models under differential support excitation through linear and non-linear RHA. For the bridges examined in Chapter 3, we consider both linear and non-linear models, and investigate the effect of ground motion spatial variability on pier drifts, which are quantities particularly important in bridge design. Additionally, we examine the ratios of non-linear over linear drifts in order to investigate the effect of spatial variability on the accuracy of the commonly used “equal displacement” rule. Another objective of this chapter is to assess the accuracy of the MSRS method by comparisons of the mean peak linear responses from RHA with corresponding MSRS estimates.

In Chapter 6, we examine spatial variations observed during the 2004 Parkfield (California) earthquake using the UPSAR array of closely spaced acceleration records and compare coherency estimates from these data with existing theoretical and empirical models. Since the distances of the UPSAR recordings from the fault rupture are shorter than those for most arrays used in previous studies, we examine if there is a substantial difference in the coherency characteristics of these near-fault records relative the existing models. It is noted that, though near-fault, the records used in this study do not exhibit directivity pulses.

Finally, Chapter 7 summarizes the main results and conclusions of the study and provides recommendations for future studies.

Chapter 2 - Generalized and extended MSRS rule

2.1 INTRODUCTION

The MSRS (Multiple-Support Response Spectrum) modal combination rule developed by Der Kiureghian and Neuenhofer (1992) evaluates the mean peak response of multiply-supported linear structures subjected to spatially varying ground motions. Since its development in 1992, this rule has become popular as a method of analysis and has been used by a growing number of researchers to investigate seismic responses of bridges and other multiply-supported structures (e.g., Kahan et al. 1996; Soyluk, 2004; Yu and Zhou, 2008). The original formulation of this method only considered responses that could be expressed as linear functions of the total displacements at unconstrained degrees of freedom (DOF) of the structure. In this chapter, the original formulation is generalized to account for response quantities that depend not only on the displacements at the unconstrained degrees of freedom, but also on support motions. One example response in a multiply-supported structure that involves the support motion is the drift response of a pier of a bridge. Der Kiureghian and Neuenhofer (1992) suggested introducing an "unconstrained" DOF near the support point to allow computation of such a response. However, dependence on support motions is pervasive among response quantities of interest. In fact, when the structure has rotational DOF that are condensed out in the analysis, most response quantities of interest indirectly depend on the support motions.

As in modal analysis of ordinary structures, when using the MSRS rule for multiply-supported structures the analyst must truncate modes beyond a number far smaller than the total number of DOF of the structure. In this chapter, following a discussion of mode truncation criteria for the case of differential support motions, an extended version of the MSRS rule is developed to account for the quasi-static contribution of the truncated modes. This formulation introduces new terms in the MSRS formula, which include three new sets of cross-correlation coefficients. A parametric study of the newly introduced cross-correlation coefficients is performed to gain insight into their behavior and identify cases of ground motion variability for which these terms are significant.

Finally, an overview of the computer program developed for the implementation of the generalized and extended MSRS method is presented and the main computational issues are addressed.

2.2 GENERALIZED FORMULATION OF THE MSRS RULE

2.2.1 Equations of motion

Consider a N-DOF linear structural model subjected to motions at m support DOF. Let $\mathbf{x} = [x_1 \quad \cdots \quad x_N]^{\mathrm{T}}$ be the N-vector of total displacements at the unconstrained DOF and $\mathbf{u} = [u_1 \quad \cdots \quad u_m]^{\mathrm{T}}$ be the m-vector of prescribed support displacements. Both $\mathbf{x}$ and $\mathbf{u}$ may contain translational as well as rotational components. The equations of motion for the model can be written in the matrix form (Der Kiureghian and Neuenhofer, 1992)

$$\begin{bmatrix} \mathbf{M} & \mathbf{M}_c \\ \mathbf{M}_c^{\mathrm{T}} & \mathbf{M}_g \end{bmatrix} \begin{Bmatrix} \ddot{\mathbf{x}} \\ \ddot{\mathbf{u}} \end{Bmatrix} + \begin{bmatrix} \mathbf{C} & \mathbf{C}_c \\ \mathbf{C}_c^{\mathrm{T}} & \mathbf{C}_g \end{bmatrix} \begin{Bmatrix} \dot{\mathbf{x}} \\ \dot{\mathbf{u}} \end{Bmatrix} + \begin{bmatrix} \mathbf{K} & \mathbf{K}_c \\ \mathbf{K}_c^{\mathrm{T}} & \mathbf{K}_g \end{bmatrix} \begin{Bmatrix} \mathbf{x} \\ \mathbf{u} \end{Bmatrix} = \begin{Bmatrix} \mathbf{0} \\ \mathbf{F} \end{Bmatrix} \tag{2.1}$$

where $\mathbf{M}$, $\mathbf{C}$ and $\mathbf{K}$ are $N \times N$ mass, damping and stiffness matrices associated with the unconstrained DOF, respectively; $\mathbf{M}_g$, $\mathbf{C}_g$ and $\mathbf{K}_g$ are $m \times m$ matrices associated with the support DOF; $\mathbf{M}_c$, $\mathbf{C}_c$ and $\mathbf{K}_c$ are $N \times m$ coupling matrices associated with both sets of DOF; and $\mathbf{F}$ is the m-vector of reacting forces at the support DOF.

The total displacement vector at the unconstrained DOF is decomposed into pseudo-static and dynamic components: $\mathbf{x} = \mathbf{x}^s + \mathbf{x}^d$. The pseudo-static component, $\mathbf{x}^s$, is the response of the system when dynamic effects are neglected and is obtained from the set of equations for unconstrained DOF in Eqn. (2.1) in terms of the support displacements as $\mathbf{x}^s = \mathbf{R}\mathbf{u}$, where $\mathbf{R} = -\mathbf{K}^{-1}\mathbf{K}_c$ is the influence matrix. The kth column of the influence matrix, $\mathbf{r}_k$, can be interpreted as the displacements at the unconstrained DOF when the kth support DOF is displaced by a unit amount, while all other support DOF remain fixed. Employing the above decomposition in Eqn. (2.1), the equation of motion for the dynamic component of the response is obtained as

$$\mathbf{M}\ddot{\mathbf{x}}^d + \mathbf{C}\dot{\mathbf{x}}^d + \mathbf{K}\mathbf{x}^d = -(\mathbf{M}\mathbf{R} + \mathbf{M}_c)\ddot{\mathbf{u}} - (\mathbf{C}\mathbf{R} + \mathbf{C}_c)\dot{\mathbf{u}} \tag{2.2}$$

The damping forces on the right-hand side are usually much smaller than the inertia forces on the same side and can be neglected (Chopra, 2001). Thus, for a lumped mass model, i.e., $\mathbf{M}_c = 0$, the dynamic component of the response is obtained in the differential form

$$\mathbf{M}\ddot{\mathbf{x}}^d + \mathbf{C}\dot{\mathbf{x}}^d + \mathbf{K}\mathbf{x}^d = -\mathbf{M}\mathbf{R}\ddot{\mathbf{u}} \tag{2.3}$$

Assuming classical damping, let $\mathbf{\Phi} = [\boldsymbol{\phi}_1 \quad \cdots \quad \boldsymbol{\phi}_N]$, ω_i and ζ_i, $i = 1, \dots, N$, respectively denote the modal matrix, natural frequencies, and modal damping ratios of the fixed-base structure. Using the transformation $\mathbf{x}^d = \mathbf{\Phi}\mathbf{y}$, $\mathbf{y} = [y_1 \quad \cdots \quad y_N]^{\mathrm{T}}$, in Eqn. (2.3) and employing the orthogonality of the mode shapes, the decoupled equations of motion are

$$\ddot{y}_i(t) + 2\zeta_i\omega_i\dot{y}_i(t) + \omega_i^2 y_i(t) = -\sum_{k=1}^{m} \beta_{ki}\ddot{u}_k(t) \tag{2.4}$$

where $\beta_{ki} = \boldsymbol{\phi}_i^{\mathrm{T}}\mathbf{M}\mathbf{r}_k / \boldsymbol{\phi}_i^{\mathrm{T}}\mathbf{M}\boldsymbol{\phi}_i$ is the modal participation factor associated with mode i and support DOF k. We can write

$$y_i(t) = \sum_{k=1}^{m} \beta_{ki}s_{ki}(t) \tag{2.5}$$

where $s_{ki}(t)$ is the normalized response of mode i to the kth support motion, which is obtained as the solution to

$$\ddot{s}_{ki}(t) + 2\zeta_i\omega_i\dot{s}_{ki}(t) + \omega_i^2 s_{ki}(t) = -\ddot{u}_k(t) \tag{2.6}$$

Substituting for the pseudo-static component of $\mathbf{x}$ in terms of the support displacements and for the dynamic component in terms of the normalized modal responses, we obtain

$$\mathbf{x}(t) = \sum_{k=1}^{m} \mathbf{r}_k u_k(t) + \sum_{k=1}^{m}\sum_{i=1}^{N} \boldsymbol{\phi}_i\beta_{ki}s_{ki}(t) \tag{2.7}$$

A generic response quantity of interest, $z(t)$, such as the relative displacement between two DOF or an internal force component, can be written as a linear combination of the support displacements and the displacements at the unconstrained DOF, i.e.

$$z(t) = \mathbf{q}_u^{\mathrm{T}}\mathbf{u}(t) + \mathbf{q}_x^{\mathrm{T}}\mathbf{x}(t) \tag{2.8}$$

where $\mathbf{q}_u = [q_{u,1} \quad \cdots \quad q_{u,m}]^{\mathrm{T}}$ and $\mathbf{q}_x = [q_{x,1} \quad \cdots \quad q_{x,N}]^{\mathrm{T}}$ are coefficient vectors. Eqn. (2.8) represents a generalization of the original formulation by Der Kiureghian and Neuenhofer (1992), which considered $z(t)$ a function of only $\mathbf{x}(t)$. This generalization allows consideration of response quantities that are functions of displacements at both the constrained as well as the support DOF, e.g., the drift of a bridge column or an internal force of a structural model with condensed rotational degrees of freedom. Eqn. (2.8) can be written as

$$z(t) = \sum_{k=1}^{m} a_k u_k(t) + \sum_{k=1}^{m} \sum_{i=1}^{N} b_{ki} s_{ki}(t) \tag{2.9}$$

where

$$a_k = q_{u,k} + \mathbf{q}_x^{\mathrm{T}} \mathbf{r}_k \tag{2.10}$$

is interpreted as the response quantity of interest when the kth support DOF is statically displaced by a unit amount with all other support DOF remaining fixed, and

$$b_{ki} = \mathbf{q}_x^{\mathrm{T}} \boldsymbol{\Phi}_i \beta_{ki} \tag{2.11}$$

called the effective modal participation factor (Der Kiureghian and Neuenhofer, 1992), is interpreted as the contribution of the ith mode to the response $z(t)$ arising from the excitation at the kth support DOF when the normalized modal response $s_{ki}(t)$ is equal to unity. The coefficients a_k and b_{ki} depend only on the structural properties and the response quantity of interest and, as described in Section 2.6.1, can be computed by use of any conventional static analysis program. Properties of these coefficients have been derived by Nakamura et al. (1993) for the original MSRS formulation and are given next for the generalized formulation.

The properties of the coefficients a_k remain the same, as in the original formulation: When the vector $\mathbf{u}$ contains only translational components, $\sum_{k=1}^{m} a_k = 1$, if $z(t)$ is a nodal translational displacement, and $\sum_{k=1}^{m} a_k = 0$, if $z(t)$ is a nodal rotational displacement or an internal force component. These identities are derived by employing the principle of superposition (which holds for the response of linear systems) and noticing that the sum of the a_k coefficients represents the response quantity of interest when all support DOF are statically displaced by a unit amount, i.e., $\mathbf{u} = \mathbf{1}$. Note that when the vector $\mathbf{u}$ contains only translational components, the state $\mathbf{u} = \mathbf{1}$ corresponds to a rigid body motion, which causes no rotations or internal forces in the structure.

However, for the generalized formulation, the identity $a_k = \sum_{i=1}^{N} b_{ki}$ (Nakamura et al., 1993) holds under the condition that the response quantity of interest depends only on the displacements at the unconstrained DOF and not on the support displacements, i.e., the case where $q_{u,k} = 0$ in Eqn. (2.8). This identity is derived by using the definition of β_{ki} in conjunction with the orthogonality properties of the modal eigenvectors to obtain $\mathbf{M}\mathbf{r}_k = \sum_{\mathrm{i}=1}^{\mathrm{N}} \mathbf{M}\boldsymbol{\Phi}_i \beta_{ki}$ and by multiplying both sides of the latter equation by $\mathbf{q}_x^{\mathrm{T}} \mathbf{M}^{-1}$.

The above properties can be used to check the accuracy of the computed a_k and b_{ki} coefficients under the specified conditions. The b_{ki} coefficients do not necessarily decrease in magnitude with increasing mode number, and hence, the latter identity is useful only when all modes of the structure are included in the analysis.

2.2.2 The MSRS rule

In earthquake engineering practice, it is common to specify the design ground motion in terms of response spectra. Hence, methods for computing structural response directly in terms of the response spectra defining input support motions are of interest. The MSRS rule provides a fundamental solution to this problem. Using Eqn. (2.9) and the principles of stationary random vibration theory, Der Kiureghian and Neuenhofer (1992) have shown that, for the case of translational support motions, the mean of the peak of the generic response quantity $z(t)$ can be approximately obtained in the form

$$\begin{aligned}\mathrm{E}[\max|z(t)|] \approx \Bigg[& \sum_{k=1}^{m}\sum_{l=1}^{m} a_k a_l \rho_{u_k u_l} u_{k,\max} u_{l,\max} \\ & + 2\sum_{k=1}^{m}\sum_{l=1}^{m}\sum_{j=1}^{N} a_k b_{lj} \rho_{u_k s_{lj}} u_{k,\max} D_l(\omega_j,\ \zeta_j) \\ & + \sum_{k=1}^{m}\sum_{l=1}^{m}\sum_{i=1}^{N}\sum_{j=1}^{N} b_{ki} b_{lj} \rho_{s_{ki} s_{lj}} D_k(\omega_i,\ \zeta_i) D_l(\omega_j,\ \zeta_j)\Bigg]^{1/2}\end{aligned} \tag{2.12}$$

The preceding equation represents the MSRS combination rule. The first, double-sum term inside the square brackets is the pseudo-static component of the response, the third, quadruple-sum term is the dynamic component, and the second, triple-sum term is a cross term of the pseudo-static and dynamic components. The mean of the peak response is given in terms of the structural properties as reflected in the coefficients a_k and b_{ki}, the mean peak ground displacements, $u_{k,\max}$, the ordinates of the mean displacement response spectrum, $D_k(\omega_i,\ \zeta_i)$, for each support motion and each modal frequency and damping ratio, and three sets of cross correlation coefficients: $\rho_{u_k u_l}$, describing the correlation between the kth and lth support displacements, $\rho_{u_k s_{lj}}$, describing the correlation between the kth support displacement and the response of mode j to the lth support motion, and $\rho_{s_{ki} s_{lj}}$, describing the correlation between the responses of modes i and j to the kth and lth support motions, respectively. These cross-correlation coefficients are given by

$$\begin{aligned}\rho_{u_k u_l} &= \frac{1}{\sigma_{u_k}\sigma_{u_l}}\int_{-\infty}^{\infty} G_{u_k u_l}(\omega)d\omega \\ \rho_{u_k s_{lj}} &= \frac{1}{\sigma_{u_k}\sigma_{s_{lj}}}\int_{-\infty}^{\infty} H_j(-\omega)G_{u_k \ddot{u}_l}(\omega)d\omega \\ \rho_{s_{ki} s_{lj}} &= \frac{1}{\sigma_{s_{ki}}\sigma_{s_{lj}}}\int_{-\infty}^{\infty} H_i(\omega)H_j(-\omega)G_{\ddot{u}_k \ddot{u}_l}(\omega)d\omega\end{aligned} \tag{2.13}$$

where $G_{xy}(\omega)$ denotes the cross-power spectral density (PSD) of processes x and y, $H_i(\omega) = -(\omega_i^2 - \omega^2 + 2i\zeta_i\omega_i\omega)^{-1}$ represents the i-th mode frequency response function (FRF) for relative displacement response with respect to the base acceleration; and σ_{u_k} and $\sigma_{s_{ki}}$ are the root-mean-squares of $u_k(t)$ and $s_{ki}(t)$, respectively, given by

$$\begin{aligned} \sigma_{u_k}^2 &= \int_{-\infty}^{\infty} G_{u_k u_k}(\omega) d\omega \\ \sigma_{s_{ki}}^2 &= \int_{-\infty}^{\infty} |H_i(\omega)|^2 G_{\ddot{u}_k\ddot{u}_k}(\omega) d\omega \end{aligned} \tag{2.14}$$

To circumvent the dependence of the cross-correlation coefficients on the PSDs of the support motions, we use the correspondence between the response spectrum and the PSD of a ground acceleration process. Der Kiureghian and Neuenhofer (1992) have derived the following approximate relation

$$G_{\ddot{u}_k\ddot{u}_k}(\omega) = \frac{\omega^{p+2}}{\omega^p + \omega_f^p}\left(\frac{2\zeta\omega}{\pi} + \frac{4}{\pi\tau}\right)\left[\frac{D_k(\omega,\zeta)}{p_s(\omega)}\right]^2 \tag{2.15}$$

in which p and ω_f are parameters selected by adjusting the PSD for low frequencies so that it is consistent with the peak ground displacement (the condition $p \gg 2$ satisfies the requirement that the spectral density of the ground displacement approaches a finite or zero value as $\omega \to 0$), τ is the duration of the strong motion phase of the ground motion, ζ is a reference damping ratio, and $p_s(\omega)$ is a peak factor associated with the response of an oscillator (Der Kiureghian, 1980). Der Kiureghian and Neuenhofer (1992) have shown that the correlation coefficients in Eqns. (2.13) are relatively insensitive to the selection of the parameters p, ω_f, ζ and τ. In the current study, we use $p = 3$, $\zeta = 0.05$ and $\tau = 10$ s. According to Der Kiureghian and Neuenhofer (1992), the value of ω_f that is consistent with $p = 3$ is $\omega_f = 0.705$.

The cross-PSD of ground accelerations can be obtained in terms of the auto-PSDs and a coherency function that characterizes the spatial variability of ground motion, as described in the following section. All the other required PSDs can be evaluated using the well known relation for the PSD of a derivative process:

$$G_{x^{(r)}y^{(r)}}(\omega) = (\mathrm{i}\omega)^r\,(-\mathrm{i}\omega)^s G_{xy}(\omega) \tag{2.16}$$

where $x^{(r)}$ denotes the r-th derivative of $x(t)$. The above analysis shows that the cross-correlation coefficients $\rho_{u_k u_l}$ are only functions of the support excitations, whereas the cross-correlation coefficients $\rho_{u_k s_{lj}}$ and $\rho_{s_{ki} s_{lj}}$ additionally depend on the modal frequencies and damping ratios of the structure. The set of response spectra for all support DOF (including the limits at infinite period, which equal the respective peak ground displacements) and the set of coherency functions for all pairs of support motions represent a complete specification of the input ground motions for the evaluation of the needed cross-correlation coefficients.

2.2.3 The coherency function

The coherency function characterizes the spatial variability of the ground motion random field in the frequency domain. Spatial variations of earthquake-induced ground motions occur due to four distinct phenomena (Der Kiureghian, 1996). The first phenomenon, known as the *incoherence effect*, arises from the loss of coherency of the motion as a result of the propagation of seismic waves in a heterogeneous medium with numerous reflections and refractions, and of the differential super-positioning of waves arriving from different parts of an extended source. The second phenomenon, known as the *wave-passage effect*, arises due to the difference in the arrival times of waves at separate stations. The third is the *site-response effect*, i.e., the effect of the local soil profiles on the amplitude and frequency content of the bedrock motion as it propagates upward at each support location. Finally, the *attenuation effect* is the gradual decay of wave amplitudes with distance from the source of the earthquake. The latter effect is insignificant for the distances of interest and is neglected in the following analysis.

For a pair of stationary ground acceleration processes $\ddot{u}_k(t)$ and $\ddot{u}_l(t)$, the complex-valued coherency function is a normalized version of their cross-PSD:

$$\gamma_{kl}(\omega) = \frac{G_{\ddot{u}_k\ddot{u}_l}(\omega)}{\left[G_{\ddot{u}_k\ddot{u}_k}(\omega)G_{\ddot{u}_l\ddot{u}_l}(\omega)\right]^{1/2}} \tag{2.17}$$

Der Kiureghian (1996) has shown that the modulus of the coherency function characterizes the incoherency effect, whereas its phase angle characterizes the wave passage and variable site-response effects. Thus, the coherency function can be written in the form

$$\gamma_{kl}(\omega) = |\gamma_{kl}(\omega)|^{ic} \exp\{\mathrm{i}[\theta_{kl}(\omega)^{wp} + \theta_{kl}(\omega)^{sr}]\} \tag{2.18}$$

One form of the incoherence component that has been extensively used is (Luco and Wong , 1986)

$$|\gamma_{kl}(\omega)|^{ic} = \exp\left[-\left(\frac{\alpha d_{kl}\omega}{v_s}\right)^2\right] \tag{2.19}$$

in which d_{kl} is the distance between the sites k and l, v_s is the average shear wave velocity of the ground medium along the wave travel path, and α is an incoherence coefficient that can be empirically estimated from data (Luco and Wong, 1986) or determined in terms of the soil properties and depth of the layers (Zerva and Harada, 1984). The phase shift due to the wave-passage effect is given by (Luco and Wong, 1986; Der Kiureghian, 1996)

$$\theta_{kl}(\omega)^{wp} = \frac{\omega d_{kl}^{L}}{v_{app}} \tag{2.20}$$

where d_{kl}^{L} is the projected algebraic horizontal distance in the longitudinal direction of propagation of waves and v_{app} is the surface apparent wave velocity. The phase shift due to the site-response effect is given by (Der Kiureghian, 1996)

$$\theta_{kl}(\omega)^{sr} = \tan^{-1}\frac{\mathrm{Im}[h_k(\omega)h_l(-\omega)]}{\mathrm{Re}[h_k(\omega)h_l(-\omega)]} \tag{2.21}$$

where $h_s(\omega)$, $s = k, l$, is the FRF for the absolute acceleration response of the site associated with the sth support DOF. The derivation of Eqn. (2.21) is based on the assumptions of linear (or linearized) behavior of the soil column, vertical wave propagation at each site and neglect of dynamic interaction between sites. Further details on the modeling of the soil FRF are presented below.

2.2.4 Modeling of the site response

The FRF at each support point is required for two purposes: (a) to determine the response spectrum at the site when the input response spectrum is specified for only a reference site, (b) to evaluate the site-response component of the coherency function. The FRF of a site is also used later in this study to simulate arrays of coherent ground motions, see Chapter 4.

When a detailed description of the soil profile at a site is available, i.e., soil types, thicknesses and constitutive properties of the various layers, the site FRF can be determined as the Fourier transform of the unit-impulse response function of the soil column, which is obtained by time-domain analysis to an impulsive loading at the bedrock level. The impulsive load may be scaled to approximately account for nonlinear soil behavior (Der Kiureghian et al., 1997). If down-hole recorded motions are available at the surface and bedrock levels, an empirical estimate of the FRF is given by the ratio of the cross-PSD of the surface and bedrock motions over the auto-PSD of the bedrock motion (see Der Kiureghian et al., 1997, for example cases). Alternatively, the FRF of the soil layer can be described using theoretical models, as described below.

A theoretical model that properly reflects the physics of vertical propagation of shear waves in an elastic medium is given by (Safak, 1995)

$$h_k(\omega) = \frac{\left(1 + r_k - \mathrm{sgn}(\omega)\frac{\mathrm{i}}{4Q_k}\right)\exp\left[-\mathrm{i}\omega\tau_k\left(1 - \mathrm{sgn}(\omega)\frac{\mathrm{i}}{2Q_k}\right)\right]}{1 + \left(r_k - \mathrm{sgn}(\omega)\frac{\mathrm{i}}{4Q_k}\right)\exp\left[-2\mathrm{i}\omega\tau_k\left(1 - \mathrm{sgn}(\omega)\frac{\mathrm{i}}{2Q_k}\right)\right]} \tag{2.22}$$

In the above expression, the subscript k refers to the kth site, τ_k is the time it takes for waves to travel from the bedrock to the ground surface, Q_k is a quality factor, r_k is the reflection coefficient of vertically propagating waves and $\mathrm{sgn}(\cdot)$ is the signum function. If the depth to bedrock is z_k and the shear wave velocity of the soil layer is $v_{s,k}$, then $\tau_{s,k} = z_k/v_{s,k}$. The quality factor is related to the damping of the soil layer, ζ_k, through $Q_k = 1/2\zeta_k$. Finally, the reflection coefficient is given by $r_k = (\rho_b v_b - \rho_{s,k} v_{s,k})/(\rho_b v_b + \rho_{s,k} v_{s,k})$, in which the sets (ρ_b, v_b) and $\left(\rho_{s,k}, v_{s,k}\right)$ represent the density and shear wave velocity of the bedrock and the soil layer at the kth site, respectively. According to this model, the resonant frequencies of the soil layer are $\omega_{j,k} = j\pi v_{s,k}/2z_k, j = 1, 3, 5, \ldots$. The rate of decay of the corresponding peaks in the modulus of the FRF depends on the Q_k factor. We note that the $\mathrm{sgn}(\omega)$ function in Eqn. (2.22) does not appear in the expression given by Safak (1995), but is introduced here to obtain an FRF consistent with rules in random vibration theory, where negative frequencies are also considered.

When the behavior of the soil column is dominated by its first mode, or when high-frequency components of the ground motion do not have significant contributions to the structural response, a single-degree-of-freedom (SDOF) filter idealization of the soil column can be used. In this case, the site FRF is given by (Clough and Penzien, 1993)

$$h_k(\omega) = \frac{\omega_k^2 + 2\mathrm{i}\zeta_k \omega_k \omega}{\omega_k^2 - \omega^2 + 2\mathrm{i}\zeta_k \omega_k \omega} \tag{2.23}$$

where ω_k and ζ_k represent the filter frequency and damping ratio. The frequency ω_k can be approximated by the first resonant frequency of the soil layer, $\omega_k = \pi v_{s,k}/2z_k$, where z_k and $v_{s,k}$ are the corresponding depth and effective shear wave velocity, respectively. The filter damping ratio, ζ_k, primarily controls the bandwidth of the process and tends to be larger for firmer grounds. Values of this parameter for various soil types have been suggested by Der Kiureghian and Neuenhofer (1992). When the response spectrum at a site is known, one way to select these two parameters for the site FRF is to fit the theoretical acceleration PSD to the approximate PSD estimated through Eqn. (2.15), using, for example, least-squares minimization. Under the assumptions of linear (or linearized) behavior of the soil column and vertical wave propagation, a theoretical model that relates the acceleration PSD at the surface of site k, $G_{\ddot{u}_k\ddot{u}_k}(\omega)$, to the corresponding PSD at the bedrock level, $G_{\ddot{u}_k\ddot{u}_k}(\omega)^{bedrock}$, is

$$G_{\ddot{u}_k\ddot{u}_k}(\omega) = |h_k(\omega)|^2 G_{\ddot{u}_k\ddot{u}_k}(\omega)^{bedrock} \tag{2.24}$$

Assuming for simplicity that the motion at the bedrock level is a white noise process, the theoretical PSD is given by the squared modulus of $h_k(\omega)$ factored by a constant. The parameters to estimate then are ω_k, ζ_k and the scale parameter.

Selection among the methods for modeling the site-response described above should be based on the available information.

2.3 MODE TRUNCATION CRITERIA FOR RESPONSE TO DIFFERENTIAL SUPPORT MOTIONS

In practical application of the MSRS rule, it is often necessary to truncate the modal contributions beyond a mode $n \ll N$. Of course this truncation only affects the dynamic component of the response, i.e., the triple- and quadruple-sum terms in Eqn. (2.12). For the sake of simplicity in developing criteria for modal truncation, we neglect the triple-sum cross term and the cross-modal contributions in the quadruple-sum term. We also consider the extreme cases of uniform support motions and totally incoherent (statistically independent) support motions. In the case of uniform support motions, $\rho_{s_{ki}s_{li}} = 1$ for all k, l and, thus, the main term in Eqn. (2.12) affected by modal truncation is $\sum_{i=1}^{N}\left[\sum_{k=1}^{m} b_{ki}D_k(\omega_i,\ \zeta_i)\right]^2$. In the case of totally incoherent support motions, $\rho_{s_{ki}s_{li}} = 1$ when $k = l$ and $\rho_{s_{ki}s_{li}} = 0$ when $k \neq l$ leading this term to $\sum_{i=1}^{N}\sum_{k=1}^{m}\left[b_{ki}D_k(\omega_i,\ \zeta_i)\right]^2$. Under the stated conditions, the ith modal contribution in the case of uniform support motions is $\left[\sum_{k=1}^{m} b_{ki}D_k(\omega_i,\ \zeta_i)\right]^2 = (\mathbf{q}_x^{\mathrm{T}}\boldsymbol{\phi}_i)^2\left[D_k(\omega_i,\ \zeta_i)\right]^2(\sum_{k=1}^{m}\beta_{ki})^2$, whereas in the case of totally incoherent support motions it is $\sum_{k=1}^{m}\left[b_{ki}D_k(\omega_i,\ \zeta_i)\right]^2 = (\mathbf{q}_x^{\mathrm{T}}\boldsymbol{\phi}_i)^2\left[D_k(\omega_i,\ \zeta_i)\right]^2\sum_{k=1}^{m}\beta_{ki}^2$. Thus, for a given response quantity and specified response spectra, the relation between the modal contributions in the two cases depends on the relation between $(\sum_{k=1}^{m}\beta_{ki})^2$ and $\sum_{k=1}^{m}\beta_{ki}^2$. We note that if the modal participation factors of the ith mode, β_{ki}, have the same sign for all k, then $(\sum_{k=1}^{m}\beta_{ki})^2 = (\sum_{k=1}^{m}|\beta_{ki}|)^2$ and the ith modal contribution is the largest in the case of uniform support excitations among all cases of ground motion spatial variability. If the modal participation factors β_{ki} have alternating signs so that $\sum_{k=1}^{m}\beta_{ki} = 0$, then the ith modal contribution is the smallest in the case of uniform support excitations among all other cases.

The extreme cases of uniform and totally incoherent support motions, discussed above, can be used to provide simplified guidelines for mode truncation for intermediate cases of spatial variability. In order to derive an expression for the modal contributions that is independent of the input support motions, we assume the modal frequencies fall in the region of constant spectral pseudo-acceleration and that the modal damping ratios are all identical. In that case, each $D_k(\omega_i,\ \zeta_i)$ is proportional to $1/\omega_i^2$. Using this simplification, in the case of uniform support motions, the contribution of the ith mode is proportional to $(\sum_{k=1}^{m} b_{ki})^2/\omega_i^4$. Specializing for the total base shear, the latter expression becomes $\left(M_i\gamma_i^2\right)^2$, where $M_i = \boldsymbol{\phi}_i^{\mathrm{T}}\mathbf{M}\boldsymbol{\phi}_i$ and $\gamma_{\mathrm{i}} = \sum_{k=1}^{m}\beta_{ki}$ (Kahan et al., 1996). Employing the identity $\sum_{i=1}^{N} M_i\gamma_i^2 = \mathbf{s}^{\mathrm{T}}\mathbf{M}\mathbf{s}$, where $\mathbf{s} = \sum_{k=1}^{m}\mathbf{r}_k$, the ratio

$$r_n^U = \frac{\sum_{i=1}^{n} M_i\gamma_i^2}{\mathbf{s}^{\mathrm{T}}\mathbf{M}\mathbf{s}} = \frac{\sum_{i=1}^{n} M_i(\sum_{k=1}^{m}\beta_{ki})^2}{\sum_{k=1}^{m}\mathbf{r}_k^{\mathrm{T}}\,\mathbf{M}\sum_{k=1}^{m}\mathbf{r}_k} \tag{2.25}$$

is introduced, which provides a measure of the participating modal mass for the case of uniform support motions. This ratio is commonly used in engineering practice to determine the number of modes required in the dynamic analysis of ordinary structures. In the case of totally incoherent support motions, the ith modal contribution is proportional to $\sum_{k=1}^{m} b_{ki}^2/\omega_i^4$. Kahan et al. (1996) have shown that for the total base shear the latter expression becomes $\left(M_i \sum_{k=1}^{m} \beta_{ki}^2\right)^2$. Accounting for the property $\sum_{i=1}^{N} M_i \sum_{k=1}^{m} \beta_{ki}^2 = \sum_{k=1}^{m} \mathbf{r_k^{\mathrm{T}} M r_k}$ (Kahan et al., 1996), the ratio

$$r_n^{TI} = \frac{\sum_{i=1}^{n} M_i \sum_{k=1}^{m} \beta_{ki}^2}{\sum_{k=1}^{m} \mathbf{r_k^{\mathrm{T}} M r_k}} \tag{2.26}$$

is introduced, which provides a measure of the participating modal mass for the case of totally incoherent support motions. This ratio is proposed by Kahan et al. (1996) as a measure of the number of modes required in the MSRS analysis. The ratios r_n^U and r_n^{TI} have the advantages of being non-decreasing in n and not depending on the modal properties of the truncated modes. These ratios are indicative of the accuracy of the dynamic component only and not of the total response, since the latter also depends on the pseudo-static component, not affected by mode truncation. Numerical examination of these ratios for example bridge models is presented in Chapter 3.

2.4 EXTENDED MSRS RULE

When high-frequency modes are truncated, an improved approximation of the response can be obtained by accounting for the quasi-static contributions of the truncated modes. This concept has been previously used for structures subjected to uniform support motions (Singh and McCown, 1986; Leger and Wilson, 1988; Der Kiureghian and Nakamura, 1993). Here, we apply the method to spatially varying support motions by extending the MSRS rule.

When ω_i is large relative to important frequencies of the input excitation, the last term in the left-hand side of Eqn. (2.6) is dominant and the ith normalized modal response to the kth support motion can be approximated as $s_{ki}(t) \approx -\omega_i^{-2}\ddot{u}_k(t)$. Using this relation in Eqn. (2.7) for modes $i > n$, we have

$$z(t) \approx \sum_{k=1}^{m} a_k u_k(t) + \sum_{k=1}^{m} \left[\sum_{i=1}^{n} b_{ki} s_{ki}(t) - \sum_{i=n+1}^{N} \frac{b_{ki}}{\omega_i^2} \ddot{u}_k(t)\right] \tag{2.27}$$

The effective modal participation factors b_{ki} for $i > n$ can be eliminated from Eqn.(2.27) by employing the identity

$$-\sum_{i=1}^{N} \frac{b_{ki}}{\omega_i^2} = -\mathbf{q}_x^{\mathrm{T}} \mathbf{K}^{-1} \mathbf{M} \mathbf{r}_k \tag{2.28}$$

The right-hand side of this equality represents the response $\mathbf{q}_x^{\mathrm{T}} \mathbf{x}^d$ when a static excitation defined by $\ddot{u}_k = 1$ and $\ddot{u}_l = 0$ for $l \neq k$ is specified in Eqn. (2.3). The left-hand side is the same response obtained by modal decomposition, i.e., from Eqn. (2.6) and the second term in Eqn. (2.9). Rearranging terms, one obtains

$$\sum_{i=n+1}^{N} \frac{b_{ki}}{\omega_i^2} = \mathbf{q}_x^{\mathrm{T}} \mathbf{K}^{-1} \mathbf{M} \mathbf{r}_k - \sum_{i=1}^{n} \frac{b_{ki}}{\omega_i^2} = d_k \tag{2.29}$$

Using the above identity, Eqn. (2.27) can be written in a form that involves the dynamic properties of only the first n modes:

$$z(t) \approx \sum_{k=1}^{m} a_k u_k(t) + \sum_{k=1}^{m} \sum_{i=1}^{n} b_{ki} s_{ki}(t) - \sum_{k=1}^{m} d_k \ddot{u}_k(t) \tag{2.30}$$

Note that this improved expression of the response now additionally involves the support accelerations, $\ddot{u}_k(t)$.

Assuming jointly stationary, zero-mean support motions $u_k(t)$, and following the steps involved in the derivation of the original MSRS rule (Der Kiureghian and Neuenhofer, 1992), we can obtain the mean of the extreme peak of the process $z(t)$ in Eqn. (2.30). The derivation involves (i) using Eqn. (2.30) to obtain the PSD of the generic response $z(t)$ in terms of the auto- and cross-PSDs of the processes $u_k(t)$, $\ddot{u}_k(t)$ and $s_{ki}(t)$, (ii) integrating over the frequency domain to obtain the mean-square of $z(t)$, $\sigma_z^2 = \int_{-\infty}^{\infty} G_{zz}(\omega) d\omega$, in terms of the mean-squares of $u_k(t)$, $\ddot{u}_k(t)$ and $s_{ki}(t)$ and their covariances, (iii) replacing the root-mean squares of $u_k(t)$, $\ddot{u}_k(t)$ and $s_{ki}(t)$ by respectively the mean peak ground displacement, the mean peak ground acceleration, and the mean response spectrum ordinate for mode i, each divided by its corresponding peak factor (Der Kiureghian, 1980), (iv) multiplying the root-mean square of $z(t)$ with its peak factor to obtain the mean of the extreme peak response, and (v) approximating the ratios of the peak factors by unity. The latter assumption is valid since the peak factors are only mildly dependent on the characteristics of each process (Der Kiureghian, 1980). This procedure leads to the following extended MSRS rule:

$$
\begin{aligned}
\mathrm{E}[max|z(t)|] \approx \Bigg[& \sum_{k=1}^{m}\sum_{l=1}^{m} a_k a_l \rho_{u_k u_l} u_{k,\max} u_{l,\max} \\
& + 2\sum_{k=1}^{m}\sum_{l=1}^{m}\sum_{j=1}^{n} a_k b_{lj} \rho_{u_k s_{lj}} u_{k,\max} D_l(\omega_j,\ \zeta_j) \\
& + \sum_{k=1}^{m}\sum_{l=1}^{m}\sum_{i=1}^{n}\sum_{j=1}^{n} b_{ki} b_{lj} \rho_{s_{ki} s_{lj}} D_k(\omega_i,\ \zeta_i) D_l(\omega_j,\ \zeta_j) \\
& + \sum_{k=1}^{m}\sum_{l=1}^{m} d_k d_l \rho_{\ddot{u}_k \ddot{u}_l} \ddot{u}_{k,\max} \ddot{u}_{l,\max} - 2\sum_{k=1}^{m}\sum_{l=1}^{m} \rho_{u_k \ddot{u}_l} u_{k,\max} \ddot{u}_{l,\max} \\
& - 2\sum_{k=1}^{m}\sum_{l=1}^{m}\sum_{i=1}^{n} b_{ki} d_l \rho_{s_{ki} \ddot{u}_l}\, D_k(\omega_i,\ \zeta_i) \ddot{u}_{l,\max} \Bigg]^{1/2}
\end{aligned}
\tag{2.31}
$$

In comparison to the original MSRS rule, the extended MSRS rule additionally involves the last three terms. The first of these terms represents the quasi-static contribution of the truncated modes. The second term arises from the covariances of the support displacements and accelerations, and the last term arises from the covariances between the responses of the included modes and the quasi-static responses of the truncated modes. These terms involve three sets of new cross-correlation coefficients, $\rho_{\ddot{u}_k \ddot{u}_l}$, $\rho_{u_k \ddot{u}_l}$ and $\rho_{s_{ki} \ddot{u}_l}$, which, respectively, represent the correlation between the ground accelerations at support DOF k and l, the correlation between the ground displacement at support DOF k and the ground acceleration at support DOF l, and the correlation between the ith modal response to the excitation at support DOF k and the ground acceleration at support DOF l. The newly introduced cross-correlation coefficients are given by

$$
\begin{aligned}
\rho_{\ddot{u}_k \ddot{u}_l} &= \frac{1}{\sigma_{\ddot{u}_k}\sigma_{\ddot{u}_l}} \int_{-\infty}^{\infty} G_{\ddot{u}_k \ddot{u}_l}(\omega) d\omega \\
\rho_{u_k \ddot{u}_l} &= \frac{1}{\sigma_{u_k}\sigma_{\ddot{u}_l}} \int_{-\infty}^{\infty} G_{u_k \ddot{u}_l}(\omega) d\omega \\
\rho_{s_{ki} \ddot{u}_l} &= \frac{1}{\sigma_{s_{ki}}\sigma_{\ddot{u}_l}} \int_{-\infty}^{\infty} H_i(\omega) G_{\ddot{u}_k \ddot{u}_l}(\omega) d\omega
\end{aligned}
\tag{2.32}
$$

In the above expression, the root-mean-squares σ_{u_k} and $\sigma_{s_{ki}}$ are given in Eqn. (2.14), whereas the root mean square of $\sigma_{\ddot{u}_k}$ is given by

$$\sigma_{\ddot{u}_k}^2 = \int_{-\infty}^{\infty} G_{\ddot{u}_k \ddot{u}_k}(\omega) d\omega \tag{2.33}$$

Recall that the PSDs in these expressions are all given in terms of the response spectra defining the support motions, see Eqns. (2.15) and (2.16).

The parametric study in the following section provides insight into the behavior of the three new cross-correlation coefficients.

2.5 PARAMETRIC ANALYSIS OF THE NEW CROSS-CORRELATION COEFFICIENTS

A parametric study of the cross-correlation coefficients $\rho_{\ddot{u}_k \ddot{u}_l}$, $\rho_{u_k \ddot{u}_l}$ and $\rho_{s_{ki} \ddot{u}_l}$ is presented in this section in order to determine the influences of various model parameters and evaluate the significances of the new cross-terms in the extended MSRS rule. For this purpose, we adopt the coherency model described in Section 2.2.3. Considering the range of values that might be of engineering interest, the parameter $\alpha d_{kl}/v_s$ of the coherency function (see Eqn. (2.19)) is varied between 0 and 2 s, and the parameter d_{kl}^L/v_{app} (see Eqn. (2.20)) is given the values 0, 0.5, and 1 s. The case $\alpha d_{kl}/v_s = 0$ neglects the incoherence effect, whereas the case $d_{kl}^L/v_{app} = 0$ neglects the wave passage effect. For the PSD of the ground acceleration at each station k we consider a modified version of the Kanai-Tajimi spectral density (Clough and Penzien, 1993). The Kanai-Tajimi model assumes that the input acceleration at the bedrock level is a white noise and the soil layer behaves as a SDOF oscillator. This model implies an infinite power for ground displacement when $\omega \to 0$. This problem is solved in the Clough-Penzien model by introducing a high-pass filter, such that the modified PSD is given by

$$H_k(\omega) = G_{kk} \frac{\omega_{fk}^4 + 4\zeta_{fk}^2 \omega_{fk}^2 \omega^2}{\left(\omega_{fk}^2 - \omega^2\right)^2 + 4\zeta_{fk}^2 \omega_{fk}^2 \omega^2} \frac{\omega^4}{\left(\omega_{gk}^2 - \omega^2\right)^2 + 4\zeta_{gk}^2 \omega_{gk}^2 \omega^2} \tag{2.34}$$

in which G_{kk} is a scale factor, ω_{fk} and ζ_{fk} are the filter parameters of the Kanai-Tajimi model representing, respectively, the natural frequency and damping of the soil layer at station k, and ω_{gk} and ζ_{gk} are parameters of the high-pass filter. For $\omega_{gk} \ll \omega_{fk}$, the second filter influences only the region of very low frequencies, since the second quotient quickly approaches unity with increasing ω. The filter parameter values for firm, medium and soft soils, as suggested by Der Kiureghian and Neuenhofer (1992), are listed in Table 2.1. The corresponding PSDs for the ground acceleration and ground displacement are shown in Figure 2.1 and Figure 2.2, respectively.

2.5.1 Cross-correlation coefficient between ground accelerations at stations *k* and *l*

Figure 2.3 shows plots of the cross-correlation coefficient $\rho_{\ddot{u}_k\ddot{u}_l}$ for pairs of sites with firm, medium and soft soil conditions. The charts on the left are for identical soil conditions at the two sites, while those on the right are for dissimilar soil conditions. In the top chart on the left, the ground motion spatial variability arises only from the incoherence effect. The correlation coefficient is consistently smaller for firmer soil conditions, for which the acceleration process is richer in high-frequency components. We note that waves with such frequencies tend to lose coherency faster than low-frequency waves. In the top right chart, the lack of perfect correlation when $\alpha d_{kl}/v_s = 0$ is indicative of the differential site effect. In both the aforementioned charts, $\rho_{\ddot{u}_k\ddot{u}_l}$ takes only positive values. However, in the presence of the wave passage effect, the correlation coefficient can take on positive or negative values, typically smaller in magnitude than those in the cases without the wave passage effect. In all cases, the correlation between the two ground acceleration processes is nearly negligible for $\alpha d_{kl}/v_s \geq 0.5$.

Figure 4 in the paper by Der Kiureghian and Neuenhofer (1992) shows plots of the correlation coefficient $\rho_{u_k u_l}$ between ground displacements for similar site conditions and coherency function parameters. A comparison of Figure 2.3 with that figure reveals that the correlation coefficient $\rho_{\ddot{u}_k\ddot{u}_l}$ decays much faster with increasing incoherence and wave passage than $\rho_{u_k u_l}$. This is due to the higher frequency content of the acceleration processes.

2.5.2 Cross-correlation coefficient between ground displacement at station *k* and ground acceleration at station *l*

Figure 2.4 shows plots of the cross-correlation coefficient $\rho_{u_k\ddot{u}_l}$ against the parameter $\alpha d_{kl}/v_s$ for the selected values of d_{kl}^L/v_{app} and for identical (left) and variable (right) soil conditions. For the latter, we only consider the cases where station k (displacement) has firmer soil than station l (acceleration). In absence of the wave-passage effect, the ground displacement at station k is negatively correlated with the ground acceleration at station l. (Note that the displacement and acceleration at a given site generally are negatively correlated processes.) This correlation is generally more significant for softer soils and for cases where the soil for the acceleration site is softer than the soil for the displacement site. Both the incoherence and wave-passage effects tend to reduce the correlation between the two processes. For $\alpha d_{kl}/v_s > 1$ or $d_{kl}^L/v_{app} \geq 1$, $\rho_{u_k\ddot{u}_l}$ is close to zero.

2.5.3 Cross-correlation coefficient between oscillator response at station *k* and ground acceleration at station *l*

Figures 2.5-2.8 show selected plots of the cross-correlation coefficient $\rho_{s_{ki}\ddot{u}_l}$ against the oscillator frequency ω_i when the oscillator damping ratio is $\zeta_i = 0.05$. Sites with firm or soft soil conditions are considered. Figures 2.5 and 2.6 are for identical soil conditions at the two stations, whereas Figures 2.7 and 2.8 are for dissimilar soil conditions. Furthermore, Figures 2.5 and 2.7 are for waves arriving first at station k and then at station l, whereas Figures 2.6 and 2.8 are for waves travelling in the opposite direction. The charts from top to bottom are for increasing values of the magnitude of the wave passage parameter d_{kl}^{L}/v_{app}, which is varied from 0 to ∓ 1 s. The curves in each chart represent three different values of the incoherence parameter, $\alpha d_{kl}/v_s = 0$, 0.1 and 0.2 s.

For $\omega_i \to \infty$, i.e., for an infinitely stiff oscillator, $s_{ki} \to -\ddot{u}_k/\omega_i^2$ and thus $\rho_{s_{ki}\ddot{u}_l} \to -\rho_{\ddot{u}_k\ddot{u}_l}$. If we additionally consider identical soil conditions and neglect the wave passage and incoherence effects, the ground motions at the two stations would be perfectly correlated and hence $\rho_{s_{ki}\ddot{u}_l} \to -1$. In Figures 2.5 and 2.6, for the cases with $\alpha d_{kl}/v_s = 0$ and $d_{kl}^{L}/v_{app} = 0$, when ω_i is large, $\rho_{s_{ki}\ddot{u}_l}$ assumes large negative values that approach -1 at a pace that is faster for softer than for firmer soils. The wave-passage effect and the wave direction strongly influence the correlation between the two processes. When the waves propagate from the oscillator site to the acceleration site (Figures 2.5 and 2.7), $\rho_{s_{ki}\ddot{u}_l}$oscillates with ω_i at a period of approximately v_{app}/d_{kl}^{L}. This is because of the correlation of the oscillator response with the ground acceleration at an earlier time. When the direction of the wave passage is reversed (Figures 2.6 and 2.8), the correlation is practically zero for ground accelerations on firm soil. This is because the oscillator response is independent of the later excitation when the excitation is broadband.

2.6 COMPUTER IMPLEMENTATION OF THE EXTENDED MSRS RULE

The MSRS rule evaluates the mean peak response in terms of the structural properties, reflected in the coefficients a_k and b_{ki} for each response quantity of interest, the support motions as described in terms of the peak ground displacements and the response spectra, and three sets of cross-correlation coefficients. The extended MSRS rule additionally requires the coefficients d_k, which are functions of the structural properties, the peak ground accelerations, and three additional sets of cross-correlation coefficients. The cross-correlation coefficients, in turn, involve the coherency function describing the spatial variability of the ground motion random field. Once the support motions have been specified in terms of response spectra, peak ground displacements, peak ground accelerations, and a coherency function, the implementation of the extended MSRS rule only requires computation of the coefficients a_k, b_{ki} and d_k and the cross-correlation coefficients. In the remainder of this section we describe the computation of the latter quantities, as implemented in the computer code developed for this study.

2.6.1 Computation of the a_k, b_{ki} and d_k coefficients

Any existing structural analysis code that allows specification of imposed nodal displacements and forces can be used to compute the coefficients a_k, b_{ki} and d_k. For the present study, we have used the open-source software OpenSees; however, any 'black-box' structural analysis program that provides restricted access to the code can also be used.

For a response quantity of interest, the coefficient a_k is computed as the response of the structure to a unit static displacement at the kth support DOF, while all other support DOF remain fixed. Thus, the computation of the full set of the coefficients a_k for a set of desired response quantities requires m static analyses.

Considering Eqns. (2.8) and (2.11), the coefficient b_{ki} is interpreted as the response quantity of interest when the displacements at the support DOF are zero and the displacements at the unconstrained degrees of freedom are $\mathbf{x} = \boldsymbol{\phi}_i \beta_{ki}$. Hence, using the notion of equivalent static forces, the coefficient b_{ki} is determined by static analysis of the fixed-base structure subjected to the set of forces $\mathbf{f}_{ki} = \mathbf{K}\boldsymbol{\phi}_i \beta_{ki} = \omega_i^2 \mathbf{M}\boldsymbol{\phi}_i \beta_{ki}$ applied at the unconstrained degrees of freedom. Thus, once the natural frequencies and modal shapes of the fixed-base structure have been determined and provided the mass matrix is available, the set of n b_{ki} coefficients can be computed through $m \times n$ static analyses.

Finally, the coefficient d_k is computed form Eqn. (2.29), in which the term $\mathbf{q}_x^{\mathrm{T}} \mathbf{K}^{-1} \mathbf{M} \mathbf{r}_k$ is obtained as the static response of the fixed-base structure to the set of forces $\mathbf{M}\mathbf{r}_k$. Thus, the full set of the coefficients d_k is determined in terms of the b_{ki} coefficients and the results from m static analyses.

2.6.2 Computation of the cross-correlation coefficients

Evaluation of the cross-correlation coefficients constitutes the main computational effort in the MSRS analysis. For a structure with many support points and a large number of contributing modes, the number of coefficients to be computed can be very large. This has prompted several investigators to declare the MSRS rule as “impractical” and to develop further approximations (Loh and Ku, 1995; Wang and Chen, 2005). However, by careful consideration of the properties of these coefficients and the behavior of the integrands involved, it is possible to develop highly efficient algorithms that perform the required computations in a reasonable time. Below, we discuss computational aspects of the algorithm developed in this study, and specifically, the symmetries considered, the integration scheme and selection of the cuf-off frequency. This algorithm has been implemented in a MATLAB code.

Symmetries

In the original MSRS rule, the total number of cross-correlation coefficients is $m^2 + m^2 N + m^2 N^2$, where n is the number of modes considered and m the number of support motions. Accounting for the symmetries $\rho_{u_k u_l} = \rho_{u_l u_k}$ and $\rho_{s_{ki} s_{lj}} = \rho_{s_{lj} s_{ki}}$ and the identities $\rho_{u_k u_k} = 1$ and $\rho_{s_{ki} s_{ki}} = 1$, the number of distinct coefficients to be computed reduces to $m(m + 2mn + mn^2 - n - 1)/2$. The extended MSRS rule involves $m^2(2 + n)$ additional coefficients. However, accounting for the symmetries $\rho_{\ddot{u}_k \ddot{u}_l} = \rho_{\ddot{u}_l \ddot{u}_k}$ and $\rho_{u_k \ddot{u}_l} = \rho_{u_l \ddot{u}_k}$ and the identity $\rho_{\ddot{u}_k\ddot{u}_k} = 1$, the number of additional coefficients to be computed is $m^2(1+n)$. Obviously, the additional computational effort required by the extended rule is small.

The computational time can be further reduced by noticing that the integrands in Eqns. (2.13) and (2.32) have symmetric real and antisymmetric imaginary parts. Thus, the integrals can be evaluated in the interval $(0,\infty)$ by neglecting the imaginary parts and doubling the real parts of the integrand quantities. The integrals in (2.14) and (2.33) have real and symmetric integrands and can also be evaluated over the interval $(0,\infty)$ and doubled.

Integration method

The integration scheme developed in this study is based on dividing the integration domain in frequency intervals $(\hat{\omega}_r, \hat{\omega}_{r+1})$ within which the integrands vary slowly. Assuming that within these intervals the integrand can be approximated by a low-degree polynomial, we evaluate the corresponding integral with an n point Gaussian quadrature rule, where n is selected according to the desired accuracy. As described next, the discretization along the frequency domain is determined by accounting for the behavior of the relevant integrand.

Design response spectra are usually defined at discrete frequency points, denoted herein as $\tilde{\omega}_s$. Eqn. (2.15) is used to determine the consistent auto-PSDs, $G_{\ddot{u}_k\ddot{u}_k}(\omega)$, at these points, whereas linear interpolation is employed for intermediate points. These functions together with the coherency function are used to compute the cross-PSDs $G_{\ddot{u}_k\ddot{u}_l}$, $G_{u_k\ddot{u}_l}$ and $G_{u_k u_l}$. Since both the auto-PSDs and the coherency function are smooth functions of frequency, all PSDs that appear in Eqns. (2.13)-(2.14) and (2.32)-(2.33) can be well described by low-degree polynomials in the intervals $(\tilde{\omega}_s, \tilde{\omega}_{s+1})$.

The integrands in the expressions for the root-mean-squares $\sigma_{u_k}$and $\sigma_{\ddot{u}_k}$ and the correlation coefficients $\rho_{u_k u_l}$ and $\rho_{u_k\ddot{u}_l}$ only involve the PSDs of the support motions. In this case, the frequency points $\tilde{\omega}_s$ define the discretization along the frequency axis for the evaluation of the corresponding integrals. The integrands in the expressions for the root-mean-squares $\sigma_{s_{ki}}$ and the correlation coefficients $\rho_{s_{ki}s_{lj}}$, $\rho_{u_k s_{lj}}$ and $\rho_{s_{ki}\ddot{u}_l}$ additionally involve one or two modal FRF and, thus, include sharp peaks around the corresponding modal frequencies. To ensure accurate representation of the integrands in these cases, the discretization along the frequency axis, additionally to the points $\tilde{\omega}_s$, includes closely spaced points in the neighbourhoods of the modal frequencies involved.

As an example of the computational efficiency of the developed integration scheme, for a model with $m = 7$ and $n = 30$ (Auburn Ravine Bridge in the example application of Chapter 3), computation of the required 23,436 correlation coefficients in the original MSRS rule (for one direction of excitation) with 3 significant-digit accuracy takes 489s with our MATLAB code on an Intel Core2 Duo computer. The additional time for the extended MSRS rule is only 23s. It is noted that only one set of correlation coefficients is needed for all response quantities of interest. However, new sets of correlation coefficients must be computed if the support response spectra or coherency function are altered.

2.6.3 Cut-off frequency

Eqns. (2.13)-(2.14) and (2.32)-(2.33) assume unbounded frequency content in the input excitation. However, an upper bound is implicitly assumed in most seismic analysis (Der Kiureghian and Nakamura, 1993). When the input excitation is described in terms of the time history of the ground motion, this upper bound is related to the size of the time step. When a design response spectrum is used, the upper bound is defined by the frequency beyond which the pseudo-spectral acceleration is effectively equal to the peak ground acceleration. In the current study, the cut-off frequency for each type of integral is selected such that the values of the integrand beyond this point are considered negligible. The cut-off frequency in the evaluation of the terms σ_{u_k}, $\sigma_{\ddot{u}_k}$, $\rho_{u_k u_l}$, and $\rho_{u_k \ddot{u}_l}$ depends only on the power of the input excitation, whereas the cut-off frequency for the evaluation of $\sigma_{s_{ki}}$, $\rho_{u_k s_{lj}}$, $\rho_{s_{ki} s_{lj}}$, and $\rho_{s_{ki} \ddot{u}_l}$ additionally depends on the frequencies of the relevant modes.

2.7 SUMMARY

In this chapter, first, the MSRS method was generalized to allow consideration of response quantities that involve the support DOFs. Following an investigation of mode truncation criteria for the case of differential support motions, the MSRS rule was extended to account for the quasi-static contributions of the truncated modes. A parametric study of additional cross-correlation coefficients introduced in the extended MSRS method was performed to gain insight into their behavior. Finally, an overview of the computer program developed for the implementation of the generalized and extended MSRS method was presented and the main computational issues were addressed.

Table 2.1: PSD filter parameters for model soil types.

soil type	ω_{fk}, rad/s	ζ_{fk}	ω_{gk}, rad/s	ζ_{gk}
firm	15.0	0.6	1.5	0.6
medium	10.0	0.4	1.0	0.6
soft	5.0	0.2	0.5	0.6

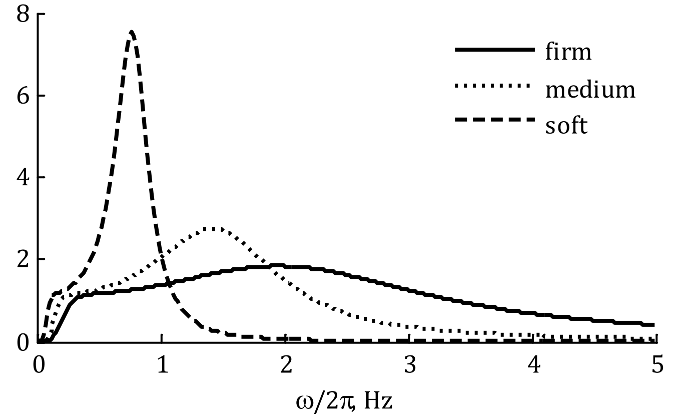

Figure 2.1: Power spectral densities of ground accelerations for firm, medium and soft soils.

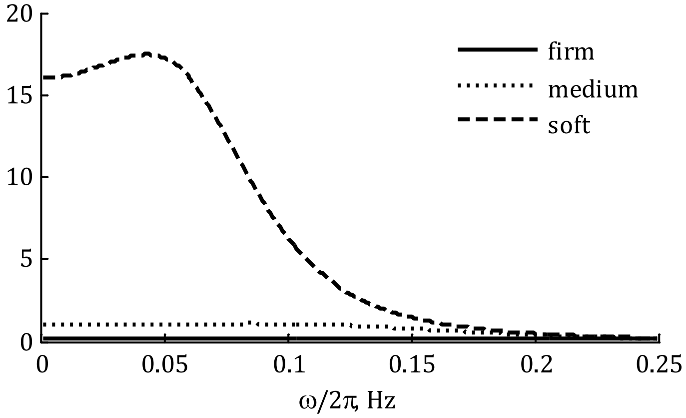

Figure 2.2: Power spectral densities of ground displacements for firm, medium and soft soils.

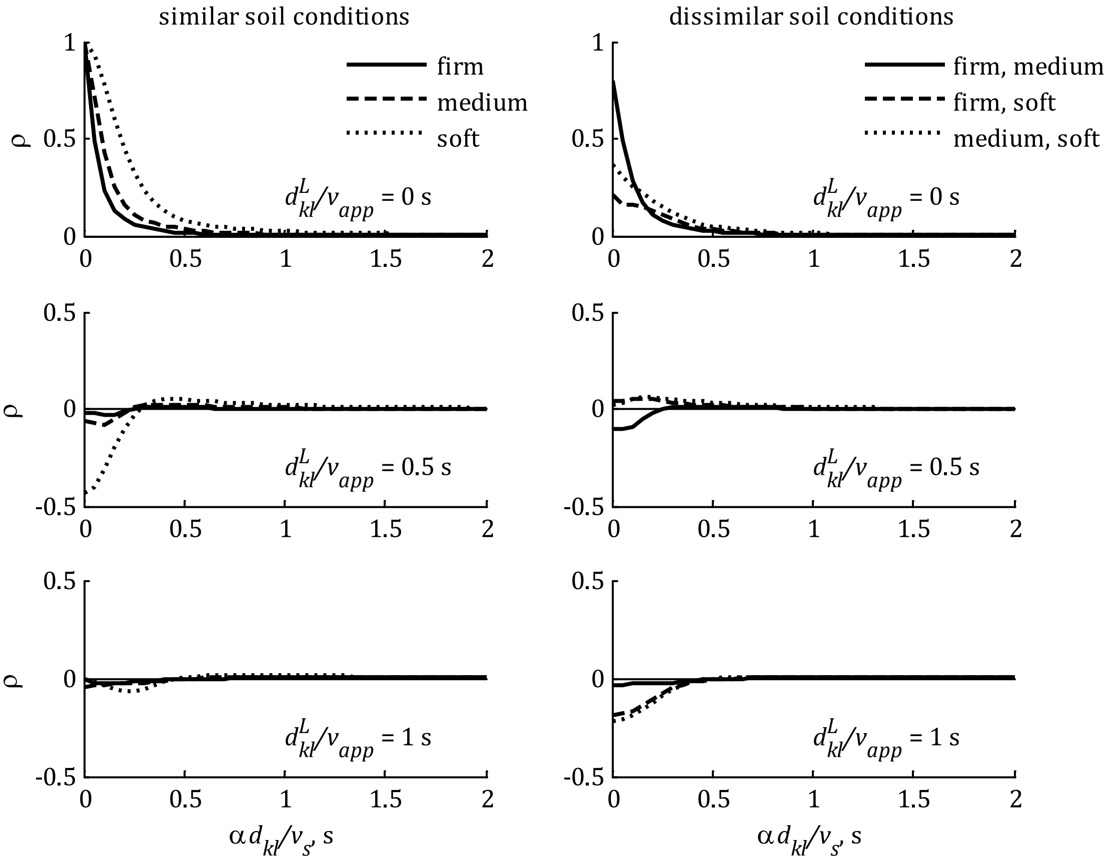

Figure 2.3: Cross-correlation coefficient between ground accelerations at stations *k* and *l*.

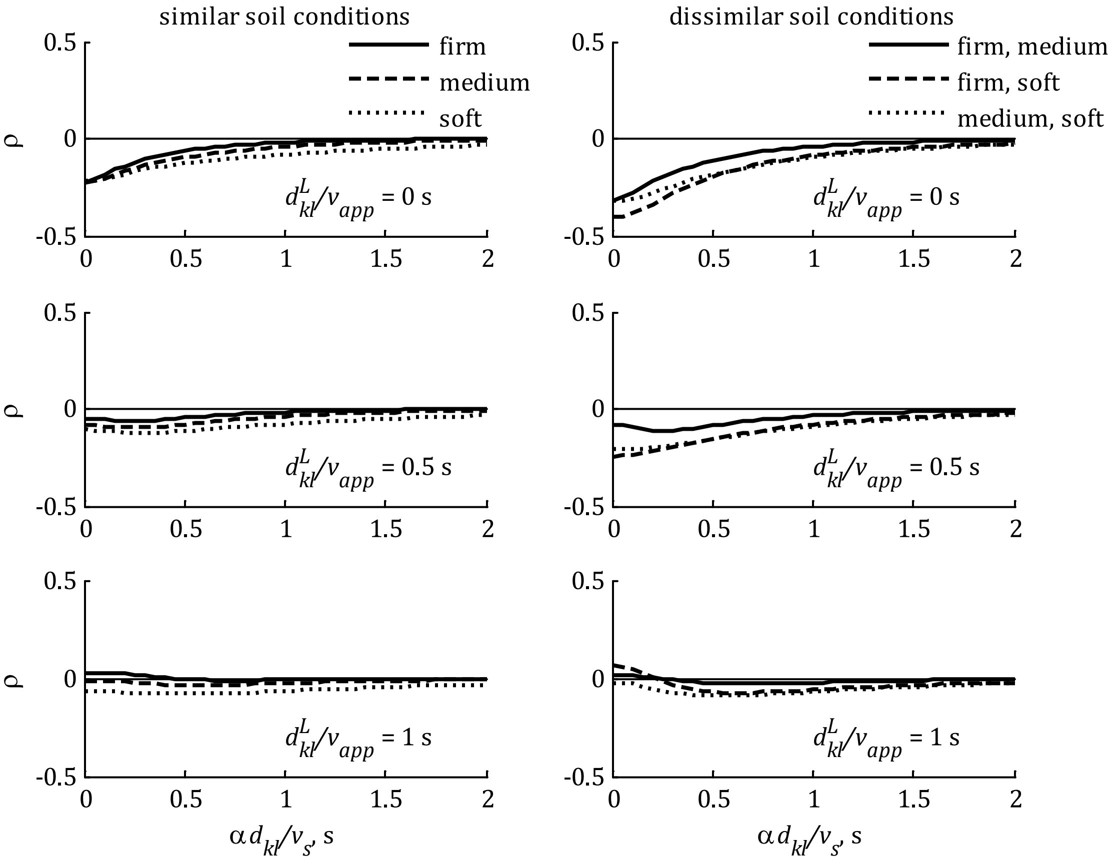

Figure 2.4: Cross-correlation coefficient between ground displacement at station *k* and ground acceleration at station *l*.

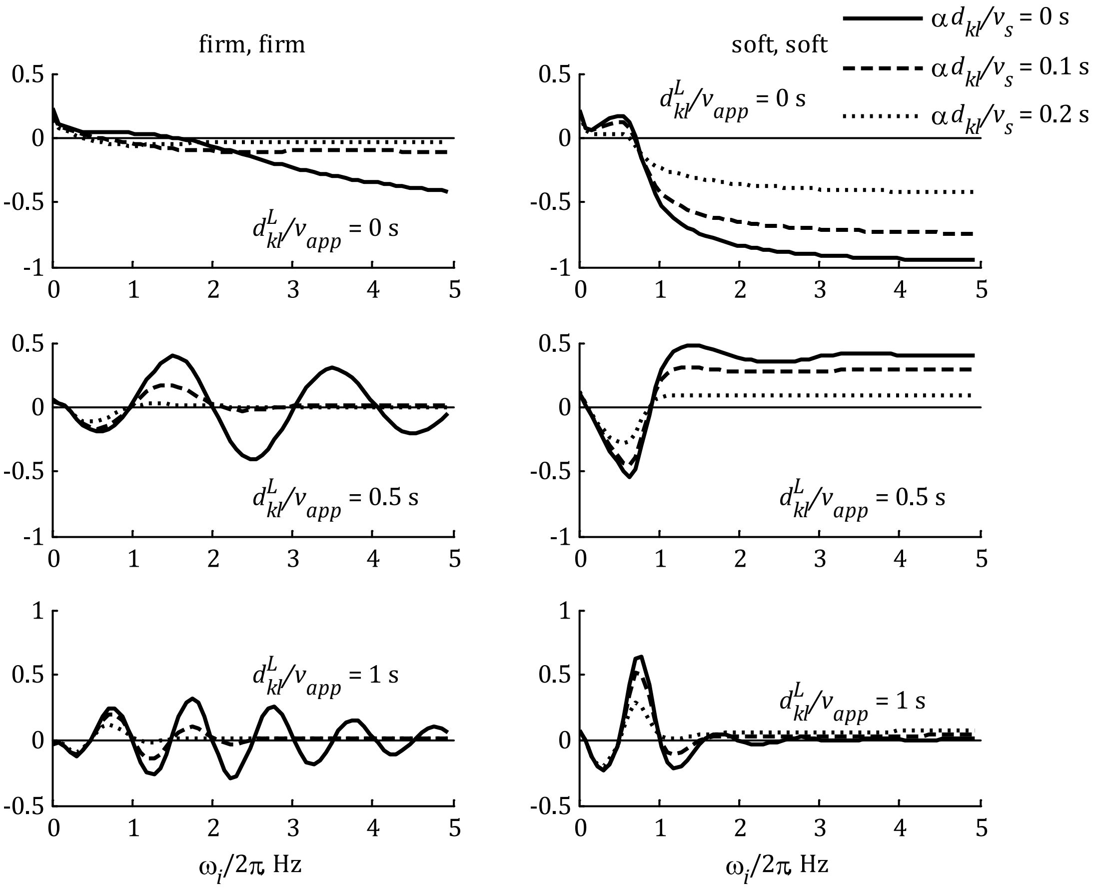

Figure 2.5: Cross-correlation coefficient between oscillator response at station *k* and ground acceleration at station *l* for similar soil conditions and wave direction *k* to *l*.

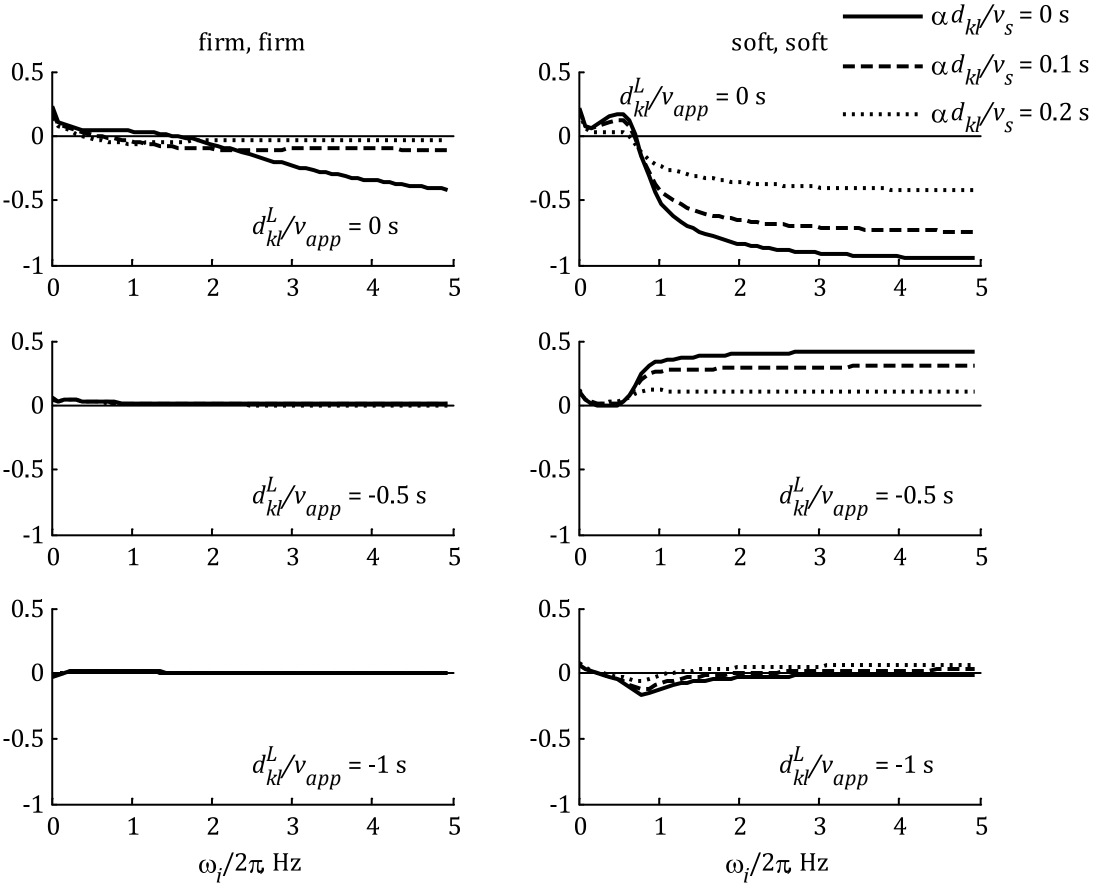

Figure 2.6: Cross-correlation coefficient between oscillator response at station *k* and ground acceleration at station *l* for similar soil conditions and wave direction *l* to *k*.

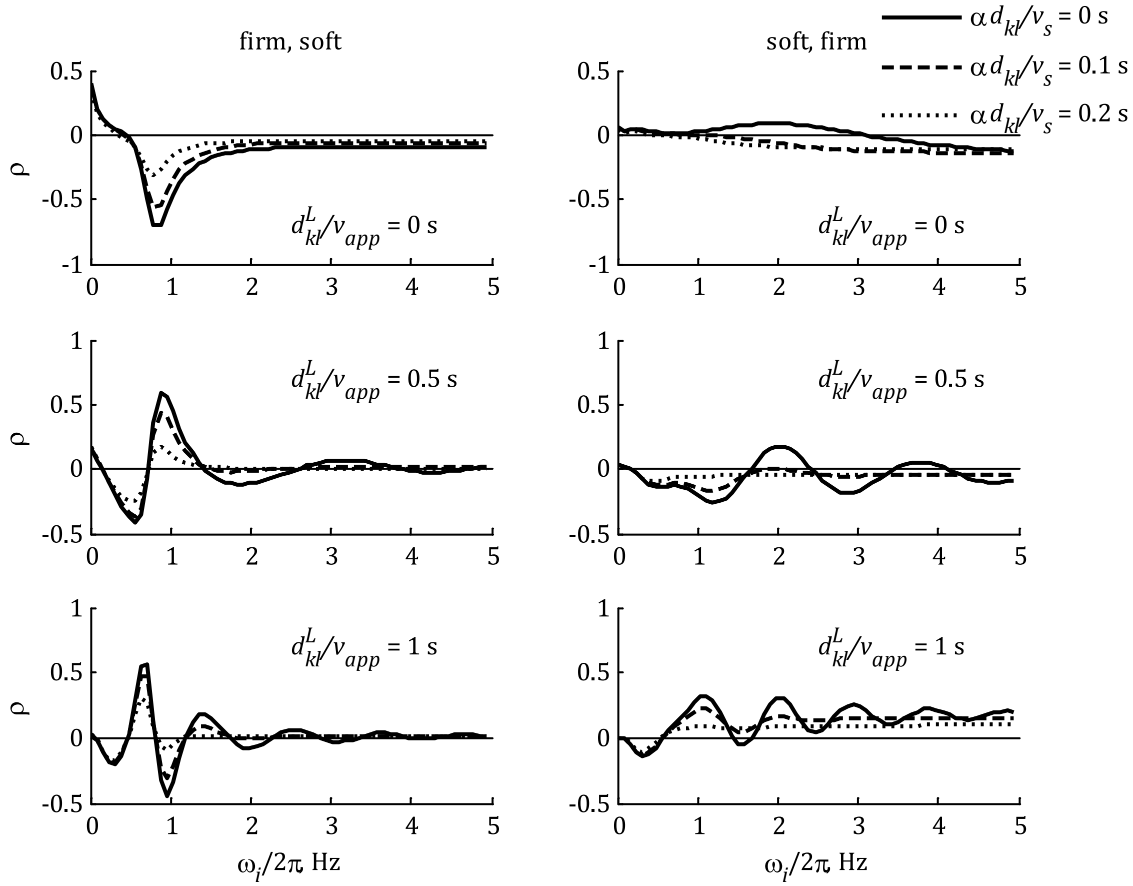

Figure 2.7: Cross-correlation coefficient between oscillator response at station *k* and ground acceleration at station *l* for dissimilar soil conditions and wave direction *k* to *l*.

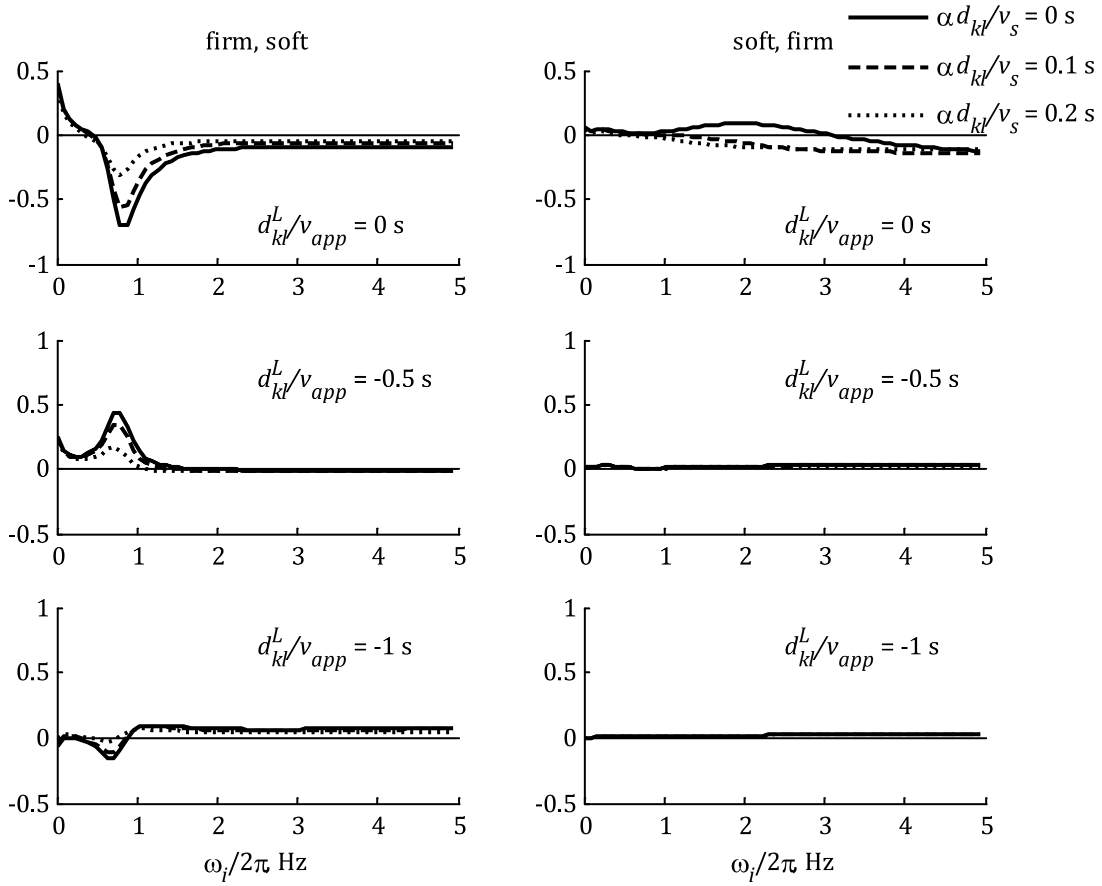

Figure 2.8: Cross-correlation coefficient between oscillator response at station *k* and ground acceleration at station *l* for dissimilar soil conditions and wave direction *l* to *k*.

Chapter 3 - Application of extended MSRS rule to real bridge models

3.1 INTRODUCTION

In this chapter, we apply the theory presented in Chapter 2 to investigate the effect of ground motion spatial variability on four real bridges designed by the California Department of Transportation (Caltrans). The bridges have been selected so that they have vastly different characteristics, e.g. length, number of spans, number of piers per bent, fundamental period. In Section 3.2, we describe the models developed for each bridge following Caltrans' specifications (Caltrans Seismic Design Criteria, 2004). The bridge models are presented in order of increasing fundamental period, i.e. from the stiffest bridge to the most flexible bridge. In Section 3.3, we describe the earthquake input in terms of response spectra and an assumed coherency function. We consider three cases: uniform support motions, varying support motions due to wave-passage and incoherence only, and varying support motions due to wave-passage, incoherence and site-effect. In Section 3.4, we select the number of modes considered for each bridge using the mode truncation criteria described in the previous chapter. Next, in Section 3.5, we perform a comprehensive response analysis of the four bridge models using the MSRS rule and investigate the total, pseudo-static and dynamic responses for the three cases of excitation. The response quantities examined are element forces along the deck and pier drifts. Finally, in Section 3.6, we compare the accuracies of the extended versus the original MSRS rules when only the first few modes are included and discuss conditions under which the extended rule provides improved approximations.

3.2 DESCRIPTION OF BRIDGE MODELS

In this section, we describe the models of four real bridges designed by Caltrans: the Auburn Ravine Bridge, the South Ingram Slough Bridge, the Big Rock Wash Bridge and the Penstock Bridge. The models were developed based on drawings provided by Caltrans.

3.2.1 Auburn Ravine Bridge

The Auburn Ravine Bridge is a reinforced-concrete, six-span bridge with two piers per bent. The elevation and plan of the bridge model are shown in Figure 3.1. The deck has a constant vertical grade of 0.3% and a horizontal curvature of radius $R = 1616$ m. The box-girder cross-section of the bridge is shown in Figure 3.2. The piers have circular cross sections of diameter $D = 1.38$ m. The concrete material of the bridge has a nominal compressive strength of 25 MPa for the piers and 28 MPa for the girders. The reinforcing steel has a nominal yield strength of 420 MPa. The longitudinal reinforcement of each pier consists of 25 equally spaced bundles, with two #32 bars per bundle, whereas the transverse reinforcement consists of #22 hoops at a spacing of 0.125 m. Moment-curvature analysis indicated that the flexural stiffness of the piers should be reduced to 42% of its initial value to account for cracking. Following Caltrans' specifications, the effective torsional moment of inertia is taken to be 20% of its uncracked value.

The piers are considered rigidly connected to the deck at the top, whereas the bottom supports are fixed in all translational directions and free in all rotational directions. The two ends of the bridge are supported on seat abutments. The abutment response is modeled through two translational springs, one longitudinal and one transverse. The stiffness values of these springs are calculated according to Caltrans' specifications: The stiffness of the longitudinal spring, K_x, is calculated by adjusting the initial embankment fill stiffness proportional to the backwall height. The stiffness of the nominal transverse spring, K_y, is equal to 50% of the transverse stiffness of the adjacent bent. These stiffness values are shown in Table 3.1. Vertical translations at the end supports are fully constrained.

The finite element model of the bridge consists of 3 elements per pier and 4 elements per span. The longitudinal axis of the deck elements passes through the centroid of the girder cross-section. The top of each pier is connected with the deck through two rigid frame elements: one vertical and one in the direction of the line connecting the tops of the piers in the bent. Condensing out the rotational degrees of freedom and accounting for the constraints imposed by the rigid elements, the structure has 163 translational unconstrained degrees of freedom and 36 translational support degrees of freedom. The fundamental period of the bridge model is $T = 0.59$ s. The first 8 modes, together with the corresponding natural frequencies, are shown in Figure 3.3. All modes are assumed to have 5% damping.

3.2.2 Big Rock Wash Bridge

The Big Rock Wash Bridge is a prestressed-concrete, three-span bridge with three piers per bent. The elevation and plan of the bridge model are shown in Figure 3.4. In the elevation, two numbers are given for the pier height at each bent, denoting the height of the central pier (number on the left) and the common height of the side piers (number on the right). The longitudinal axis of the bridge, X, is a straight line. The deck is characterized by a constant profile grade of 0.5%. The box-girder cross-section of the bridge is shown in Figure 3.5. The piers have circular cross sections of diameter $D = 1.68$ m. The concrete material throughout has a nominal compressive strength of 28 MPa. The reinforcing steel has a nominal yield strength of 420 MPa. The longitudinal reinforcement of each pier consists of 28 equally spaced #32 bars, whereas the transverse reinforcement consists of #19 hoops at a spacing of 0.12 m. Moment-curvature analysis indicated a reduction of 27% in the flexural stiffness of the piers to account for cracking. The effective torsional moment of inertia of the piers is 20% of its uncracked value. No stiffness reduction is required for the prestressed concrete box girder (Caltrans Seismic Design Criteria, 2004).

The piers are assumed to be rigidly connected to the deck at the top, whereas the bottom supports are fixed in all translational directions and free in all rotational directions. The two ends of the bridge are supported on seat abutments. The abutment response is modeled through two translational springs, one longitudinal and one transverse. The stiffness values of these springs are calculated according to Caltrans' specifications (see Section 3.2.1) and listed in Table 3.1. Vertical translations at the end supports are fully constrained.

The finite element model of the bridge consists of 3 elements per pier and 4 elements per span. The longitudinal axis of a girder element passes through the centroid of the box girder cross-section. Vertical rigid frame elements are used for the connection of the upper column elements with the girder elements. Condensing out the rotational degrees of freedom and accounting for the constraints imposed by the rigid elements, the structure is modeled with 89 translational unconstrained degrees of freedom and 24 translational support degrees of freedom. The fundamental period of the structure is $T = 0.61$ s. The first 8 mode shapes and the corresponding natural frequencies are shown in Figure 3.6. All modes are assumed to have 5% modal damping.

3.2.3 South Ingram Slough Bridge

The South Ingram Slough Bridge is a prestressed-concrete, two-span bridge with two piers per bent. The elevation and plan of the bridge model are shown in Figure 3.7. In the elevation, two numbers describe the height of the bent, each corresponding to one of the piers. The deck has a vertical grade, varying from -0.52% to -0.85%, and a constant horizontal curvature of radius $R = 1542.3$ m. The box-girder cross-section of the bridge is shown in Figure 3.8. The piers have circular cross sections of diameter $D = 1.68$ m. The structure is made of concrete with a nominal compressive strength of 25 MPa for the piers and 28 MPa for the girder. The reinforcing steel has a nominal yield strength of 420 MPa. The longitudinal reinforcement of each column consists of 22 equally spaced bundles, with two #36 bars per bundle, whereas the transverse reinforcement consists of #22 hoops at a spacing of 0.15m. Moment-curvature analysis indicated a reduction of 35% in the flexural stiffness of the piers to account for cracking. The effective torsional moment of inertia of the piers is 20% of its uncracked value. No stiffness reduction is required for the prestressed concrete box girder.

The columns are considered rigidly connected to the deck at the top and fixed in all translational and rotational directions at the bottom. The two ends of the bridge are supported on seat abutments. The abutment response is modeled through two translational springs, one longitudinal and one transverse. The stiffness values of these springs are calculated according to Caltrans' specifications (see Section 3.2.1) and listed in Table 3.1. Vertical translations at the end supports are fully constrained.

The finite element model of the bridge consists of 3 elements per pier and 6 elements in each span. The longitudinal axis of the girder elements passes through the centroid of the girder cross-section. Vertical rigid frame elements are used to connect the tops of the piers with the deck. Condensing out the rotational degrees of freedom and accounting for the constraints imposed by the rigid elements, the structure has 55 translational unconstrained degrees of freedom and 12 translational support degrees of freedom. The fundamental period of the bridge model is $T = 1.24$ s. The first 8 modes, together with the corresponding natural frequencies, are shown in Figure 3.9. All modes are assumed to have 5% damping.

3.2.4 Penstock Bridge

The Penstock bridge is a prestressed-concrete, four-span bridge with a single pier per bent. The elevation of the bridge model is shown in Figure 3.10. The deck has a vertical grade, varying from 0.3% to 2.1%, and a constant horizontal curvature of radius $R = 458$ m. The box-girder cross-section of the bridge is shown in Figure 3.11. The piers have circular cross sections of diameter $D = 2.13$ m. The structure is made of concrete with a nominal compressive strength of 25 MPa for the piers and 28 MPa for the girder. The reinforcing steel has a nominal yield strength of 420 MPa. The longitudinal reinforcement of each column consists of 40 equally spaced #36 bars, whereas the transverse reinforcement consists of #25 hoops at a spacing of 0.15m. Moment-curvature analysis indicated a reduction of 28% in the flexural stiffness of the piers to account for cracking. The effective torsional moment of inertia of the piers is 20% of its uncracked value. No stiffness reduction is required for the prestressed concrete box girder.

The columns are considered rigidly connected to the deck at the top and fixed in all translational and rotational directions at the bottom. The two ends of the bridge are supported on seat abutments. The abutment response is modeled through two translational springs, one longitudinal and one transverse. The stiffness values of these springs are calculated according to Caltrans' specifications (see Section 3.2.1) and listed in Table 3.1. Vertical translations at the end supports are fully constrained.

The finite element model of the bridge consists of 3 elements per pier and 6, 8, 8 and 4 elements in spans 1, 2, 3 and 4, respectively. The longitudinal axis of the girder elements passes through the centroid of the girder cross-section. Vertical rigid frame elements are used to connect the tops of the piers with the deck. Condensing out the rotational degrees of freedom and accounting for the constraints imposed by the rigid elements, the structure has 103 translational unconstrained degrees of freedom and 15 translational support degrees of freedom. The fundamental period of the bridge model is $T = 2.38$ s. The first 8 modes, together with the corresponding natural frequencies, are shown in Figure 3.12. All modes are assumed to have 5% damping.

3.3 DESCRIPTION OF INPUT EXCITATIONS THROUGH RESPONSE SPECTRA AND A COHERENCY FUNCTION

The supports of each bridge are subjected to translational ground motions in the longitudinal, X, transverse, Y, and vertical, Z, directions. The three components of the ground motion are assumed to be statistically independent. In the response analysis of each bride, three cases of ground motion spatial variability are considered: uniform support motions (case 1), variable support motions with incoherency ($v_s/\alpha = 600$ m/s) and wave passage ($v_{app} = 400$ m/s) but uniform soil conditions (case 2), and case 2 but with varying soil conditions (case 3). For each bridge, the soil types at the supports for both uniform and varying soil conditions are given in Table 3.2. Characteristics of the corresponding soil profiles according to Caltrans' Seismic Design Criteria (2004) are listed in Table 3.3. For cases 2 and 3, the waves are assumed to propagate in the opposite direction of the X axis; furthermore, the incoherence in the Y direction is considered negligible for the dimensions of the bridges examined. Thus, for the bridge models with multiple piers per bent, if the piers are aligned in the direction of the Y axis, they all undergo the same support motion. This is the case for the Big Rock Wash Bridge and the South Ingram Slough Bridge. However, the piers of the bents of the Auburn Ravine Bridge are not aligned in the Y direction; in this case, we assume they undergo the motion corresponding to the point midway between the two piers.

The horizontal components of the support motions are described by Acceleration Response Spectra (ARS) provided by Caltrans Seismic Design Criteria (2004). The appropriate ARS curve is selected in terms of the peak rock acceleration and moment magnitude for the maximum credible earthquake and the soil type at the relevant support. The vertical components are described by response spectra proposed by Bozorgnia and Campbell (2004). The proposed spectrum for the latter consists of a flat portion with amplitude A_{vs}, for periods $T \leq 0.15$ s, and a decaying portion described by $A_{vs}(0.15/T)^{0.75}$, for periods $T > 0.15$ s. The amplitude of the flat portion, A_{vs}, is determined in terms of the horizontal spectral acceleration at $T = 0.1$ s, the source-to-site distance and the soil type. In our analyses, a distance of 20 km from the earthquake source is assumed in all cases. Both sets of spectra are defined for frequencies greater than 0.25 Hz. For lower frequencies, a spectral shape varying in proportion to the square of the frequency is assumed. To estimate the corresponding peak ground displacements, which occur at zero frequency, a reduction factor of 1.39 is applied to the peak spectral displacement (Newmark and Hall, 1969).

The Auburn Ravine Bridge, the South Ingram Slough Bridge and the Penstock Bridge have all been designed for the same event magnitude of $M_w = 6.5$ and a peak rock acceleration of $\ddot{u}_{max}^{rock} = 0.3\ g$. Figure 3.13 shows the acceleration response spectra for soil types B, C and D, normalized by the corresponding Peak Ground Acceleration (PGA). Figure 3.14 shows the corresponding consistent auto-PSDs obtained by the method described in Section 2.2.2. The latter, together with the coherency function, are used to compute the correlation coefficients in the MSRS method. The Big Rock Wash Bridge has been designed for an event magnitude of $M_w = 8.0$ and a peak rock acceleration of $\ddot{u}_{max}^{rock} = 0.6\ g$. Figure 3.15 shows the acceleration response spectra for soil types B, C and D, normalized by the corresponding PGA, whereas Figure 3.16 shows the corresponding consistent auto-PSDs. For each case, the PGAs for each soil type and direction of excitation are summarized in Table 3.4.

The site response effect is modeled using the SDOF idealization of the soil layer, i.e., Eqn. (2.23) for the soil FRF in determining the corresponding phase angle of the coherency function (see Eqn. (2.21)). For each response spectrum, the values of ω_s and ζ_s in Eqn. (2.23) are determined by fitting the Kanai-Tajimi PSD to the corresponding PSD in Figure 3.13 or Figure 3.15 by use of a non-linear least-squares minimization method. The resulting ω_s values are listed in Table 3.5. The resulting ζ_s values are 0.8 in all cases.

3.4 MODE TRUNCATION BASED ON PARTICIPATING MODAL MASS

In Section 2.3 we investigated criteria for mode truncation in dynamic analysis of structures subjected to differential support motions. In this section, we use these criteria to select the number of modes to include in the MSRS analysis of the bridge models described earlier.

Figures 3.17 through 3.20 show how the ratios r_n^U and r_n^{TI} (given by Eqn. (2.25) and Eqn. (2.26), respectively) vary with mode number for the four bridge models. The number of modes to be included in the response analysis of each bridge model (see the following section) is selected so that both ratios have values greater than 0.90. For each bridge, the number of modes included and the corresponding values of r_n^U and r_n^{TI} are given in Table 3.6. In the following analysis, the mean peak responses computed with these numbers of modes are considered “exact”’.

3.5 INVESTIGATION OF THE EFFECTS OF GROUND MOTION SPATIAL VARIABILITY

3.5.1 Auburn Ravine Bridge

3.5.1.1 Total responses

Figure 3.21 shows the mean peak responses, i.e., axial forces, F_x, shear forces, F_y and F_z, torques, M_x, and bending moments, M_y and M_z, along the deck for the three cases of ground motion spatial variability described in Section 3.3. The subscripts of these forces are consistent with the local axes of the cross-section shown in Figure 3.2. Figure 3.21 allows comparison of the absolute values of the mean peak forces between the cases of uniform support excitations (case 1) and differential support excitations under uniform or varying soil conditions (cases 2 and 3, respectively). In order to elaborate on the effect of ground motion spatial variability on structural response, in Figure 3.22, we plot the same mean peak responses of cases 2 and 3, but normalized with respect to the corresponding mean peak responses of case 1. Normalized responses smaller than unity indicate cases where the ground motion spatial variability has a beneficial effect, i.e. it reduces the demand imposed on the structure. When normalized responses exceed unity, the ground motion spatial variability amplifies the response and its neglect may lead to non-conservative designs.

First consider cases 1 and 2. Figure 3.22 shows that the ground motion spatial variability has a more severe effect on the axial forces and torques, for which the ratios of responses in case 2 over responses in case 1 can be as large as 12.7 or 3.0, respectively. These responses, however, are typically small in absolute magnitude and normally do not control the design. The effects on shear forces and bending moments, which are more critical in design, are smaller and the corresponding normalized responses vary in the range 0.7-1.9. The normalized values of a specified force along the deck can be smaller or larger than unity depending on the location of the cross section within the bridge. Now, comparing cases 2 and 3 in Figure 3.22, it is seen that variation of soil conditions results in large amplifications of all response quantities with the exception of F_x. We note that in order to assess the significance of the response amplifications from a design standpoint, Figure 3.22 should be examined in conjunction with Figure 3.21.

Table 3.7 lists the mean peak values of the percent pier drifts (pier top displacement divided by pier height) in the global X and Y directions for the three cases examined above. The ratios of responses in case 2 over responses in case 1 vary in the range 0.7-1.1 for the X drifts and in the range 0.6-1.0 for the Y drifts. Thus, for this bridge, the combined effect of wave passage and incoherence is more mild on pier drifts than on element forces along the deck. The effect of soil variation is significant only on piers located on softer (type D) soils. For these piers, the site-effect causes amplification of the response, which is more pronounced in the X direction.

As the MSRS rule in Eqn. (2.12) indicates, the total response is composed of pseudo-static and dynamic contributions as well as a cross term between them. In the following sections, we separately examine the two contributions in order to gain insight into the nature of the effect of spatial variability on bridge response.

3.5.1.2 Pseudo-static responses

Figure 3.23 shows the pseudo-static contributions, i.e. the square-root of the first double-sum in the MSRS rule in Eqn. (2.12), to the generalized element forces along the deck. Note that uniform support motions do not generate pseudo-static forces and, hence, all contributions for case 1 are zero. In case 2, the pseudo-static shear forces and bending moments induced by the variability in the support motions tend to be balanced out by reductions in the corresponding dynamic forces, resulting in only small changes in the total response (see previous section and Figure 3.22). Comparison between cases 2 and 3 indicates that the variation of soil conditions largely amplifies the pseudo-static forces, except for F_x. Figure 3.24 shows the relative contributions of the pseudo-static forces to the total responses, represented by the ratio z_s^2/z^2, where z_s^2 is the double-sum term in the MSRS rule and z is the mean peak total response. This figure indicates that, under varying soil conditions (case 3), most responses tend to be dominated by pseudo-static contributions. Also, comparison of Figure 3.24 with Figure 3.22 indicates that amplification of bridge responses is associated with large pseudo-static contributions.

Table 3.8 lists the relative pseudo-static contributions, z_s^2/z^2, for pier drifts in global X and Y directions, and for cases 2 and 3. For both cases 2 and 3, these contributions are much larger in X direction, in which the bridge is stiffer. Soil variation largely increases pseudo-static contributions for piers located on softer soil (type D), but has a smaller influence on other piers.

3.5.1.3 Dynamic responses

To investigate the effect of differential support motions on the dynamic component of the response, i.e. the quadruple-sum in the MSRS rule, we separately examine the individual modal contributions $\sum_{k=1}^{m}\sum_{l=1}^{m} b_{ki}b_{li}\rho_{s_{ki}s_{li}}D_k(\omega_i,\ \zeta_i)D_l(\omega_i,\ \zeta_i)$, $i = 1,2,\dots,n$. For each mode, this term includes the correlations arising from the multiple support excitations, but neglects the correlations between different modes. For the three cases of support motions described above, Figure 3.25 shows the contributions of each of the first 10 modes to the generalized element forces at two locations along the deck of Auburn Ravine Bridge: the middle of span 3 and the left end of span 4. These example locations were selected because they are critical for the design of the bridge, as indicated by Figure 3.21. We observe that the modal contributions between cases 2 and 3 differ only slightly. However, comparison of these cases with case 1 indicates that modal responses to differential support motions can differ largely from modal responses to uniform excitation. For example, spatial variability significantly reduces the contributions of modes 1 and 2 and amplifies the contributions of modes 5 and 8. The latter observations are consistent with the analysis in Section 2.3, since

$(\sum_{k=1}^{m} \beta_{ki})^2 \approx (\sum_{k=1}^{m} |\beta_{ki}|)^2$ for mode 1 in direction Y and for mode 2 in direction X, but $(\sum_{k=1}^{m} \beta_{ki})^2 / \sum_{k=1}^{m} \beta_{ki}^2 \approx 0$ for modes 5 and 8, in direction Z.

To assess the relative importance of modal contributions to the total responses, in Figure 3.26 we plot the mean peak total values of the generalized element forces examined in Figure 3.25, computed by including n modes in the MSRS rule, $n = 1, \dots, 10$, and normalized with the 'exact' mean peak total responses. Two main observations are: 1) Depending on the response quantity, variability of the support motions can make the contributions of higher modes more or less significant. 2) When differential support motions induce large pseudo-static contributions, only the first few modes are sufficient to obtain good approximations of the total responses, even in cases when higher modes are important for a fairly accurate representation of the dynamic component. To gain insight, let us look at some representative cases: For the torques at both locations, higher modes are more significant under varying support motions. As a result, in case 2, despite the large contributions from pseudo-static forces, a certain level of accuracy requires a larger number of modes than in case 1. Next, we examine M_y in the middle of span 3. This response quantity is characterized by small pseudo-static contributions in both cases 2 and 3. When 10 modes are included in the MSRS rule, the approximation is fairly good in cases 2 and 3, but extremely poor in case 1, which indicates the large influence of the ground motion spatial variability on the dynamic component of the M_y response. Last, we look at the F_z response at the left end of span 4. Comparing cases 1 and 2, we observe that higher modes have larger contributions under uniform support motions: 80% accuracy requires 9 modes in case 2, but more than 10 modes in case 1. We note that the same level of accuracy is achieved only with 1 mode in case 3, due to the large pseudo-static forces induced by the variation in soil conditions.

Pier drifts are generally contributed by the first 2 or 3 modes and are not shown here.

3.5.2 Big Rock Wash Bridge

3.5.2.1 Total responses

Figure 3.27 and Figure 3.28 show the mean peak responses and normalized mean peak responses with respect to the case of uniform excitations, respectively, for the generalized element forces along the deck of Big Rock Wash Bridge. The three cases of excitation described in Section 3.3 are investigated. These figures suggest that ground motion spatial variability has a relatively mild effect on F_z and M_y. In particular, the effect on F_z is beneficial along the deck for both cases 2 and 3. The influence of spatial variability is more pronounced on F_x, F_y and M_z. (The large normalized values of M_x in Figure 3.28 are of no engineering significance, since the corresponding absolute values are very small.) To assess the significance of the large normalized values of F_x along the deck from a design viewpoint, we should examine in parallel the corresponding absolute values of the F_x mean peak response. Variation of soil conditions significantly amplifies F_y and M_z at certain locations, but only slightly affects other responses.

Table 3.9 lists the mean peak values of the percent pier drifts in the global X and Y directions for the same three cases of excitation. The combined effect of wave passage and incoherence is reduction of all pier drifts. Soil variation increases all pier drifts in X direction, but has negligible influence on pier drifts in Y direction.

3.5.2.2 Pseudo-static responses

Figure 3.29 shows pseudo-static contributions to the mean peak generalized element forces along the deck (cases 2 and 3). Their relative importance can be assessed by examining the ratios of their squared values to the corresponding squared mean peak responses, shown in Figure 3.30. In both cases 2 and 3, the pseudo-static components dominate the F_x response. Under uniform soil conditions (case 2), pseudo-static contributions are particularly large for F_y and M_z at certain locations. Variation of soil conditions (case 3) amplifies all pseudo-static responses except from F_x. Similarly with the Auburn Ravine Bridge, when pseudo-static contributions are dominant, the corresponding total responses of Big Rock Wash Bridge tend to be amplified. However, we note that although the pseudo-static contributions for F_z and M_y are significant at certain locations, the corresponding total responses are only slightly affected, which indicates that ground motion spatial variability reduces the corresponding dynamic responses.

Table 3.10 lists the percent pseudo-static contributions for the pier drifts in the global X and Y directions for cases 2 and 3. These are much larger in X direction, in which the bridge is stiffer. Variation of soil conditions increases these contributions for all pier drifts in both directions.

3.5.2.3 Dynamic responses

Figure 3.31 shows the individual modal contributions (neglecting cross-modal correlations, but including cross-support and cross-support-modal correlations) for the generalized element forces at two example locations along the deck: the left end and the middle of span 2. The figure indicates that the combined effect of wave passage and incoherence on modal responses is significant, whereas the additional effect of soil variation is only slight. In particular, ground motion spatial variability (cases 2 and 3) largely amplifies the response of modes 3, 4, 8, 9 and 10, but significantly reduces the response of modes 1, 2 and 6.

For the same response quantities, in Figure 3.32, we examine how the ground motion spatial variability affects the level of accuracy of the total mean peak values when a certain number of modes is considered. This depends on the individual modal contributions and also, on the pseudo-static contributions. As a result, convergence can be faster under uniform or differential support motions, depending on the response quantity examined.

Pier drifts are generally contributed by the first 2 or 3 modes and are not shown here.

3.5.3 South Ingram Slough Bridge

3.5.3.1 Total responses

Figure 3.33 shows the mean peak generalized element forces along the deck of South Ingram Slough Bridge for the three cases of excitation described in Section 3.3. The figure indicates that except for F_x, the effect of ground motion variability on bridge response is mild and tends to be beneficial at locations that are critical for design. For F_x, spatial variability significantly amplifies the response around the middle support resulting in a more uniform variation of axial forces along the deck. For cases 2 and 3, Figure 3.34 shows the same responses normalized with the responses in case 1. Except for F_x, the normalized responses at most locations vary close to unity. Comparing with Figure 3.34 with Figure 3.33, we observe that the few locations where the normalized responses exceed unity are not critical in terms of design.

Table 3.11 lists the mean peak pier drifts in the global X and Y directions for the three cases examined above. The combined effect of wave-passage and incoherence is reduction of all pier drifts. Additional variation of soil conditions has only slight influence.

3.5.3.2 Pseudo-static responses

Figure 3.35 shows pseudo-static contributions to the mean peak generalized element forces along the deck (cases 2 and 3). For all generalized element forces, soil variation amplifies the pseudo-static responses at all locations examined. To assess the relative importance of these responses, Figure 3.36 shows the ratios of their squared values to the corresponding squared mean peak responses. Similarly with the two bridges examined previously, the F_x response along the deck of South Ingram Slough Bridge is dominated by the pseudo-static forces. For the other response quantities, the pseudo-static contributions are very small, except for a few locations, at which the total response is not critical in terms of design (compare Figure 3.36 with Figure 3.33).

Table 3.12 lists the percent pseudo-static contributions to pier drifts. These are much smaller than the pseudo-static contributions to pier drifts of the two stiffer bridges studied earlier. In direction Y, they are negligible for both cases 2 and 3. In direction X, they are amplified by variation of soil conditions.

3.5.3.3 Dynamic responses

Figure 3.37 shows how individual modal contributions vary in the three cases of excitation for the generalized element forces at the middle of span 1 and the left end of span 2. Again, the individual modal contributions are computed by neglecting correlations between different modes, but including the correlations between support motions and between support motions and modal responses. Compared to the case of uniform support motions, the modal responses under differential support motions are higher for modes 2 and 4, smaller for modes 3 and 5 and vary closely for modes 1, 6, 7 and 10. As for the bridges examined previously, variation of soil conditions is not significant for the individual modal contributions.

For the same response quantities, Figure 3.38 shows the accuracy in the total mean peak values when $n = 1, \ldots, 10$ modes are considered. Except for the axial force, the pseudo-static contributions in case 2 are small, and thus, comparison of cases 1 and 2 is indicative of the effect of spatial variability on the convergence of the dynamic component with n. We note that under differential support motions, the contribution of higher modes is more significant for F_z, among other responses. In case 3, increased pseudo-static contributions can make convergence faster.

Pier drifts are contributed by the first 2 or 3 modes and are not shown here.

3.5.4 Penstock Bridge

3.5.4.1 Total responses

Figure 3.39 shows the mean peak generalized element forces along the deck of Penstock Bridge. Figure 3.40 shows the responses under differential support motions normalized with the responses under uniform support motions. The combined effect of wave passage and incoherence is mild on F_z, M_y and M_z, but more pronounced on F_x, F_y and M_x. In case 2, the normalized F_y and M_z responses always exceed unity, whereas the other normalized responses are greater or smaller than unity depending on the location along the deck. Variation of soil conditions reduces F_y, M_x and M_z and amplifies F_z and M_y.

Table 3.13 lists the mean peak pier drifts in the global *X* and *Y* directions. The combined effect of wave passage and incoherence is a small reduction of the drifts in *X* direction and a small increase of the drifts in *Y* direction. In *X* direction, variation of soil conditions increases the drift of the middle pier, which is located on softer (type D) soil, and has negligible effect on other pier drifts. In *Y* direction, variation of soil conditions decreases all pier drifts.

3.5.4.2 Pseudo-static responses

For the pseudo-static generalized element forces along the deck, Figure 3.41 and Figure 3.42 show their mean peak values and relative contributions to the total response, respectively. Under uniform soil conditions, the pseudo-static contributions are very small, except for the axial force. The variation of soil conditions is more critical for the F_z and M_y responses causing large amplifications of the pseudo-static contributions and also, of the total responses (compare Figure 3.42 with Figure 3.39). These responses have large contributions from excitation in the vertical direction, in which the bridge is stiffer and the support motions are richer in high-frequency components and thus, more incoherent.

Table 3.14 lists the pseudo-static contributions to pier drifts for cases 2 and 3. Similarly with the bridges examined previously, these contributions are much larger in X (than in Y) direction, in which the bridge is stiffer. For all responses examined herein, variation of soil conditions increases pseudo-static contributions. This increase is more pronounced in X direction.

3.5.4.3 Dynamic responses

In Figure 3.43, we examine the individual modal contributions to the element forces at the middle of span 2 and the left end of span 3, for the three cases of excitation. These are computed as for the bridges studied earlier. However, in contrast with the results for the other bridges, herein, the modal responses are influenced not only by wave-passage and incoherence, but also by variation of soil conditions.

Next, we examine the convergence of the corresponding total responses as a function of the number of modes considered, shown in Figure 3.44 for the three cases of excitation. For this bridge an interesting observation is made for modes 7 and 8, which have closely spaced frequencies of 25.8 rad/s and 25.9 rad/s, respectively. As can be seen in the charts for F_y, when 7 modes are considered, the response can be largely overestimated. However, this overestimation is balanced when the 8th mode is also considered. The corresponding charts in Figure 3.43 indicate that these two modes individually make significant contributions of nearly equal magnitude to the F_y responses at both locations. However, the cross term arising from these two modes has nearly twice the magnitude and a negative sign so that the total contribution of these two modes is rather small. This observation indicates the importance of cross-modal terms for closely spaced frequencies. It also highlights the importance of not truncating modes in the middle of a group of closely spaced modes.

The pier drifts are contributed from the first 2 or 3 modes and are not shown here.

3.5.5 Summary of results

The previous analysis demonstrated that ground motion spatial variability affects the bridge response in a rather complex way: Although differential support motions induce pseudo-static forces, which are not present in the case of uniform excitations, they can either amplify or reduce the total response depending on their additional influence on the dynamic component of the response. The effect on the dynamic component is the additive effect on individual modal responses. Ground motion spatial variability reduces contributions of certain modes and amplifies contributions of others, and thus, the total effect on the dynamic component of a response quantity is often hard to predict. However, in cases when pseudo-static contributions are dominant, the dynamic component is of less importance, and ground motion spatial variability can cause large response amplifications. In this section, we summarize the effects of ground motion spatial variability, analyzed earlier for each individual model, and identify general trends.

In Table 3.15 we list the range of values for the ratio of responses in case 2 over responses in case 1 for each bridge model and each response quantity. Thus, this table provides a summary of the combined effect of incoherence and wave passage on bridge response. We note that wave passage together with incoherence amplify or reduce element forces depending on the response quantity and the location along the deck examined. Their combined effect tends to be more severe (larger ratios) on F_x, F_y, M_x and M_z, which have larger contributions from horizontal excitations, and more mild or beneficial (smaller ratios) on F_z and M_y, which have larger contributions from the vertical excitation. Also, their effect is more pronounced for the two stiffer bridges, i.e. the Auburn Ravine Bridge and the Big Rock Wash Bridge. For pier drifts, wave passage and incoherence tend to reduce their mean peak values; only small amplifications occur in few cases.

In Table 3.16 we list the range of values for the ratio of responses in case 3 over responses in case 2, for each bridge model and each response quantity. Thus, this table provides a summary of the additional effect of soil variation on bridge response. Previous analyses demonstrated that, except for a few cases, variation of soil conditions increased pseudo-static responses. For the dynamic responses, the additional effect of soil variation was significant only for the more flexible Penstock Bridge. Table 3.16 indicates that additional variation of soil conditions has small influence on F_x, but amplifies all other responses for the three stiffer bridges. The effect is more pronounced for the Auburn Ravine Bridge. Looking at pier drifts, variation of soil conditions is more significant in the X direction, causing amplification of the responses in all cases.

3.6 ASSESSMENT OF EXTENDED MSRS RULE

In this section, we compare the accuracy in the approximations of the mean peak total responses, with $n = 1, \dots, 10$ modes included in the analysis, using the extended versus using the original MSRS rule. For each bridge model, we look into the same response quantities examined in the analyses of the dynamic components and we investigate cases 2 and 3 separately. In the assessment of the extended MSRS rule, consideration should be given to the modal frequencies of each bridge in conjunction with the normalized acceleration response spectra $A(\omega)/\mathrm{PGA}$ in Figure 3.13 or Figure 3.15 (whichever applies). We expect that the extended MSRS rule significantly improves the results when truncated modes with significant contributions have frequencies ω_i such that $A(\omega_i)/\ddot{u}_g \approx 1$. When truncated modes with large contributions have frequencies ω_i such that $A(\omega_i)/\ddot{u}_g \ll 1$, the extended MSRS rule may overestimate the response. Finally, when truncated modes with large contributions have frequencies ω_i such that $A(\omega_i)/\ddot{u}_g \gg 1$, the extended rule provides smaller improvements.

3.6.1 Auburn Ravine Bridge

We begin by examining the Auburn Ravine Bridge. Figure 3.45 and Figure 3.46 show the ratio of the response when n modes are included, z_n, over the 'exact' response, z, for the generalized element forces at the middle of span 3 and the left end of span 4, respectively. In each figure, the upper charts are for case 2 and the bottom charts for case 3. In each chart, the mean peak total response is evaluated with the original and also, with the extended MSRS rule.

Let us first look into case 2, i.e. the upper charts in Figure 3.45 and Figure 3.46. In assessing the effectiveness of the extended MSRS rule, F_x in Figure 3.45, and F_x and F_y in Figure 3.46 are not of interest, since they are almost perfectly approximated by only the 1st mode. Examining the other responses, we note that in some cases the extended MSRS rule provides small improvements in the approximation of the response (F_y, F_z and M_z in Figure 3.45; M_z in Figure 3.46), while in others, it provides significant improvements (M_x and M_y in Figure 3.45; F_z, M_x and M_y in Figure 3.46). For the latter responses, the approximation with the extended MSRS rule is nearly perfect when only 1 or 2 modes are included, whereas the approximation of the original MSRS rule with the same number of modes is very poor. We also note that in some cases the extended MSRS rule converges to unity from larger values, i.e. can overestimate the responses. For the responses examined herein, this overestimation is more pronounced for F_z in Figure 3.46, but is generally not significant.

To interpret the above results, we need to examine the values of $A(\omega)/\mathrm{PGA}$ in Figure 3.13 for the modal frequencies of the Auburn Ravine Bridge. Let us examine these values for the first 8 modal frequencies, given in Figure 3.3: The curve that corresponds to horizontal excitation and soil type C takes values between 1 and 2.5, but greater than 2 for $n > 2$. Thus, for the forces that are dominated from the response to horizontal excitation (in either x or y direction), we expect that the extended MSRS rule will provide only small improvements. The curve that corresponds to vertical excitation (same for all soil types) takes values < 0.5 for $n \leq 3$, but is close to unity for $n > 4$. Thus, for the forces that are dominated from the response to vertical excitation, the MSRS rule will generally provide much better approximations, but can also overestimate the response. The above analysis is consistent with the results shown in Figure 3.45 and Figure 3.46 if we consider the directions of excitation that contribute to each response: At the middle of span 3, F_y, F_z and M_z are mainly contributed from horizontal excitations, M_y from vertical excitation, and M_x has nearly equal contributions from horizontal and vertical excitations. At the left end of span 4, M_z is dominated from the bridge response to horizontal excitations, F_z from the response to vertical and M_x and M_y have significant contributions from both.

Now, let us look in case 3. Comparing the charts for case 3 with the corresponding ones for case 2, we note somewhat faster convergence of modal responses for case 3 for both the original and extended MSRS rules. This is due to larger contributions of the pseudo-static components in case 3 relative to case 2 (see Figure 3.24).

3.6.2 Big Rock Wash Bridge

A similar analysis with the above is performed in this section for the Big Rock Wash Bridge. To understand the way the extended rule influences the approximation of the response with a certain number of modes, we first examine the values of the normalized pseudo-acceleration in Figure 3.15 for the modal frequencies given in Figure 3.6. In the horizontal directions, $A(\omega)/\mathrm{PGA}$ takes values larger than unity, which exceed 2 for modes 1 through 7. In the vertical direction, the values of $A(\omega)/\mathrm{PGA}$ are very small (< 0.5) for the first 4 modes, but are close to unity or unity for $n > 4$. Also, we should note that the Big Rock Wash Bridge is not curved in the XY plan and thus, its response is uncoupled in the XZ and XY plans. As a result, F_y, M_x and M_z are entirely contributed from the bridge response to excitation in Y direction, whereas F_x, F_z and M_y are additively contributed from the bridge response to excitations in X and Z directions.

Figure 3.47 and Figure 3.48 compare the approximations of the mean peak generalized element forces at the left end of span 2 and the middle of span 2, respectively, with the extended versus the original MSRS rule with $n = 1, \dots, 10$ modes in the analysis. Again, we first examine analytically the results for case 2, i.e. the upper charts in these figures. The forces contributed only from the bridge response to excitation in the Y direction are F_y, M_x and M_z. We note that the results for M_x are of no particular engineering interest, since the absolute values of M_x are very small. For F_y and M_z, when the contributions of higher modes are not negligible, use of the extended MSRS rule provides small improvements. The other forces are contributed additively from the bridge response to excitations in the X and Z directions. Apparently, F_x is of no interest in our analysis. For the F_z and M_y responses, use of the extended MSRS rule results in smaller absolute error than the original rule, as long as 4 or more modes are considered. If fewer modes are considered, the MSRS rule can largely overestimate the response. Comparing the charts for case 2 with the corresponding charts for case 3, we observe that the higher pseudo-static contributions in case 3 (see Figure 3.30) results in improved approximations in all cases with the original or the extended MSRS rule.

3.6.3 South Ingram Slough Bridge

In a similar way as in the previous sections, Figure 3.49 and Figure 3.50 compare the original and extended MSRS rules for the generalized element forces at the middle of span 1 and the left end of span 2, respectively, of the South Ingram Slough Bridge. We look into the modal frequencies in Figure 3.9 and the corresponding values of the relevant curves in Figure 3.13. For the first 8 modes, the curve for the horizontal excitations takes values in the range from ≈ 1 to ≈ 2.5. The curve for the vertical excitation, takes values < 0.5 for the first 3 modes, but equal to unity for $n > 5$. The South Ingram Slough Bridge is characterized by only a small curvature in the XY plan which results in nearly uncoupled bridge response in the XZ and YZ plans. Again, we examine separately the groups of responses contributed by the excitation in Y direction or by excitations in X and Z directions. We note that the M_x response is of no engineering significance, since the corresponding absolute values are very small. For the F_x, F_y and M_z responses, which are contributed $\approx 100\%$ by excitation in either X or Y direction, the extended MSRS rule is slightly better than the original rule, when higher mode contributions are not negligible. For the F_z and M_y responses, including fewer than 5 modes can result in large overestimation of the response. This overestimation is smaller in case 3.

3.6.4 Penstock Bridge

Figure 3.51 and Figure 3.52 compare the mean peak response estimates for the generalized element forces at the middle of span 2 and the left end of span 3, respectively. Penstock Bridge is the most flexible among the bridges considered in this study. For the horizontal direction of excitation, the normalized pseudo-acceleration curve for soil C in Figure 3.13 takes values smaller than unity for the first 2 modes, but exceeds unity for the other modes. The maximum values of the curve occur at the modal frequencies of the closely-spaced 7th and 8th modes. For the excitation in vertical direction, the pseudo-acceleration curve takes values in the range 0.1-0.5 for the first 5 modes and in the range 0.5-0.7 for modes 6 through 8.

Let us now use the above information to study Figure 3.51 and Figure 3.52. We begin with case 2. In both figures, the F_x response is of no interest since it is almost perfectly estimated by only the 1st mode. The F_y, M_x and M_z responses are almost entirely due to horizontal excitations. For these response quantities, the extended MSRS rule can provide significant improvements compared to the original rule for $n = 1$, and smaller improvements for larger n. The generalized forces F_z and M_y are mainly contributed from the bridge response to excitation in vertical direction. The corresponding charts demonstrate that when truncated modes have very small $A(\omega)/\mathrm{PGA}$ values, i.e. for $n < 6$, the extended rule can result in very large overestimations, but when truncated modes have $A(\omega)/\mathrm{PGA}$ values close to unity, i.e. for $n \geq 6$, the extended rule provides improved approximations. When variation of soil conditions significantly increases the pseudo-static contributions (F_z at middle of span 2, M_y at left end of span 3), both the original and the extended rules are more accurate in case 3 than in case 2 for a certain number of modes considered.

3.7 SUMMARY

The MSRS analysis of four real bridge models demonstrated the complex way in which differential support motions influence structural response. The analysis showed that neglecting spatial variability of the support motions, in some cases leads to conservative design, but in other cases is highly non-conservative. The effect of spatial variability was, in general, more severe on element forces along the deck and milder on pier drifts. Also, for pier drifts it was beneficial, i.e. decreased the response, more often than for element forces. Under varying support motions and except for Penstock Bridge (the most flexible among the bridges examined), variation of soil conditions, increased all responses except for M_x.

Compared to the original MSRS rule, the extended rule provided improved approximations of the responses, when truncated modes had nearly static responses, i.e. pseudo-acceleration responses nearly equal to the corresponding peak ground acceleration. Another important result of this chapter is that a pair of closely-spaced modes should not be separated in the analysis, i.e. the modes should be either both included or both truncated.

Table 3.1: Stiffness values of the springs used to model the abutment responses.

bridge name	left abutment		right abutment	
	K_x (KN/m)	K_y (KN/m)	K_x (KN/m)	K_y (KN/m)
Auburn Ravine Bridge	59,604	33,800	59,604	24,300
Big Rock Wash Bridge	131,520	60,301	131,520	54,709
South Ingram Slough Bridge	76,763	9,430	76,763	9,430
Penstock Bridge	59,556	4,897	59,556	6,875

Table 3.2: Soil types at each support for each case of ground motion spatial variability.

bridge name	case	support number: soil type
Auburn Ravine Bridge	1 & 2	all supports: **C**
	3	1: **B**, 2: **C**, 3: **D**, 4: **C**, 5: **D**, 6: **C**, 7: **B**
Big Rock Wash Bridge	1 & 2	all supports: **D**
	3	1: **C**, 2: **D**, 3: **D**, 4: **C**
South Ingram Slough Bridge	1 & 2	all supports: **C**
	3	1: **B**, 2: **C**, 3: **D**
Penstock Bridge	1 & 2	all supports: **C**
	3	1: **B**, 2: **C**, 3: **D**, 4: **C**, 5: **B**

Table 3.3: Soil type characteristics according to Caltrans specifications.

soil type	description	shear wave velocity (m/s)
B	rock	$760 < v_s < 1500$
C	very dense soil/soft rock	$360 < v_s < 760$
D	stiff soil	$180 < v_s < 360$

Table 3.4: Peak Ground Acceleration (PGA) for each soil-type and direction of excitation.

soil type	PGA (g)			
	case: $M_w = 6.5$, $\ddot{u}_{max}^{rock} = 0.3\ g$		case: $M_w = 8.0$, $\ddot{u}_{max}^{rock} = 0.6\ g$	
	horizontal	vertical	horizontal	vertical
B	0.30	0.51	0.60	1.06
C	0.33	0.56	0.60	1.06
D	0.36	0.75	0.60	1.30

Table 3.5: Frequencies of soil columns modeled with the SDOF-oscillator idealization.

excitation direction: soil type	$\omega_k/2\pi$ (Hz)	
	case: $M_w = 6.5$, $\ddot{u}_{max}^{rock} = 0.3\ g$	vase: $M_w = 8.0$, $\ddot{u}_{max}^{rock} = 0.6\ g$
horizontal: B	3.25	2.50
horizontal: C	2.50	1.75
horizontal: D	2.25	1.25
vertical: B, C, D	7.50	7.50

Table 3.6: Measures of participating modal mass, $r_n{}^U$ and $r_n{}^{TI}$, for the number of modes, *n*, included in the analysis of each bridge model.

Bridge name	n	r_n^U	r_n^{TI}
Auburn Ravine Bridge	30	0.90	0.94
Big Rock Wash Bridge	25	0.95	0.91
South Ingram Slough Bridge	25	0.99	0.99
Penstock Bridge	30	0.96	0.93

Table 3.7: Auburn Ravine Bridge: Mean peaks of pier drifts.

pier location		% drift in X direction			% drift in Y direction		
		case 1	case 2	case 3	case 1	case 2	case 3
bent 2	left pier	0.77	0.72	0.73	0.53	0.54	0.54
	right pier	0.81	0.74	0.75	0.56	0.55	0.56
bent 3	left pier	0.77	0.54	0.81	0.73	0.55	0.63
	right pier	0.79	0.55	0.82	0.77	0.57	0.64
bent 4	left pier	0.73	0.48	0.48	0.88	0.57	0.65
	right pier	0.74	0.49	0.48	0.92	0.58	0.66
bent 5	left pier	0.69	0.57	0.78	0.91	0.55	0.62
	right pier	0.68	0.56	0.79	0.93	0.56	0.63
bent 6	left pier	0.72	0.79	0.80	0.93	0.60	0.62
	right pier	0.70	0.78	0.79	0.94	0.61	0.63

Table 3.8 Auburn Ravine Bridge: Pseudo-static contributions to mean peaks of pier drifts (z_s^2/z^2).

pier location		% drift in X direction		% drift in Y direction	
		case 2	case 3	case 2	case 3
bent 2	left pier	70.5	72.5	3.7	9.5
	right pier	69.6	71.4	4.7	9.7
bent 3	left pier	50.0	87.7	6.7	36.8
	right pier	49.4	87.2	6.8	35.2
bent 4	left pier	42.1	42.8	6.8	14.9
	right pier	42.7	43.8	6.6	14.3
bent 5	left pier	59.6	85.4	6.9	33.6
	right pier	60.6	87.1	6.6	34.7
bent 6	left pier	73.4	73.6	7.2	12.3
	right pier	74.4	75.3	7.2	12.7

Table 3.9: Big Rock Wash Bridge: Mean peaks of pier drifts.

pier location		% drift in X direction			% drift in Y direction		
		case 1	case 2	case 3	case 1	case 2	case 3
bent 2	middle pier	1.56	1.37	1.59	1.91	1.52	1.53
	side pier 1	1.60	1.49	1.68	1.97	1.57	1.57
	side pier 2	1.60	1.49	1.68	1.97	1.57	1.57
bent 3	middle pier	1.51	1.36	1.53	2.14	1.44	1.41
	side pier 1	1.55	1.48	1.63	2.20	1.48	1.45
	side pier 2	1.55	1.48	1.63	2.20	1.48	1.45

Table 3.10: Big Rock Wash Bridge: Pseudo-static contributions to mean peaks of pier drifts (z_s^2/z^2).

pier location		% drift in X direction		% drift in Y direction	
		case 2	case 3	case 2	case 3
bent 2	middle pier	58.9	80.6	4.3	17.2
	side pier 1	59.8	79.4	4.3	17.2
	side pier 2	59.8	79.4	4.3	17.2
bent 3	middle pier	59.2	79.4	4.5	19.4
	side pier 1	60.2	78.2	4.5	19.4
	side pier 2	60.2	78.2	4.5	19.4

Table 3.11: South Ingram Slough Bridge: Mean peaks of pier drifts.

pier location		% drift in X direction			% drift in Y direction		
		case 1	case 2	case 3	case 1	case 2	case 3
bent 2	pier 1	0.30	0.21	0.22	0.70	0.64	0.62
	pier 2	0.30	0.21	0.22	0.69	0.64	0.62

Table 3.12: South Ingram Slough Bridge: Pseudo-static contributions to mean peaks of pier drifts (z_s^2/z^2).

pier location		% drift in X direction		% drift in Y direction	
		case 2	case 3	case 2	case 3
bent 2	pier 1	9.5	19.7	0.3	0.8
	pier 2	9.7	20.2	0.3	0.8

Table 3.13: Penstock Bridge: Mean peaks of pier drifts.

pier location	% drift in X direction			% drift in Y direction		
	case 1	case 2	case 3	case 1	case 2	case 3
bent 2	0.38	0.31	0.30	0.88	0.95	0.76
bent 3	0.39	0.29	0.37	0.81	0.84	0.69
bent 4	0.43	0.34	0.33	0.72	0.78	0.62

Table 3.14: Penstock Bridge: Pseudo-static contributions to mean peaks of pier drifts (z_s^2/z^2).

pier location	% drift in X direction		% drift in Y direction	
	case 2	case 3	case 2	case 3
bent 2	33.1	67.3	6.3	7.7
bent 3	25.3	87.0	9.0	20.7
bent 4	31.9	66.1	6.9	10.5

Table 3.15: Range of values for ratios of responses in case 2 over responses in case 1.

Bridge	F_x	F_y	F_z	M_x	M_y	M_z	X drift	Y drift
Auburn Ravine	1.3-12.7	0.7-1.9	0.7-1.0	0.9-3.0	0.7-1.1	0.8-1.5	0.7-1.1	0.6-1.0
Big Rock Wash	1.8-43.0	0.7-3.1	0.7-0.9	2.6-2.6	0.7-1.3	0.9-3.7	0.9-1.0	0.7-0.8
S. Ingram Slough	0.9-10.3	0.9-1.2	0.7-1.0	0.8-0.9	0.7-1.0	0.9-1.2	0.7-0.7	0.9-0.9
Penstock	0.9-1.8	1.1-1.7	0.7-1.2	0.7-1.7	0.7-1.2	1.1-1.2	0.7-0.8	1.0-1.1

Table 3.16: Range of values for ratios of responses in case 3 over responses in case 2.

Bridge	F_x	F_y	F_z	M_x	M_y	M_z	X drift	Y drift
Auburn Ravine	0.9-1.1	1.1-2.1	1.1-3.4	1.1-2.6	1.1-3.3	1.3-2.1	1.0-1.5	1.0-1.1
Big Rock Wash	0.9-0.9	1.0-2.1	1.0-1.2	1.0-1.0	1.0-1.2	1.2-2.1	1.1-1.2	1.0-1.0
S. Ingram Slough	1.2-1.7	1.0-1.1	1.0-1.1	1.0-1.2	1.0-1.5	1.0-1.2	1.0-1.0	1.0-1.0
Penstock	0.8-0.8	0.8-1.0	1.0-1.3	0.8-1.1	1.0-1.7	0.8-0.9	1.0-1.3	0.8-0.8

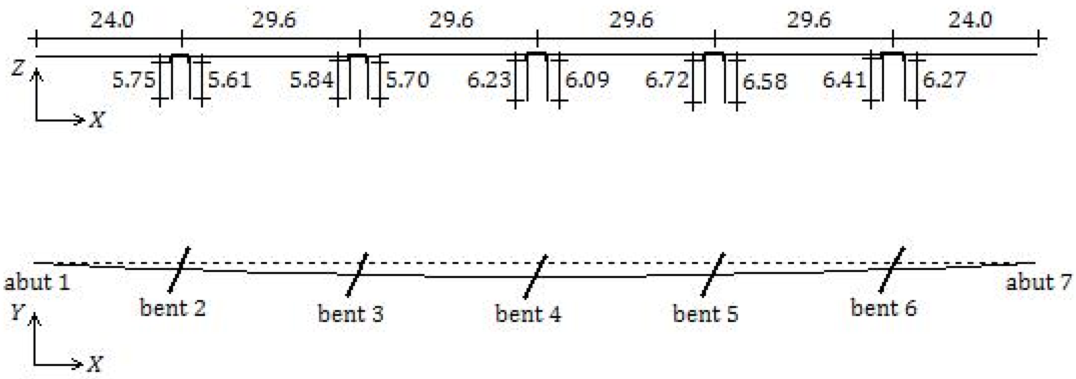

Figure 3.1: Auburn Ravine Bridge: Elevation and plan (Dimensions are in meters).

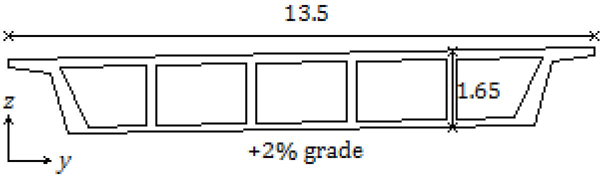

Figure 3.2: Auburn Ravine Bridge: Box-girder cross section (Dimensions are in meters).

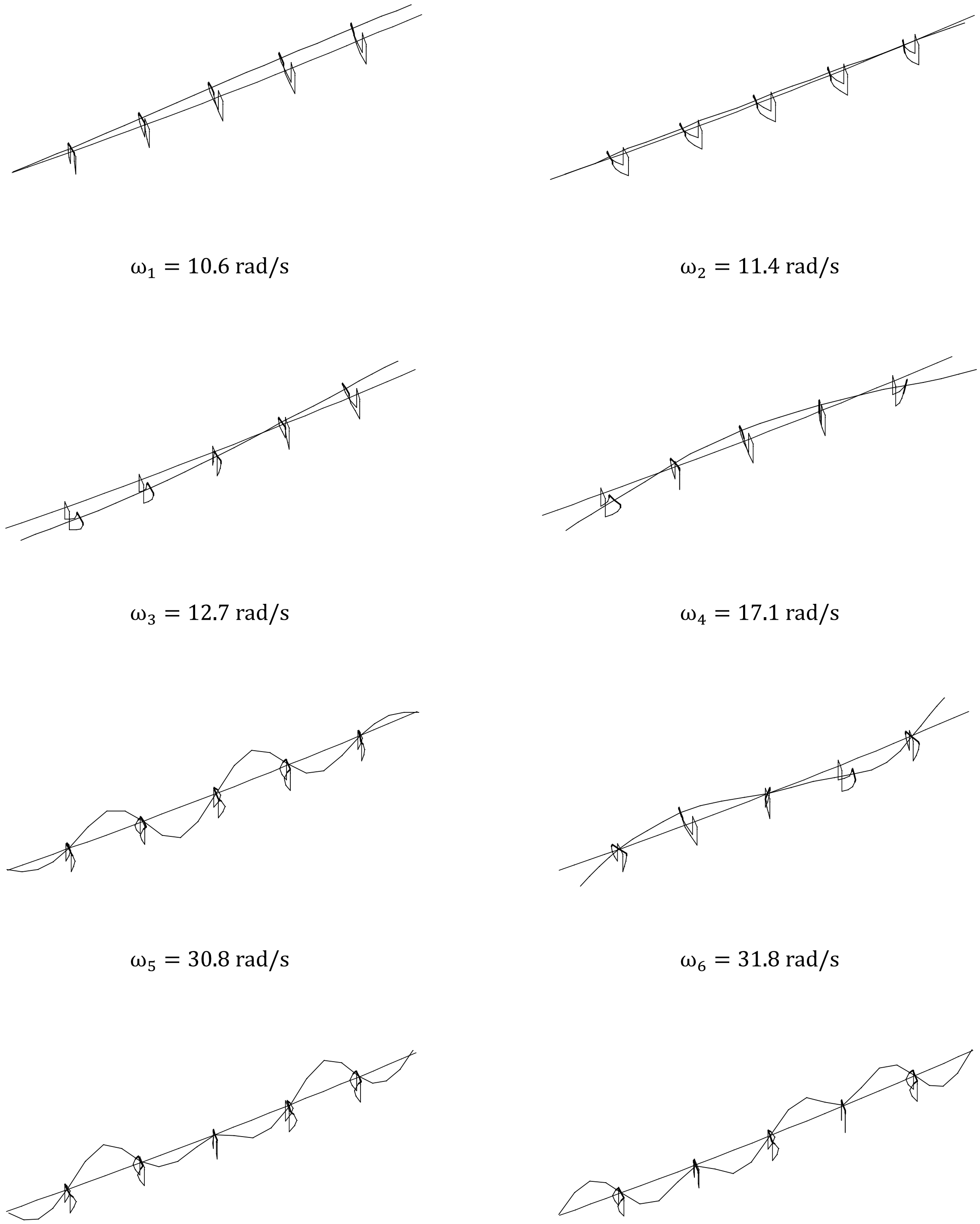

$\omega_1 = 10.6$ rad/s

$\omega_2 = 11.4$ rad/s

$\omega_3 = 12.7$ rad/s

$\omega_4 = 17.1$ rad/s

$\omega_5 = 30.8$ rad/s

$\omega_6 = 31.8$ rad/s

$\omega_7 = 34.4$ rad/s

$\omega_8 = 39.9$ rad/s

Figure 3.3: Auburn Ravine Bridge: First 8 mode shapes and modal frequencies.

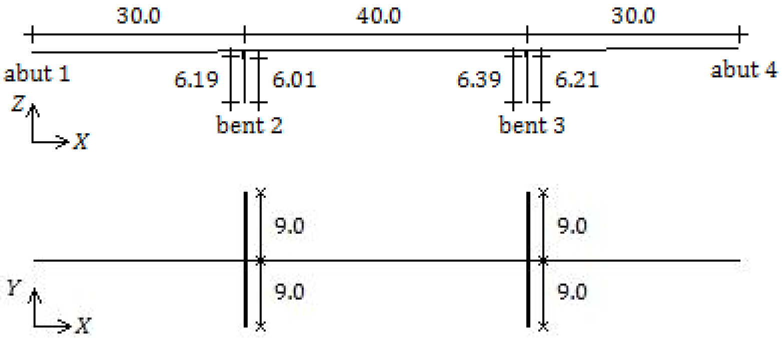

Figure 3.4: Big Rock Wash Bridge: Elevation and plan (Dimensions are in meters).

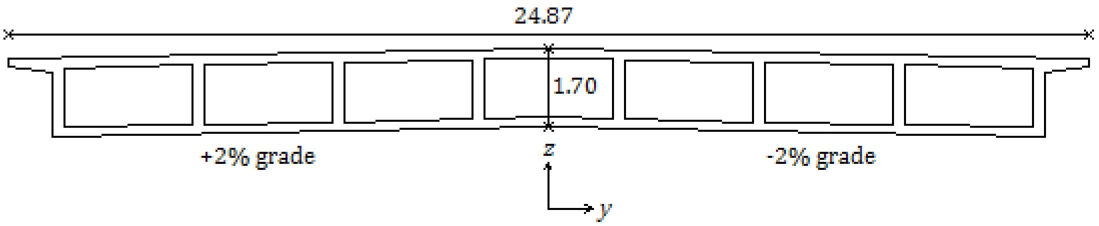

Figure 3.5: Big Rock Wash Bridge: Box-girder cross section (Dimensions are in meters).

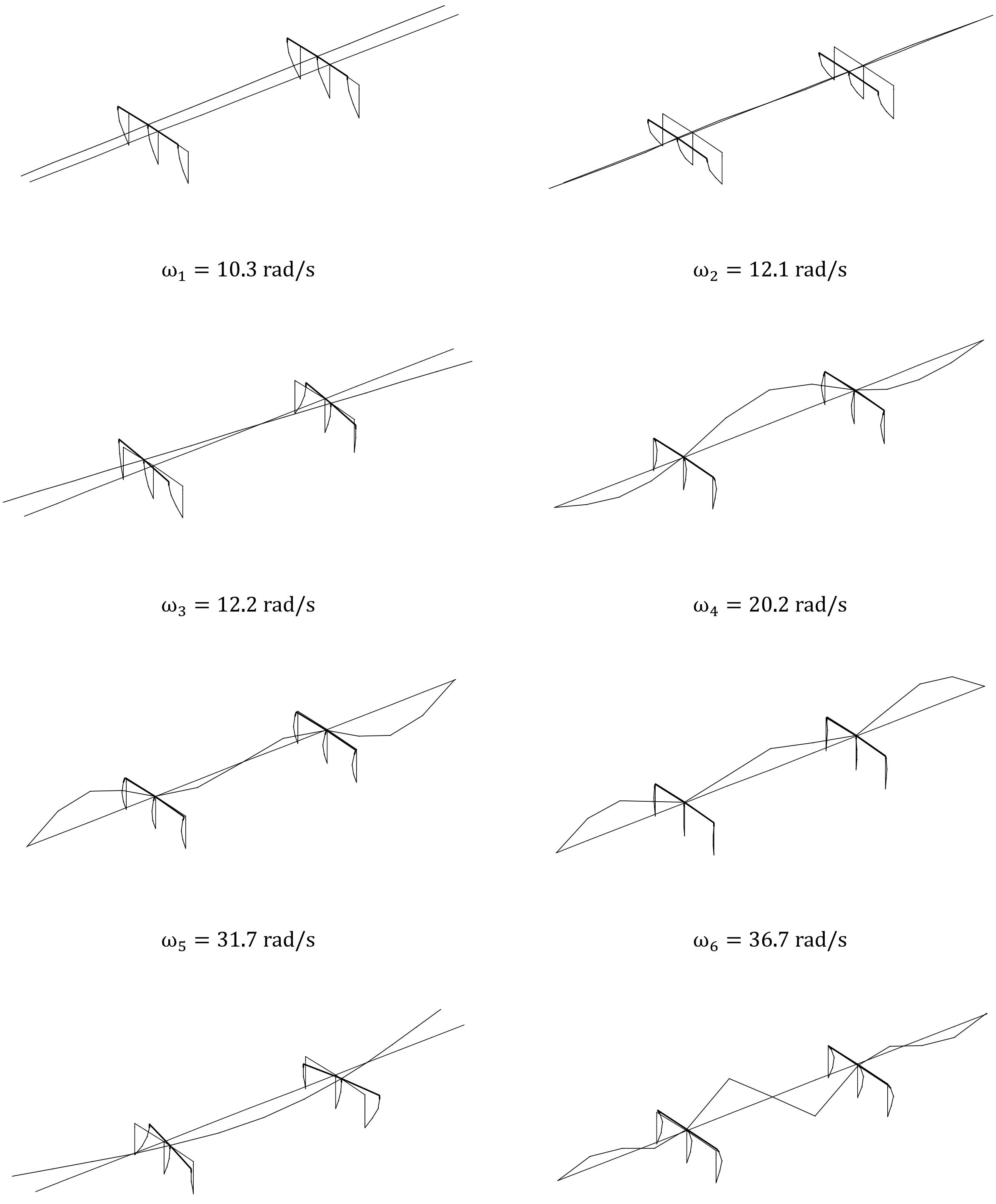

$\omega_1 = 10.3$ rad/s

$\omega_2 = 12.1$ rad/s

$\omega_3 = 12.2$ rad/s

$\omega_4 = 20.2$ rad/s

$\omega_5 = 31.7$ rad/s

$\omega_6 = 36.7$ rad/s

$\omega_7 = 54.9$ rad/s

$\omega_8 = 69.6$ rad/s

Figure 3.6: Big Rock Wash Bridge: First 8 mode shapes and modal frequencies.

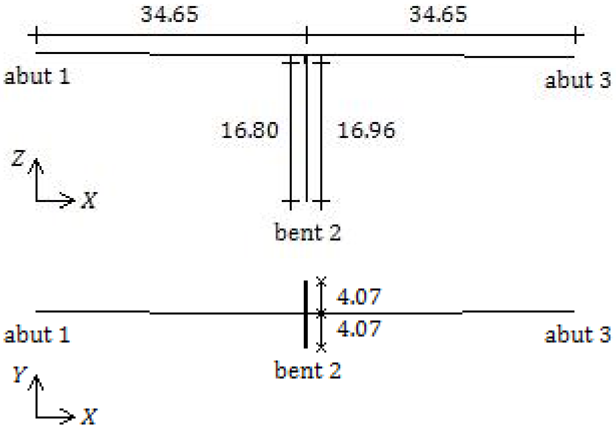

Figure 3.7: South Ingram Slough Bridge: Elevation and plan (Dimensions are in meters).

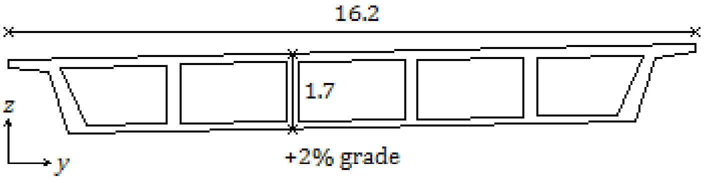

Figure 3.8: South Ingram Slough Bridge: Box-girder cross section (Dimensions are in meters).

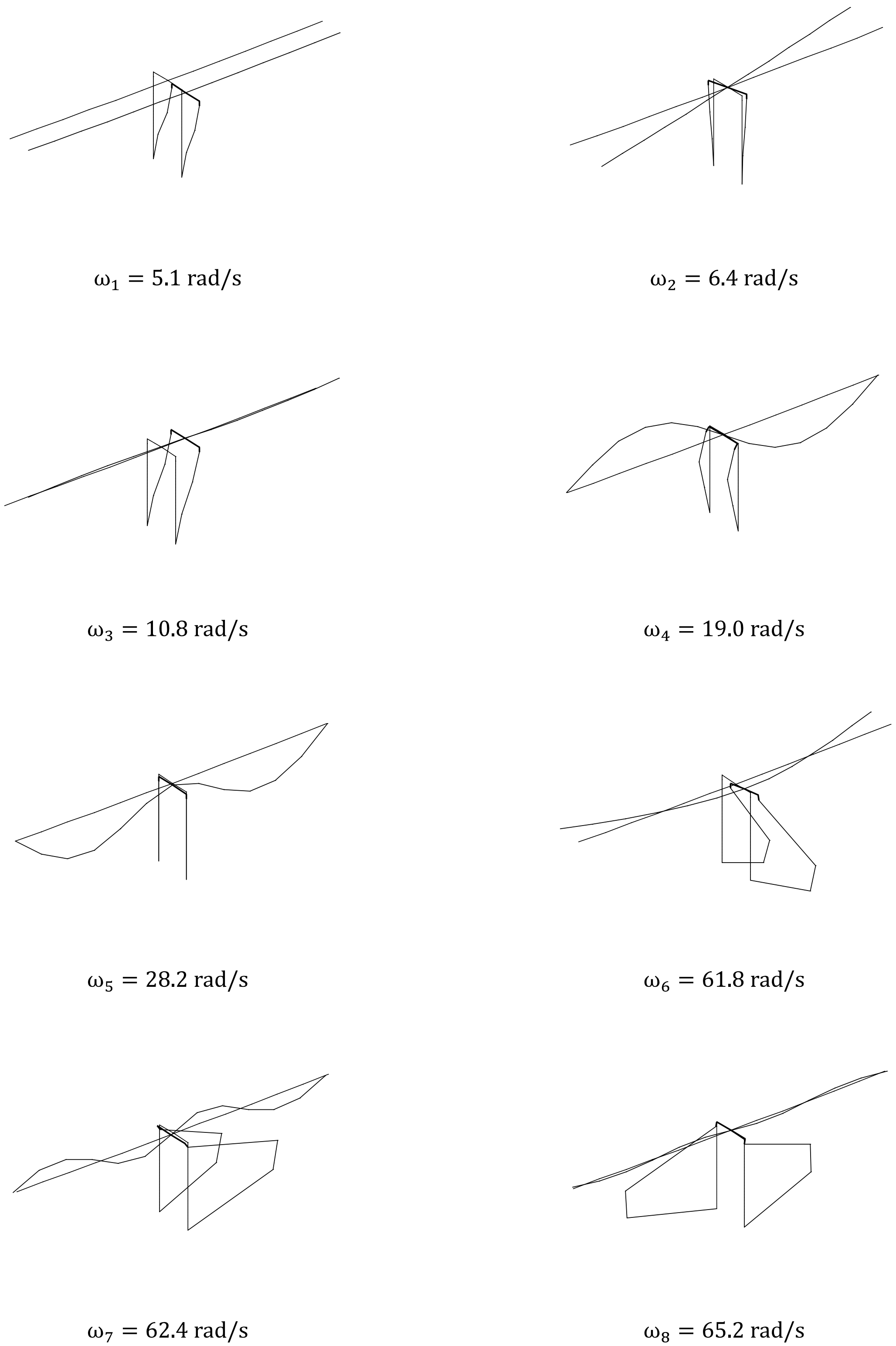

$\omega_1 = 5.1$ rad/s

$\omega_2 = 6.4$ rad/s

$\omega_3 = 10.8$ rad/s

$\omega_4 = 19.0$ rad/s

$\omega_5 = 28.2$ rad/s

$\omega_6 = 61.8$ rad/s

$\omega_7 = 62.4$ rad/s

$\omega_8 = 65.2$ rad/s

Figure 3.9: South Ingram Slough Bridge: First 8 mode shapes and modal frequencies.

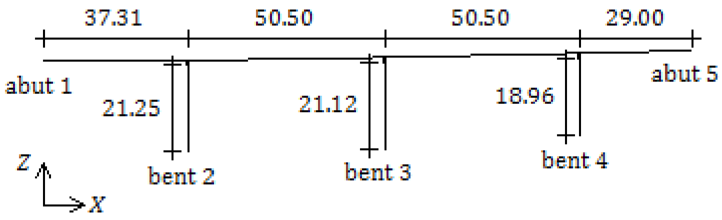

Figure 3.10: Penstock Bridge: Elevation (Dimensions are in meters).

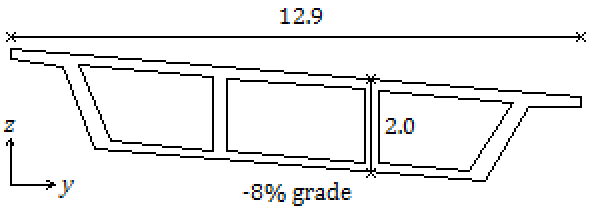

Figure 3.11: Pensotck Bridge: Box-girder cross section (Dimensions are in meters).

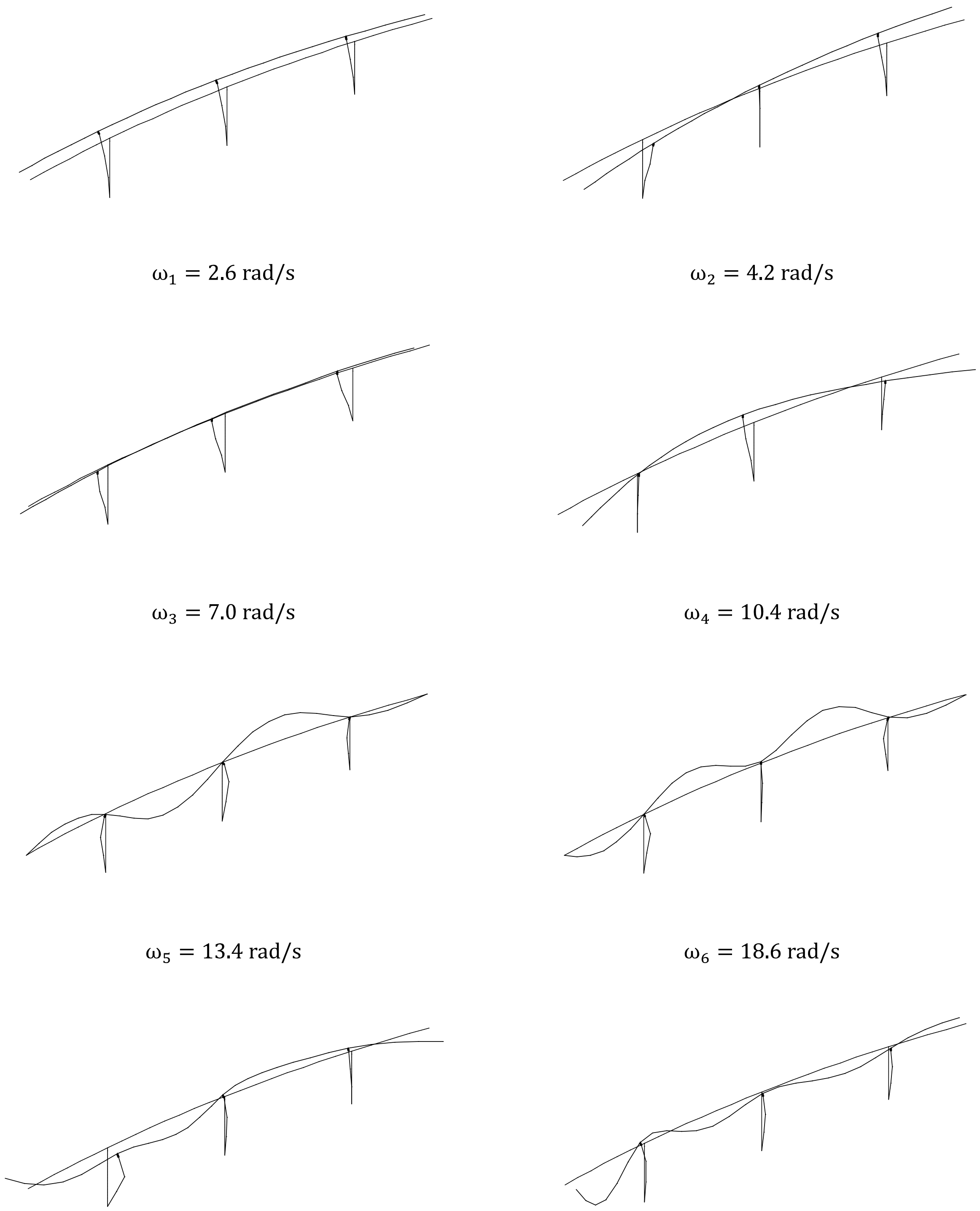

$\omega_1 = 2.6$ rad/s

$\omega_2 = 4.2$ rad/s

$\omega_3 = 7.0$ rad/s

$\omega_4 = 10.4$ rad/s

$\omega_5 = 13.4$ rad/s

$\omega_6 = 18.6$ rad/s

$\omega_7 = 25.8$ rad/s

$\omega_8 = 25.9$ rad/s

Figure 3.12: Penstock Bridge: First 8 mode shapes and modal frequencies.

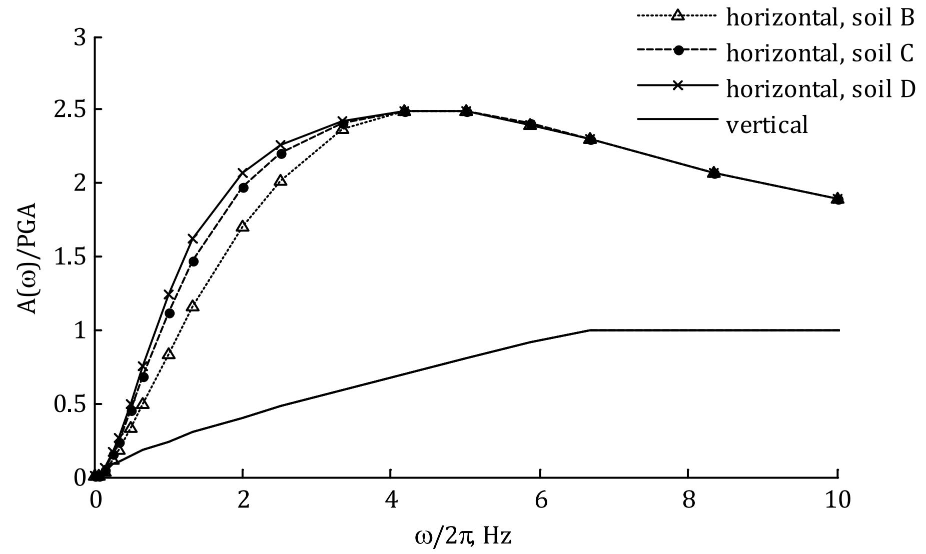

Figure 3.13: Normalized acceleration response spectra for an event of magnitude 6.5 and peak rock acceleration 0.3 *g*.

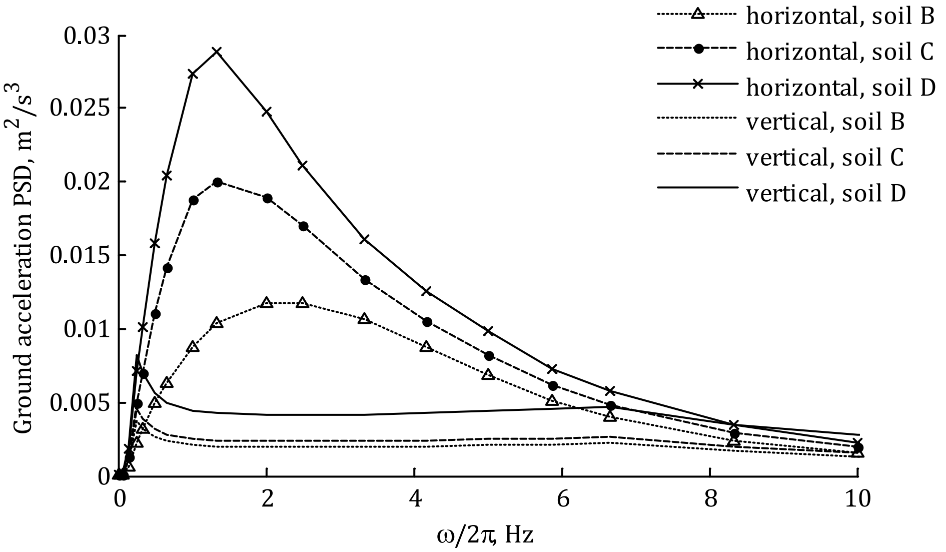

Figure 3.14: Ground acceleration PSDs for an event of magnitude 6.5 and peak rock acceleration 0.3 *g*.

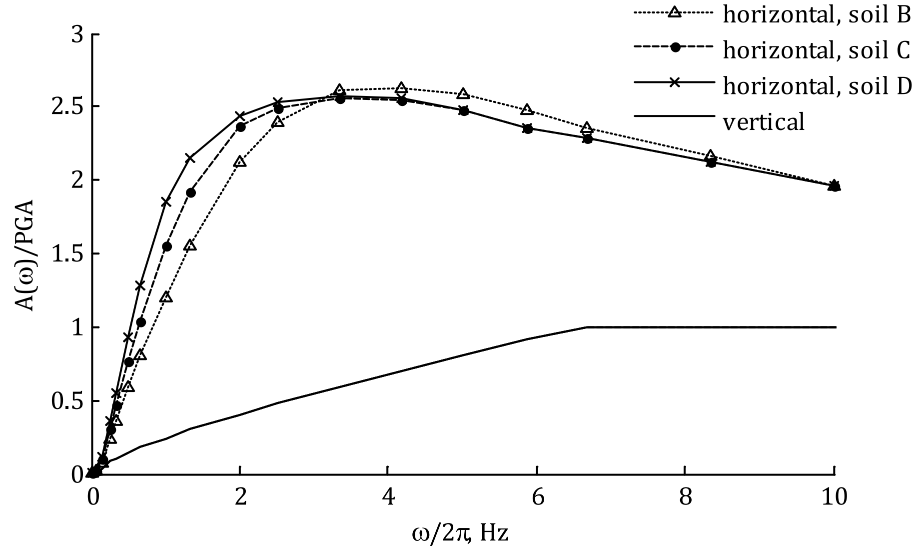

Figure 3.15: Normalized acceleration response spectra for an event of magnitude 8.0 and peak rock acceleration 0.6 *g*.

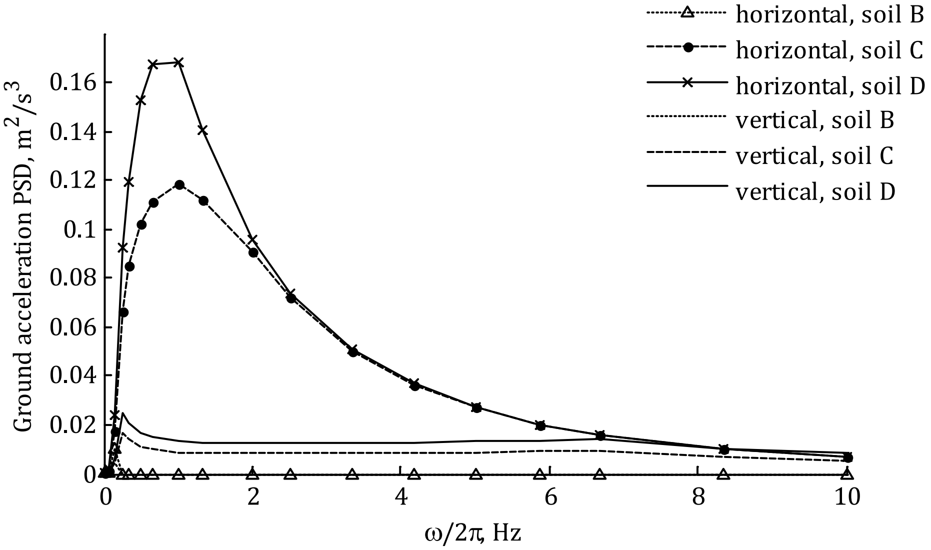

Figure 3.16: Ground acceleration PSDs for an event of magnitude 8.0 and peak rock acceleration 0.6 *g*.

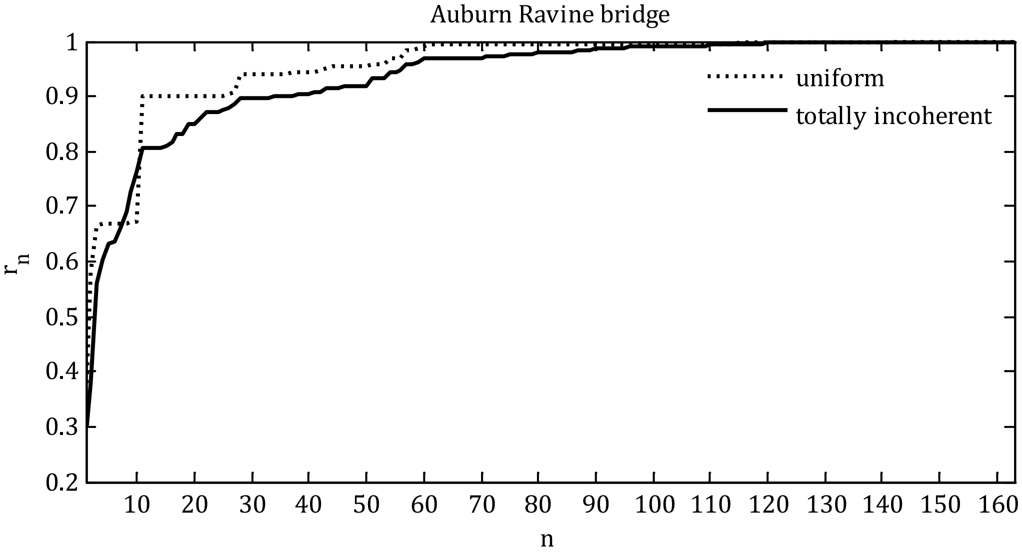

Figure 3.17: Auburn Ravine Bridge: Measures of mass participation.

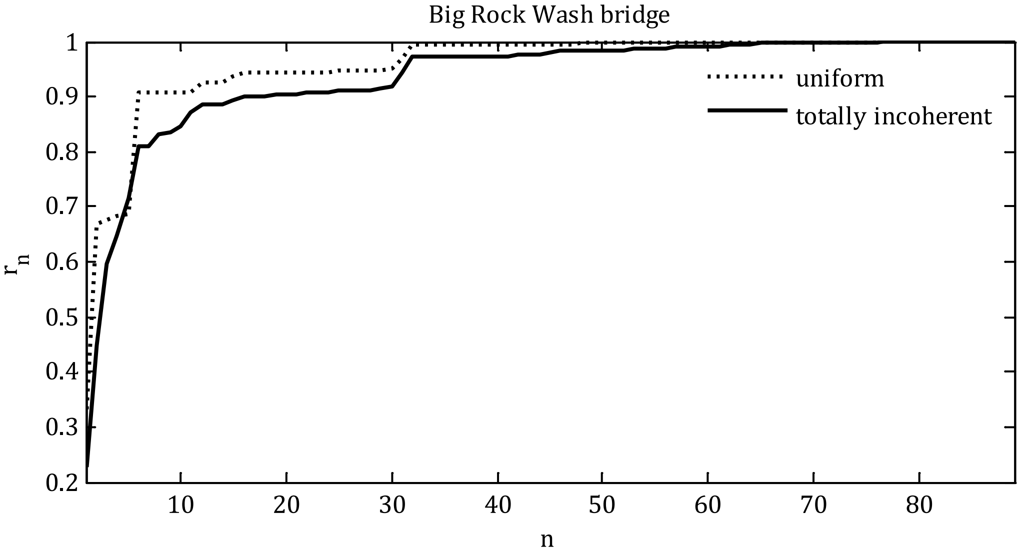

Figure 3.18: Big Rock Wash Bridge: Measures of mass participation.

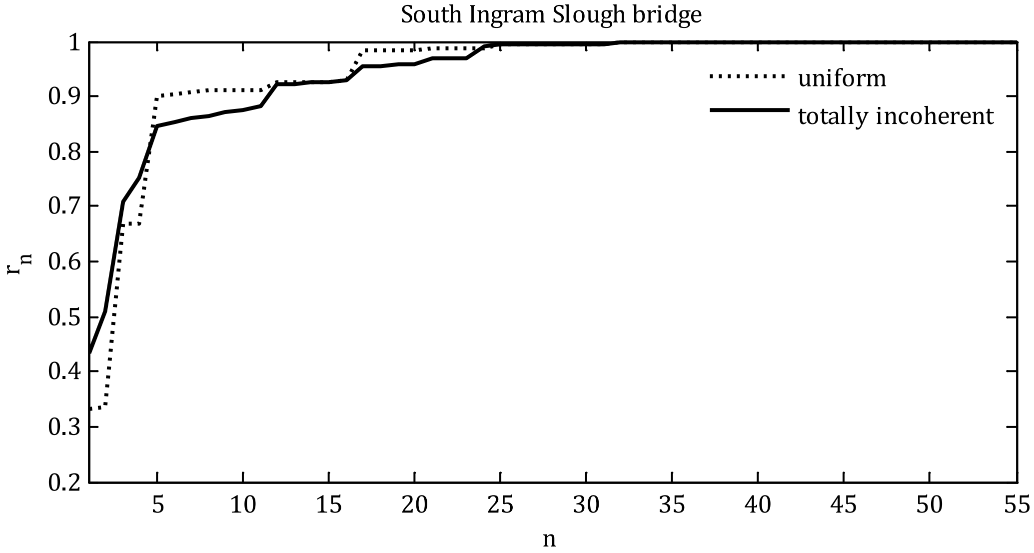

Figure 3.19: South Ingram Slough Bridge: Measures of mass participation.

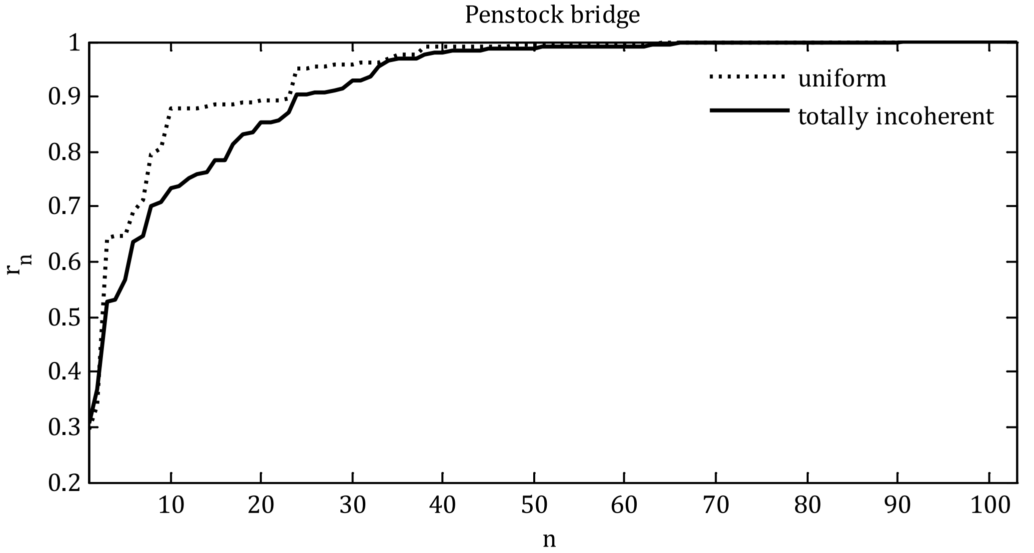

Figure 3.20: Penstock Bridge: Measures of mass participation.

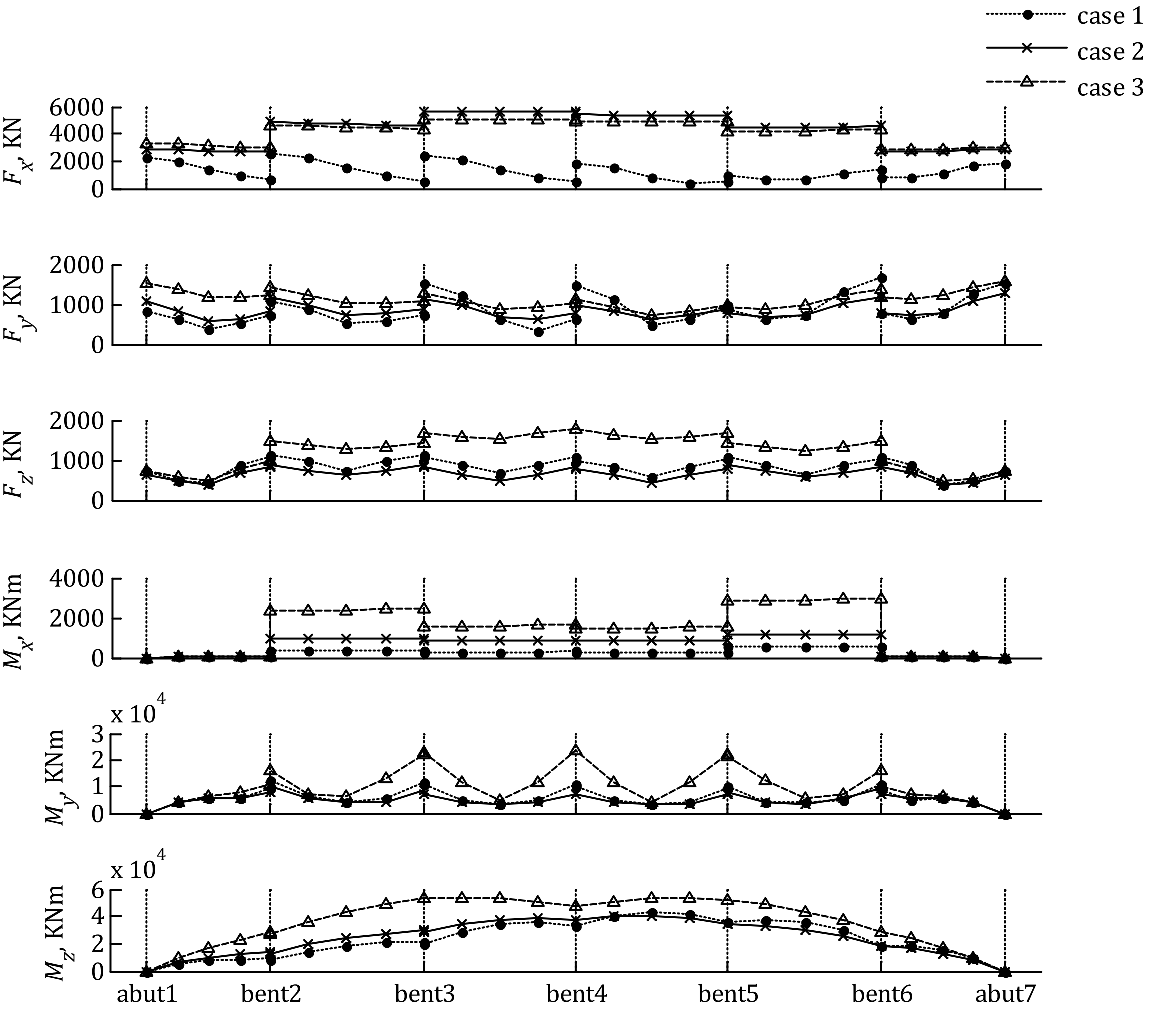

Figure 3.21: Auburn Ravine Bridge: Mean peak responses along the deck.

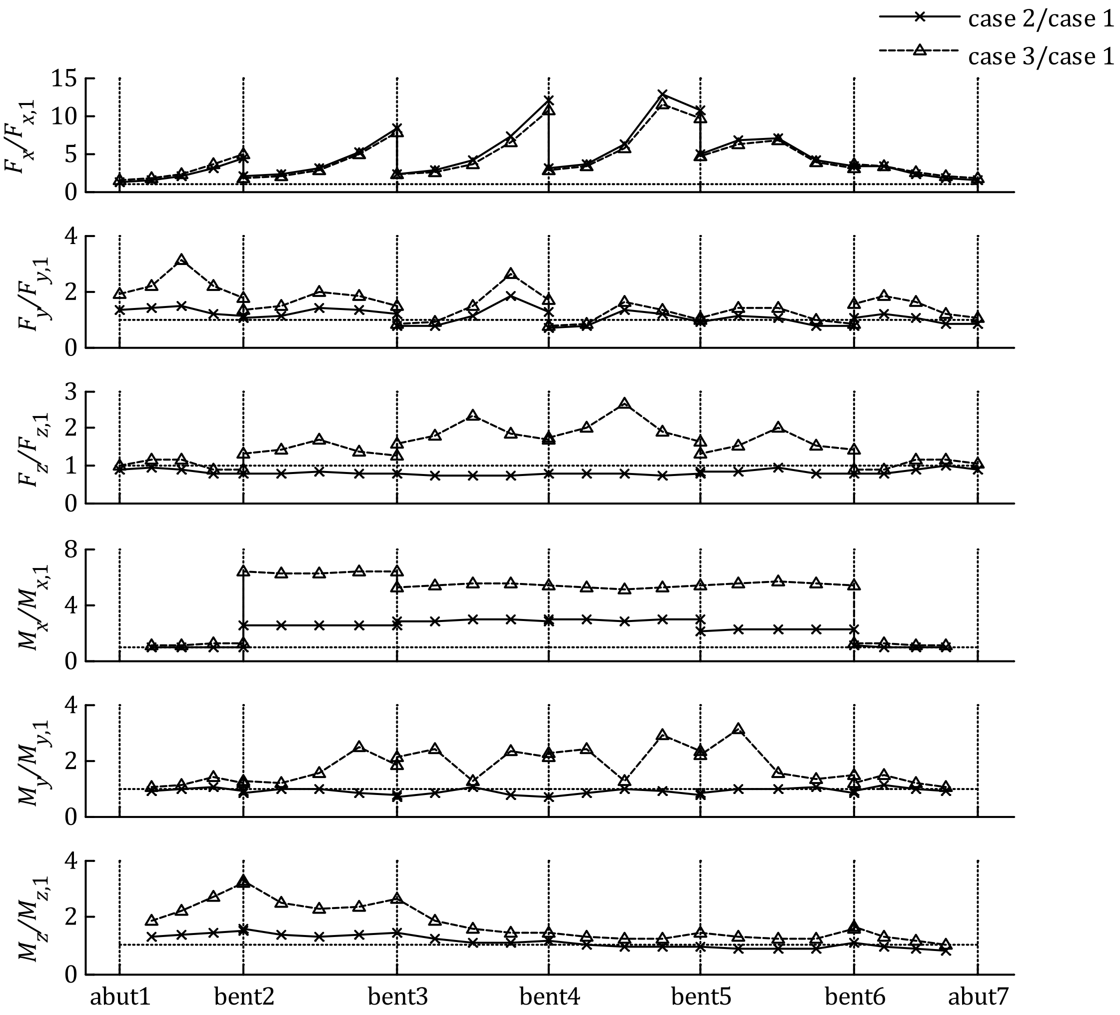

Figure 3.22: Auburn Ravine Bridge: Normalized mean peak responses with respect to the case of uniform excitation.

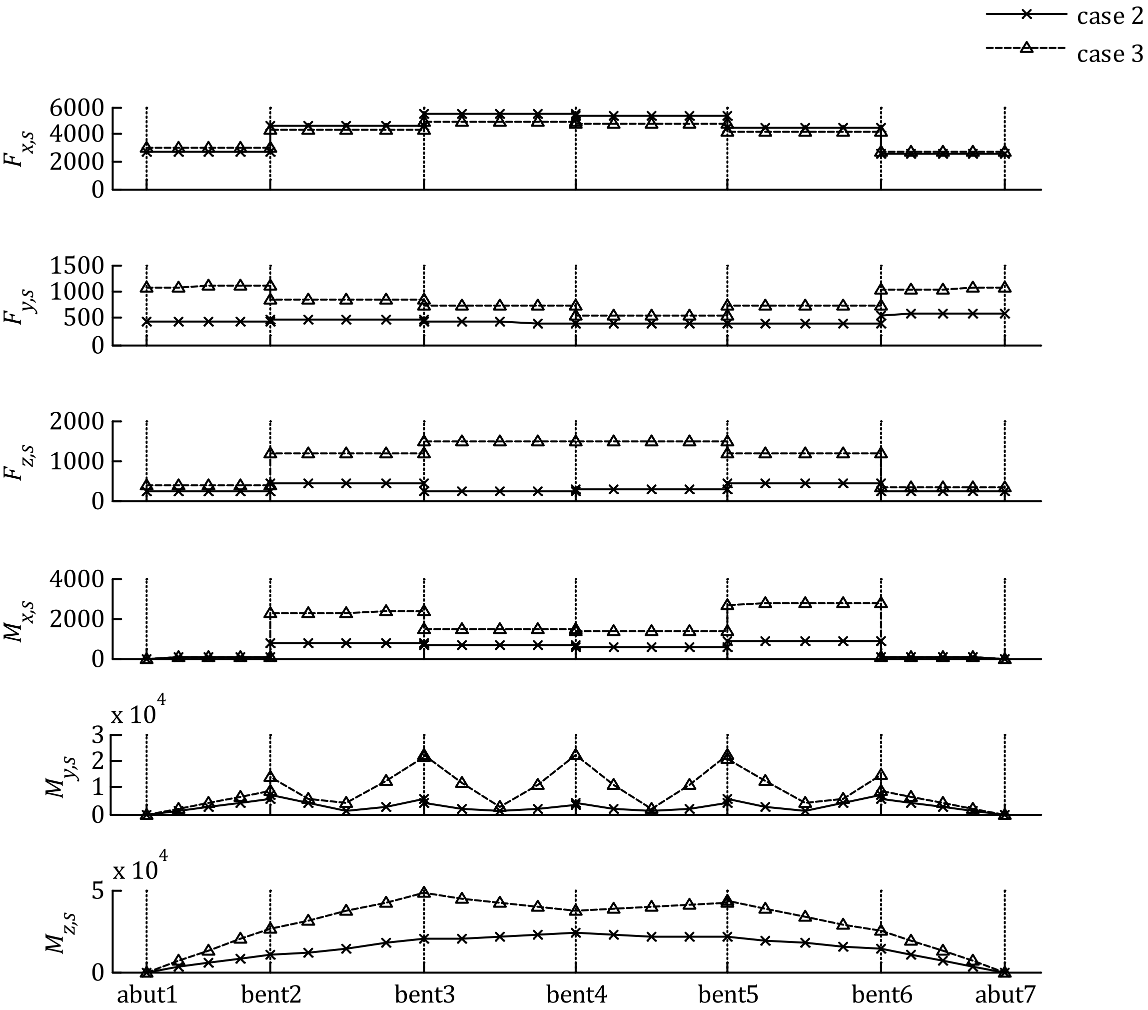

Figure 3.23: Auburn Ravine Bridge: Mean peak pseudo-static responses along the deck.

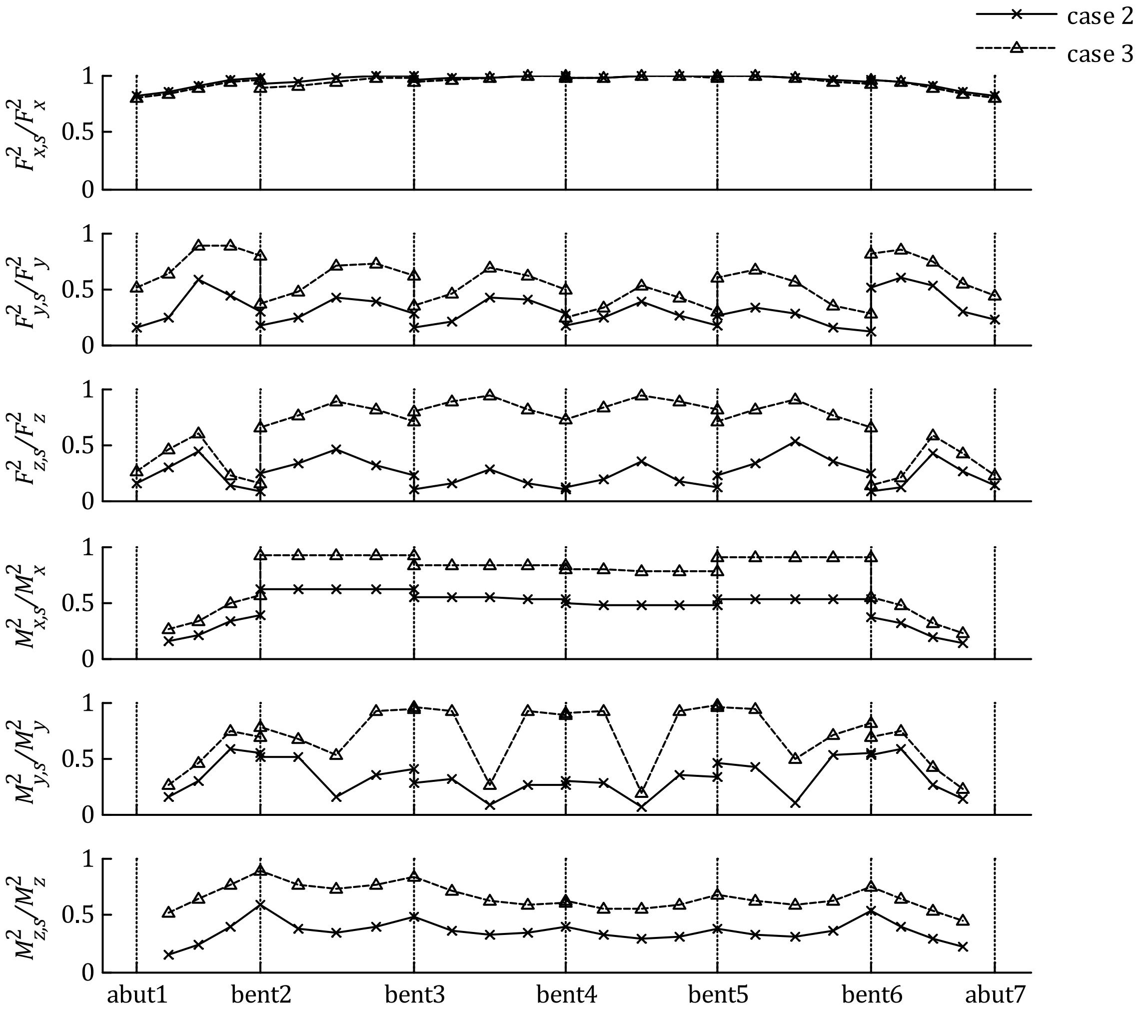

Figure 3.24: Auburn Ravine Bridge: Relative pseudo-static contributions to mean peak responses.

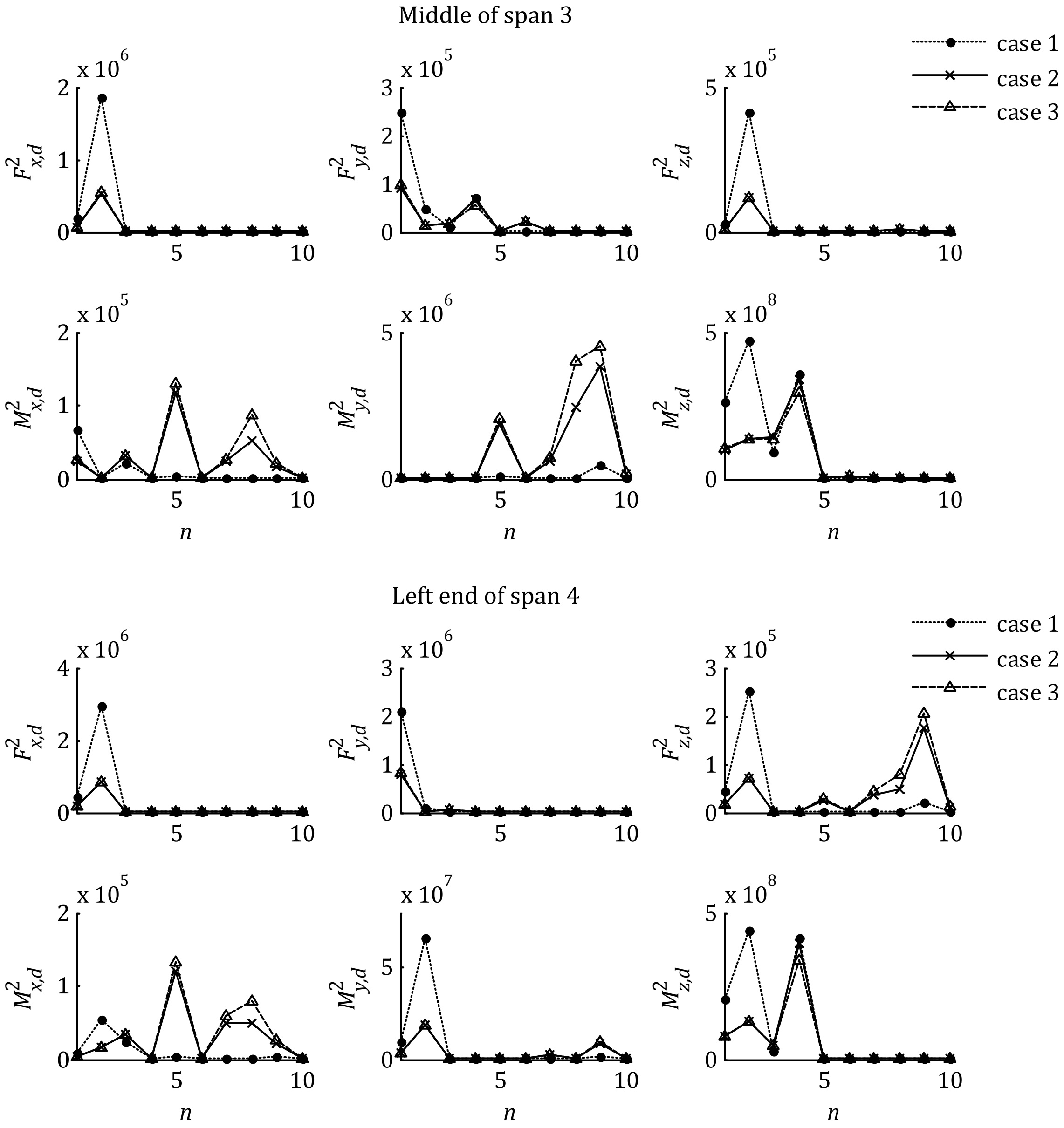

Figure 3.25: Auburn Ravine Bridge: Modal contributions to dynamic component of mean peak responses.

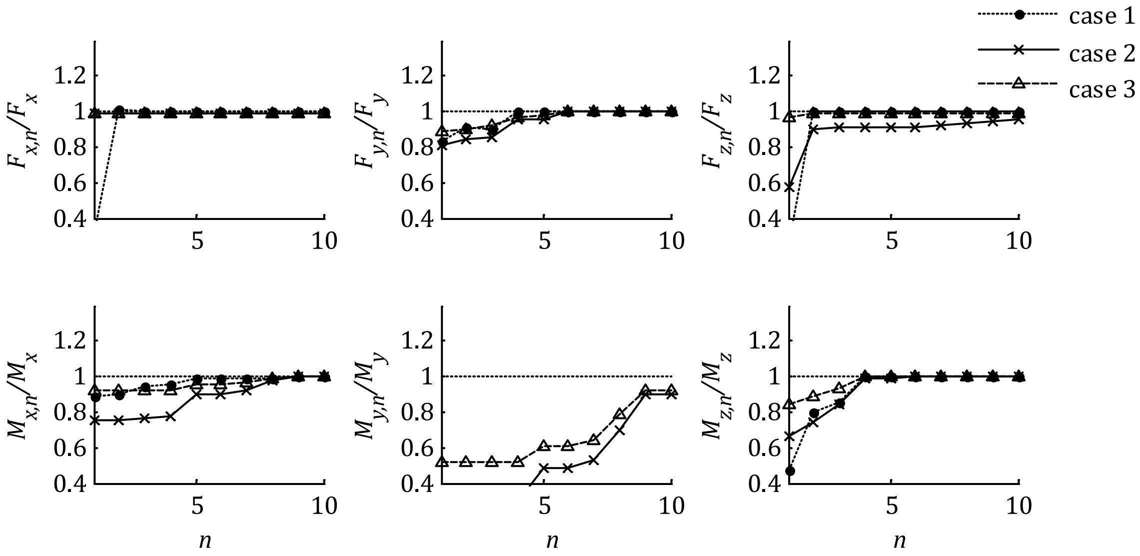
Middle of span 3

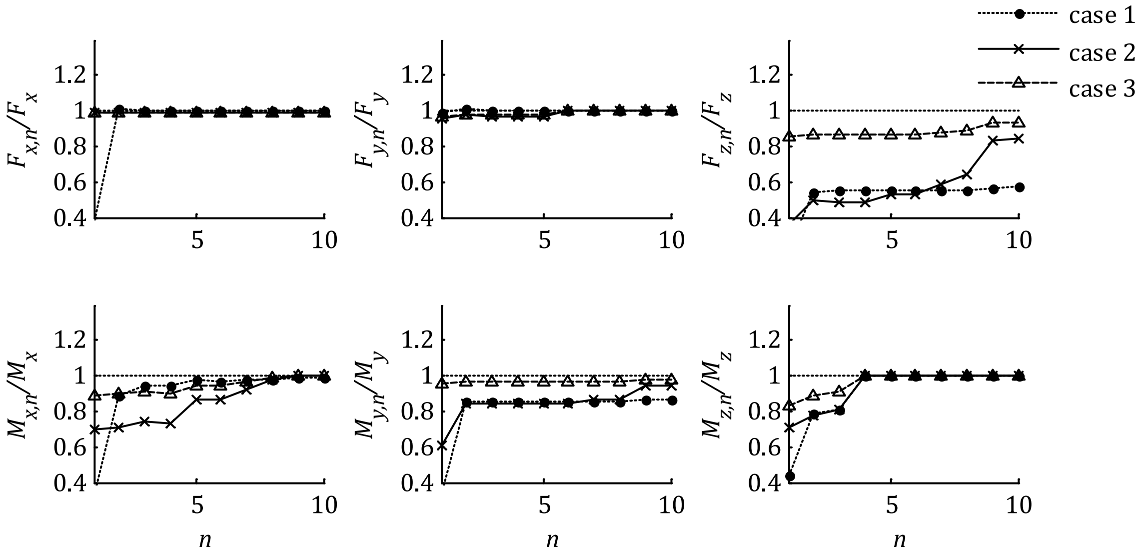
Left end of span 4

Figure 3.26: Auburn Ravine Bridge: Mean peak responses with *n* modes normalized with 'exact' mean peak responses.

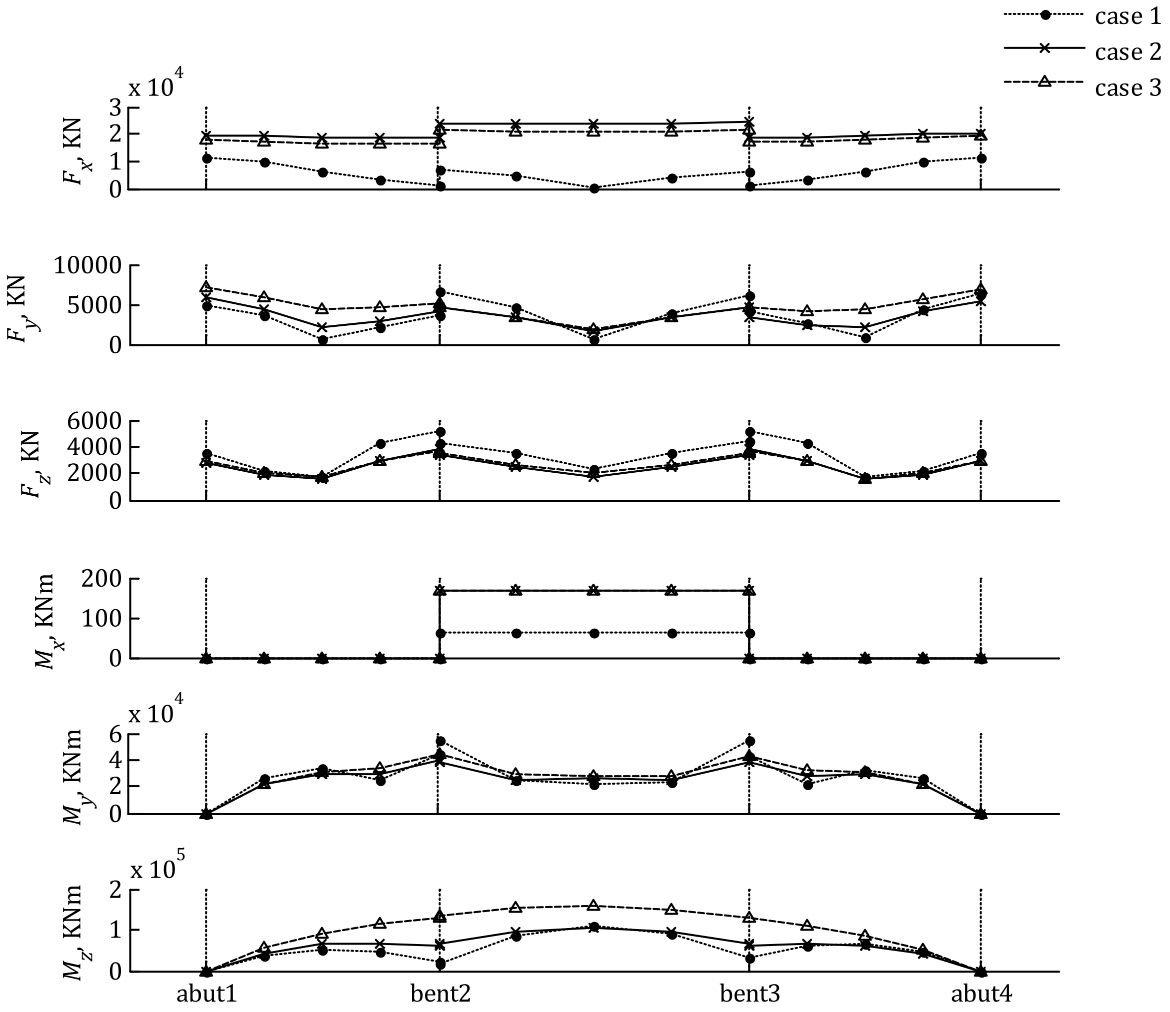

Figure 3.27: Big Rock Wash Bridge: Mean peak responses along the deck.

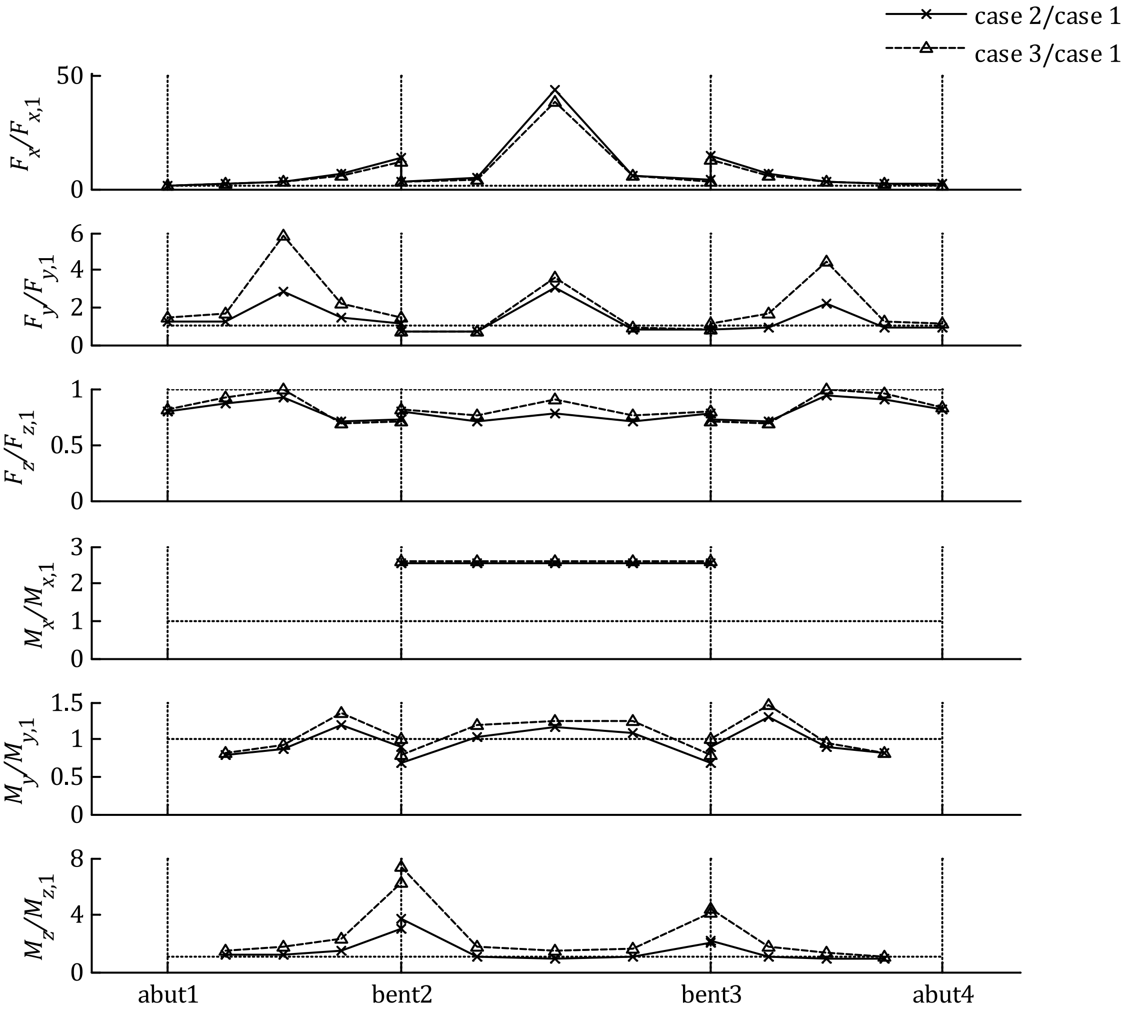

Figure 3.28: Big Rock Wash Bridge: Normalized mean peak responses with respect to the case of uniform excitation.

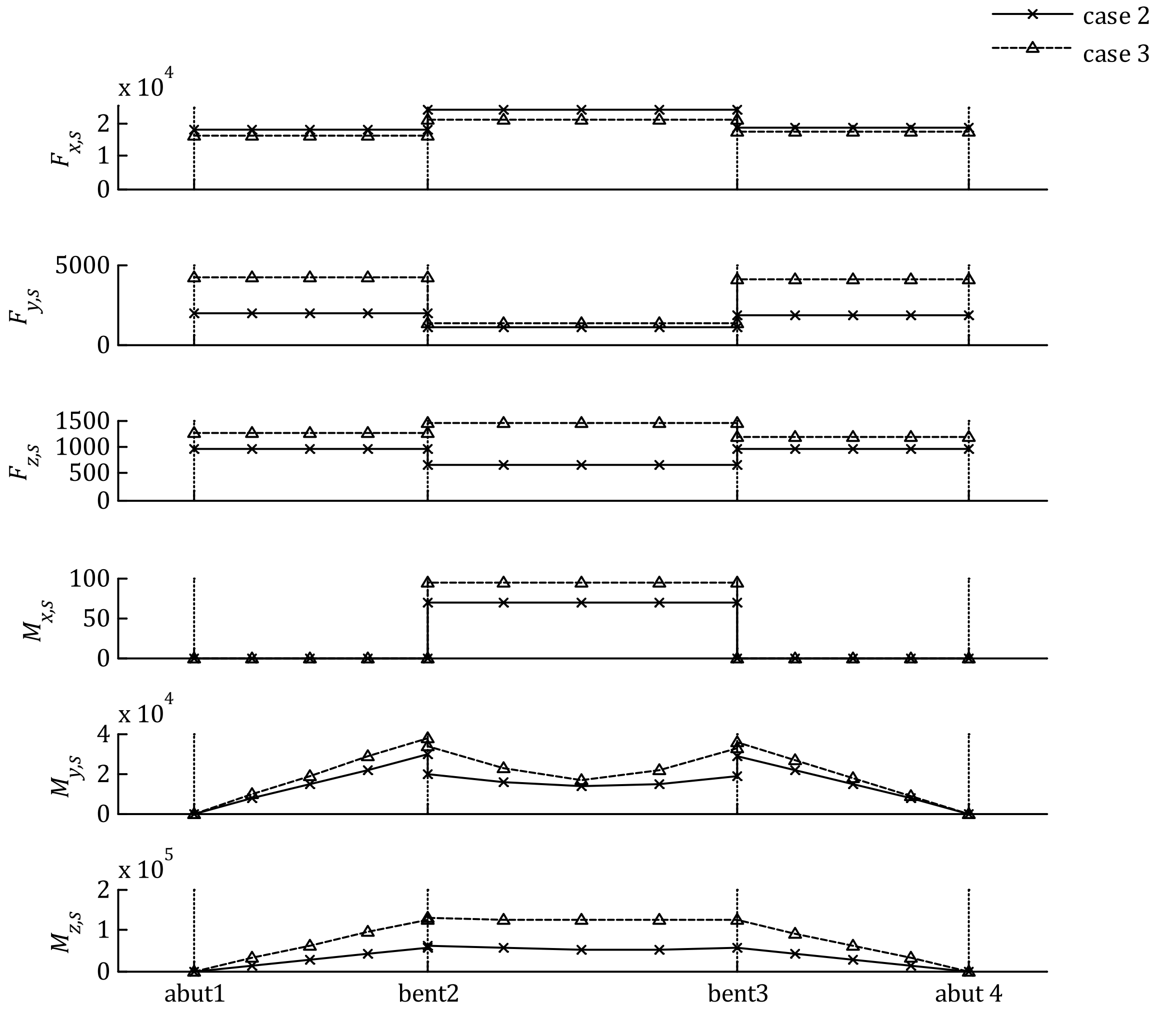

Figure 3.29: Big Rock Wash Bridge: Mean peak pseudo-static responses along the deck.

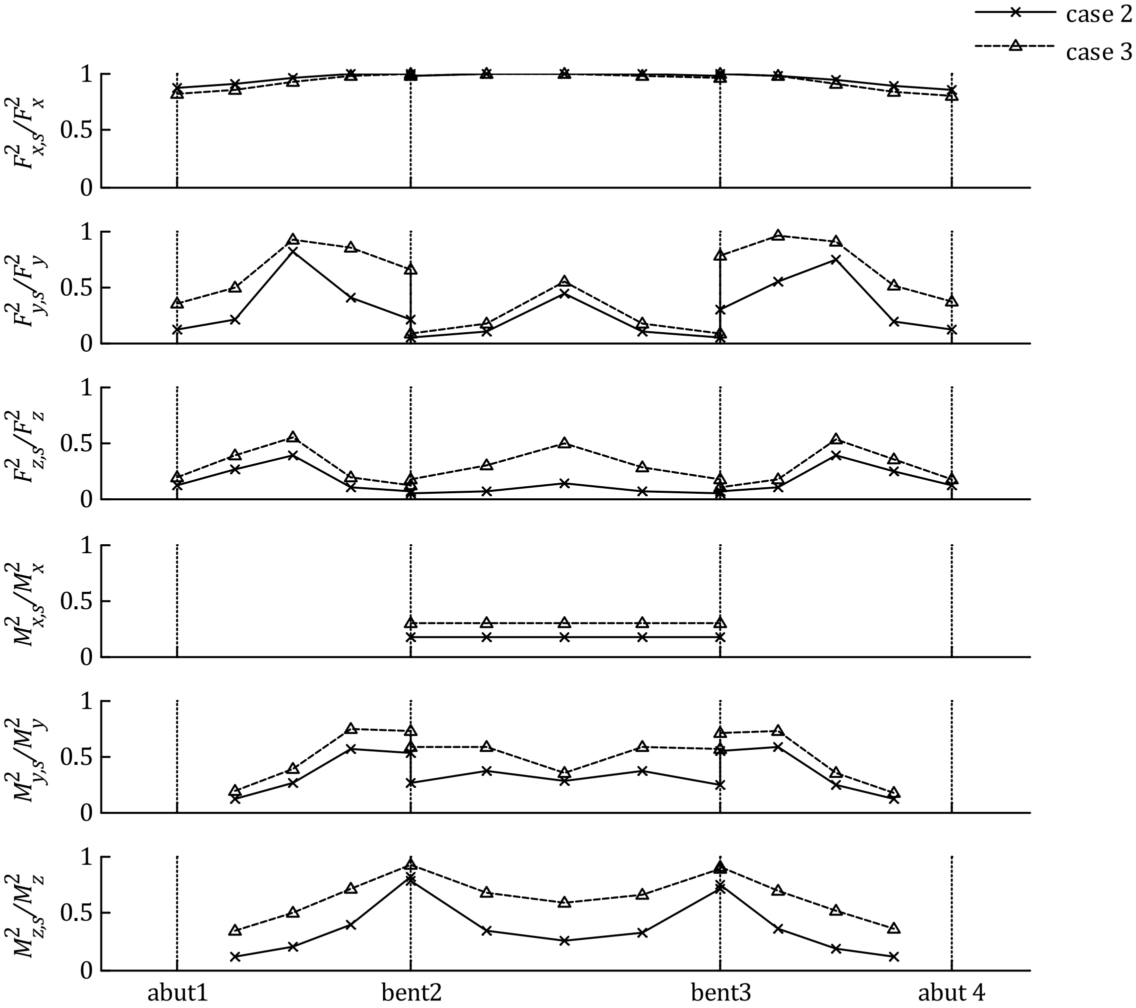

Figure 3.30: Big Rock Wash Bridge: Relative pseudo-static contributions to mean peak responses.

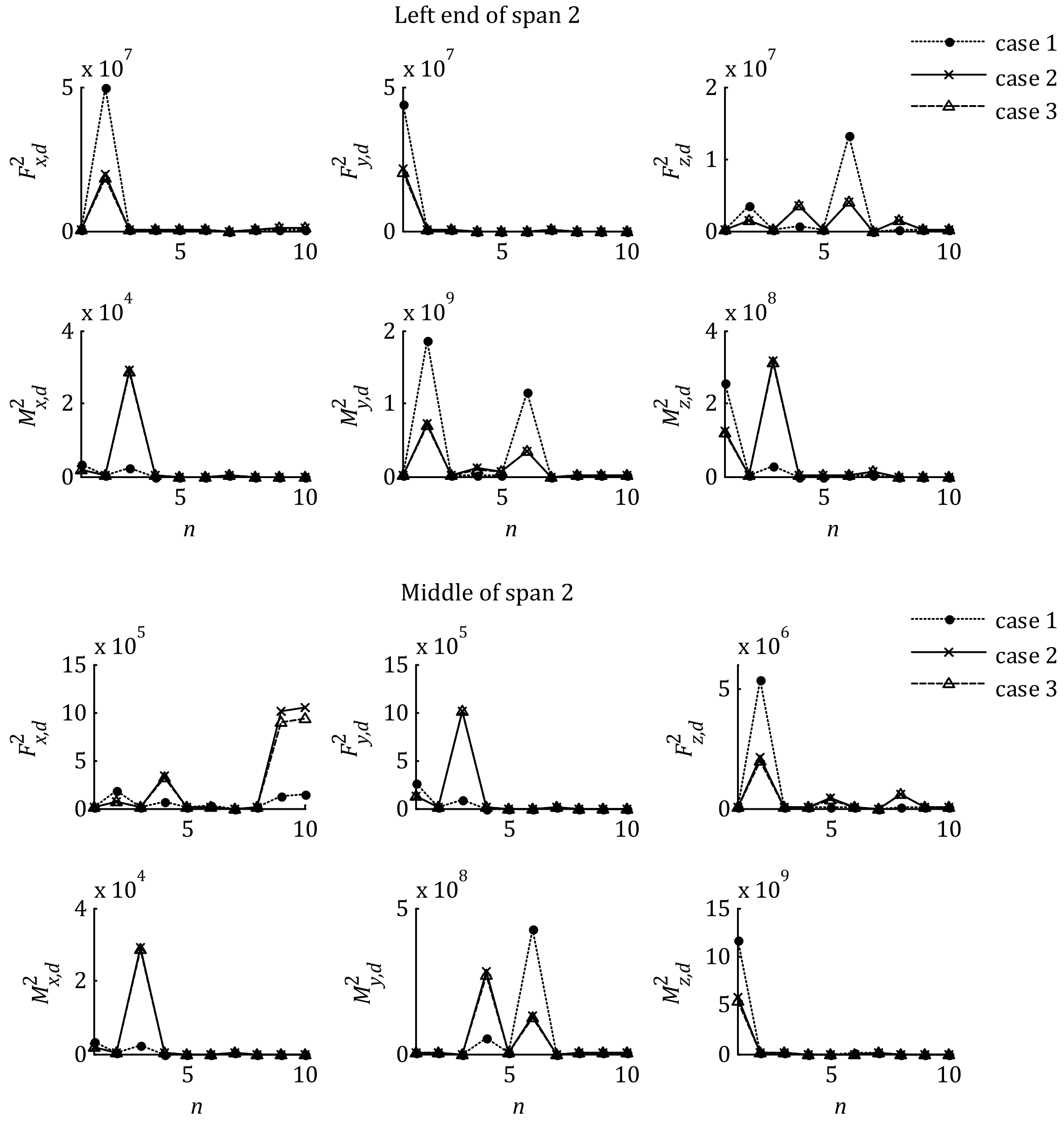

Figure 3.31: Big Rock Wash Bridge: Modal contributions to dynamic component of mean peak responses.

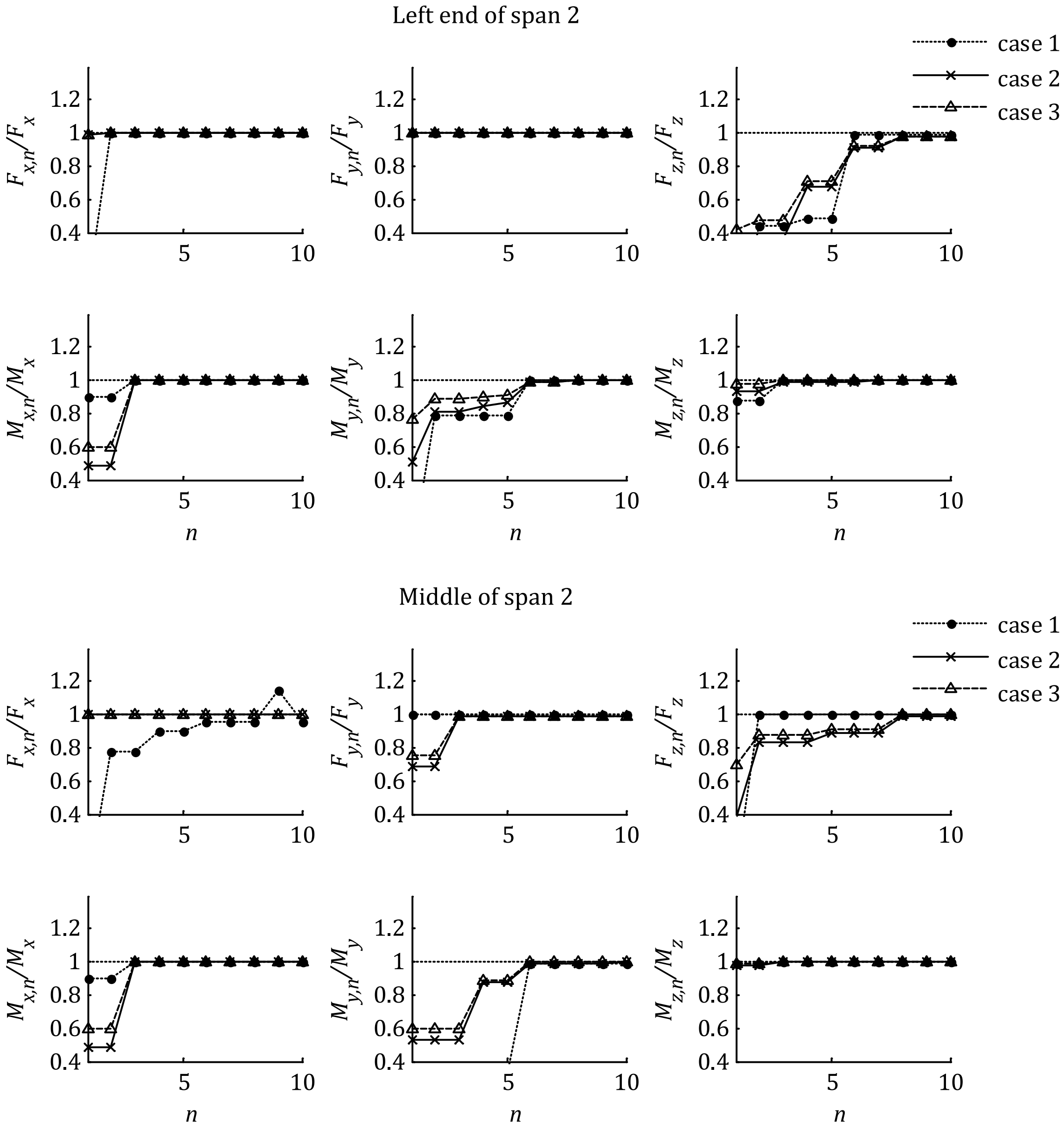

Figure 3.32: Big Rock Wash Bridge: Mean peak responses with *n* modes normalized with 'exact' mean peak responses.

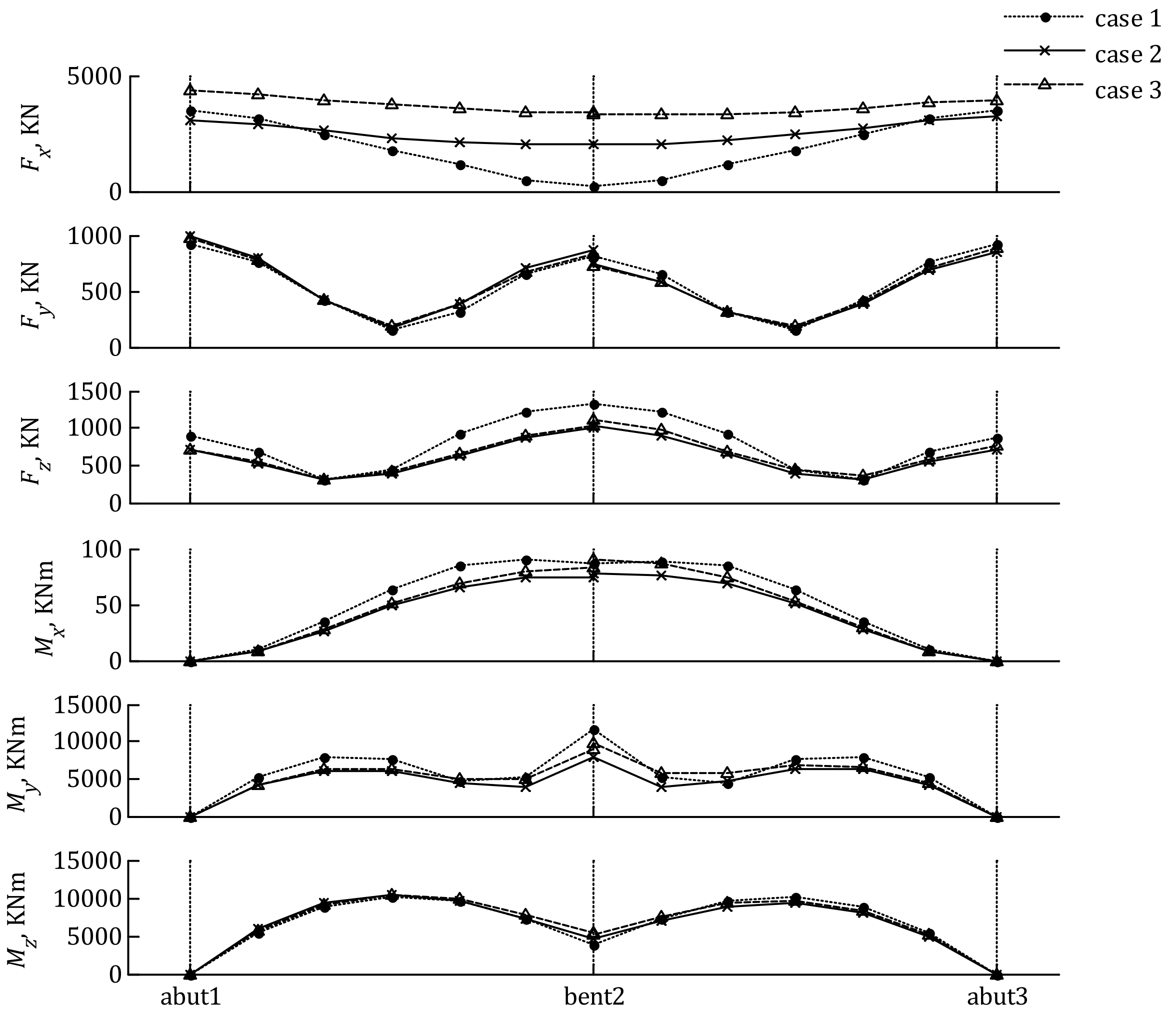

Figure 3.33: South Ingram Slough Bridge: Mean peak responses along the deck.

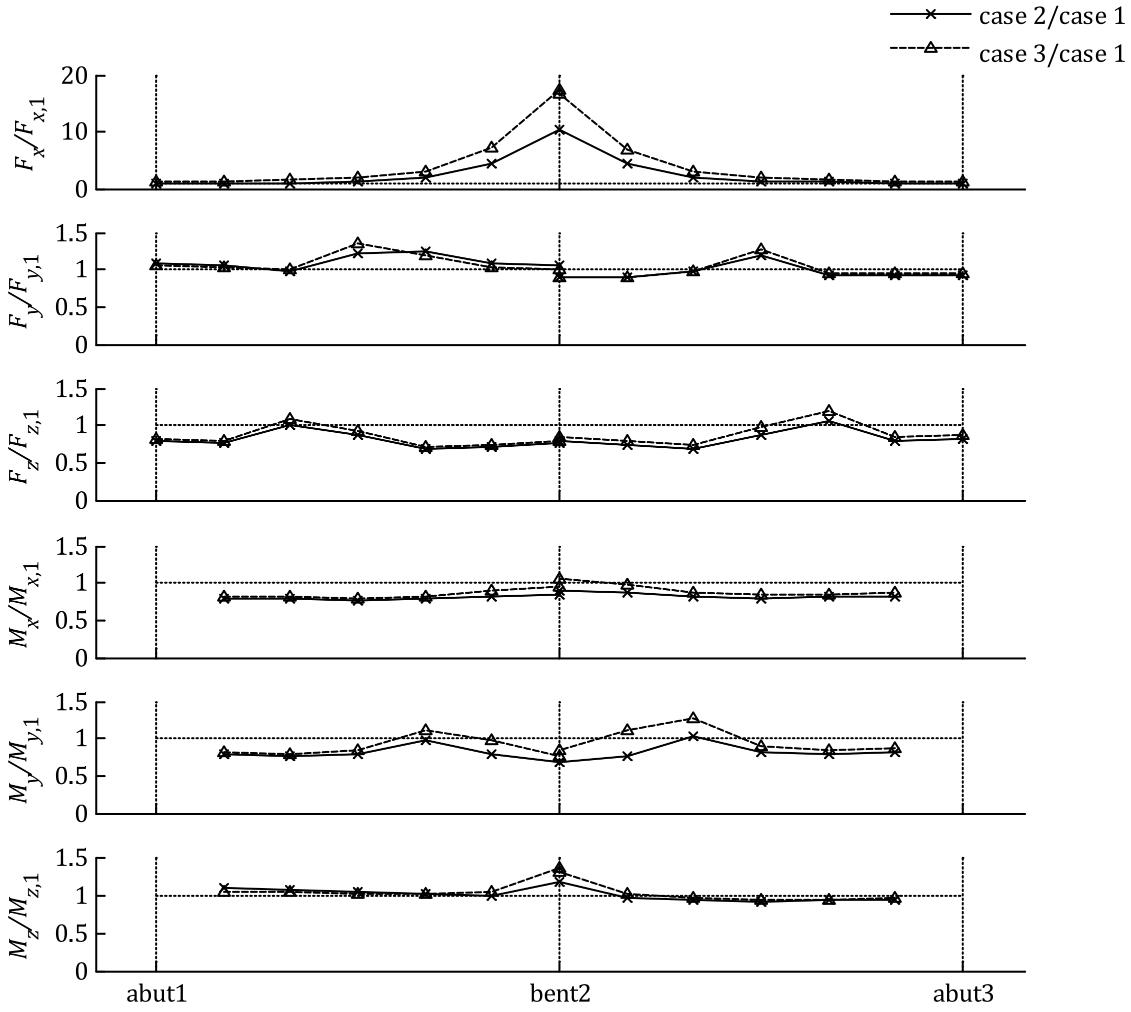

Figure 3.34: South Ingram Slough Bridge: Normalized mean peak responses with respect to the case of uniform excitation.

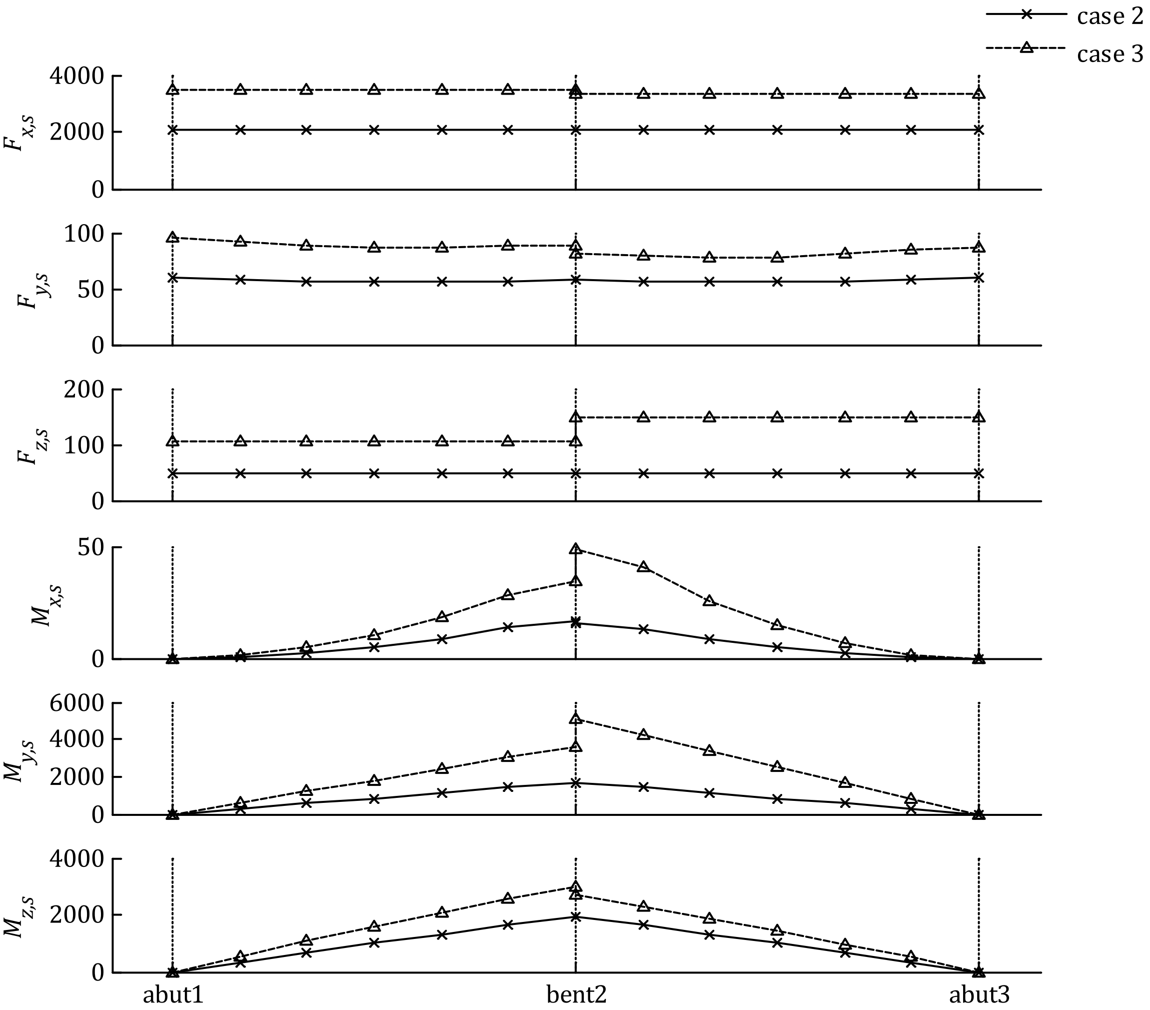

Figure 3.35: South Ingram Slough Bridge: Mean peak pseudo-static responses along the deck.

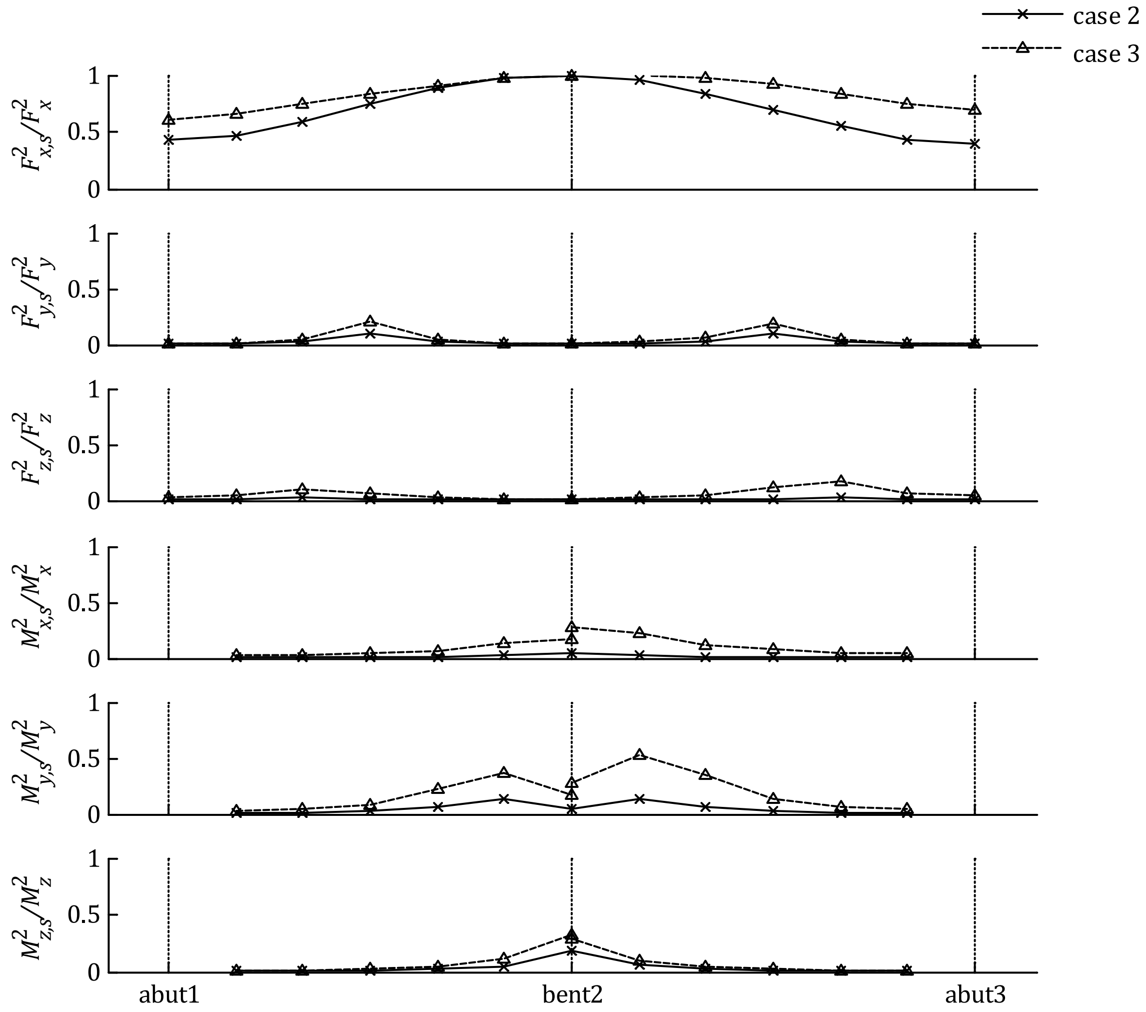

Figure 3.36: South Ingram Slough Bridge: Relative pseudo-static contributions to mean peak responses.

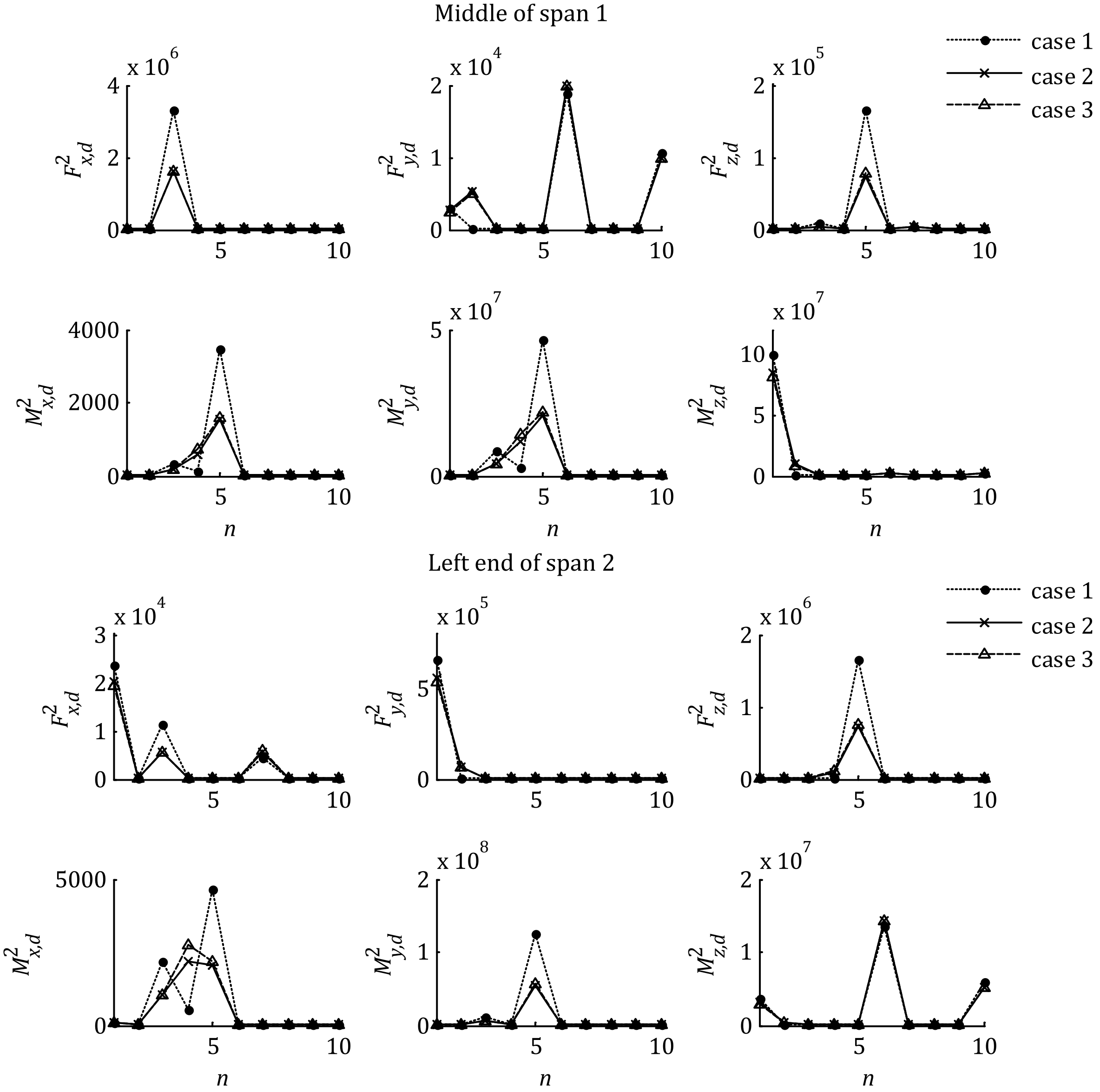

Figure 3.37: South Ingram Slough Bridge: Modal contributions to dynamic component of mean peak responses.

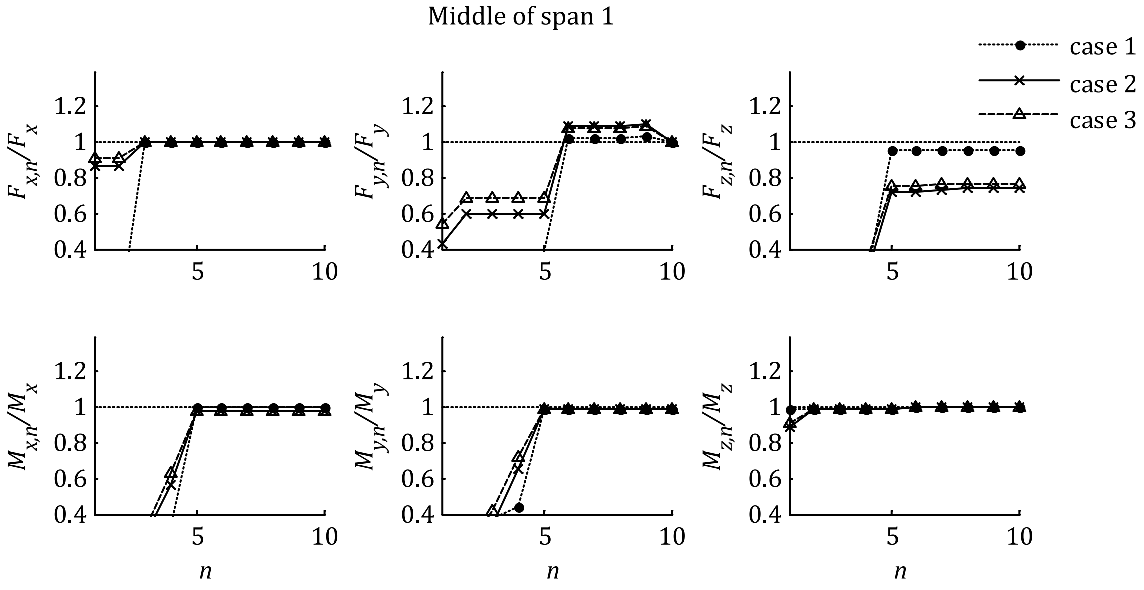
Middle of span 1

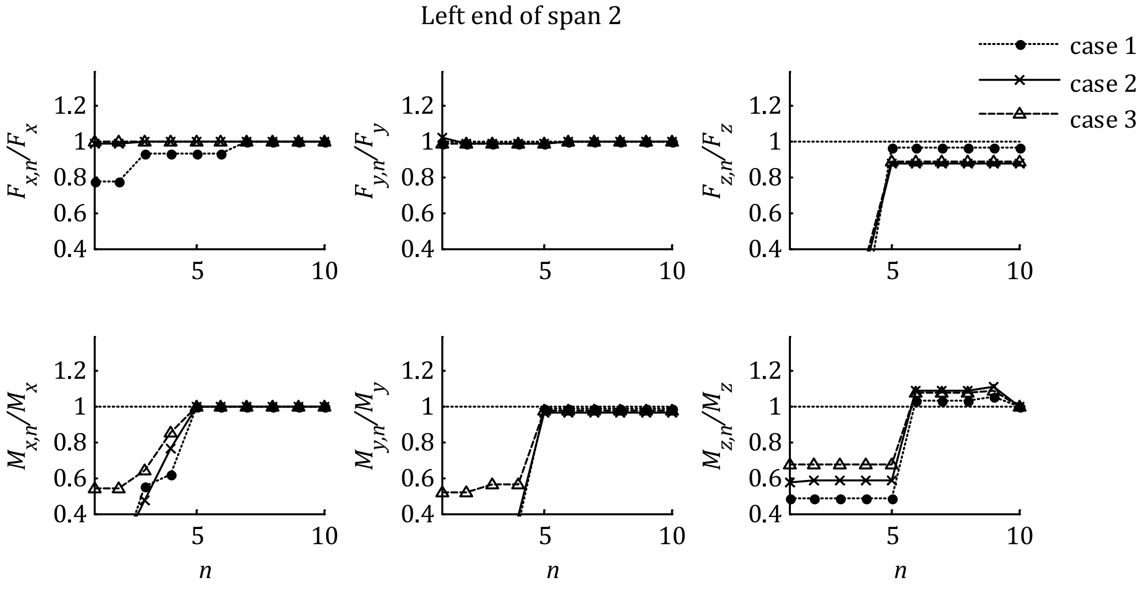
Left end of span 2

Figure 3.38: South Ingram Slough Bridge: Mean peak responses with *n* modes normalized with 'exact' mean peak responses.

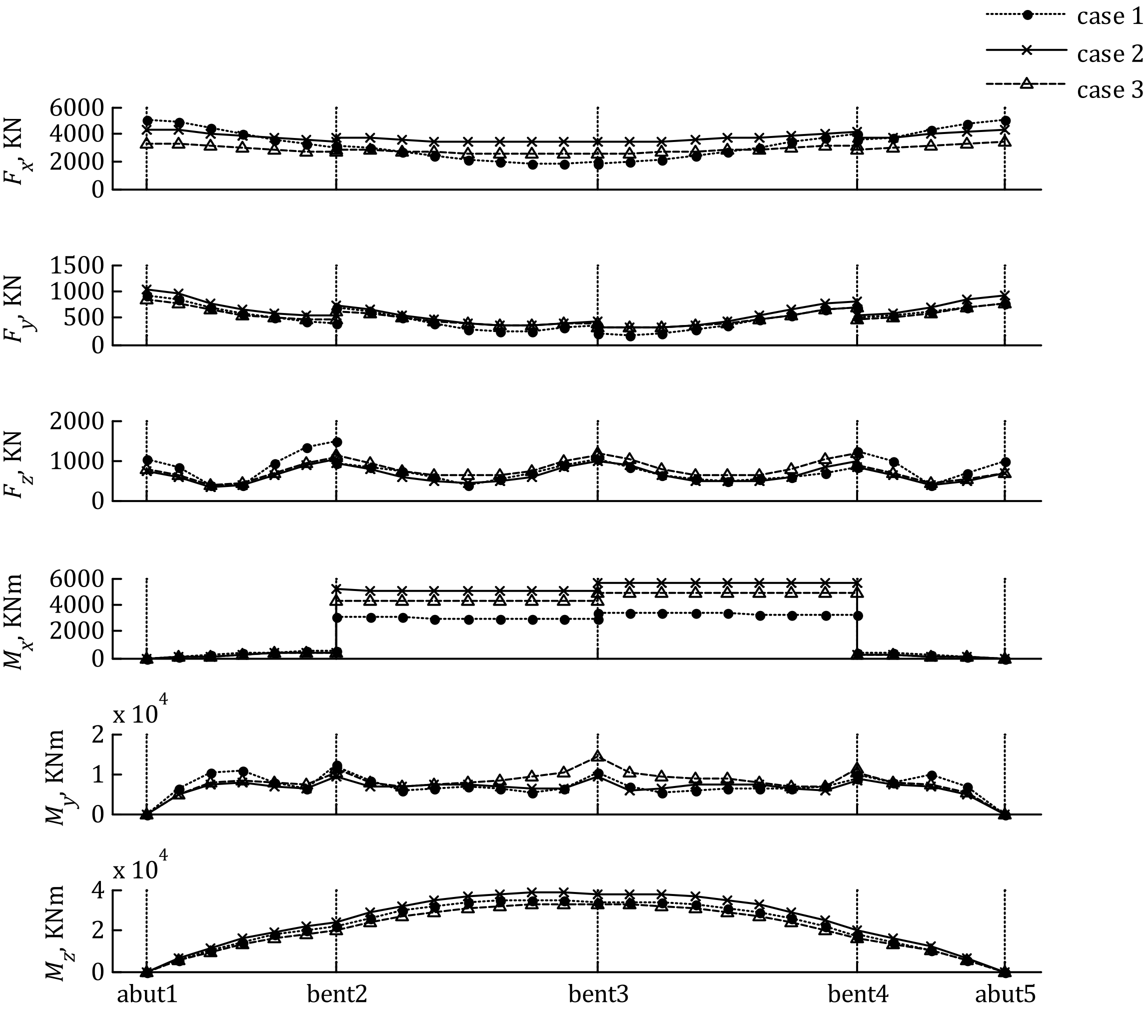

Figure 3.39: Penstock Bridge: Mean peak responses along the deck.

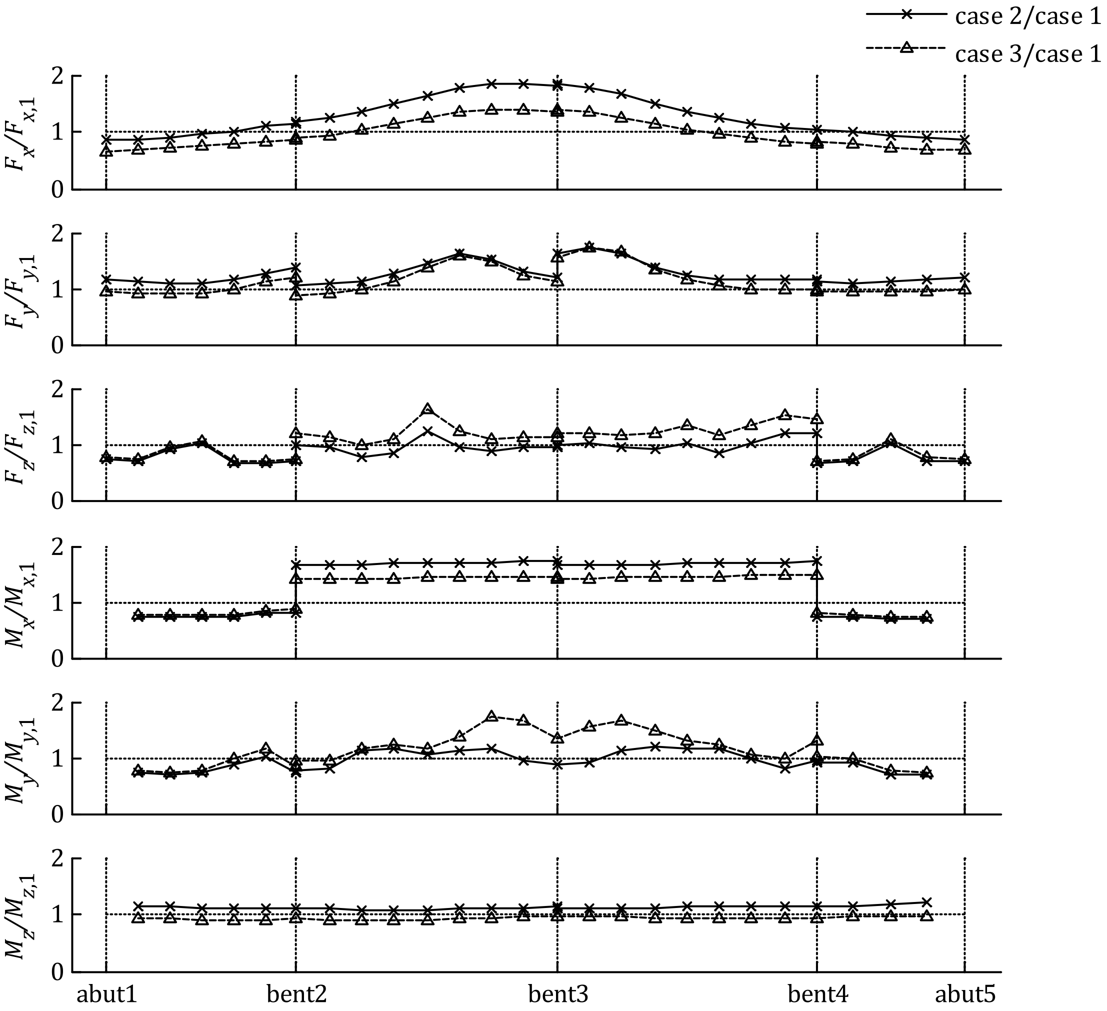

Figure 3.40: Penstock Bridge: Normalized mean peak responses with respect to the case of uniform excitation.

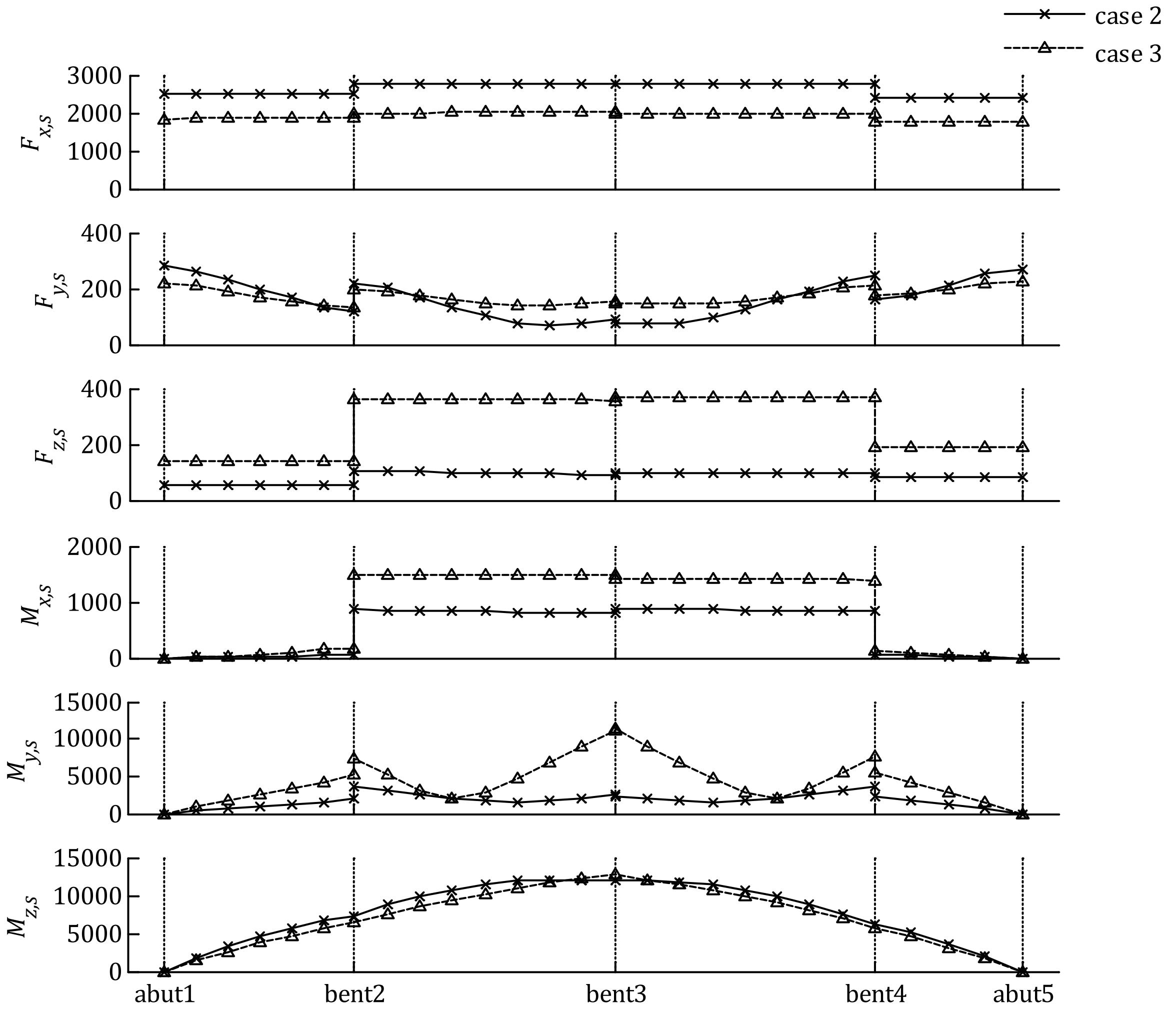

Figure 3.41: Penstock Bridge: Mean peak pseudo-static responses along the deck.

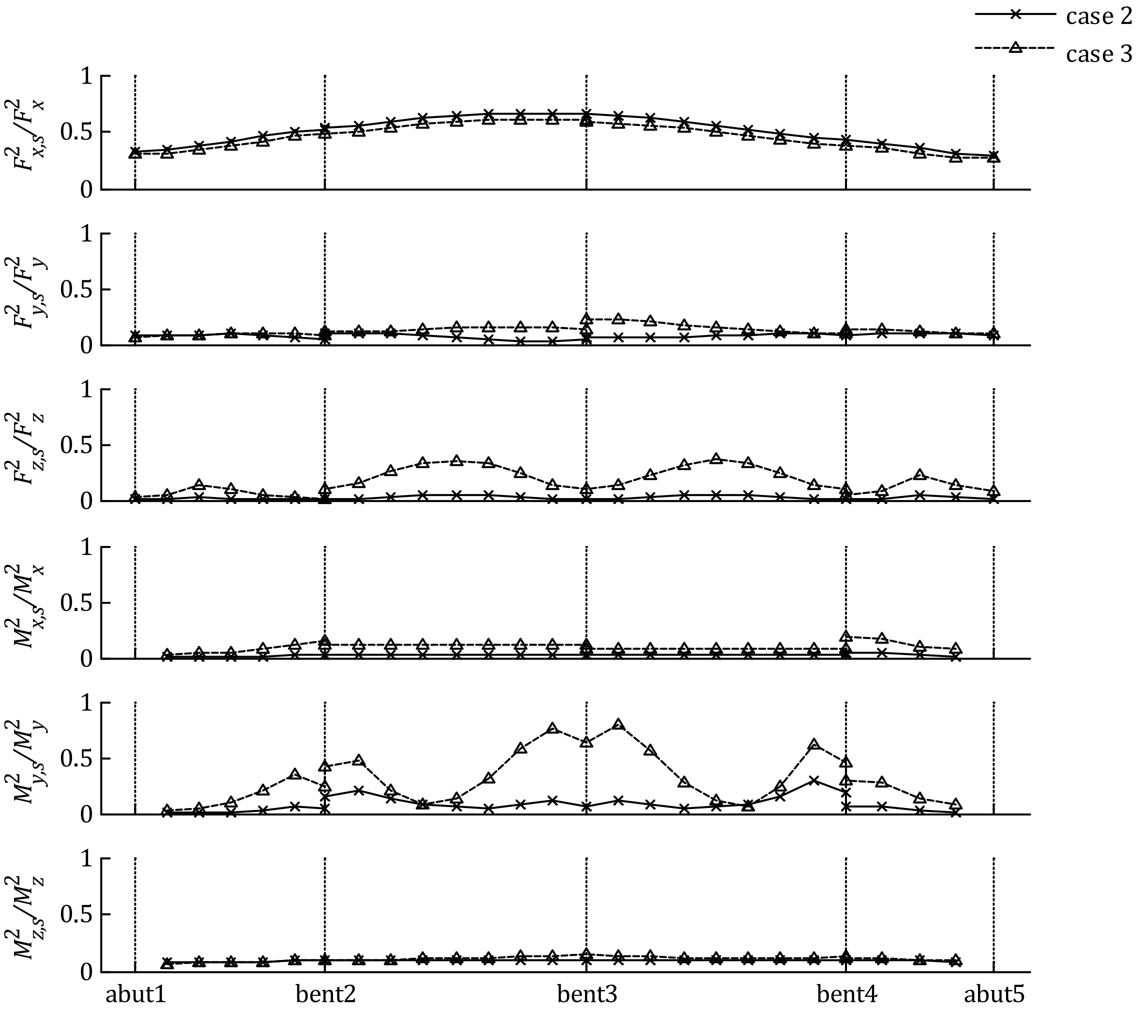

Figure 3.42: Penstock Bridge: Relative pseudo-static contributions to mean peak responses.

Middle of span 2

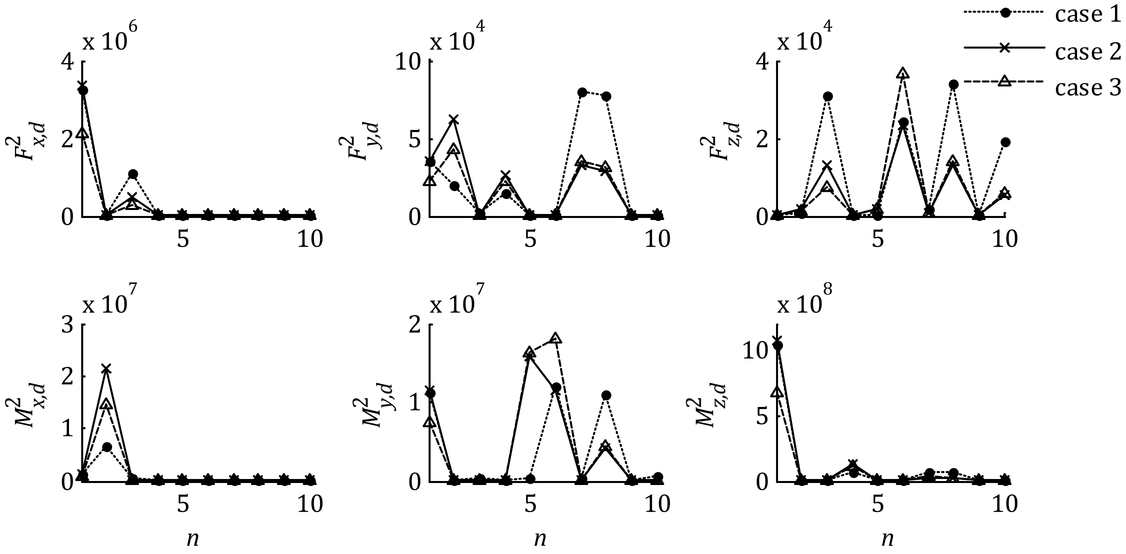

Left end of span 3

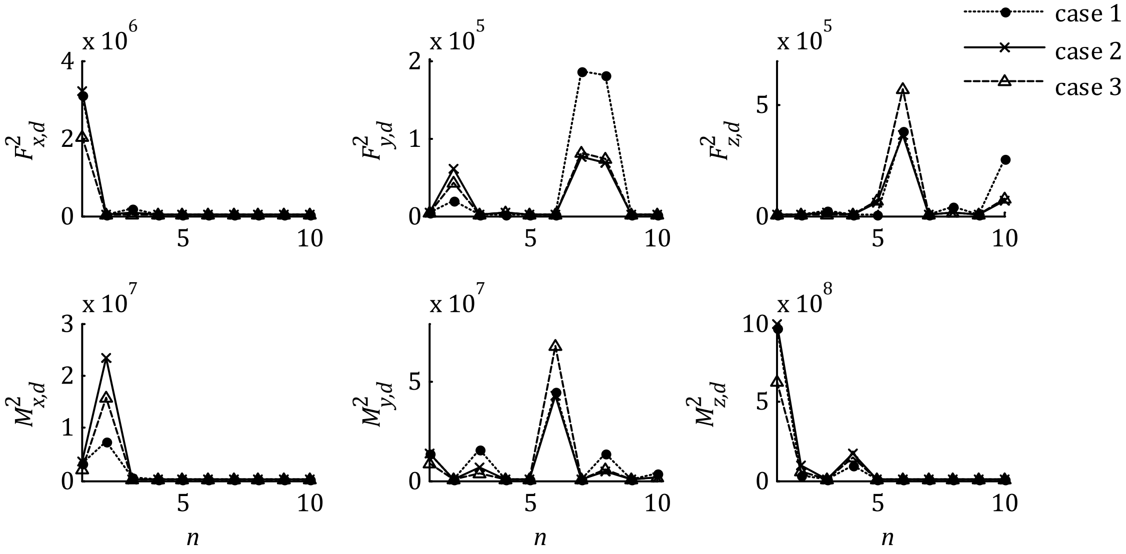

Figure 3.43: Penstock Bridge: Modal contributions to dynamic component of mean peak responses.

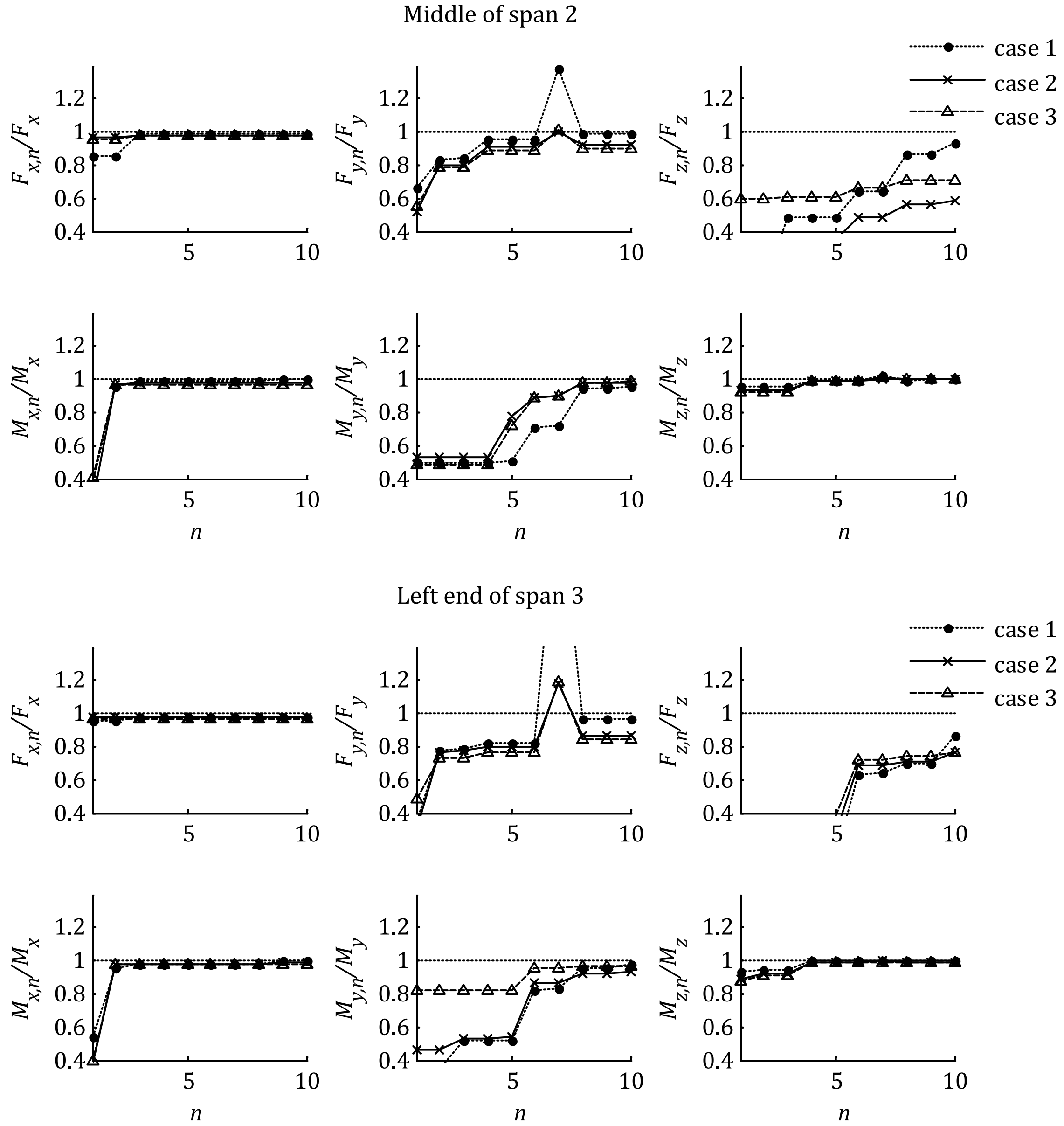

Figure 3.44: Penstock Bridge: Mean peak responses with *n* modes normalized with 'exact' mean peak responses.

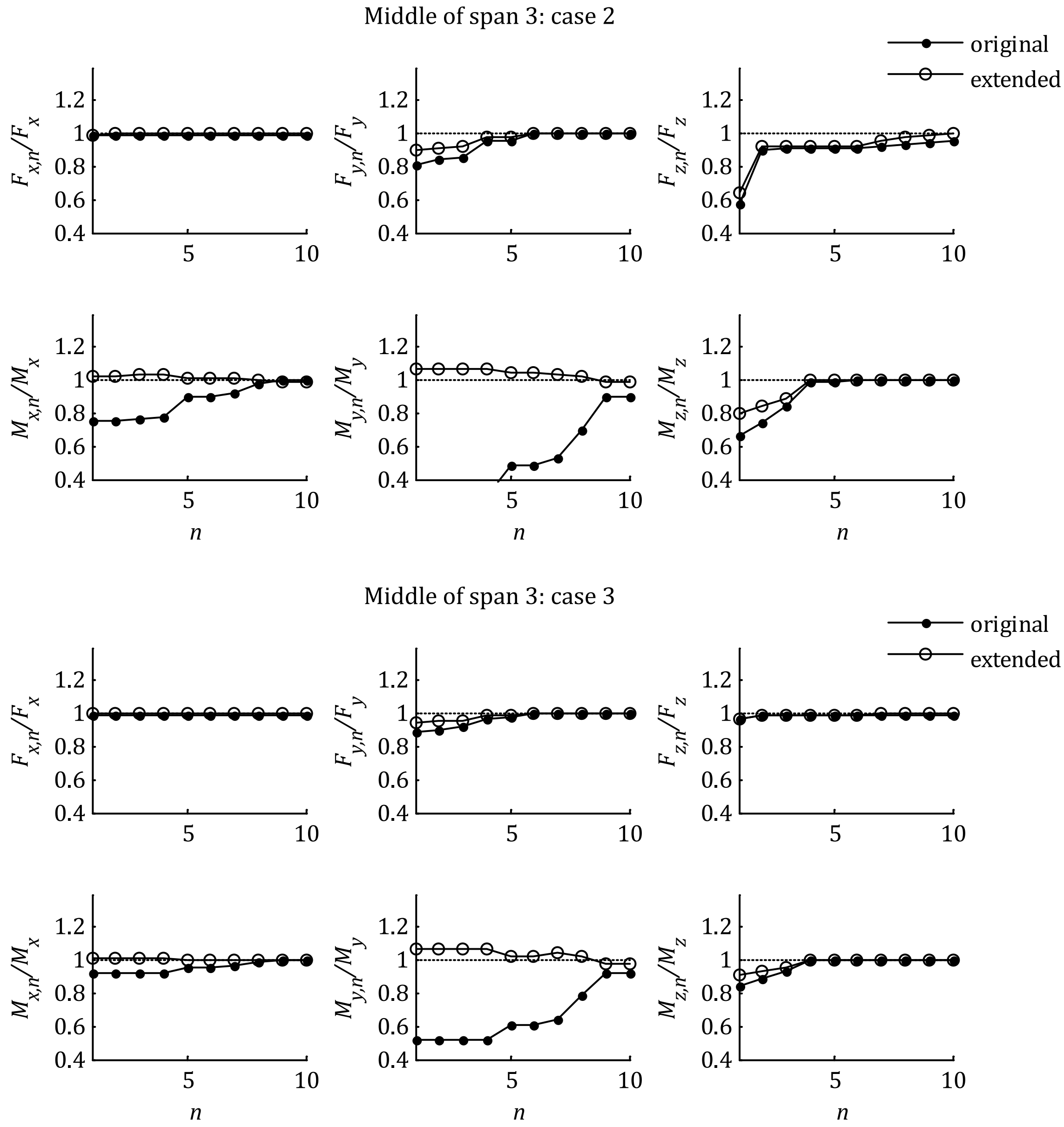

Figure 3.45: Auburn Ravine Bridge: Comparison of original and extended MSRS rules (middle of span 3).

Left end of span 4: case 2

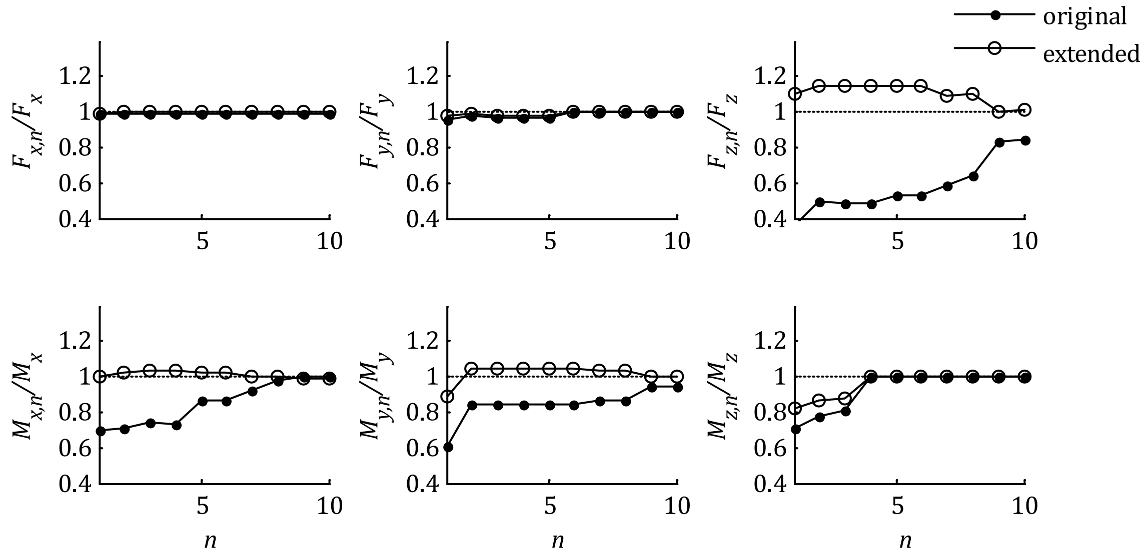

Left end of span 4: case 3

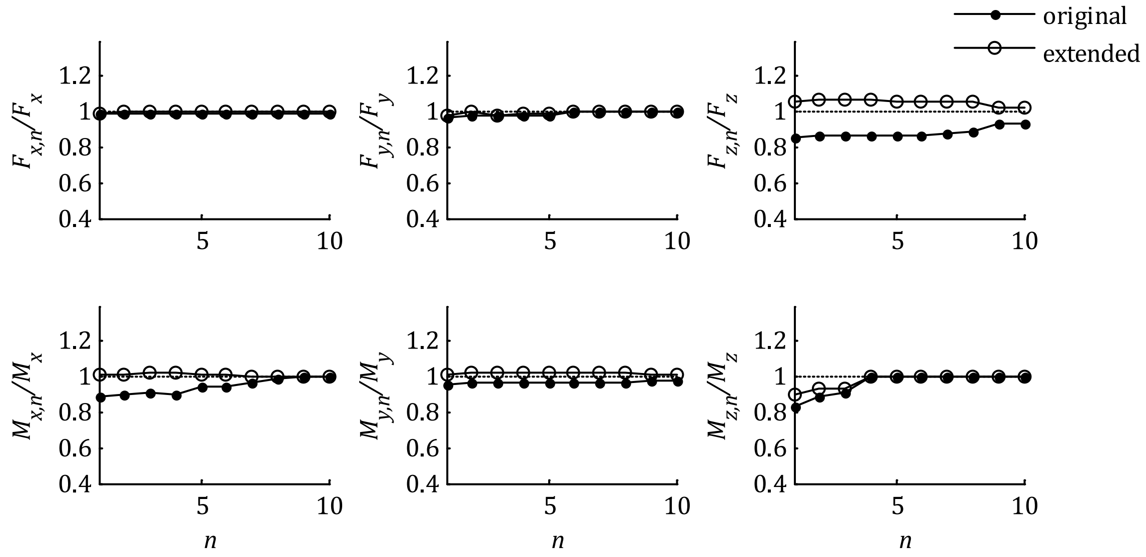

Figure 3.46: Auburn Ravine Bridge: Comparison of original and extended MSRS rules (left end of span 4).

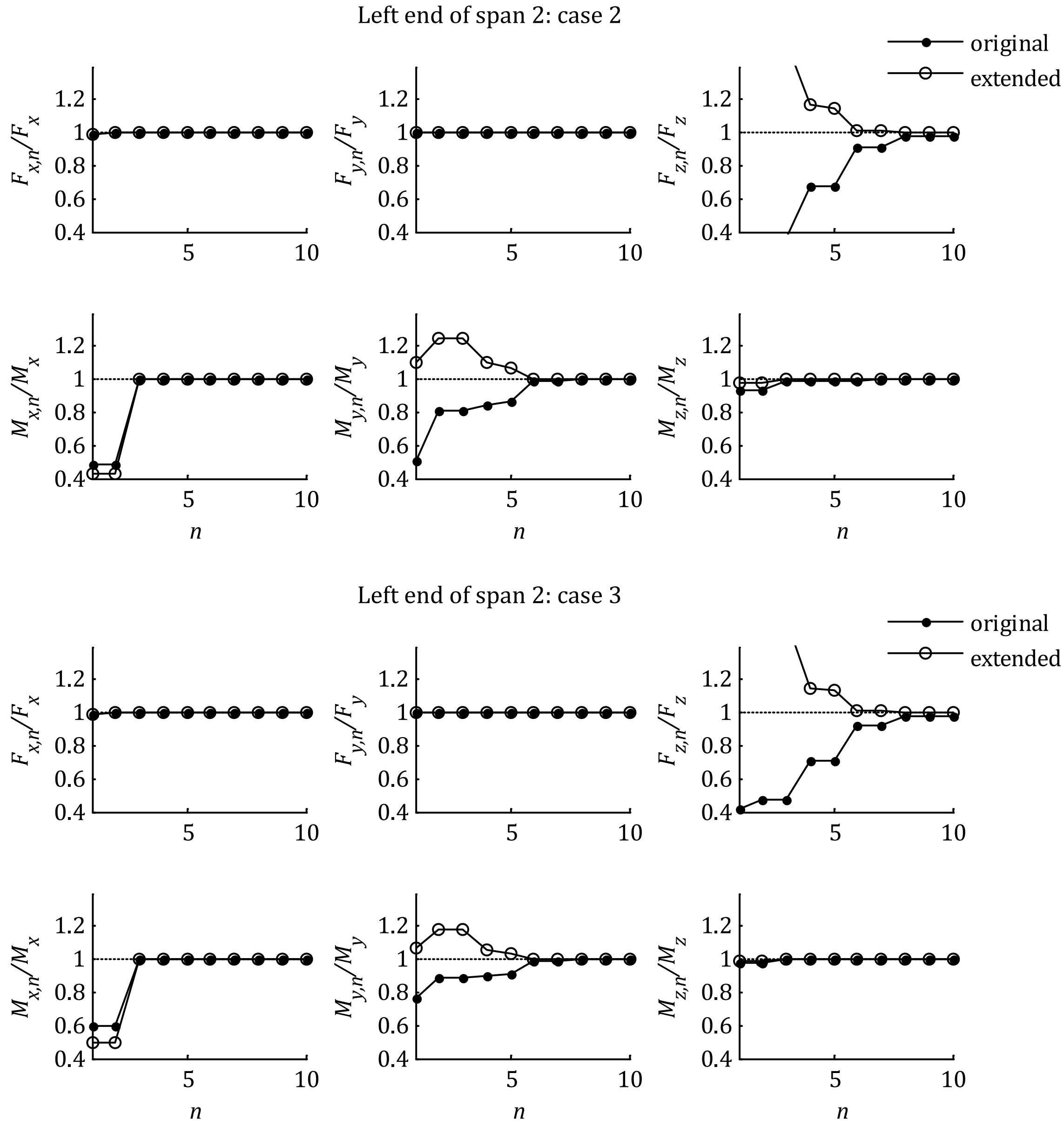

Figure 3.47: Big Rock Wash Bridge: Comparison of original and extended MSRS rules (left end of span 2).

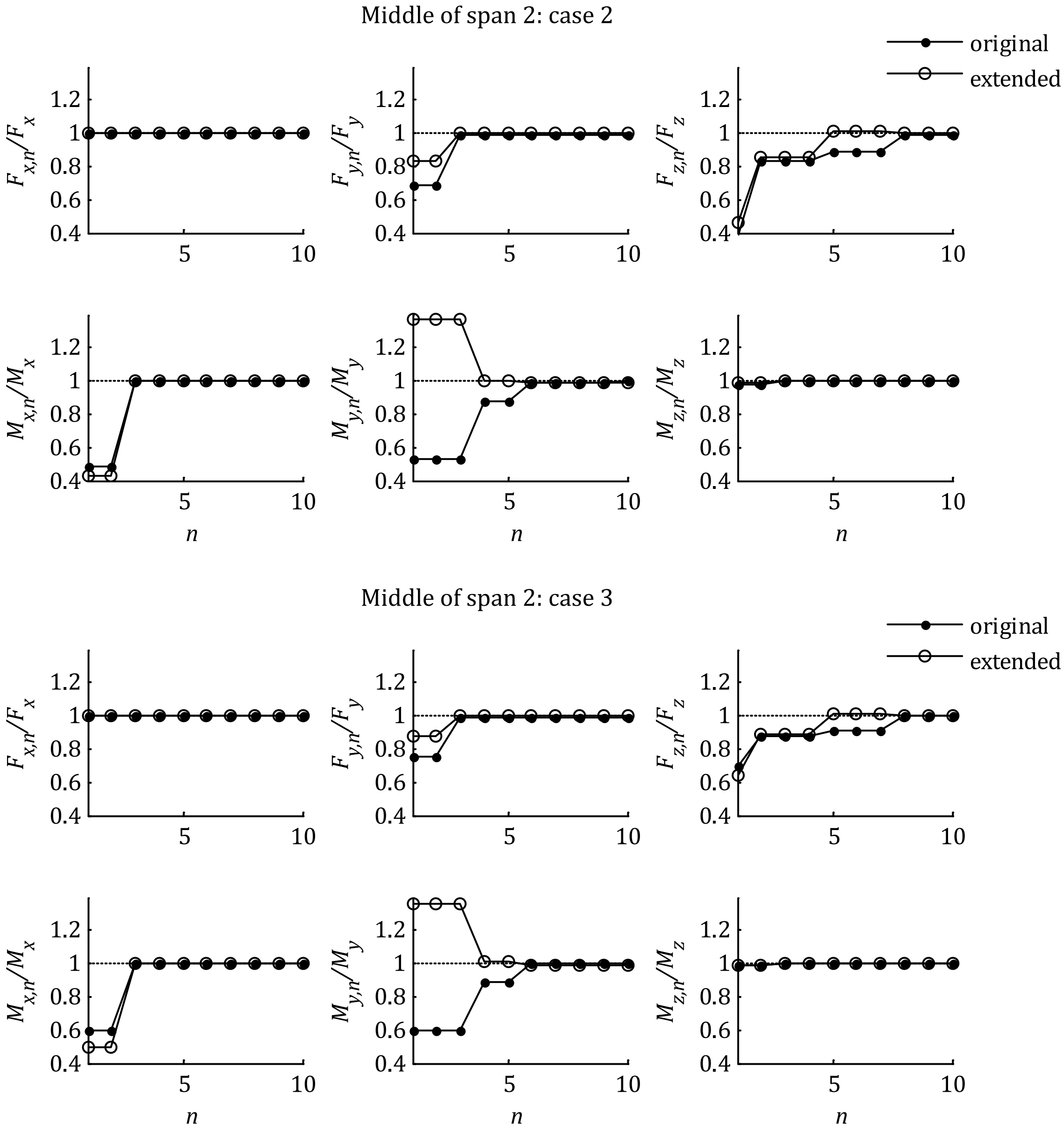

Figure 3.48: Big Rock Wash Bridge: Comparison of original and extended MSRS rules (middle of span 2).

Middle of span 1: case 2

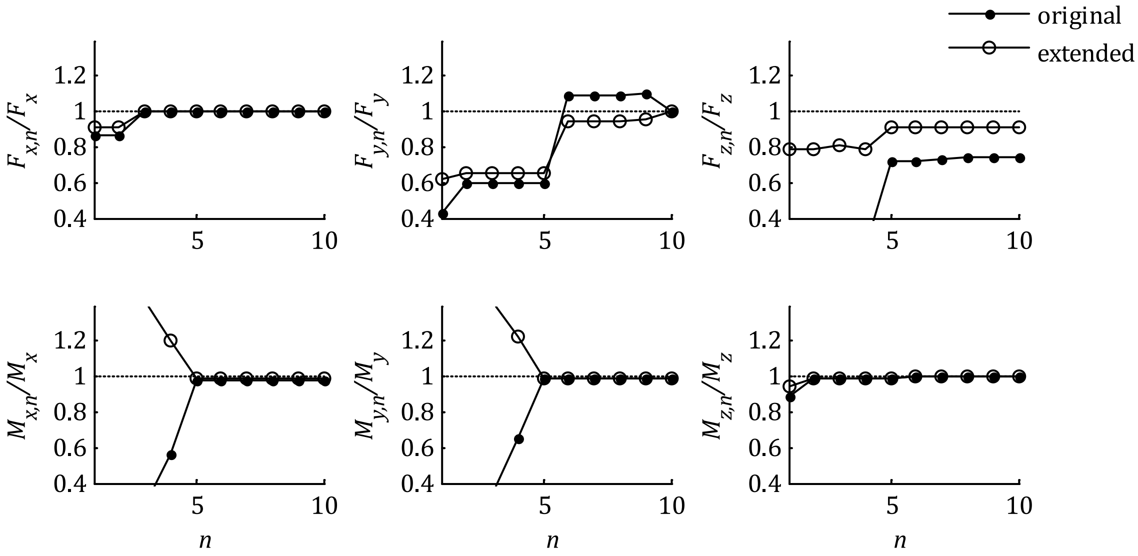

Middle of span 1: case 3

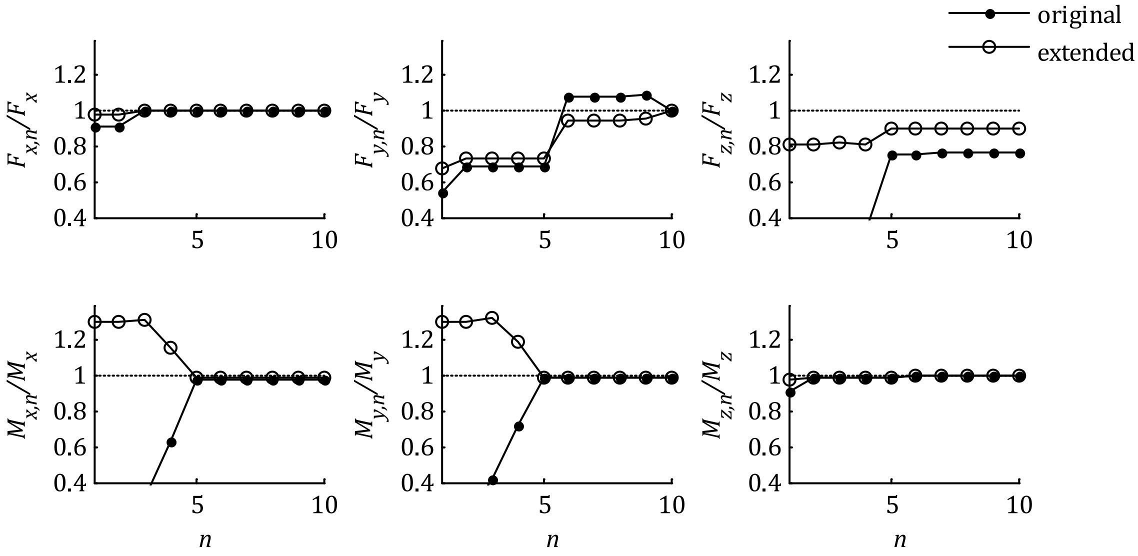

Figure 3.49: South Ingram Slough Bridge: Comparison of original and extended MSRS rules (middle of span 1).

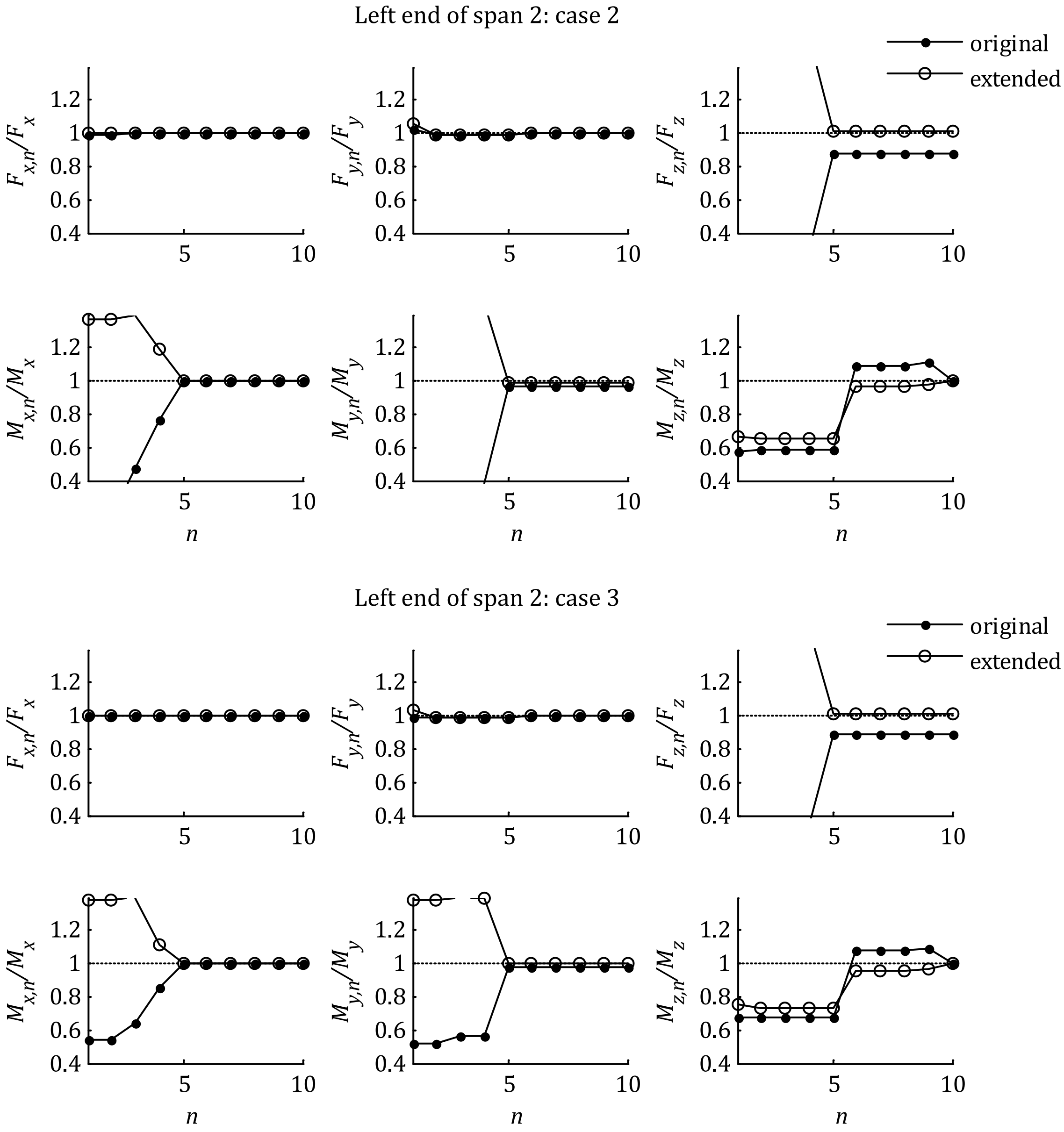

Figure 3.50: South Ingram Slough Bridge: Comparison of original and extended MSRS rules (left end of span 2).

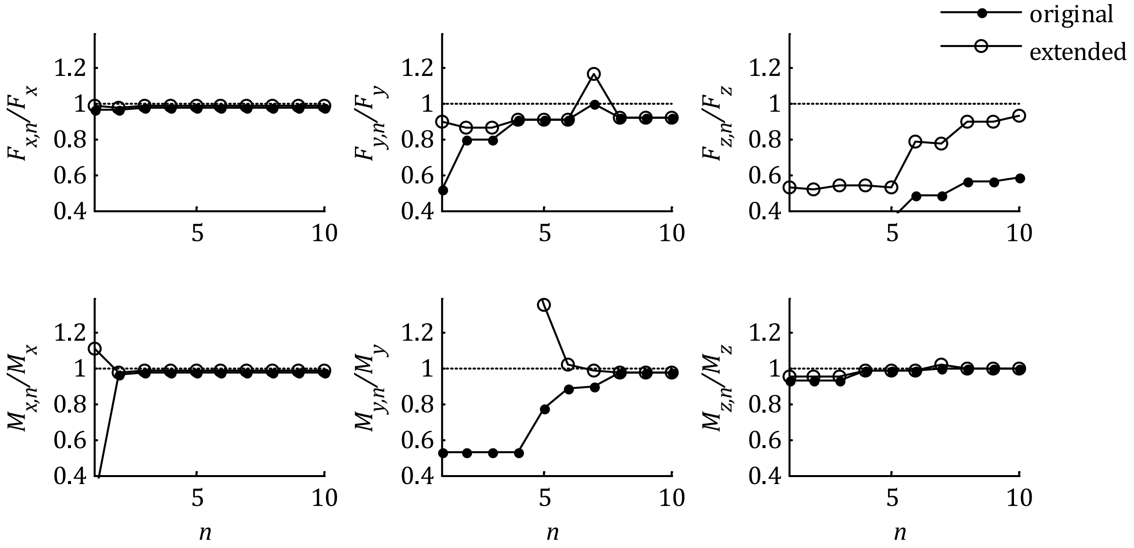
Middle of span 2: case 2

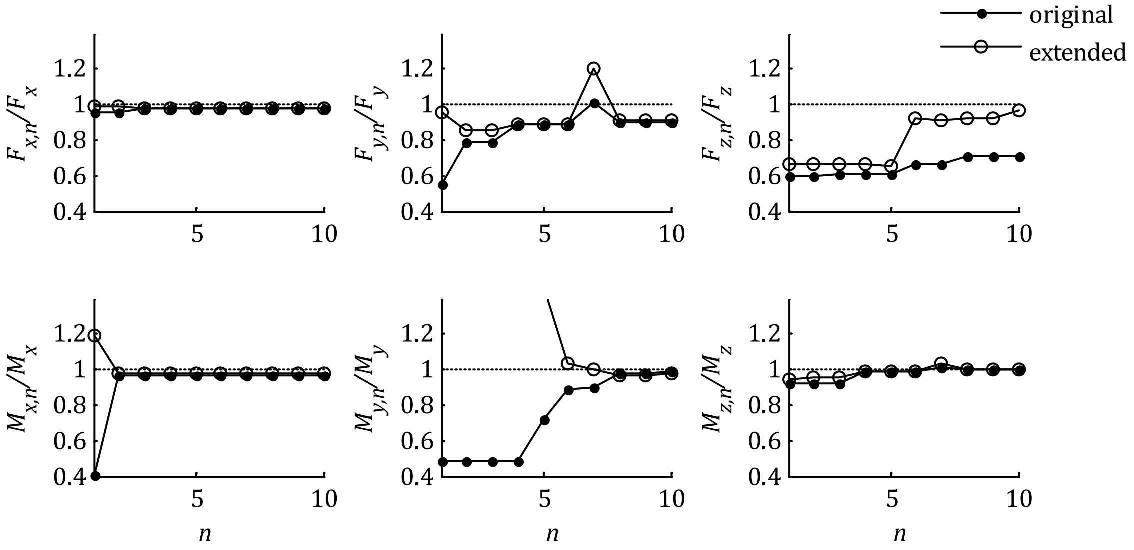
Middle of span 2: case 3

Figure 3.51: Penstock Bridge: Comparison of original and extended MSRS rules (middle of span 2).

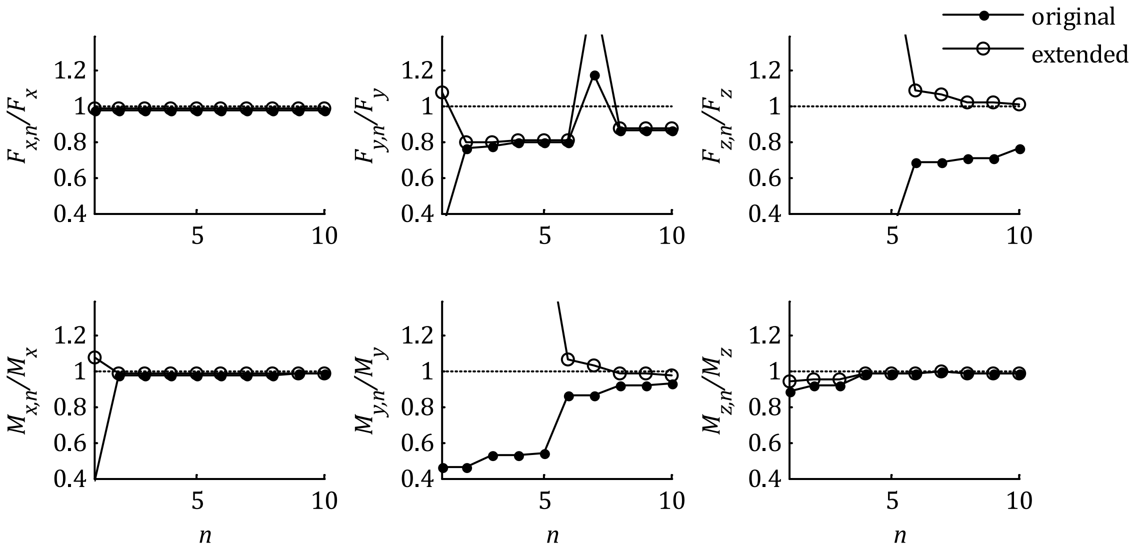
Left end of span 3: case 2

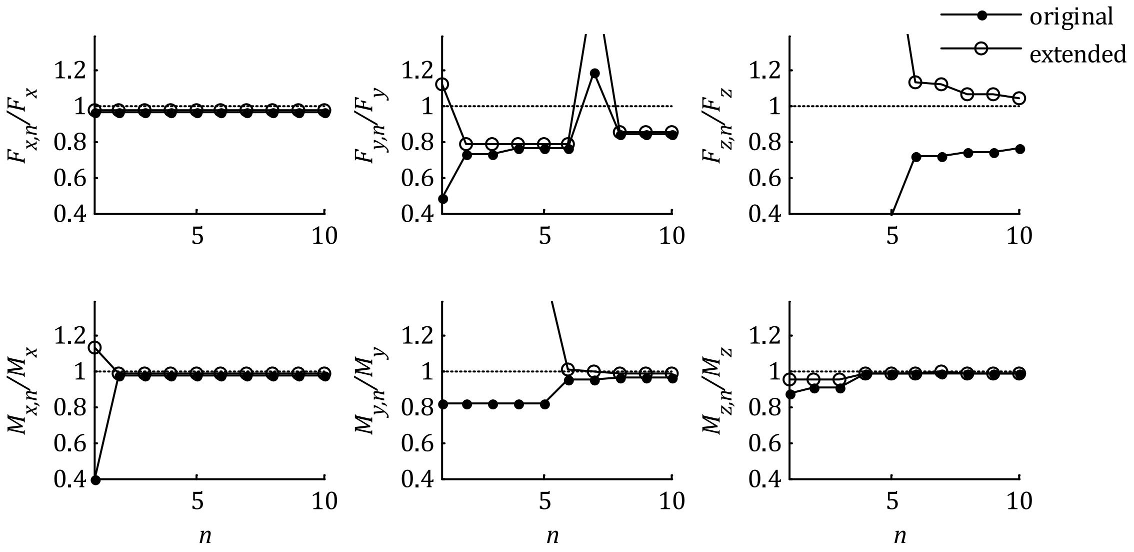
Left end of span 3: case 3

Figure 3.52: Penstock Bridge: Comparison of original and extended MSRS rules (left end of span 3).

Chapter 4 - Simulation of spatially varying ground motions

4.1 INTRODUCTION

In Chapter 3 we investigated the effect of differential support motions on bridge response using the Multiple Support Response Spectrum (MSRS) method. A main disadvantage of the response spectrum method is that it cannot account for non-linear behavior, the evaluation of which is fundamental in performance-based earthquake engineering. One way to account for nonlinear behavior is to conduct response history analysis for specified time histories of ground motions at support points of the structure. Since recordings of closely-spaced earthquake ground motions are rare, non-linear response history analysis of multiply supported structures must rely on generation of synthetic ground motions consistent with a prescribed spatial variability model for the region of interest. Synthetic arrays of ground motions are also needed when performing statistical analysis of structural response by the Monte Carlo simulation approach.

Simulation of spatially varying ground motions is based on the notion of coherency function, which models the ground motion variability in the frequency domain, under the assumption of stationarity. Simulation methods have been developed that use the coherency function in conjunction with theoretical target power spectral density functions. The resulting simulated stationary motions are then modulated in time to provide temporal non-stationarity. However, this approach cannot account for spectral non-stationarity of the ground motion, which can be critical in analysis of hysteretic structures. An alternative approach to simulation of an array of ground motions with specified coherency function is to use probabilistic conditioning with a target recorded or simulated motion at a reference site (Vanmarcke and Fenton, 1991; Kameda and Morikawa, 1992; Liao and Zerva, 2006). Segmenting in the time domain is used to preserve the non-stationary character of the ground motion. However, for an ensemble of arrays of ground motions generated by conditioning on a given accelerogram, the ensemble variance tends to increase with increasing distance from the site of the given motion. This is clearly an undesirable property when performing statistical analysis of bridge response by Monte Carlo simulation. This issue is addressed in the current study by conditioning the simulated array of motions on the Power Spectral Density (PSD) of the segmented target accelerogram rather than its specific realization. Vanmarcke and Fenton (1991) used this approach to simulate accelerograms, but did not examine the physical compliance of the simulated motions, e.g., the requirement that the velocity and displacement time series have zero residuals.

Previous works on conditional simulation of ground motions have been limited to the case of uniform soil conditions. However, variations in local soil profiles can significantly contribute to the spatial variability of ground motions and, therefore, influence the response of multiply supported structures. By incorporating the site effect, the present work provides an important extension of the previously developed methods of conditional simulation.

This chapter begins by revisiting the theory of modeling ground motions using Gaussian processes. Following an overview of the conditional simulation method for stationary processes, the extension of the method to account for non-stationarity and varying soil conditions is described. In an example application, we simulate support motions for an existing bridge in California for both cases of uniform and variable soil conditions. The application presents support motions generated by conditioning on a given segmented PSD and support motions generated by conditioning on a given record. The selection of various parameters involved in the simulation methods and their effect on the characteristics of the generated motions are discussed. To assess these methods, we compare statistical properties of the simulated motions from a sample of realizations with the corresponding target properties, as defined by theoretical models. The response spectra of the simulated motions are also examined, since they are quantities of particular interest in engineering practice.

4.2 DISCRETE REPRESENTATION OF AN ARRAY OF STATIONARY GAUSSIAN PROCESSES

Consider an array of zero-mean, jointly stationary Gaussian acceleration processes at n sites on the ground defined by auto-PSDs $G_{kk}(\omega)$, $k = 1,2,\dots,n$, and cross-PSDs $G_{kl}(\omega)$, $k,l = 1,2,\dots,n$, $k \neq l$. For each process, let N be the number of discrete observations sampled at equal time intervals Δt. We denote the corresponding time instants $t_i = i\Delta t$,

$i = 0, \dots, N-1$. To simplify the algebra, hereafter, we consider the case where N is even, but the analysis can be easily extended to the case when N is odd (see, e.g., Anderson, 1971). It is well known that such an array of processes can be represented in terms of the finite Fourier series (see, e.g., Chatfield, 2004)

$$a_k(t_i) = A_{0k} + \sum_{p=1}^{N/2-1} \left[A_{pk}\cos(\omega_p t_i) + B_{pk}\sin(\omega_p t_i)\right] + (-1)^i A_{(N/2)k} \tag{4.1}$$

in which $\omega_p = \frac{2\pi p}{N\Delta t}$ and $\{A_{pk}, B_{pk}\}$ are the Fourier coefficients. We note that the above representation uses N parameters to describe N observations and, thus, can be made to exactly fit the given realizations.

The Fourier coefficients, $\{A_{pk}, B_{pk}\}$, are zero-mean, jointly Gaussian random variables that are uncorrelated for different frequencies, i.e. $\mathrm{E}[A_{pk}A_{qk}] = \mathrm{E}[B_{pk}B_{qk}] = \mathrm{E}[A_{pk}B_{qk}] = 0$ for $p \neq q$. At frequency ω_p, the following relations hold:

$$\begin{gathered}\mathrm{E}[A_{pk}\,A_{pl}] = \mathrm{E}[B_{pk}\,B_{pl}] = \begin{cases} G_{kk}(\omega_p)\,\Delta\omega, & \text{if } k = l \\ \mathrm{Re}[G_{kl}(\omega_p)\,]\,\Delta\omega, & \text{if } k \neq l \end{cases} \\ \mathrm{E}[A_{pk}\,B_{pl}] = -\mathrm{E}[B_{pk}\,A_{pl}] = \begin{cases} 0, & \text{if } k = l \\ \mathrm{Im}[G_{kl}(\omega_p)\,]\,\Delta\omega, & \text{if } k \neq l \end{cases}\end{gathered} \tag{4.2}$$

in which $\Delta\omega = 2\pi/N\Delta t$. Thus, given the auto- and cross-PSDs, the variance/covariances of all Fourier coefficients can be determined.

The cross-PSD between the acceleration processes at sites k and l is related to the corresponding auto-PSDs through the relation

$$G_{kl}(\omega) = \gamma_{kl}(\omega)[G_{kk}G_{ll}(\omega)]^{1/2} \tag{4.3}$$

in which $\gamma_{kl}(\omega)$ is the coherency function, which is described in Section 2.2.3 of Chapter 2.

4.3 ESTIMATION OF STATISTICAL PROPERTIES OF GIVEN REALIZATIONS

Let $a_k(t_i)$, $i = 1, \dots, N$, represent a realization of the ground acceleration process at location k. Using orthogonality properties of the trigonometric terms, the Fourier coefficients in Eqn. (4.1) are evaluated as (Chatfield, 2004)

$$A_{pk} = \tfrac{2}{N}\textstyle\sum_{i=1}^{N} a_k(t_i)\cos(\omega_p t_i), \quad p = 1, \dots, N/2-1 \tag{4.4}$$

$$A_{0k} = \sum_{i=1}^{N} a_k(t_i)/N$$

$$A_{(N/2)k} = \sum_{i=1}^{N} (-1)^i a_k(t_i)/N$$

$$B_{pk} = \frac{2}{N} \sum_{i=1}^{N} a_k(t_i) \sin(\omega_p t_i), \quad p = 1, \dots, N/2 - 1$$

An estimator of the auto-PSD of the acceleration process at this location is the periodogram, given by the expression (Chatfield, 2004)

$$I_{kk}(\omega_p) = \frac{N\Delta t}{4\pi} \left(A_{pk}^2 + B_{pk}^2\right) = \frac{\Delta t}{\pi N} \left| \sum_{i=1}^{N} a_k(t_i) \exp(\mathrm{i}\omega_p t_i) \right|^2 \tag{4.5}$$

In order to obtain a consistent estimator, $I_{kk}(\omega_p)$ may be smoothed along the frequency axis with one of the various techniques available in the literature (see, e.g., Chatfield, 2004). The smoothed values at the ends are obtained by treating the periodogram as symmetric about $\omega_0 = 0$ and $\omega_{N/2} = \pi/\Delta t$.

For a given pair of realizations, $a_k(t_i)$ and $a_l(t_i)$, a consistent estimator of the cross-PSD of the corresponding processes is the smoothed cross-periodogram, $I_{kl}(\omega_p)$. The real and imaginary parts of the cross-periodogram are determined through the relations (Chatfield, 2004)

$$\begin{aligned} \mathrm{Re}\left[I_{kl}(\omega_p)\right] &= \frac{N\Delta t}{4\pi} \left(A_{pk}A_{pl} + B_{pk}B_{pl}\right) \\ \mathrm{Im}\left[I_{kl}(\omega_p)\right] &= \frac{N\Delta t}{4\pi} \left(A_{pk}B_{pl} - A_{pl}B_{pk}\right) \end{aligned} \tag{4.6}$$

In order to obtain the smoothed values at the ends, the real and imaginary parts are treated as being symmetric and anti-symmetric, respectively, about $\omega_0 = 0$ and $\omega_{N/2} = \pi/\Delta t$.

4.4 SIMULATION OF ARRAY OF STATIONARY GROUND MOTIONS WITH VARYING SITE EFFECTS

Earthquake ground motions in general have non-stationary characteristics in both time and frequency domains. However, most ground motions can be approximated with temporal segments that are nearly stationary. (An exception is the case of near-fault ground motions that contain directivity pulses. In this chapter we specifically exclude consideration of such ground motions. A separate study addresses near-fault ground motions with directivity pulse.) For this reason, the case of stationary processes is studied first.

Since ground motions result from the super-positioning of waves randomly arriving at a site from intermittent ruptures at the earthquake source, on the basis of the Central Limit Theorem, it is reasonable to assume that the ground motion process is Gaussian. This assumption may not be valid at a soft soil site under intense motion, where the soil behavior is non-linear. For this reason, we limit our study to sites with moderate to stiff soils, where the Gaussian assumption remains approximately valid. For soft sites, ground motions may be generated by first simulating Gaussian motions at the bedrock level and then propagating them to the surface by non-linear time-history analysis.

Next, we present two methods for generating realizations of an array of stationary Gaussian ground acceleration processes. These methods were named by Vanmarcke and Fenton (1991) as "unconditioned simulation" and "conditioned simulation" methods. In the unconditioned simulation method, the array of motions is consistent with the PSD of a random realization of the process at a given site. In the conditioned simulation method, the array of motions is conditioned on an observed accelerogram at a given site. The unconditioned simulation method has the advantage that the variability observed in an ensemble of realizations of the array is uniform over the array, whereas in the conditioned simulation method the variability increases with distance from the site of the observed motion. Uniform variability in the array of ground motions is essential when the synthetic motions are used for statistical analysis of the response of a multiply supported structure.

4.4.1 Unconditioned simulation

In this section, we consider the problem of simulating arrays of zero-mean stationary Gaussian acceleration processes at locations with known site conditions and for a specified spatial variability model, when a random realization of the array at one site is given. The site conditions are described through the FRFs of the corresponding soil-columns (see Section 2.2.4) and the ground motion spatial variability is described through a coherency function. The problem involves simulation of Fourier coefficients at separate frequencies and locations. At each location, the simulated Fourier coefficients are substituted in Eqn. (4.1) to obtain the corresponding realization of the acceleration time-history. The sets of Fourier coefficients at each frequency are obtained by sampling from a joint Gaussian distribution, which is fully defined in terms of the auto-PSD of the given realization, the site FRFs and the coherency function.

To elaborate, let us consider simulating zero-mean acceleration processes at locations $k = 1, \dots, n$ with specified site FRFs, $h_k(\omega)$, and consistent with a coherency function and a given realization at a site sampled at N points. Let $\mathbf{X}_p = [A_{p1} \quad B_{p1} \quad \dots \quad A_{pn} \quad B_{pn}]$ denote the set of Fourier coefficients at frequency ω_p for the n sites and let $\mathbf{\Sigma}_{pp}$ denote the

$2n \times 2n$ covariance matrix of these coefficients. We note that the covariance matrix fully defines the joint distribution of the zero-mean Gaussian vector $\mathbf{X}_p$. The elements $\Sigma_{pp,ij}$ of this matrix are determined using Eqns. (4.2). The latter equations involve the auto-PSDs $G_{kk}(\omega_p), k = 1, \ldots, n$, and the cross-PSDs, $G_{kl}(\omega_p), k, l = 1, \ldots, n, k \neq l$. To determine the auto-PSDs, first, we estimate the auto-PSD of the given realization through the (optionally smoothed) periodogram given in Eqn. (4.5). Employing the expression for the PSD of the surface ground motion described in Eqn. (2.24) (in Section 2.2.4), and assuming that the bedrock motion has the same spectral density at all sites, the auto-PSDs at two separate locations k and l are related through

$$G_{ll}(\omega) = G_{kk}(\omega) \frac{|h_l(\omega)|^2}{|h_k(\omega)|^2} \tag{4.7}$$

Using the above equation, the full set of auto-PSDs is determined in terms of the estimated auto-PSD of the given realization and the site FRFs. Eqn. (4.3) is then used to determine the full set of cross-PSDs in terms of the auto-PSDs and the coherency function. Once the covariance matrix is determined, sample vectors from the $2n$-dimensional zero-mean joint Gaussian distribution are obtained as $\mathbf{x}_p = \mathbf{L}_p^{\mathrm{T}} \mathbf{z}_p$, where $\mathbf{L}_p$ is an upper triangular matrix such that $\mathbf{L}_p^{\mathrm{T}} \mathbf{L}_p = \mathbf{\Sigma}_{pp}$ and $\mathbf{z}_p$ is a vector of $2n$ uncorrelated standard normal variables. We note that a computationally efficient and stable method to obtain $\mathbf{L}_p$ is to write it as $\mathbf{L}_p = \mathbf{D}_p \mathbf{R}_p$, where $\mathbf{D}_p$ is the diagonal matrix of standard deviations and $\mathbf{R}_p$ is the Cholesky decomposition of the correlation matrix. After sampling at all frequencies $\omega_p = \frac{2\pi p}{N\Delta t}$, $p = 0, 1, \ldots, N/2$, Eqn. (4.1) is used to obtain the acceleration time-histories at the n sites. We note that at $\omega_p = 0$ the ground motions are fully coherent and the Fourier coefficients have the same values at all locations. Thus, at $\omega_p = 0$, we only need to sample from a 1-dimensional zero-mean Gaussian distribution with variance $G_{kk}(0)\Delta\omega$. According to Eqns. (4.4) and (4.5) the periodogram has zero value at $\omega_p = 0$, but the auto-PSD estimate at zero frequency may have a small non-zero value due to smoothing.

The implemented algorithm used for unconditioned simulation is summarized as follows:

Algorithm 1: Unconditioned simulation of an array of stationary spatially varying ground accelerations

1. Estimate the auto-PSD of the given realization in terms of the periodogram in Eqn. (4.5). Smoothing of the periodogram is optional.
2. Use Eqn. (4.7) to evaluate the auto-PSDs at all sites in terms of the respective soil column FRFs.
3. Use Eqn. (4.3) to evaluate cross-PSDs for all pairs of sites in terms of the auto-PSDs and the coherency function.
4. Repeat the following steps for each frequency $\omega_p = \frac{2\pi p}{N\Delta t}, p = 1, \ldots, N/2$:
    a. Evaluate the elements of the covariance matrix $\mathbf{\Sigma}_{pp}$, using Eqns (4.2) and the estimated auto- and cross-PSDs.

b. Simulate the $2n$-dimensional vector of Fourier coefficients by sampling from the zero-mean joint Gaussian distribution defined by the covariance matrix obtained in step 4a.

For $p = 0$, sample from a 1-dimensional Gaussian distribution with variance $G_{kk}(0)\Delta\omega$, since at $\omega_p = 0$ the Fourier coefficients have identical values at all locations.

5. For each of the sites $k = 1, \dots, n$, use Eqn. (4.1) to obtain the corresponding realization of the acceleration time-history.

4.4.2 Conditioned simulation

Consider now the case where the realization of the ground motion at one or more sites is given, and acceleration time histories at other sites that are consistent with a prescribed coherency function need to be generated. As in the case of unconditioned simulation, we assume that the site characteristics at all locations are described through the site FRFs. In this case, the Fourier coefficients of the acceleration processes at the target locations are sampled from a joint Gaussian distribution derived by probabilistic conditioning.

Adopting the notation of the previous section, we consider the set of zero-mean Fourier coefficients $\mathbf{X}_p = [A_{p1} \quad B_{p1} \quad \cdots \quad A_{pn} \quad B_{pn}]$ at frequency ω_p for all n sites, and the $2n \times 2n$ covariance matrix $\mathbf{\Sigma}_{pp}$ of these coefficients. We partition $\mathbf{X}_p$ into two subsets, $\mathbf{X}_{p1} = [A_{p1} \quad B_{p1} \quad \cdots \quad A_{pm} \quad B_{pm}]$, $m < n$, and $\mathbf{X}_{p2} = [A_{p(m+1)} \quad B_{p(m+1)} \quad \cdots \quad A_{pn} \quad B_{pn}]$, where $k = 1, \dots, m$ are the sites with known ground motions. It is well known that the conditional distribution of $\mathbf{X}_{p2}$ given $\mathbf{X}_{p1} = \mathbf{x}_{p1}$ is jointly normal with mean

$$\mathbf{M}_{p,2|1} = \mathbf{\Sigma}_{pp,21} \left(\mathbf{\Sigma}_{pp,11}\right)^{-1} \mathbf{x}_{p1} \tag{4.8}$$

and covariance matrix

$$\mathbf{\Sigma}_{p,22|11} = \mathbf{\Sigma}_{pp,22} - \mathbf{\Sigma}_{pp,21}\left(\mathbf{\Sigma}_{pp,11}\right)^{-1}\mathbf{\Sigma}_{pp,12} \tag{4.9}$$

where $\mathbf{\Sigma}_{pp,ij}$ denotes the sub-matrix of $\mathbf{\Sigma}_{pp}$ giving the covariance of vectors $\mathbf{X}_{pi}$ and $\mathbf{X}_{pj}$.

In this study, we only consider the case where the acceleration process at location $k = 1$ is specified at N points in time and conditioned acceleration time-histories are simulated for locations $k = 2, \dots, n$. The $2(n-1)$-dimensional joint Gaussian distribution of the Fourier coefficients for the target $n - 1$ locations is defined through the mean vector and covariance matrix in Eqns. (4.8) and (4.9), respectively. In these equations, $\mathbf{x}_{p1} = [A_{p1} \quad B_{p1}]$ is the set of Fourier coefficients of the given realization determined from Eqns. (4.4). The covariance matrix $\mathbf{\Sigma}_{pp}$, is obtained as described in Section 4.4.1, i.e., using Steps 1-4a of Algorithm 1. At each frequency, $\omega_p = \frac{2\pi p}{N\Delta t}$, $p = 1, \dots, N/2$, a sample-set of Fourier coefficients for the target locations is obtained as $\mathbf{x}_{p2} = \mathbf{M}_{p,2|1} + \mathbf{L}_p^{\mathrm{T}}\mathbf{z}_p$, where $\mathbf{L}_p$ is an upper triangular matrix such that $\mathbf{L}_p^{\mathrm{T}}\mathbf{L}_p = \mathbf{\Sigma}_{pp,22|11}$, and $\mathbf{z}_p$ is a vector of $2(n-1)$ uncorrelated standard normal variables. As in the previous section, $\mathbf{L}_p = \mathbf{D}_p\mathbf{R}_p$, where $\mathbf{D}_p$ is the diagonal matrix of standard deviations and $\mathbf{R}_p$ is the Cholesky decomposition of the correlation matrix. We note that sampling is not required for $p = 0$, because at $\omega_p = 0$ the ground motions are fully coherent and the Fourier coefficients have the same values at all locations. (If one is given time-histories at more than one location, Eqns (4.4) and (4.6) indicate that they automatically satisfy this condition as long as their temporal averages are zero.) After the vectors $\mathbf{x}_{p2}$ at all frequencies are obtained, Eqn. (4.1) is used to assemble the realizations of acceleration time-histories at the target locations.

The implemented algorithm used for conditioned simulation is summarized as follows:

Algorithm 2: Conditioned simulation of an array of stationary spatially varying ground accelerations

1. Estimate the auto-PSD of the given realization in terms of the periodogram in Eqn. (4.5). Smoothing of the periodogram is optional.
2. Use Eqn. (4.7) to evaluate the auto-PSDs at all sites in terms of their respective soil column FRFs.
3. Use Eqn. (4.3) to evaluate cross-PSDs for all pairs of sites in terms of the auto-PSDs and the coherency function.
4. Repeat the following steps for each frequency $\omega_p = \frac{2\pi p}{N\Delta t}$, $p = 1, \ldots, N/2$:
   a. Evaluate the elements of the covariance matrix $\mathbf{\Sigma}_{pp}$ using Eqns (4.2) and the estimated auto- and cross-PSDs.
   b. Determine the Fourier coefficients of the given realization at site $k = 1$ using Equation (4.4).
   c. Using Eqns. (4.8) and (4.9), determine the conditional mean vector and covariance matrix of the Fourier coefficients at locations $k = 2, \ldots, n$.
   d. Simulate a $2(n-1)$-dimensional vector of conditioned Fourier coefficients by sampling from a joint Gaussian distribution with the mean and covariance determined in step 4c.

   For $p = 0$, only apply step 4b, since at $\omega_p = 0$ the Fourier coefficients have identical values at all locations.
5. For each of the sites $k = 2, \ldots, n$, use Eqn. (4.1) to obtain the corresponding realization of the acceleration time-history.

4.5 EXTENSION TO NON-STATIONARY MOTIONS

In Section 4.4, we developed a method for simulating stationary ground motions consistent with a given accelerogram or the PSD of a given accelerogram, and for a prescribed spatial variability model and specified site conditions. The methods described were based on the assumption of stationarity, which is unrealistic for earthquake motions. However, typical earthquake ground motions that do not contain a directivity pulse can be seen as consisting of nearly-stationary segments. Each segment can then be treated as a stationary process in the manner described in the preceding section. Vanmarcke and Fenton (1991) used an arbitrary division of a given accelerogram into stationary segments to simulate non-stationary acceleration time-histories. Liao and Zerva (2006) further investigated the problem of conditioned simulation with segmentation and incorporated necessary post-processing to obtain physically compliant motions.

In this study, the original accelerogram is divided into segments that maintain nearly time-invariant statistical characteristics. The characteristics considered are the variance, the predominant frequency and the bandwidth of the ground acceleration process. Following the work of Rezaeian and Der Kiureghian (2008), instantaneous values of these characteristics are respectively measured as the slopes of the integral of the squared acceleration in time, the cumulative count of zero-level up-crossings, and the cumulative count of negative maxima or positive minima. As an illustrative example, consider the fault normal component of the Izmit record of the 1999 Kocaeli earthquake. Figure 4.1 shows the corresponding acceleration time history and the evolving integral measures of the variance, the predominant frequency and the bandwidth, respectively denoted p_1, p_2 and p_3. The vertical dashed lines demarcate the segments where the slopes of all three curves are more or less constant and, hence, the process can be considered nearly stationary. Although the aforementioned measures provide guidance, selection of the segment bounds ultimately involves some judgment. It is important to note that a denser segmentation leads to a more accurate representation of the non-stationary nature and the high-frequency content of the original record, but alters the low-frequency content of the motion to a larger extent.

In the following, we employ the concept of segmentation to extend the simulation methods described in Section 4.4 to non-stationary motions.

4.5.1 Unconditioned simulation

The basic idea of the non-stationary extension of the unconditioned simulation method is to apply the algorithm in Section 4.4.1 to each "stationary" segment of the given accelerogram and then, for each location, assemble the entire realization by joining together the corresponding simulated time-history segments. To avoid shifting the segments for different sites, the wave-passage effect is separately applied as a deterministic time-shift on the entire realization. Further details on the implementation of the method are described below.

Following the segmentation of the given accelerogram, both ends of each segment are tapered with appropriate functions to avoid introducing fake high-frequency components in the Fourier series. In this study, the tapering is done with cosine-type functions that evolve from 0 to 1 at the left end and from 1 to 0 at the right end. Each tapered segment is used as the given realization for the unconditioned simulation of acceleration segments at all locations, employing Algorithm 1 in Section 4.4.1, but without the wave-passage effect in the coherency function. The simulated time-history segments extend beyond the time window defined by the original segment by 1-5% of the latter on each side. The overlapping regions of neighboring segments are then combined using cosine weighting functions. To account for the wave-passage effect, the resulting accelerograms are shifted in time by d_{kl}^{L}/v_{app}, where d_{kl}^{L} is the horizontal projection of the distance of the relevant station from the location with $k=0$ along the direction of propagation of waves and v_{app} is the apparent wave velocity. Finally, the shifted accelerograms are further processed following standard techniques in earthquake engineering (e.g., Boore et al, 2002; Liao and Zerva, 2006). In this study, the post-processing involves subtracting the mean value of the entire acceleration time history, application of a short cosine taper function to set the initial value to zero and, finally, application of a high-pass filter to ensure zero residual velocity and displacement values at the end of the record. The filter selected herein is the critically-damped oscillator described by the equation

$$\ddot{x}(t)+2\omega_{c}\dot{x}(t)+\omega_{c}^{2}x(t)=y(t) \tag{4.10}$$

where ω_c is the selected corner frequency of the filter and $y(t)$ and $\ddot{x}(t)$ are the input (unfiltered) and output (filtered) acceleration time-histories, respectively. The resulting acceleration time-histories are integrated to obtain the corresponding realizations of velocity and displacement time histories.

The steps involved in the non-stationary extension of the unconditioned simulation method are summarized in the following algorithm.

Algorithm 3: Unconditioned simulation of array of non-stationary spatially varying ground accelerations

1. Apply segmentation of the given accelerogram. Slopes of the integral of squared acceleration, the cumulative count of zero-level up-crossings, and the cumulative count of negative maxima and positive minima may be used to guide the selection of the segment boundaries.
2. Repeat steps 2a-2b for each segment:
    a. Taper both ends of the segment with cosine-type functions.
    b. Apply Algorithm 1 in Section 4.4.1 to simulate acceleration time-histories at locations $k=1,\cdots,n$ for a time window that extends beyond the time-window of the original segment by 1-5% of the latter on each side. Disregard the wave-passage component of the coherency function for this analysis.
3. Join the simulated time-histories in step 2 using cosine-type weighting functions over the extended overlapping intervals.
4. Make deterministic time-shift of the simulated time-histories at locations $k=2,\cdots,n$ by d_{kl}^{L}/v_{app}, where d_{kl}^{L} is the horizontal projection of the distance of the relevant station from the location with $k=1$ along the direction of propagation of waves and v_{app} is the apparent wave velocity, to account for the wave-passage effect.
5. Repeat steps 5a-5d for each location:
    a. Subtract the mean of the entire acceleration time-history.

b. Apply a cosine-type taper function to set the initial value to zero.
c. Apply a high-pass filter (e.g., the critically-damped oscillator) to enforce zero residual velocity and displacement values.
d. Integrate the filtered accelerograms to obtain corresponding velocity and displacement time-histories.

4.5.2 Conditioned simulation

The non-stationary extension for the conditioned simulation is performed with an algorithm similar to Algorithm 3 in Section 4.5.1, in which the first sentence in step 2b is modified to read:

> "Apply Algorithm 2 in Section 4.4.2 to simulate acceleration time-histories at locations $k = 2, \cdots, n$ for a time window that extends beyond the time-window of the original segment by 1-5% of the latter on each side."

To obtain a consistent set of ground motions, the given acceleration time history at location 1 must be slightly modified. Specifically, we join together tapered segments of the accelerogram and perform post-processing in a manner identical to the simulated motions. The resulting simulated motion at location 1 does not have any random characteristics but is slightly different from the given record.

The segmentation and post-processing mainly influence the low-frequency content of the motion, which is more apparent in the displacement waveform. As a result, the displacement time history of the original record can differ somewhat from the simulated displacement time history at zero distance. If accurate representation of the displacement time history of the original record is important, the following alternative procedure can be applied: (a) Separate the low-frequency content of the original record, e.g., by use of a high-pass filter and subtracting from the original record; (b) generate conditioned non-stationary simulations using the remaining motion; (c) assuming the low-frequency contents at different sites are perfectly coherent, add it back to the simulated time-histories after it has been deterministically modified to account for the wave-passage effect and, optionally, for the site-response effect. More details are given below.

Two different filters are investigated in this study for the separation of the low-frequency content of a given accelerogram: a 4th-order causal Butterworth filter (see e.g., Rabiner and Gold, 1975) and the critically damped SDOF oscillator in Eqn. (4.10), both having a corner frequency of $f_c = \frac{\omega_c}{2\pi} = 0.2$ Hz. To investigate criteria for the choice of the initial filter, we consider again the Izmit record shown in Figure 4.1. Figure 4.2 compares the original displacement time history with the simulated ones at zero distance for the two choices of the initial filter. The differences between the simulated time histories and the original one are due to the segmentation, the tapering and subsequent joining of the segments, and the post-processing of the resulting time-history. For the two filters, the left graph of Figure 4.3 compares the ratio of the PSD of the remainder motion (after extracting the low-frequency content) over the PSD of the initial accelerogram. Ideally, this ratio should be close to a step-function that evolves from 0 to 1 at the corner frequency f_c. The right graph of Figure 4.3 compares the corresponding acceleration auto-PSDs of the separated low-frequency components. It is evident from Figure 4.2 that the critically damped oscillator is a more suitable filter in terms of preserving the initial displacement time-history. However, as indicated in Figure 4.3, the Butterworth filter has the advantage of leaving less high-frequency power in the separated "coherent" component. Thus, the choice of filter depends on the criterion that is more important in the specific analysis: preserving the initial displacement waveform or excluding high-frequency power from the remainder motion.

As stated earlier, the low-frequency separated component of the motion is assumed to be perfectly coherent. This is reasonable since long period waves are less affected by heterogeneity of the ground medium. Thus, when uniform soil conditions are considered, it is only necessary to shift the separated waveform in time to account for the wave-passage effect and then add it back to the simulated time-histories at all sites. When varying soil conditions are present, the low-frequency separated waveform may need to be further modified. We suggest two approaches. In the first approach, one assumes that, for small frequencies, the site FRFs have values close to unity, i.e., the soil columns do not alter the low-frequency component of the ground motion. In that case no further modification of the low-frequency component is necessary. In the second approach, we additionally account for the site-response effect by applying a filter on the low-frequency component. The filter is applied in the frequency domain and only the steady-state response is considered; thus, it is fully described in terms of its FRF. The latter is given by the ratio of the FRF of the soil-column at the target site over the FRF of the soil-column at location $k = 1$. This filtering models an inverse propagation of the low-frequency component through the soil-column at location $k = 1$ to obtain the motion at the bedrock level and propagation of the latter to the ground surface at the location of the target site. The filter is applied to the Fourier transform of the low-frequency component, which is then transformed back to time domain and shifted in time to account for the wave passage effect.

The steps involved in the non-stationary extension of the conditioned simulation method, as described above, are summarized in the following algorithm.

Algorithm 4: Conditioned simulation of non-stationary spatially varying ground accelerations with deterministic treatment of the low-frequency content

1. Separate the low frequency content using a 4th-order causal Buterworth filter or a critically damped SDOF oscillator.
2. Apply segmentation of the remaining acceleration time-history. Slopes of the integral of squared acceleration, the cumulative count of zero-level up-crossings, and the cumulative count of negative maxima and positive minima may be used to guide the selection of the segment boundaries.
3. Repeat steps 3a-3b for each segment:
    a. Taper both ends of the segment with cosine-type functions.

   b. Apply Algorithm 2 in Section 4.4.2 to simulate acceleration time histories at locations $2, \cdots, n$ for a time window that extends beyond the time-window of the original segment by 1-5% of the latter on each side. Disregard the wave-passage component of the coherency function for this analysis.
4. Join the simulated time-histories in step 3 using cosine-type weighting functions over the extended overlapping intervals.
5. Make deterministic time-shift of the simulated time-histories at locations $2, \cdots, n$ according to the formula d_{kl}^{L}/v_{app} to account for the wave-passage effect.
6. Repeat steps 6a-6f for each location:
   a. Subtract the mean of the entire acceleration time history.
   b. Apply a cosine-type taper function to set the initial value to zero.
   c. Apply a high-pass filter (e.g., the critically-damped oscillator) to enforce zero residual velocity and displacement values.
   d. Make deterministic time-shift of the separated low-frequency component to account for the wave-passage effect and optionally, apply an additional filter to account for the site effect.
   e. Add back the modified low-frequency component.
   f. Integrate the resulting accelerograms to obtain corresponding velocity and displacement time-histories.

4.6 EXAMPLE APPLICATIONS

As an example application, we simulate support motions for the Penstock Bridge, described in Section 3.2.4. The elevation of the bridge is shown in Figure 3.10. We consider abutment 1 to be the location corresponding to site $k = 1$. The Izmit record, introduced in the analysis of Section 4.5, is used as the original motion for the simulation of unconditioned and conditioned support motions. The segments considered stationary are the ones shown in Figure 4.1. We assume that the waves propagate in the direction from abutment 1 to abutment 5. The incoherence is modeled as in Eqn. (2.19) with the parameter values $a = 0.2$ and $v_s = 600$ m/s. The time-lag caused by the wave-passage effect is determined using $v_{app} = 400$ m/s. We examine both cases of uniform and varying soil conditions.

4.6.1 Uniform soil conditions

In this section, we generate sets of support motions under the assumption that soil conditions at all sites are identical with those at the site of the given record. We analyze sets of motions simulated with the unconditioned and the conditioned methods. Unless stated otherwise, the non-smoothed periodogram of each stationary segment is used. In the conditioned method, we examine both cases of no initial filtering and initial filtering to separate the low-frequency content. Based on the analysis in Section 4.5, only the 4th order causal Butterworth filter is used for this purpose. To validate the simulation method, we compare the coherency estimates from the simulated motions with the corresponding theoretical models. The coherency estimates are obtained by averaging the estimates from 20 realizations, where the estimate for each realization is obtained by dividing the cross-PSD estimate from Eqns. (4.6) by the square roots of the corresponding auto-PSDs estimated from Eqns. (4.5). Although the time histories have been generated in segments, the entire realizations are used in the above equations. An 11-point Hamming window is applied to smooth the periodograms and cross-periodograms in evaluating the coherency estimates. The response spectra of the simulated motions are also examined.

Unconditioned simulations

An example set of unconditioned simulations of the support motions is shown in Figure 4.4. Acceleration, velocity and displacement time histories for all support points are shown. The corner frequency of the post-processing filter used is $f_c = 0.15$ Hz. Observe that the simulation method preserves the non-stationary nature of the ground motion, and that all records approach zero with increasing time (i.e., have zero residuals). The wave passage effect is clearly visible. Figure 4.5 and Figure 4.6 compare coherency estimates of the simulated support accelerations and displacements, respectively, with the corresponding theoretical models. Two example support pairs are considered: bents 3 and 4, and abutments 1 and 5. We note that, according to the theory of stationary processes, the coherency function for a process must be invariant of differentiation. Hence, the theoretical coherency models for accelerations and displacements in the two figures are the same. For the acceleration time-histories, the coherency estimates are in excellent agreement with the theoretical models over the entire range of frequencies shown in Figure 4.5. For the displacement time-histories, the coherency estimates diverge from the theoretical models for frequencies greater than about 2.5Hz. However, this is inconsequential, since the auto-PSDs of the corresponding displacement processes are practically zero for these frequencies. Figure 4.7 shows 5% damped pseudo-acceleration response spectra for 20 realizations at each support point. It is clear that the variances at all support points are similar, a desirable characteristic for ground motions to be used in statistical analyses of bridge response under differential support motions. Figure 4.8 shows the corresponding median spectra of the five support points, which are in excellent agreement over the entire frequency range considered. Compared with the spectrum of the recorded motion, which should be regarded as just one realization of the underlying random process, the median response spectra of the simulated motions are smoother and have slightly smaller values in the lower frequency range. Even smoother median response spectra are obtained by using smoothed periodograms of the stationary segments. The smoothed periodograms tend to have more power than the non-smoothed ones at frequencies close to zero. This results in larger variances for the low-frequency components of the simulated motions compared to the case with no smoothing and, thus, a higher level of post-processing is required to enforce zero velocity and displacement residuals in about the same time length. Figure 4.9 shows the median 5% damped pseudo-acceleration response spectra when the periodograms are smoothed with a 7-point Hamming window. A filter with a corner frequency of $f_c = 0.20$ was used for the post-processing of the corresponding simulations.

Conditioned simulations

Next, we examine support motions generated with the conditioned simulation method. We first consider the case of simulation without separation of the low-frequency content. (The corresponding algorithm is described at the beginning of Section 4.5.2). In this case, for all sets of simulations, the motion at abutment 1 is the same and the displacement time history is identical with that shown as a dashed line in the upper chart of Figure 4.2. Figure 4.10 shows an example set of simulations for this case. Note again the non-stationary nature of the motions, the zero velocity and displacement residuals, and the time shift due to the wave-passage effect. The coherency estimates for accelerations and displacements for the selected pairs of support motions are compared with the corresponding theoretical models in Figure 4.11 and Figure 4.12, respectively. Again, the acceleration coherency estimates are in excellent agreement with the corresponding theoretical models, while the displacement estimates diverge for frequencies greater than about 3Hz. Figure 4.13 shows 5% damped pseudo-acceleration response spectra of 20 realizations at each support. We observe increasing variance of the spectral amplitudes with increasing distance from location $k = 1$ (abutment 1), at which the variance is zero. This inconsistent variability of the support motions obviously is problematic if the simulations are to be used for statistical analysis of structural response. The median response spectra for the conditioned simulations, shown in Figure 4.14, are jagged and closely follow the response spectrum of the recorded motion, except for a range of frequencies close to the corner frequency of the post-processing filter, which is taken as $f_c = 0.1$ Hz for the present case. A lower level of filtering is required in this case, since the conditioned simulation results in smaller variations over the array than in the unconditioned case. The jagged behavior is, of course, due to the small variance of the simulated motions for locations close to the site with the specified accelerogram.

Next, we examine conditioned simulations with deterministic treatment of the low-frequency content, which is separated from the original motion with a 4th order causal Butterworth filter. In this case, a lower level of filtering is required in the post-processing to ensure zero-residual velocities and displacements. The employed corner frequency for this case is $f_c = 0.05$ Hz. An example set of support motions (accelerations, velocities, displacements) is shown in Figure 4.15. The displacement time history at abutment 1, same in all simulations, is identical to that shown as a dashed line in the middle chart of Figure 4.2. Figure 4.16 and Figure 4.17 respectively compare the acceleration and displacement coherency estimates with the corresponding theoretical models for the selected pairs of supports. The acceleration coherency estimates are in excellent agreement with the theoretical models in the whole range of frequencies considered. The displacement coherency estimates are satisfactory for frequencies less than about 2Hz. This range of frequencies is smaller than that in the case of conditioned simulations without initial filtering (see Figure 4.12), but is still inclusive of the important frequencies of the displacement processes. In Figure 4.18, we observe increasing variance of the acceleration response spectra of the simulated motions with increasing distance from abutment 1, similar to that in Figure 4.13. Finally, Figure 4.19 shows the corresponding median acceleration response spectra, which are jagged and slightly diverge from the response spectrum of the original record for frequencies less than about 1Hz. We note that in this range of frequencies, the low-frequency separated component has significant power, as indicated by Figure 4.3.

Concluding this section, we note that the decision to initially separate or not separate the low-frequency component of the motion depends on the relative importance of the target characteristics of the simulated motions, e.g., preserving the original displacement waveform, matching the target response spectrum and/or the coherency characteristics in a certain frequency range.

4.6.2 Varying soil conditions

In this section, we generate sets of support motions under the assumption of varying soil conditions. In modeling the soil profiles, we consider two approaches. In the first approach, each soil-column is modeled as a SDOF system using the FRF in Eqn. (2.23). In the second approach, each soil-column is modeled as a continuous elastic medium using the FRF in Eqn. (2.22). Again, we consider both cases of unconditioned and conditioned simulations, using Algorithms 3 and 4 in Sections 4.5.1 and 4.5.2, respectively. For the conditioned simulations, we only examine the case with initial Butterworth filtering, i.e. we only examine conditioned simulations that preserve the original low-frequency content. In all cases, the unsmoothed periodogram is used in the simulation process. To validate these proposed methods, in addition to the coherency estimates, we examine ratios of acceleration auto-PSD estimates for support points with different soil conditions. The latter are compared with the corresponding theoretical values, determined through the site FRFs, using Equation (4.7). The auto-PSD estimates are obtained by averaging the periodograms of 20 realizations, each smoothed with an 11-point Hamming window.

4.6.2.1 Modeling the soil columns using the SDOF idealization

Description of the site FRF by the SDPF model in Eqn. (2.23) requires specification of the soil-column frequency, ω_k, and damping ratio, ζ_k. At abutment 1, we assume that the site conditions are identical to those at the site of the given record. To determine the frequency and damping ratio of the soil-column at this location ($k = 1$), we employ the method described in Section 2.2.4, i.e., we assume a white-noise excitation at the bedrock level and fit the theoretical PSD of the acceleration response at the ground surface to the smoothed periodogram of the record. Non-linear least-squares minimization with MATLAB results in $\omega_1 \approx 2.07$ rad/s and $\zeta_1 \approx 0.6$, when the periodogram of the record is smoothed with a 41-point Hamming window. Comparison of the acceleration auto-PSD estimate (smoothed periodogram) of the recorded motion and the fitted theoretical model is shown in Figure 4.20. A higher-level of smoothing of the periodogram results in a higher damping value, but values larger than 0.6 are not typically used (Zembaty and Rutenberg, 2002). For the other support points, the selected frequencies and damping ratios of the soil-columns are listed in Table 4.1. Note that identical soil conditions have been assumed for abutments 1 and 5 and for bents 2 and 4.

Unconditioned simulations

Figure 4.21 shows an example set of realizations of the support motions obtained with the unconditioned simulation method. Acceleration, velocity and displacement time-histories at all support points are shown. The motions in each pair of abutments 1 and 5 and of bents 3 and 4 differ only due to the incoherence and wave passage effects, and thus, have the same spectral contents. For any other pair of support motions, the variability is due to incoherence, wave-passage and, additionally, the effect of differential site response. The latter effect also causes variations in the frequency contents of the motions, e.g., supports located on softer soils are richer in lower frequency components. The differences in frequency contents are more apparent in the acceleration time histories than in the velocity and displacement time histories. This is because different soil FRFs differ more strongly at high frequencies. In Figure 4.22 and Figure 4.23 we examine the coherency characteristics and the acceleration auto-PSD ratios for two example support pairs, each pair consisting of support points with dissimilar soil conditions. These are the pair of abutment 1 and bent 3 and the pair of bent 3 and bent 4. Excellent agreement of the estimates with the theoretical values validates the simulation method. Figure 4.24 shows the median 5% damped pseudo-acceleration response spectra of 20 simulations. Response spectra at sites with similar soil conditions, i.e. for abutments 1 and 5 and for bents 2 and 4, are in excellent agreement.

Conditioned simulations

Next, we present a similar analysis with the method of conditioned simulation with separation of the low-frequency content with a Butterworth filter and modification of the low-frequency component to account for the wave-passage effect only (see step 6d of Algorithm 4 Section 4.5.2). Figure 4.25 shows an example set of simulations. In all simulated arrays, the displacement at abutment 1 is identical with the dashed line in the middle chart of Figure 4.2. Figure 4.26 and Figure 4.27 show the estimates of the acceleration coherency and ratio of acceleration PSDs, respectively. These estimates are in good agreement with the theoretical models. Figure 4.28 shows the corresponding median pseudo-acceleration response spectra. It can be seen that sites with similar soil conditions have nearly identical median response spectra.

Next we apply modification of the extracted low-frequency component for both the wave-passage and the site-response effects. The coherency estimates and ratios of auto-PSDs for this case are shown in Figure 4.29 and Figure 4.30, respectively. Comparison of Figure 4.26 with Figure 4.29 and of Figure 4.27 with Figure 4.30 indicates that the modification of the separated low-frequency component to account for the site response effect degrades the agreement with the theoretical results. We suspect that the assumption of steady-state response for the low-frequency component of the motion, which is implicit in the frequency-domain modification, introduces an error. On the other hand, the close agreements observed in Figure 4.26 and Figure 4.27 suggest that the effect of site response on the low-frequency component of the motion is insignificant and can be neglected.

4.6.2.2 Modeling the soil columns using the theory of wave propagation through elastic media

We now consider the case where the FRF of each soil-column is given by Eqn. (2.22). With this model, the site characteristics at the kth location are fully described in terms of the damping ratio, ζ_k, the depth to bedrock, z_k, the shear-wave velocity, $v_{s,k}$, and the reflection coefficient, r_k. Assuming the typical values $v_b = 1500\,\frac{\mathrm{m}}{\mathrm{s}}$ for the shear-wave velocity and $\rho_b = 1500\,\frac{\mathrm{g}}{\mathrm{cm}^3}$ for the density at the bedrock level, evaluation of the reflection coefficient only requires additional specification of the soil-column density, $\rho_{s,k}$. Again, we assume that the site conditions at abutment 1 are identical to those at the site of the given record. The shear-wave velocity for the Izmit record is known, $v_{s,1} = 811\,\frac{\mathrm{cm}}{\mathrm{s}}$. The depth to bedrock, z_1, is selected such that the first resonant frequency of the soil-layer coincides with the frequency of the site under the SDOF idealization in Section 4.6.2.1. Assuming the bedrock is horizontal, the values of z_k at the other support points are selected such that the variation of the depths of the soil-layers is consistent with the (known) variation of the elevations of the bridge supports. The value of $v_{s,k}$ at each support is then determined so that the first resonant frequency matches the corresponding frequency considered in Section 4.6.2.1. Finally, typical values are selected for the soil-column densities $\rho_{s,k}$. Parameter values that describe the site characteristics at all support points for this model are listed in Table 4.2.

Unconditioned simulations

For the unconditioned simulation method, an example set of support motions is shown in Figure 4.31. Figure 4.32 and Figure 4.33 validate the method by examining the coherency characteristics and auto-PSDs ratios, respectively, and Figure 4.34 shows the median pseudo-acceleration response spectra. Observe that because of the multi-modal site effect, the coherency function is a lot more complicated than in the case with a SDOF idealization of the soil column. Comparisons with the theoretical models again confirm validity of the simulation method.

Conditioned simulations

Here we only consider the case of conditioned simulation with initial Butterworth filtering and only the wave-passage effect accounted for in the deterministic modification of the low-frequency component. Figure 4.35 shows an example set of simulations, Figure 4.36 examines the coherency estimates, Figure 4.37 examines the acceleration auto-PSDs ratios and Figure 4.38 presents the median pseudo-acceleration response spectra. Once again the results confirm validity of the simulation approach. The reader must, however, recall that this conditioned simulation will yield realizations with non-uniform variance for different sites.

4.7 SUMMARY

In this chapter, we developed methods for simulating an array of non-stationary differential support motions by probabilistic conditioning. Non-stationarity is achieved by considering the process as composed of stationary segments. The arrays of simulated motions properly account for the effects of incoherence, wave passage and spatially varying soil conditions. We considered two approaches: In the first, we simulated support motions characterized by uniform variance with distance by conditioning on a specified set of PSDs, which are obtained as the periodograms of "stationary" segments of a recorded motion. In the second, we simulated support motions characterized by increasing variance with distance, by conditioning on a specified realization. In the latter approach, we investigated a method that preserves the low-frequency content, and thus, the waveform of the displacement time history of the original motion. The method involves deterministic treatment of the low-frequency content of the motion, which is extracted from the original motion through high-pass filtering. The simulation methods were validated by (i) examining the physical compliance of example simulated time histories, (ii) comparing statistical characteristics of an ensemble of realizations with the corresponding target theoretical models, and (iii) investigating the response spectra of the simulated motions.

Table 4.1: Variation of soil-column properties for the SDOF model.

	abutment 1	bent 2	bent 3	bent 4	abutment 5
$\omega/2\pi$, rad/s	2.07	1.75	1.43	1.75	2.07
ζ_k	0.6	0.5	0.4	0.5	0.6

Table 4.2: Variation of soil-column properties for the elastic-medium model.

	abutment 1	bent 2	bent 3	bent 4	abutment 5
$v_{s,k}$, cm/s	811	556	459	584	835
h_k, m	98	79	80	83	101
$\rho_{s,k}$, g/cm^3	2.2	2	1.8	2.0	1.8

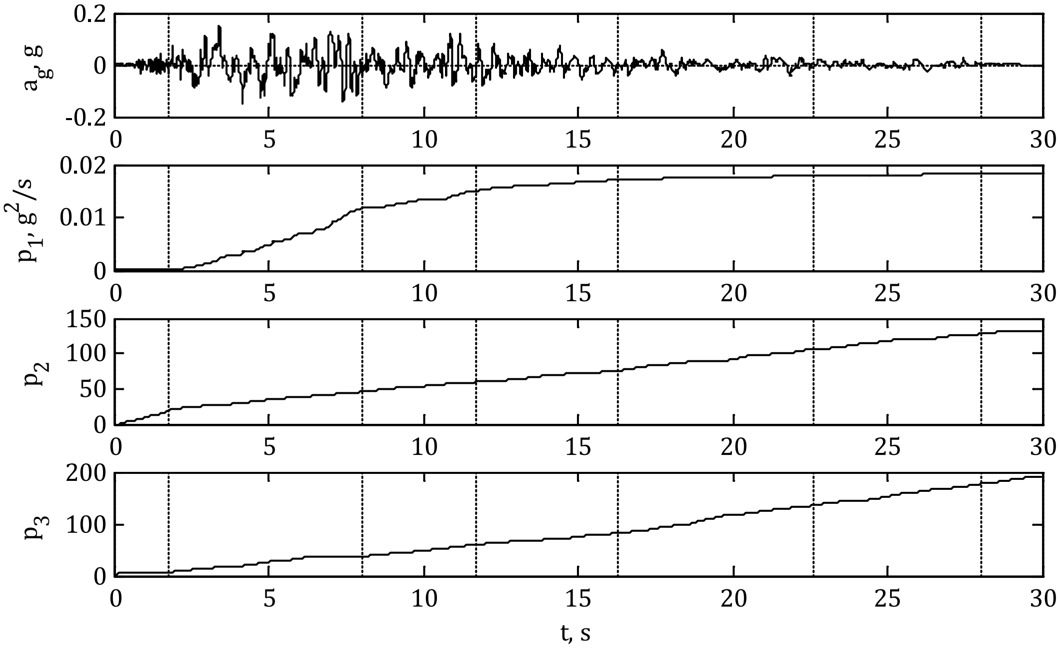

Figure 4.1: "Stationary" segments of an accelerogram selected based on integral measures of evolving cumulative energy, predominant frequency and bandwidth.

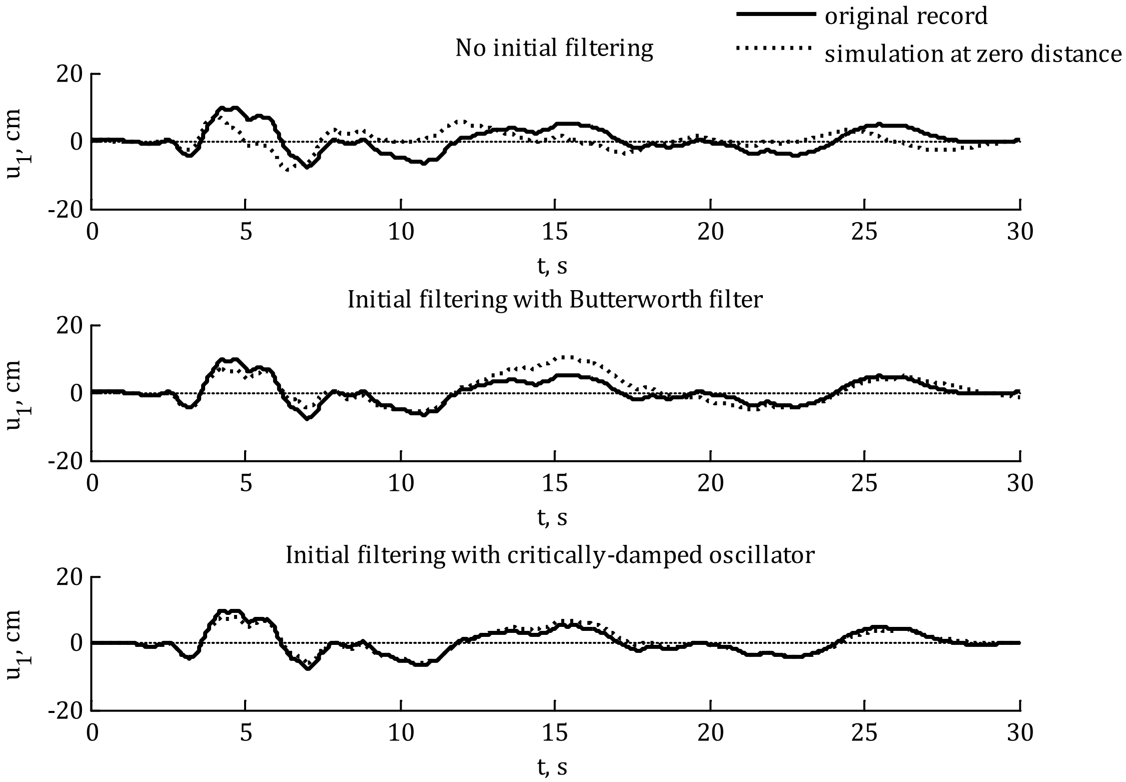

Figure 4.2: Comparison of displacement time history of the original record with conditioned simulated displacement time histories at zero distance.

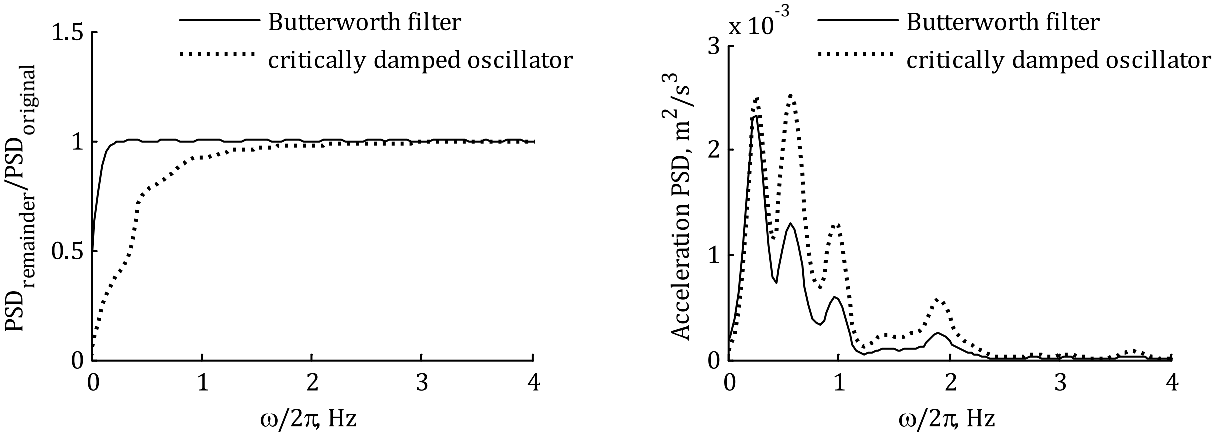

Figure 4.3: Comparison of ratios of PSDs of the remainder motion over the original motion for two filters (left) and of acceleration auto-PSDs of the corresponding low-frequency extracted motions (right).

Acceleration time-histories (g)

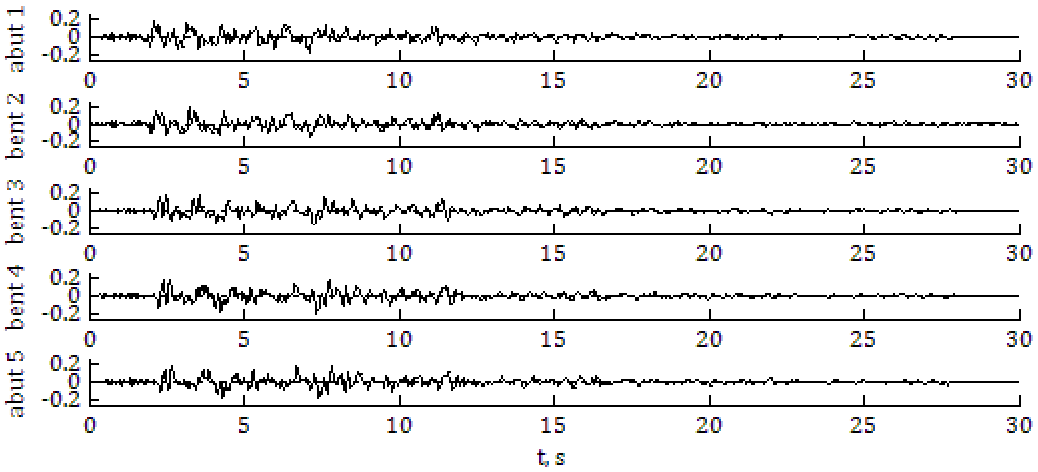

Velocity time-histories (cm/sec)

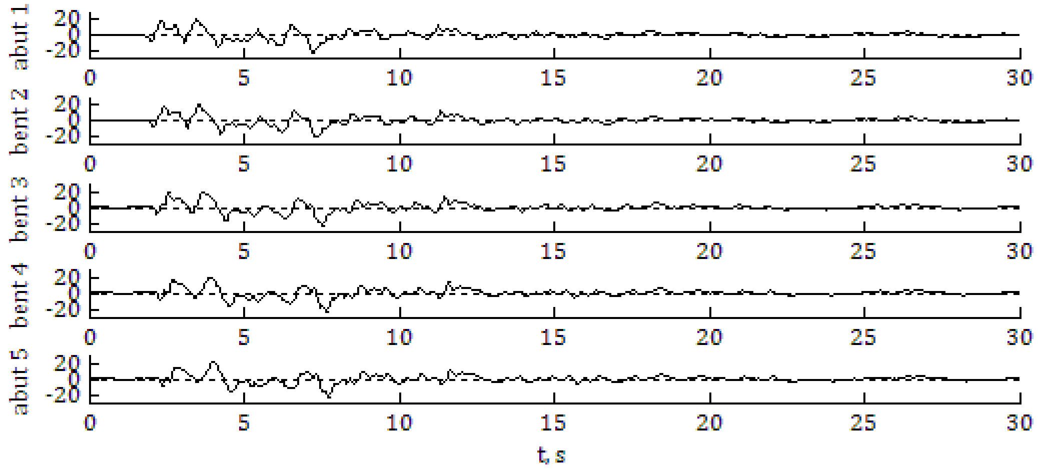

Displacement time-histories (cm)

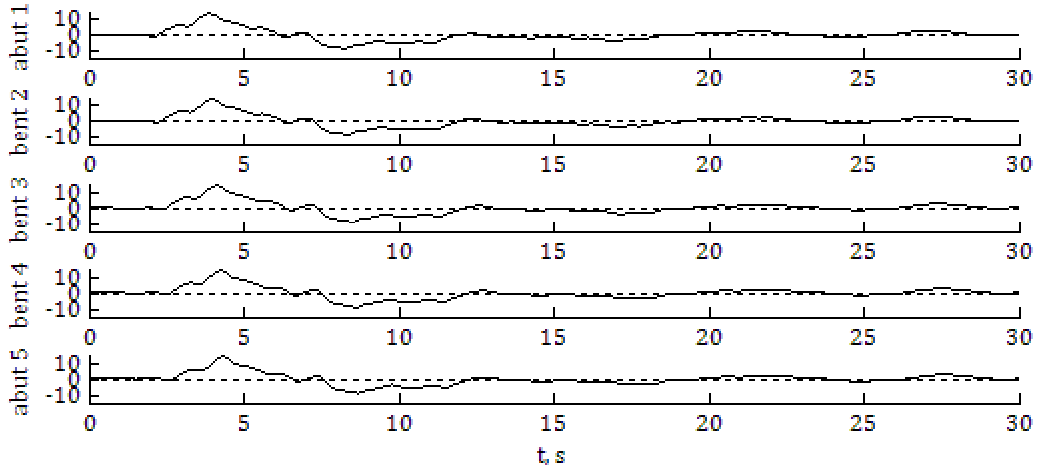

Figure 4.4: Example set of unconditioned simulations (uniform soil conditions)

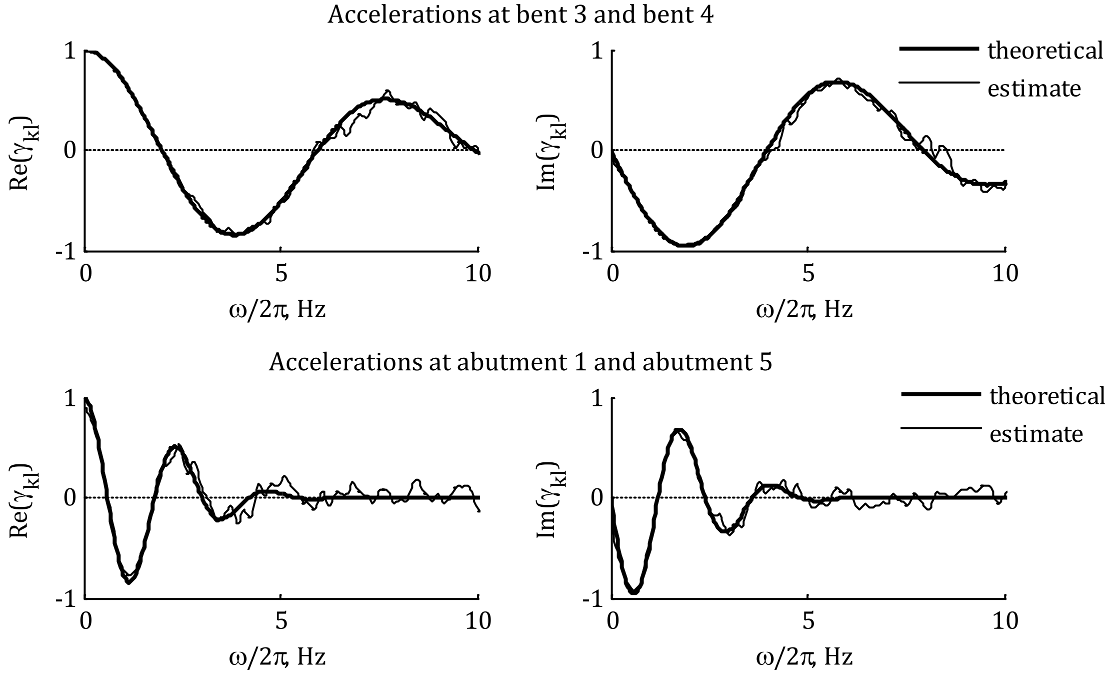
Accelerations at bent 3 and bent 4

Accelerations at abutment 1 and abutment 5

Figure 4.5: Acceleration coherency estimates from 20 unconditioned simulations (uniform soil conditions).

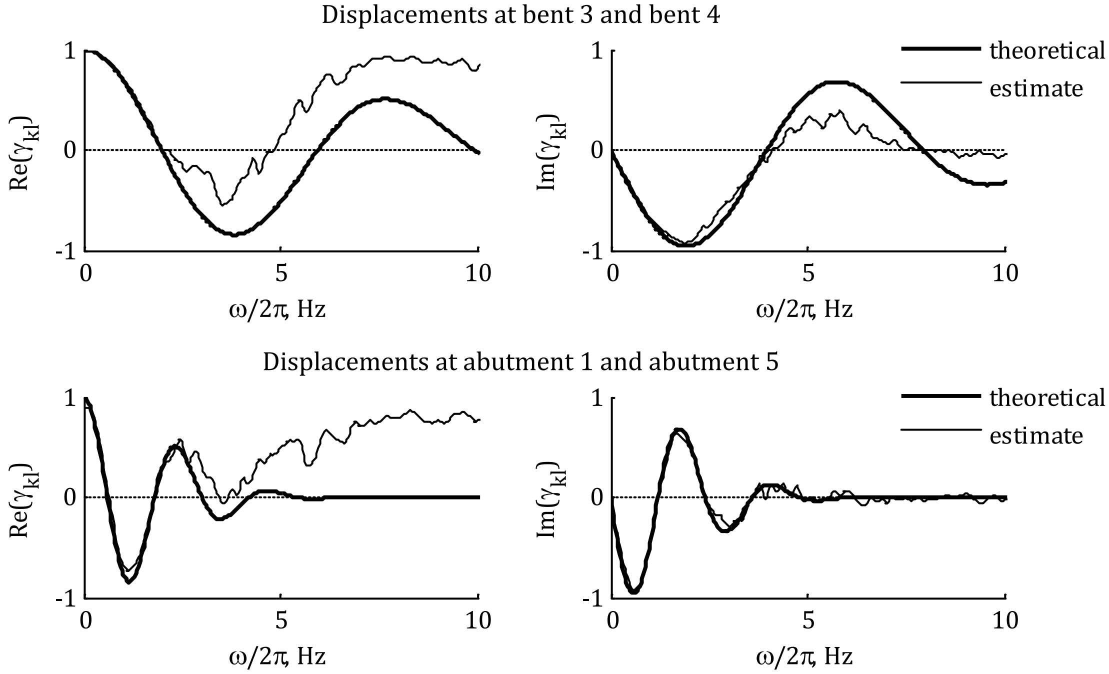
Displacements at bent 3 and bent 4

Displacements at abutment 1 and abutment 5

Figure 4.6: Displacement coherency estimates from 20 unconditioned simulations (uniform soil conditions).

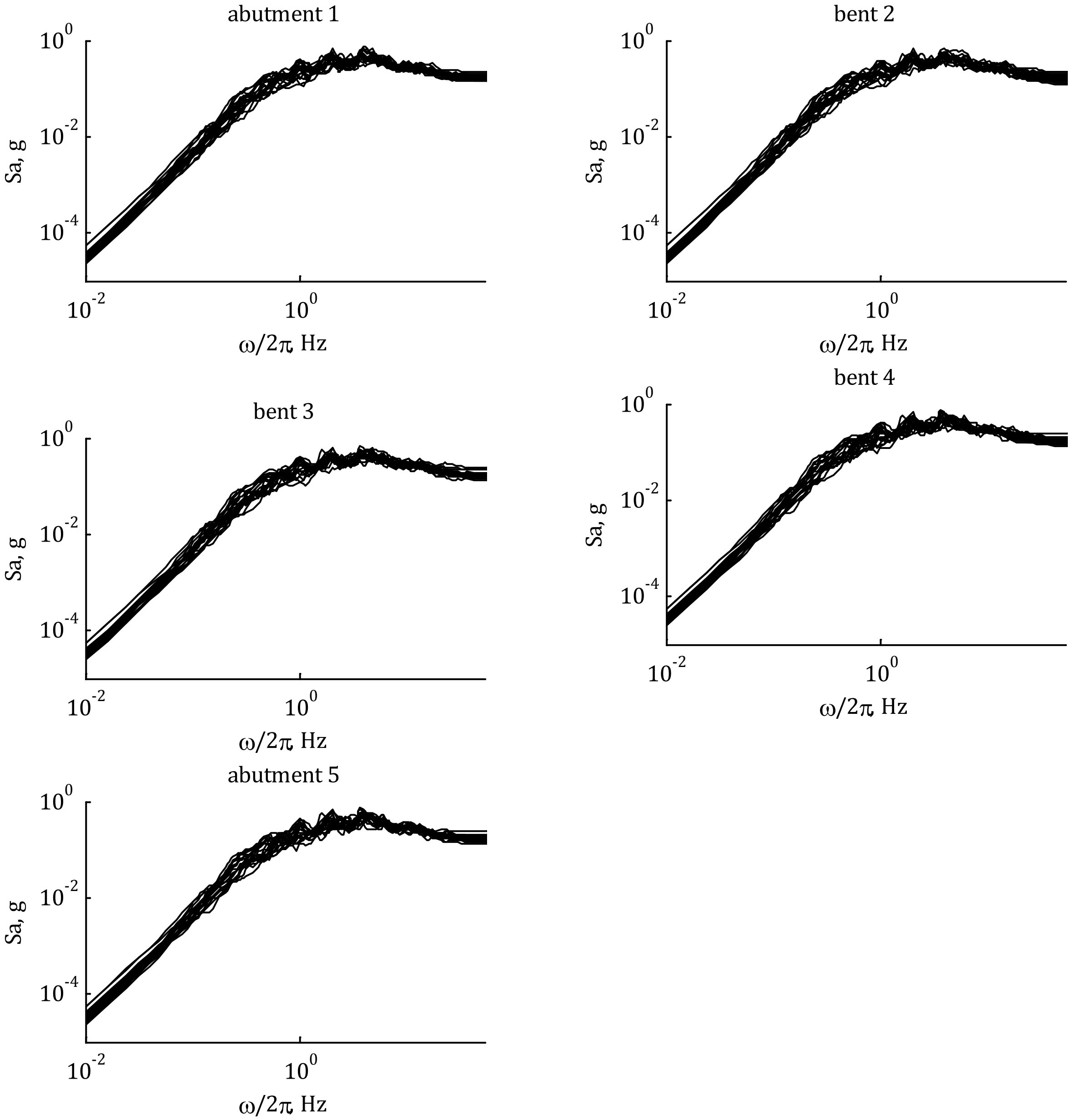

Figure 4.7: Acceleration response spectra of 20 unconditioned simulations (uniform soil conditions).

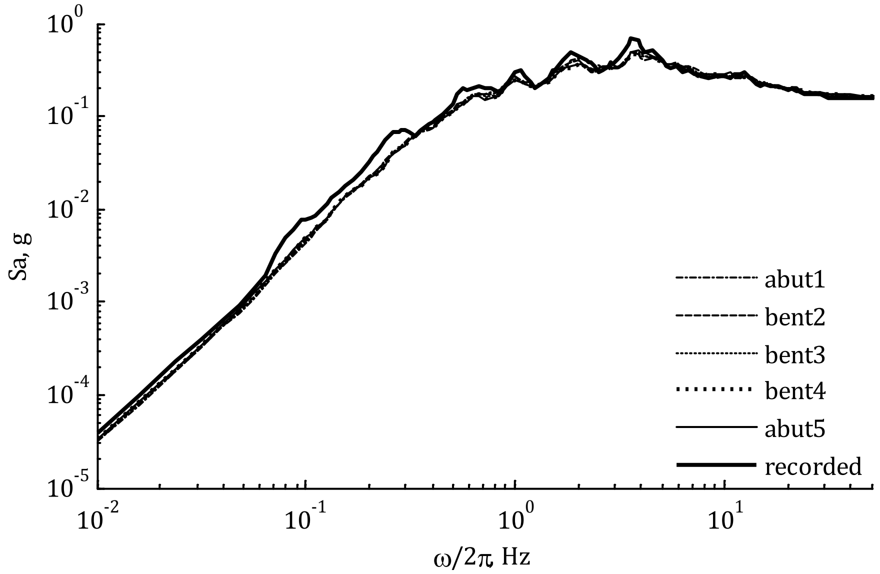

Figure 4.8: Median acceleration response spectra of 20 unconditioned simulations (uniform soil conditions).

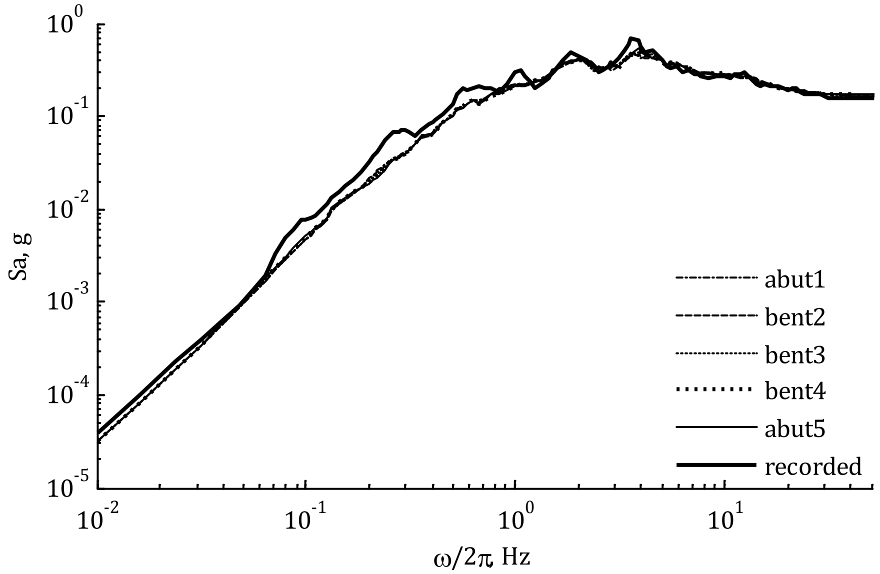

Figure 4.9: Median acceleration response spectra of 20 unconditioned simulations using smoothed periodograms (uniform soil conditions).

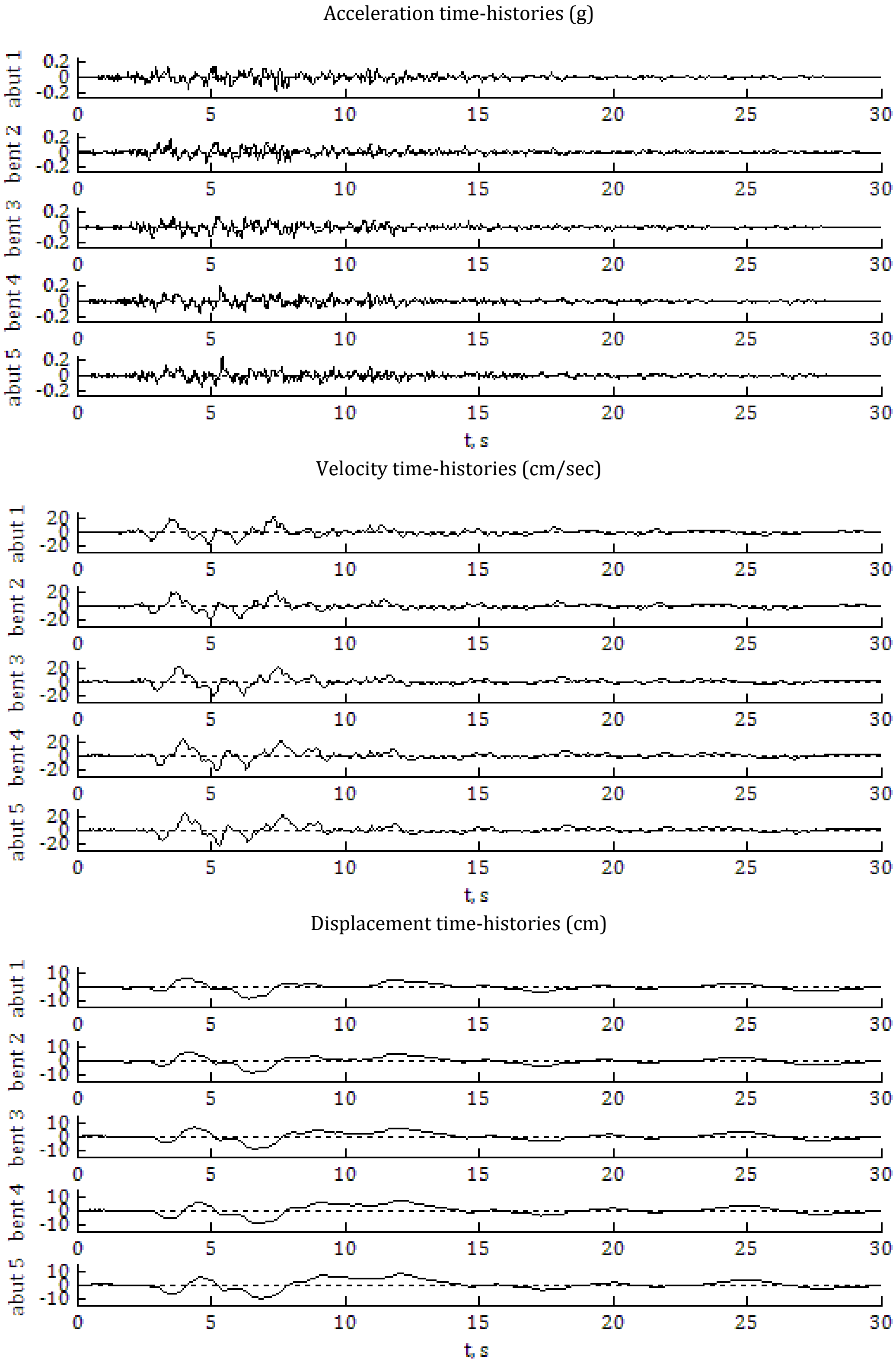

Acceleration time-histories (g)

Velocity time-histories (cm/sec)

Displacement time-histories (cm)

Figure 4.10: Example set of conditioned simulations without initial filtering (uniform soil conditions).

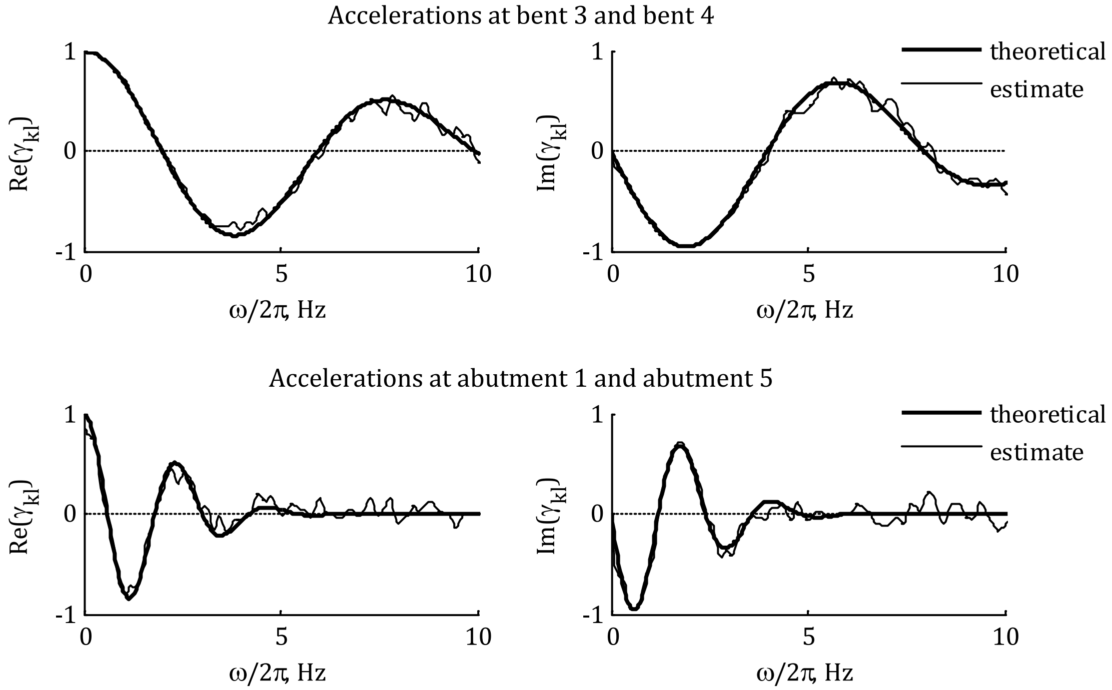
Accelerations at bent 3 and bent 4

Accelerations at abutment 1 and abutment 5

Figure 4.11: Acceleration coherency estimates from 20 conditioned simulations without initial filtering (uniform soil conditions).

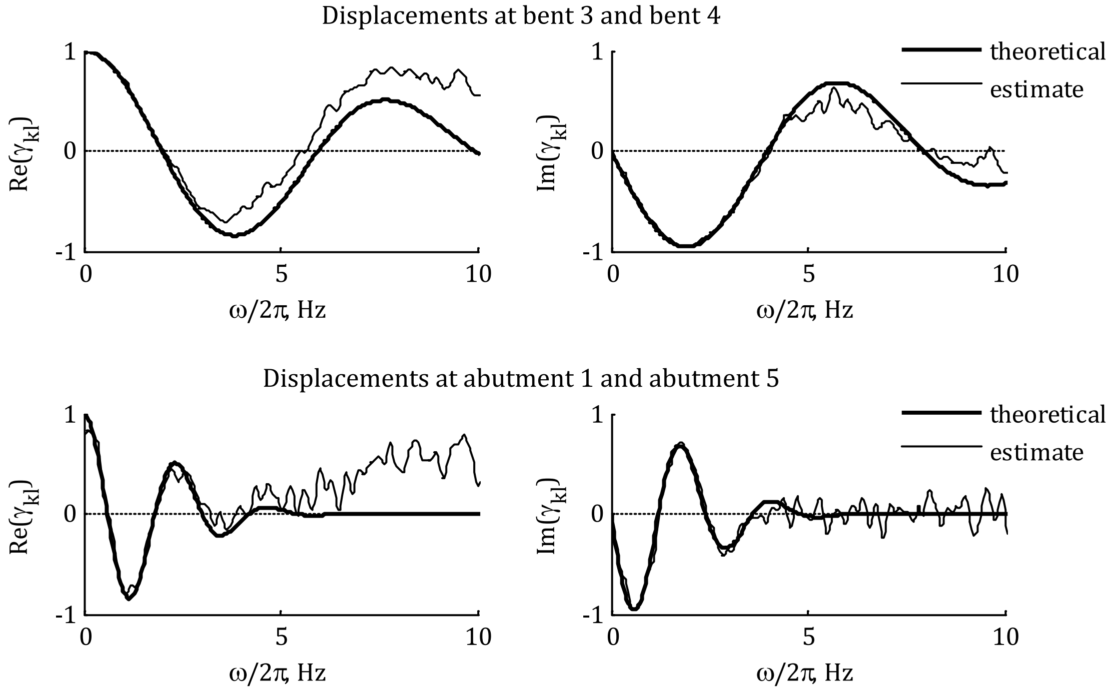
Displacements at bent 3 and bent 4

Displacements at abutment 1 and abutment 5

Figure 4.12: Displacement coherency estimates from 20 conditioned simulations without initial filtering (uniform soil conditions).

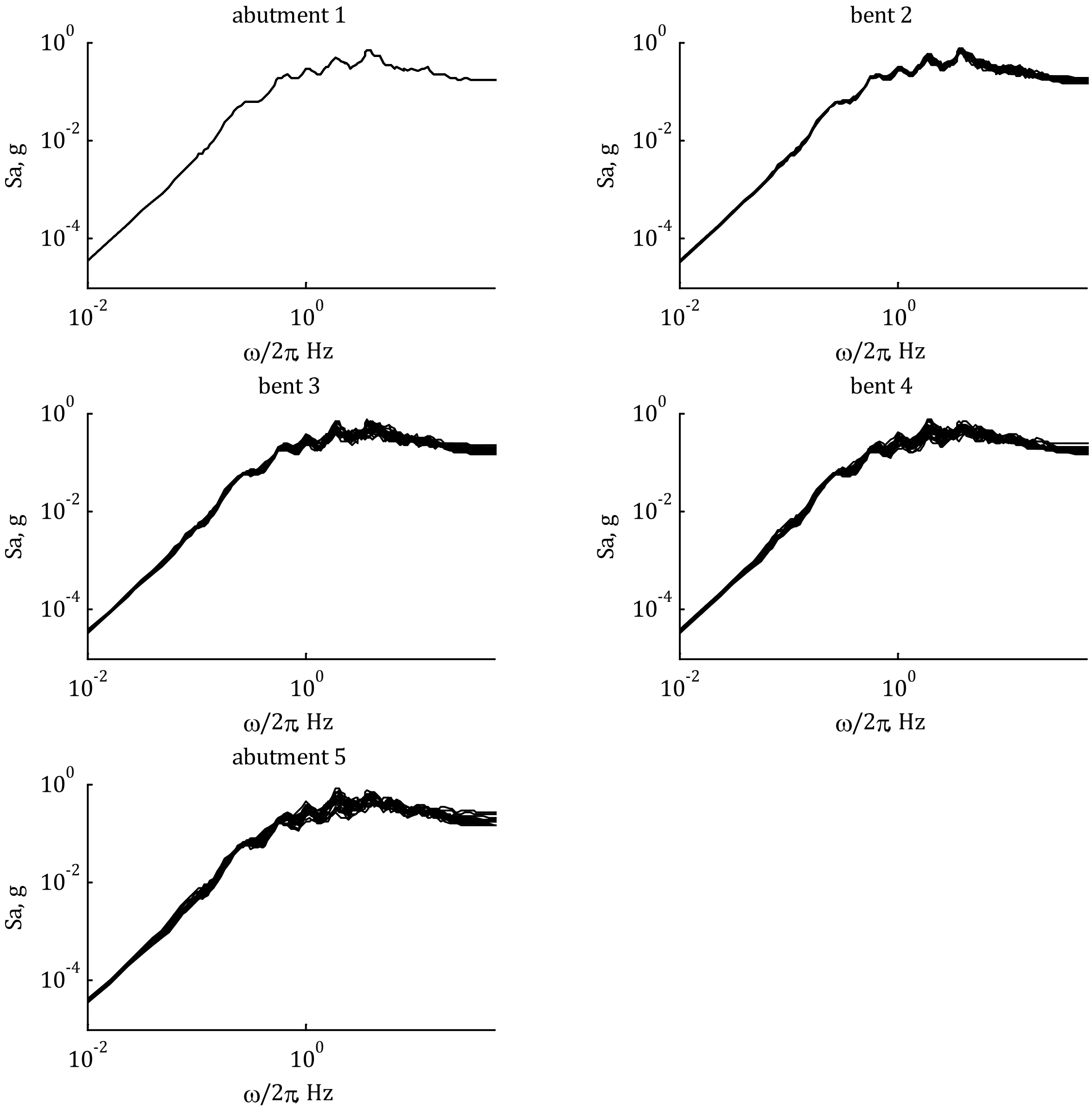

Figure 4.13: Acceleration response spectra of 20 conditioned simulations without initial filtering (uniform soil conditions).

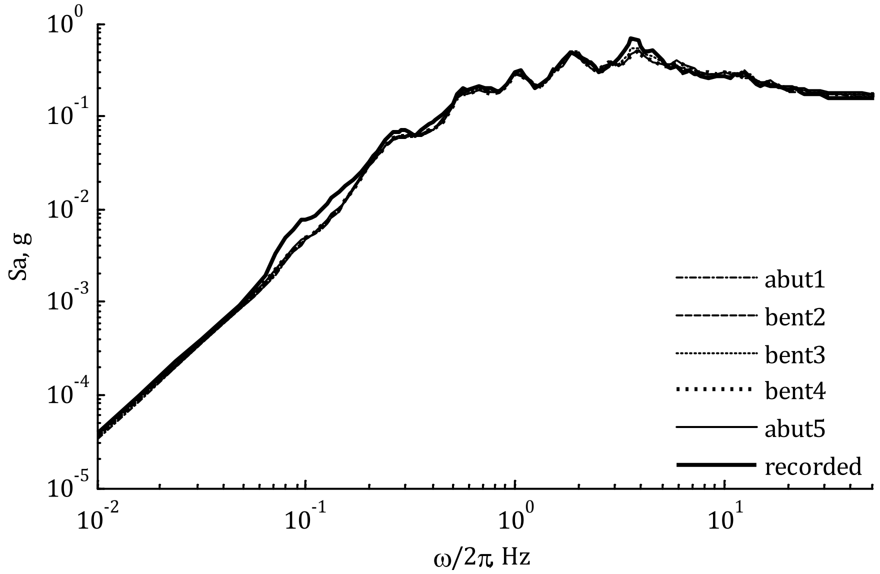

Figure 4.14: Median acceleration response spectra of 20 conditioned simulations without initial filtering (uniform soil conditions).

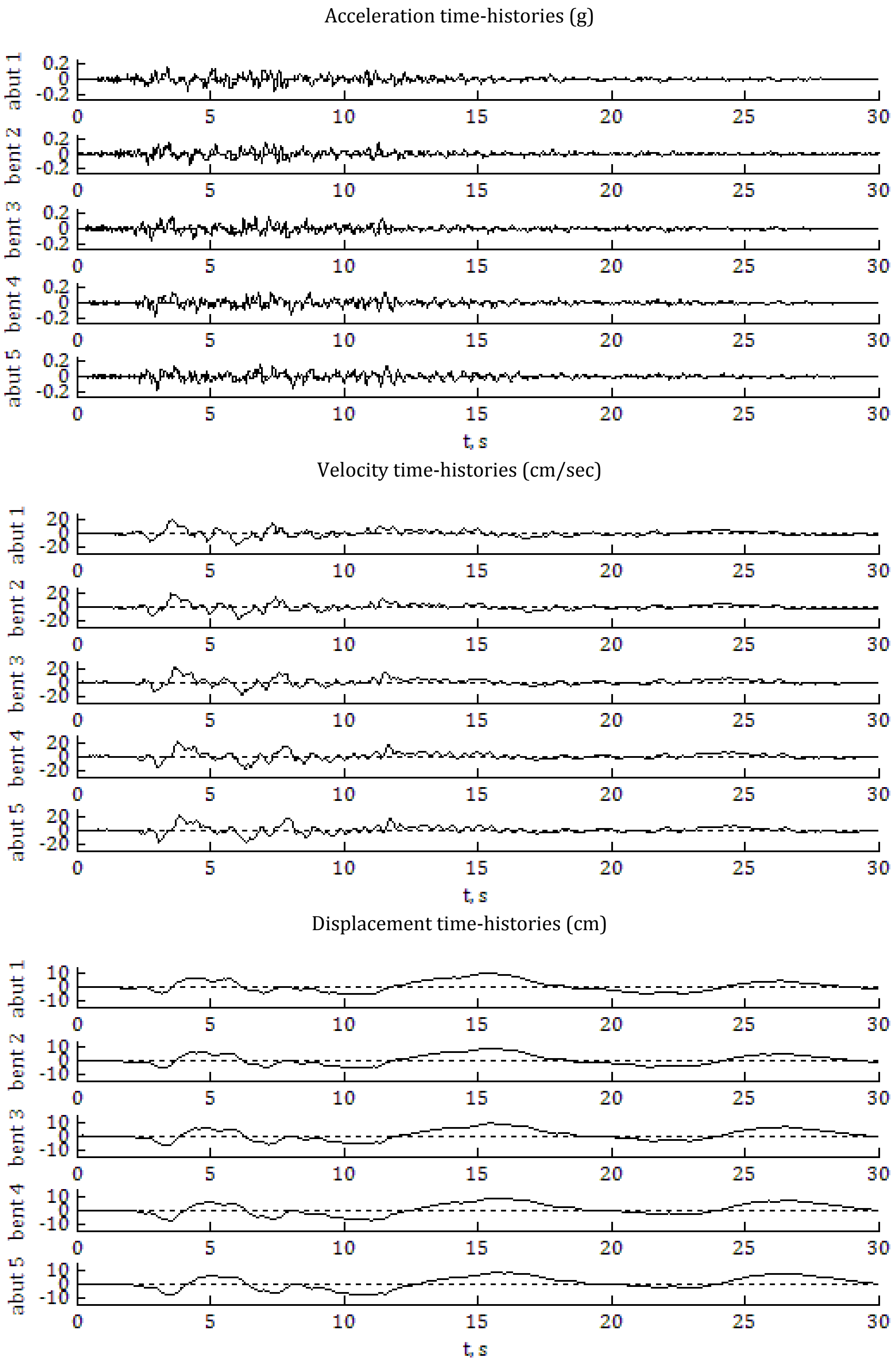

Figure 4.15: Example set of conditioned simulations with initial Butterworth filtering (uniform soil conditions).

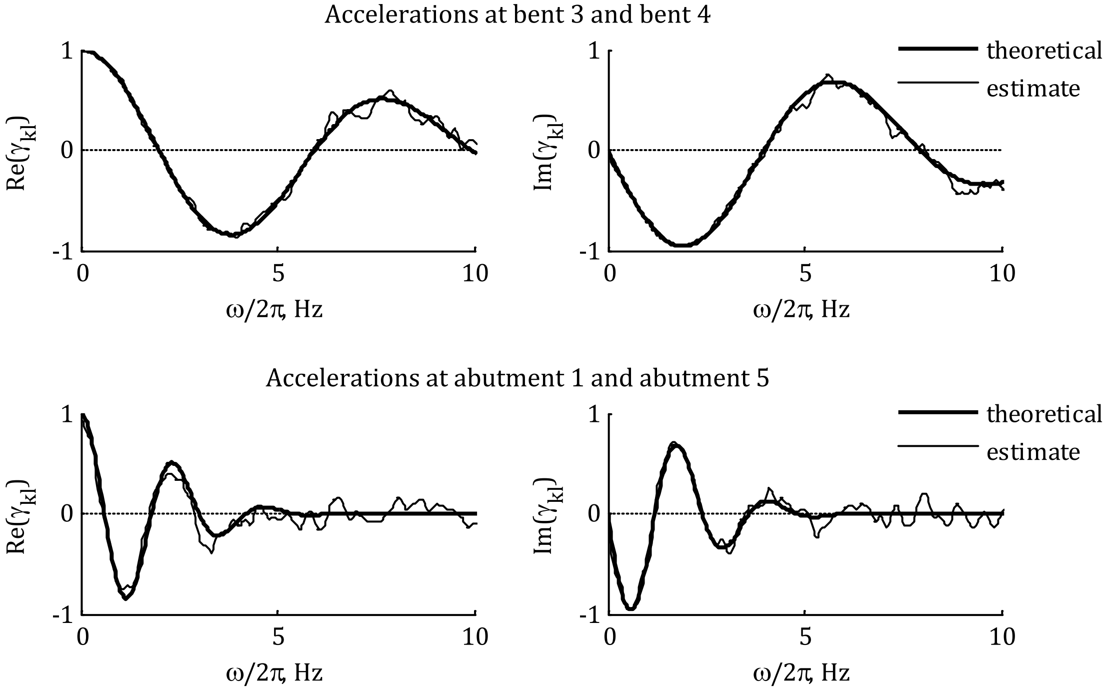

Figure 4.16: Acceleration coherency estimates from 20 conditioned simulations with initial Butterworth filtering (uniform soil conditions).

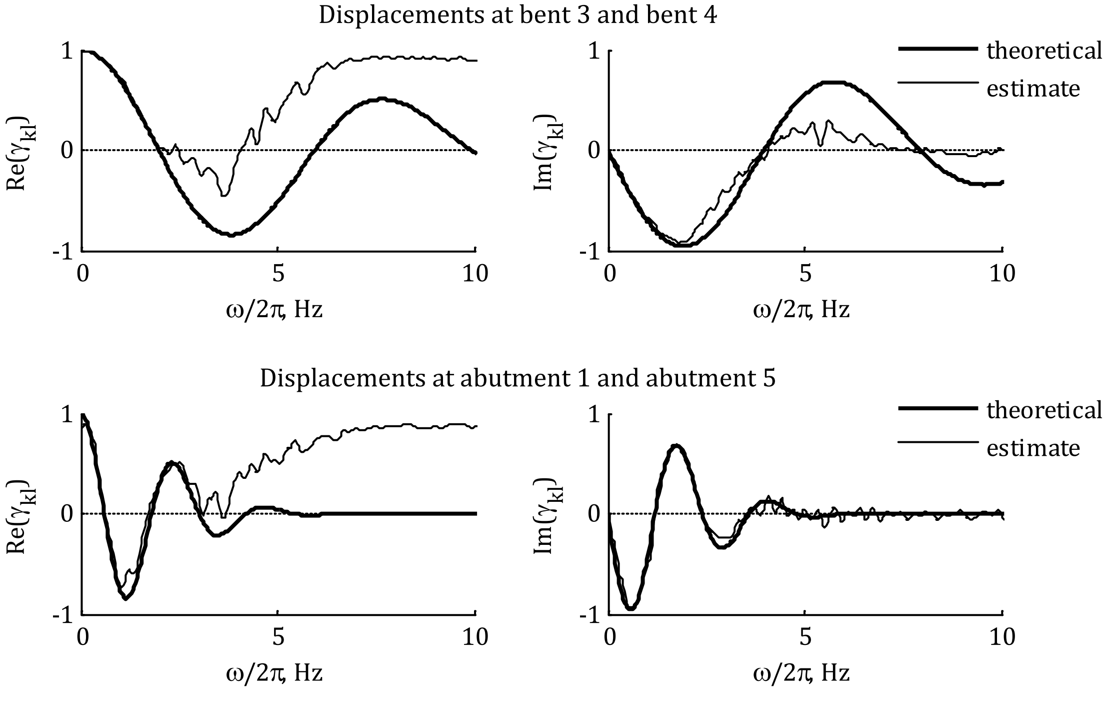

Figure 4.17: Displacement coherency estimates from 20 conditioned simulations with initial Butterworth filtering (uniform soil conditions).

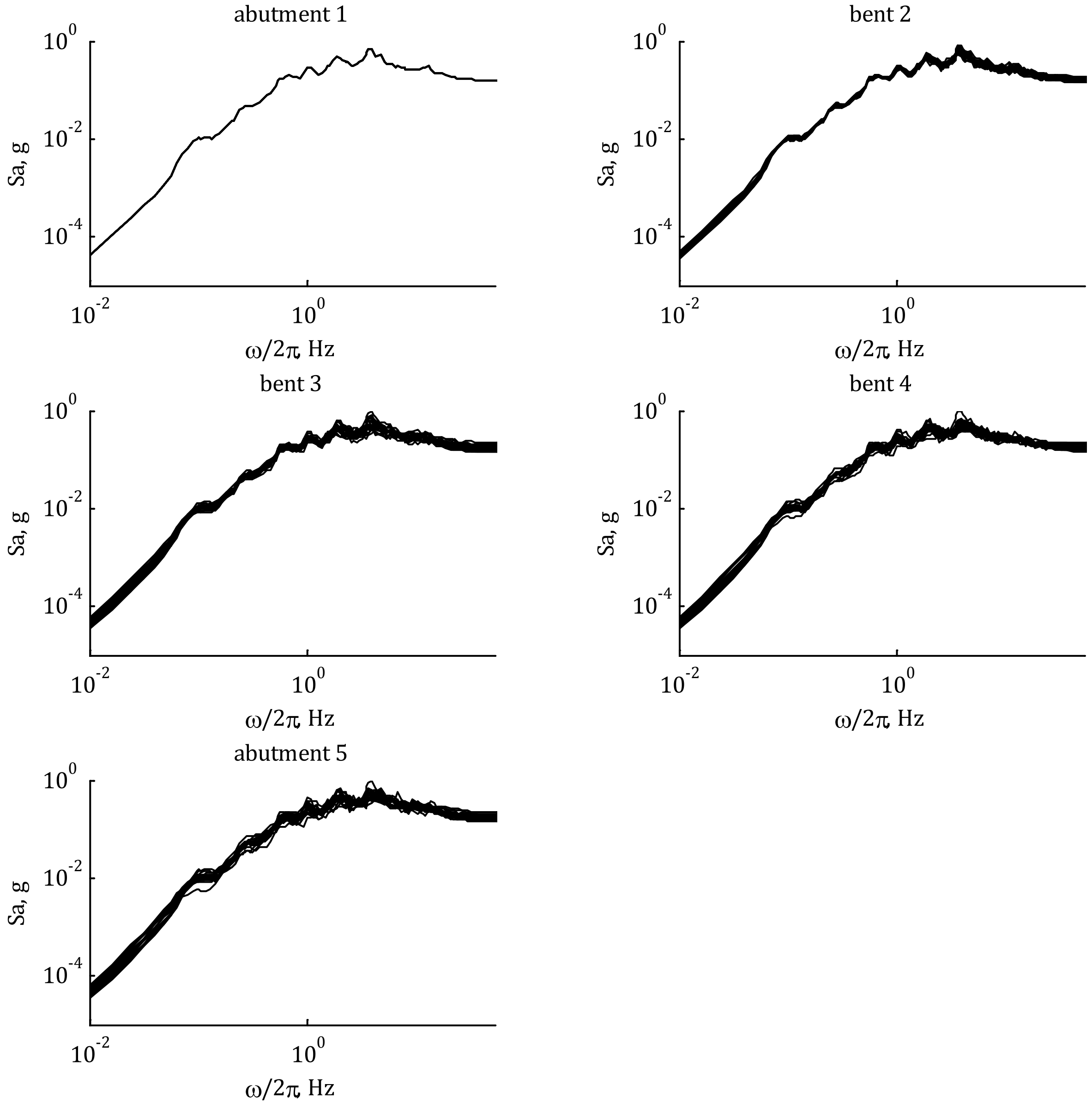

Figure 4.18: Acceleration response spectra of 20 conditioned simulations with initial Butterworth filtering (uniform soil conditions).

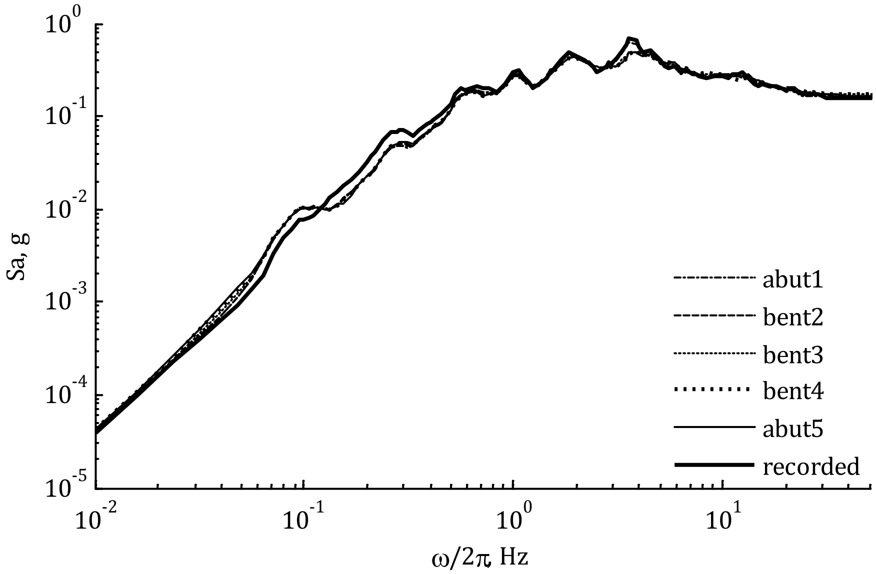

Figure 4.19: Median acceleration response spectra of 20 conditioned simulations with initial Butterworth filtering (uniform soil conditions).

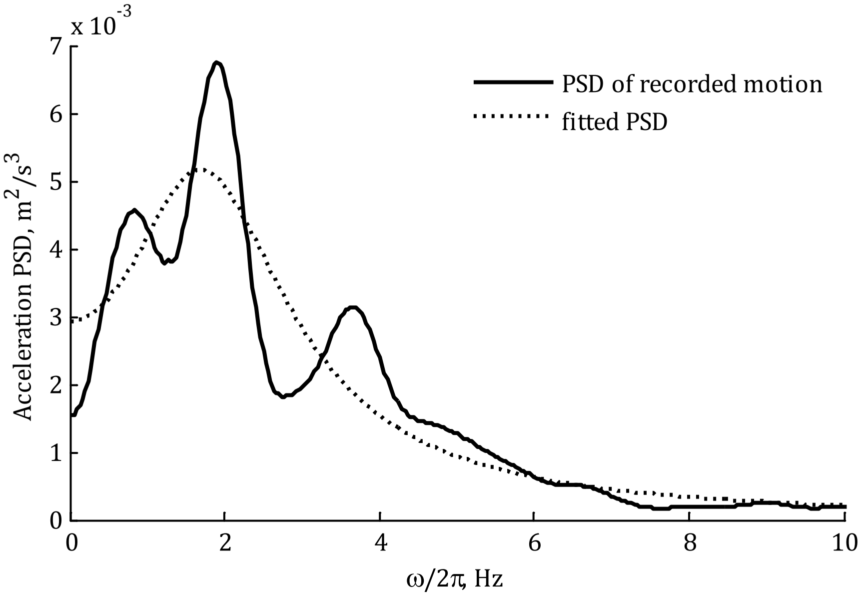

Figure 4.20: Comparison of the PSD of the recorded motion and the fitted theoretical model under the SDOF idealization.

Acceleration time-histories (g)

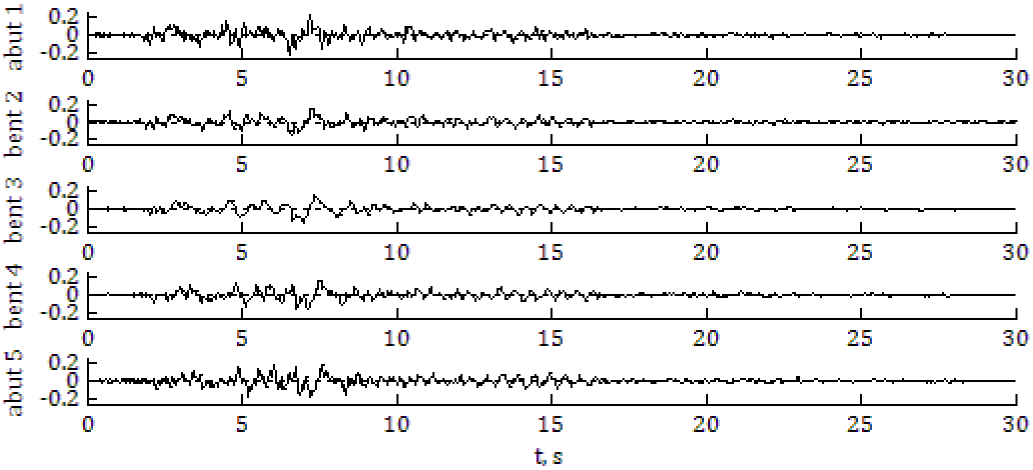

Velocity time-histories (cm/sec)

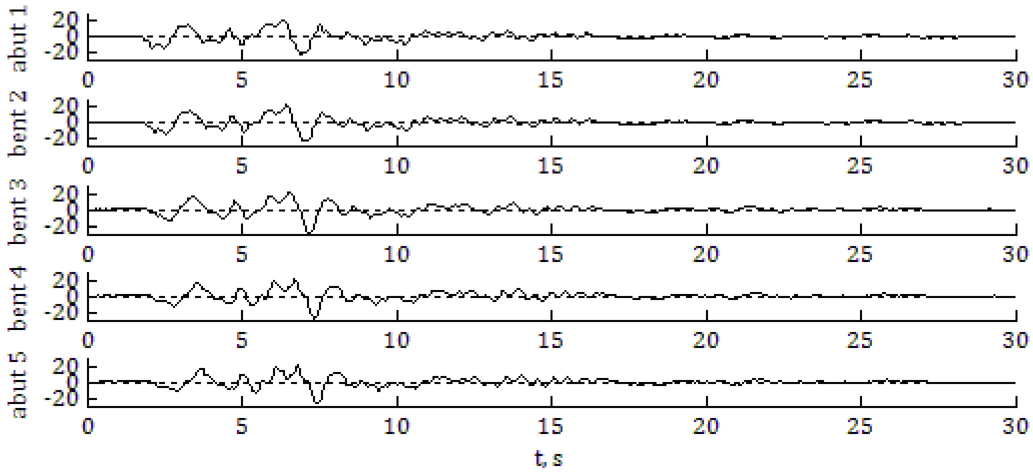

Displacement time-histories (cm)

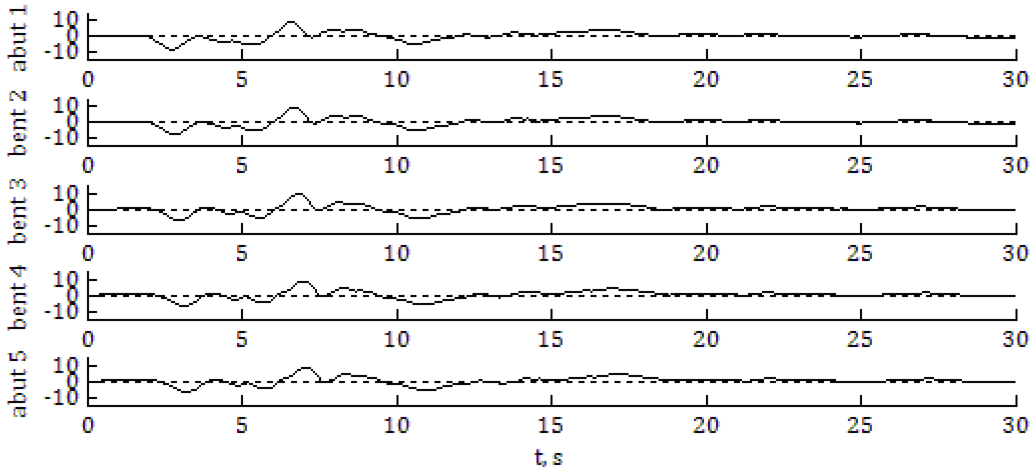

Figure 4.21: Example set of unconditioned simulations (varying soil conditions: SDOF model).

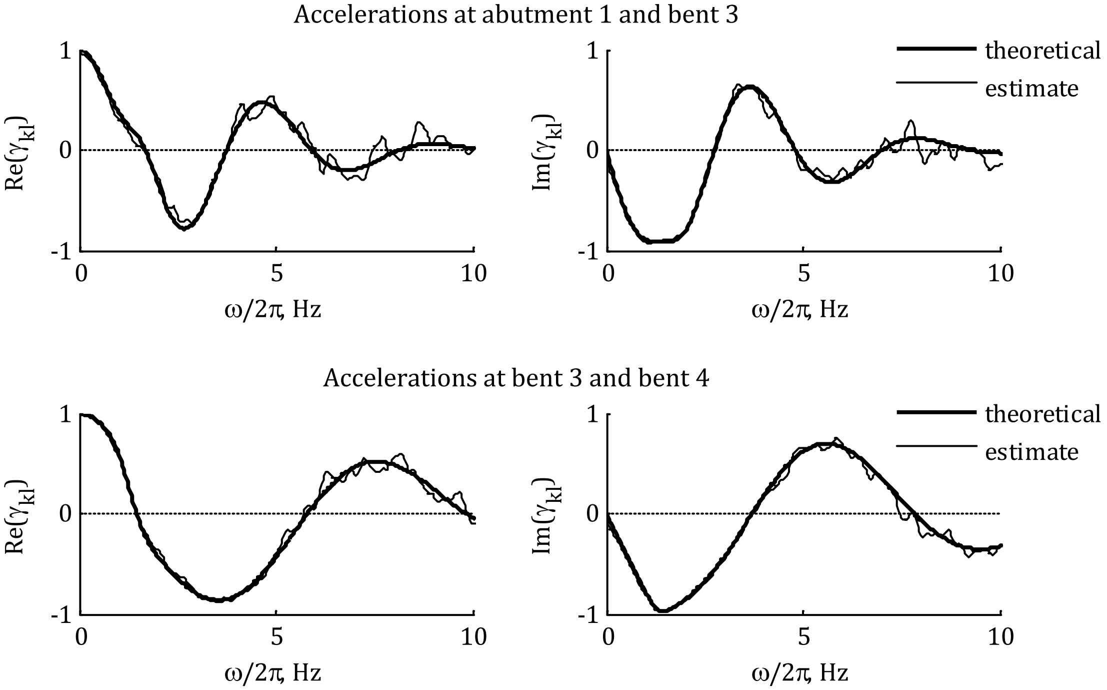

Figure 4.22: Acceleration coherency estimates from 20 unconditioned simulations (varying soil conditions: SDOF model).

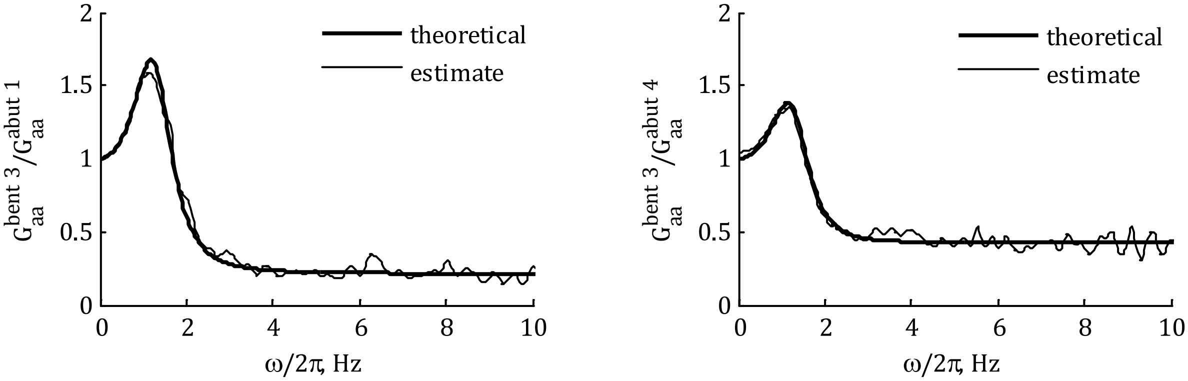

Figure 4.23: Ratios of estimated acceleration auto-PSDs from 20 unconditioned simulations (varying soil conditions: SDOF model).

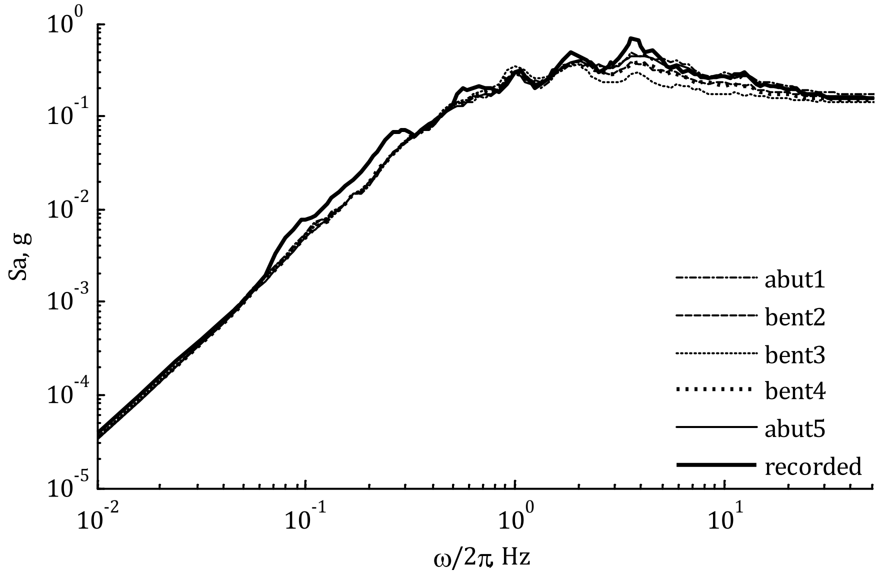

Figure 4.24: Median acceleration response spectra of 20 unconditioned simulations (varying soil conditions: SDOF model).

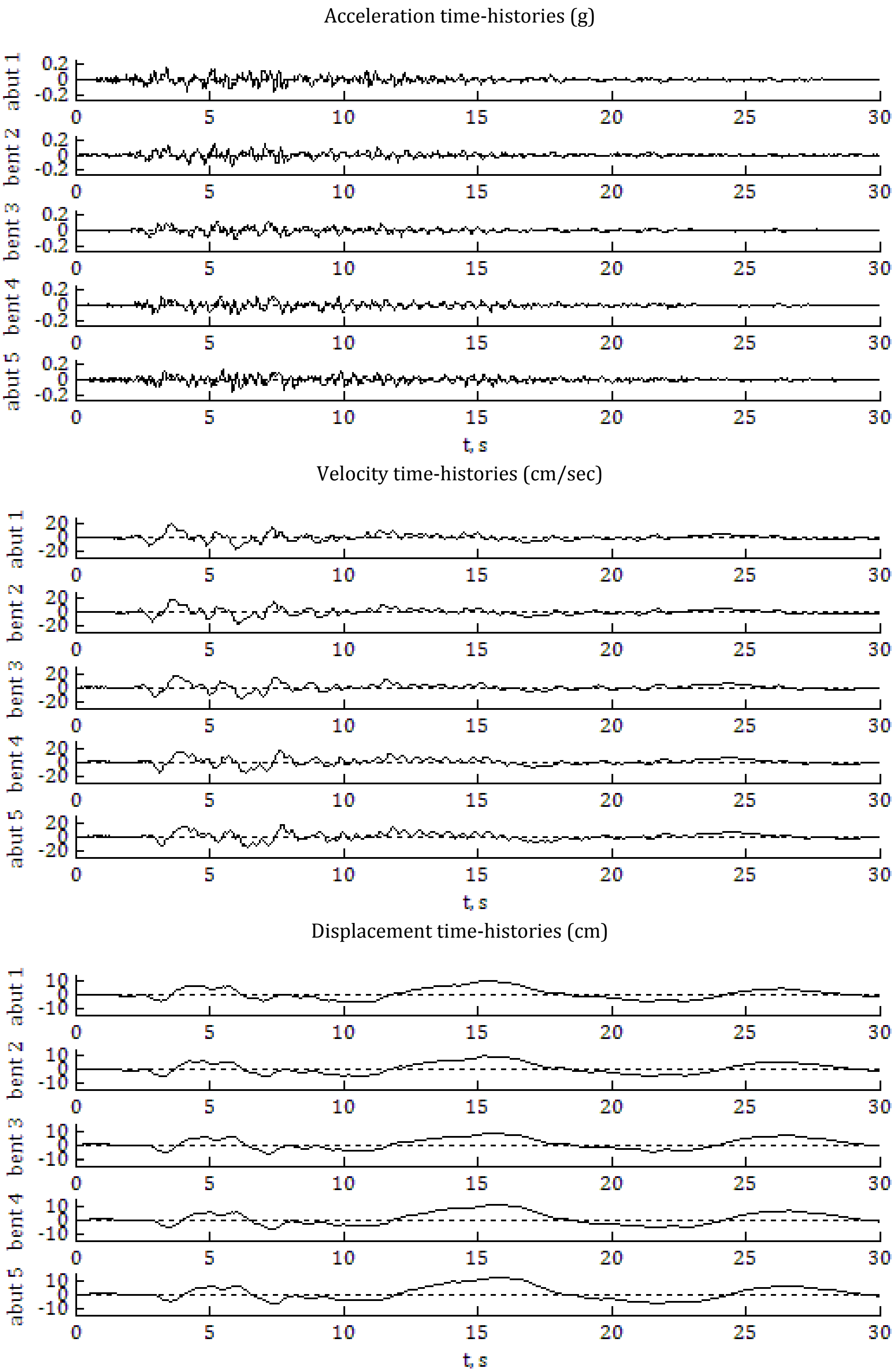

Figure 4.25: Example set of conditioned simulations with initial Butterworth filtering (varying soil conditions: SDOF model, only wave passage accounted for in low-frequency component).

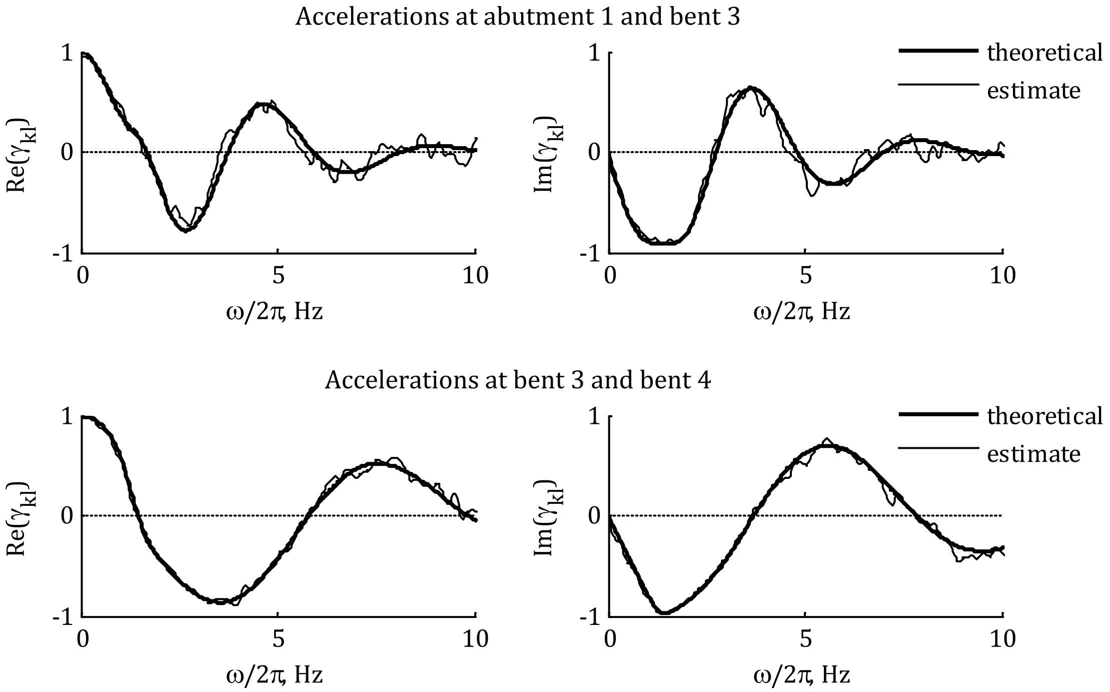

Figure 4.26: Acceleration coherency estimates from 20 conditioned simulations with initial Butterworth filtering (varying soil conditions: SDOF model, only wave passage accounted for in low-frequency component).

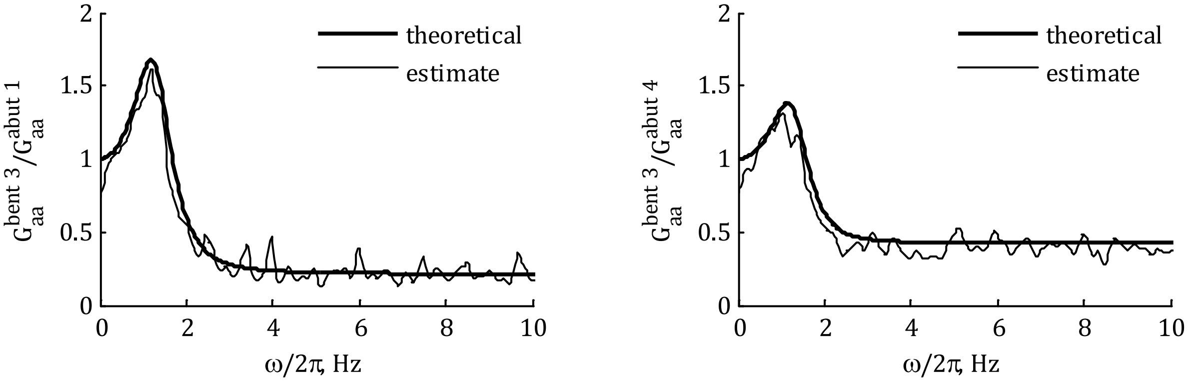

Figure 4.27: Ratios of estimated acceleration auto-PSDs from 20 conditioned simulations with initial Butterworth filtering (varying soil conditions: SDOF model, only wave passage accounted for in low-frequency component).

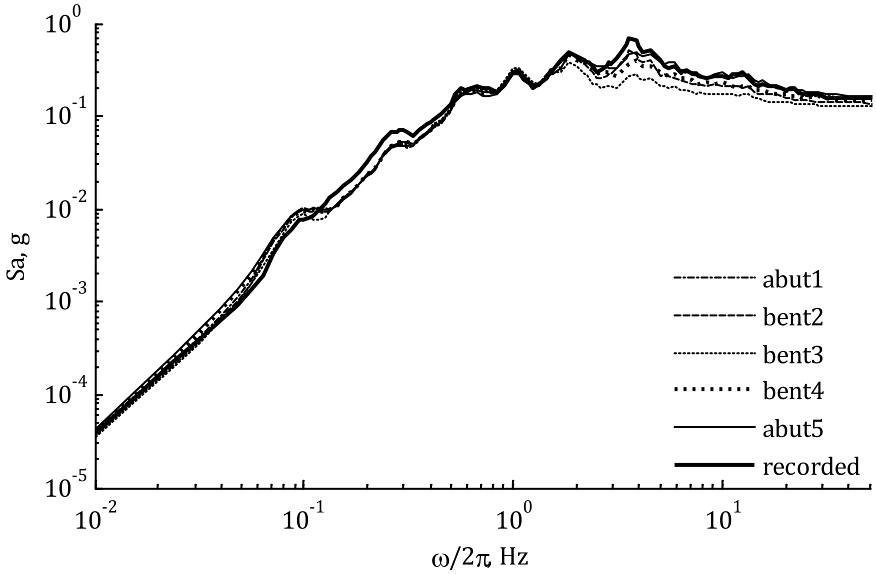

Figure 4.28: Median acceleration response spectra of 20 conditioned simulations with initial Butterworth filtering (varying soil conditions: SDOF model, only wave passage accounted for in low-frequency component).

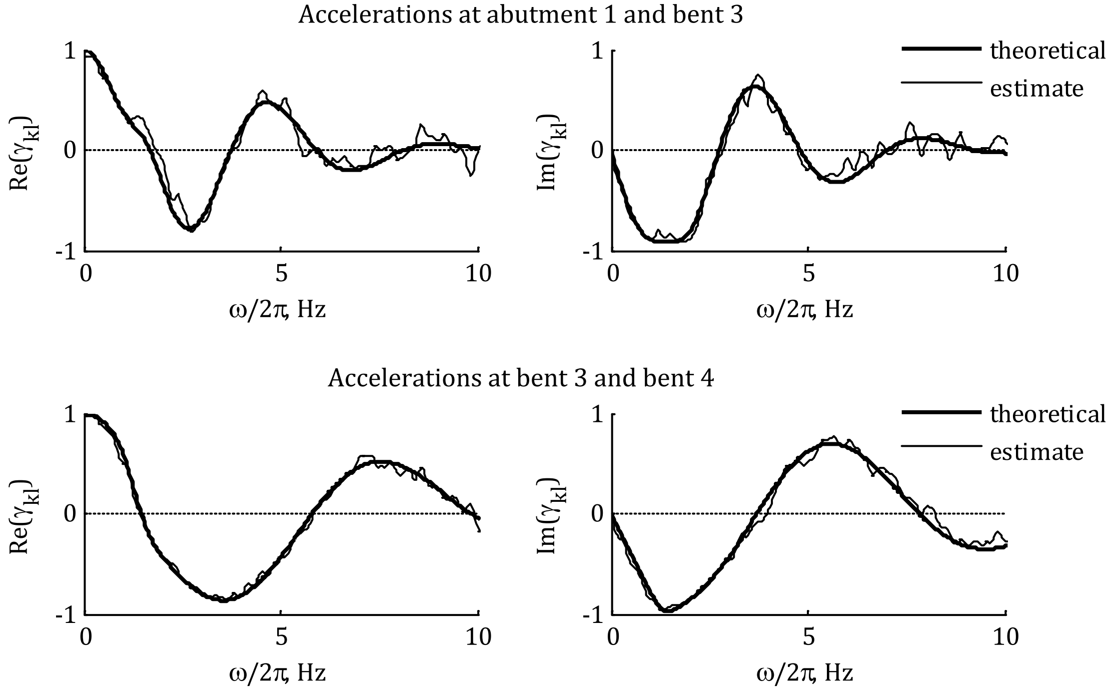

Figure 4.29: Acceleration coherency estimates from 20 conditioned simulations with initial Butterworth filtering (varying soil conditions: SDOF model, wave passage and site effect accounted for in low-frequency component).

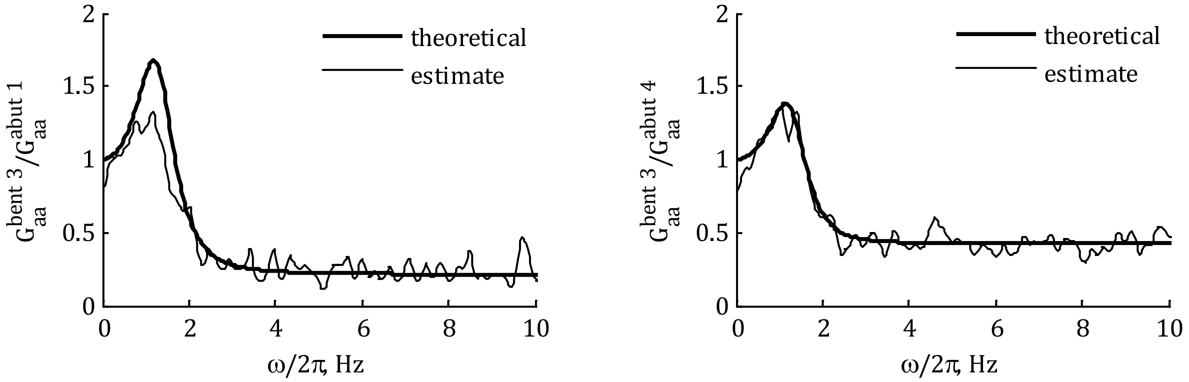

Figure 4.30: Ratios of estimated acceleration auto-PSDs from 20 simulations with initial Butterworth filtering (varying soil conditions: SDOF oscillator model, wave-passage and site effect accounted for in low-frequency component).

Acceleration time-histories (g)

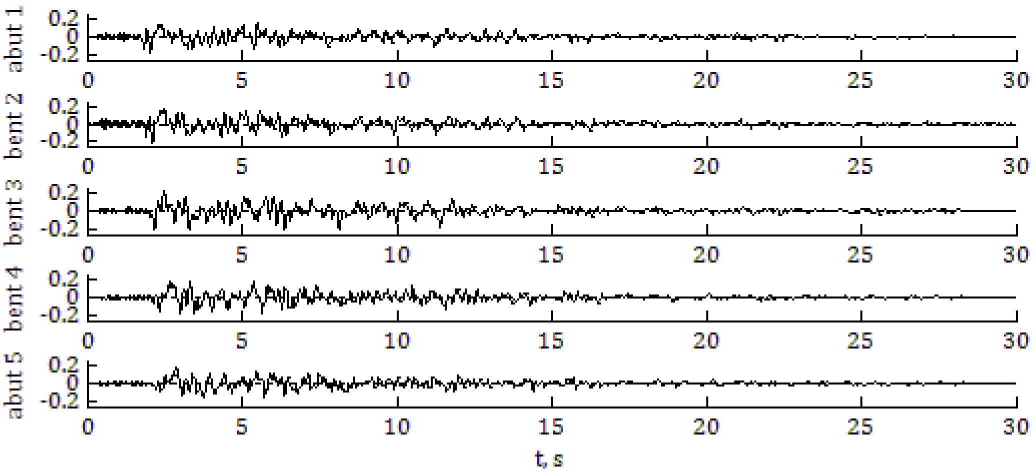

Velocity time-histories (cm/sec)

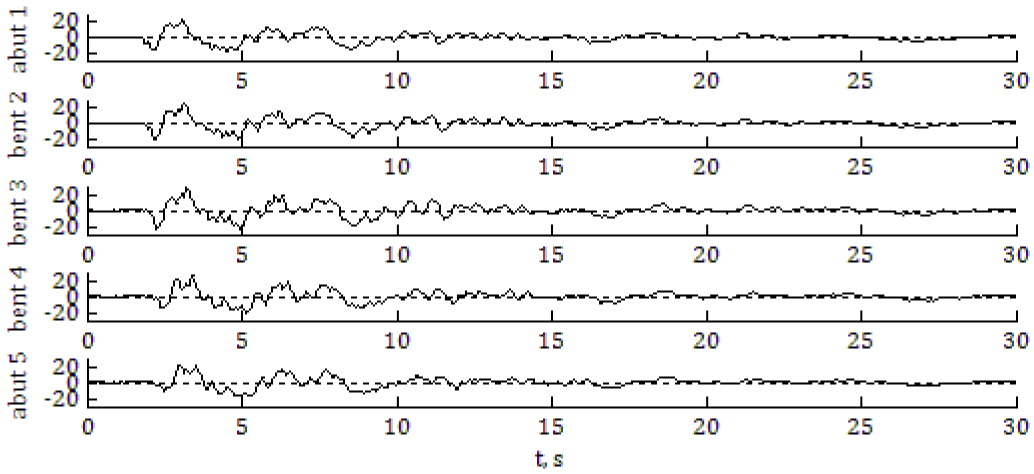

Displacement time-histories (cm)

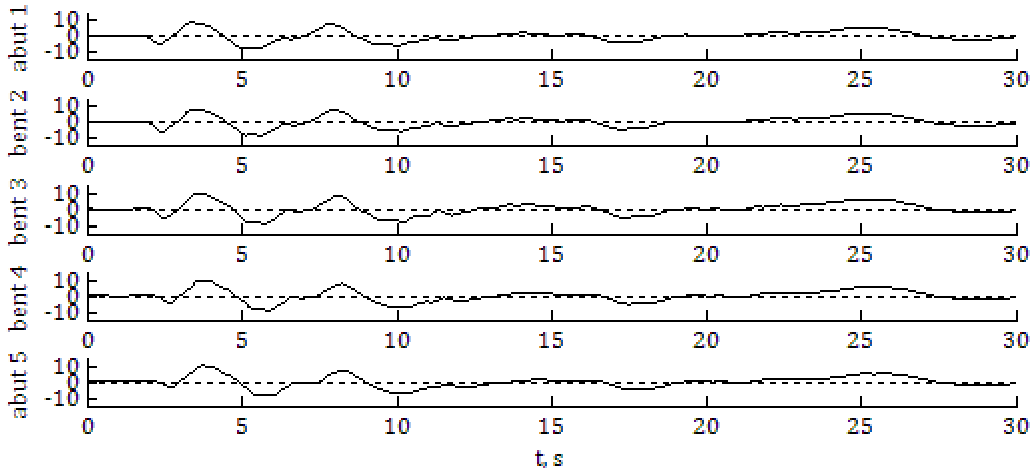

Figure 4.31: Example set of unconditioned simulations (varying soil conditions: elastic-medium model).

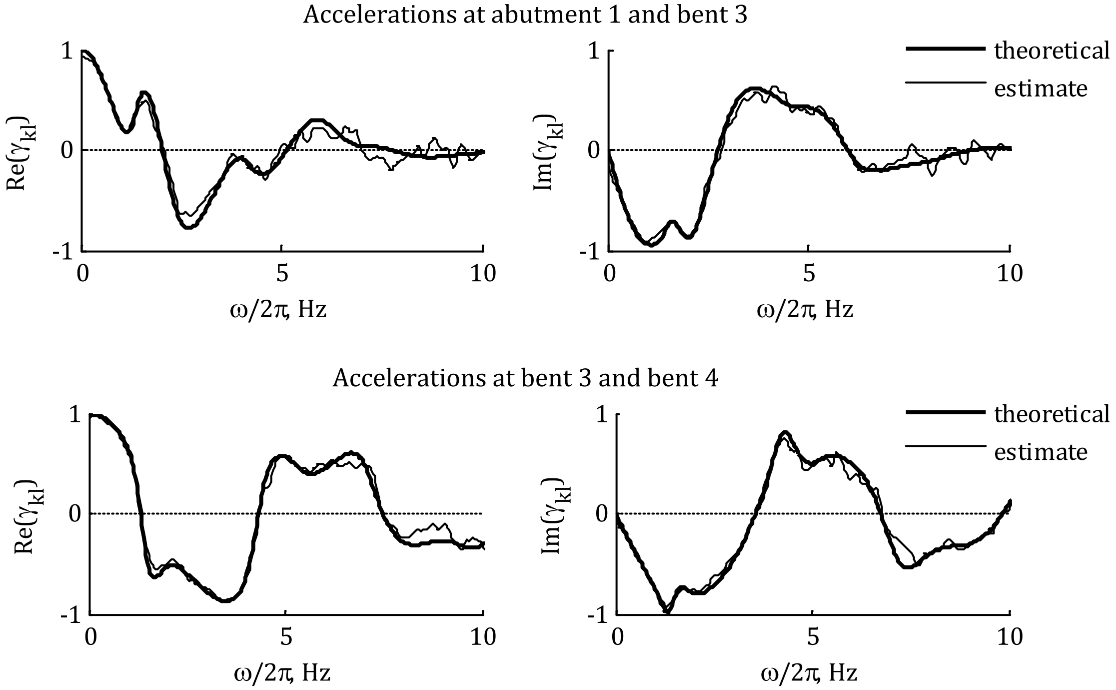

Figure 4.32: Acceleration coherency estimates from 20 unconditioned simulations (varying soil conditions: elastic-medium model).

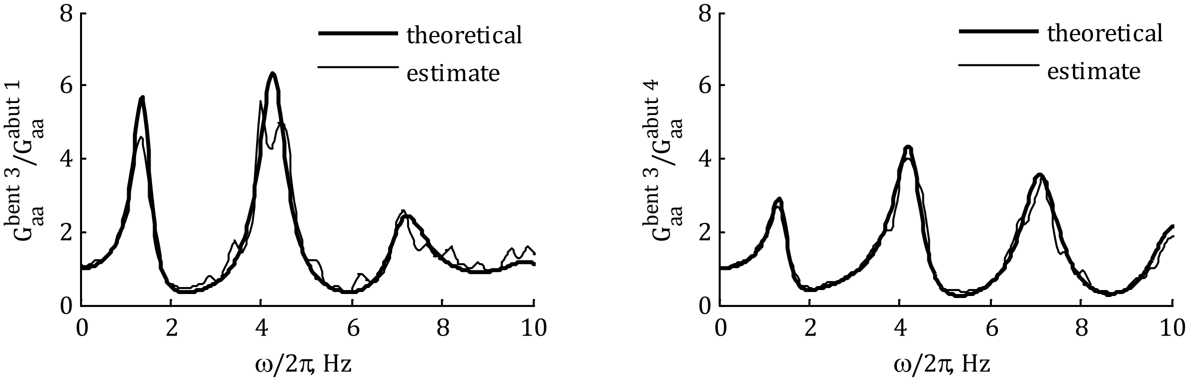

Figure 4.33: Ratios of estimated acceleration auto-PSDs from 20 unconditioned simulations (varying soil conditions: elastic-medium model).

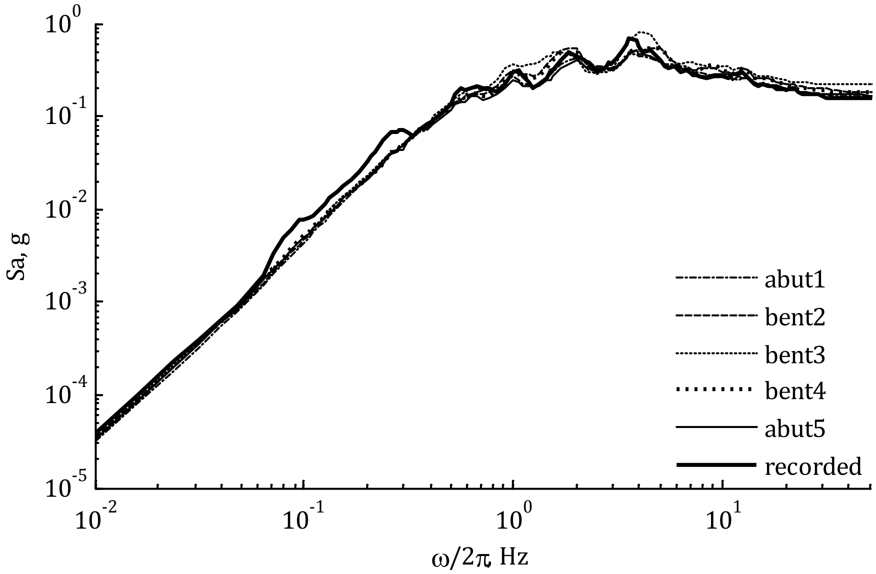

Figure 4.34: Median acceleration response spectra of 20 unconditioned simulations (varying soil conditions: elastic-medium model).

Acceleration time-histories (g)

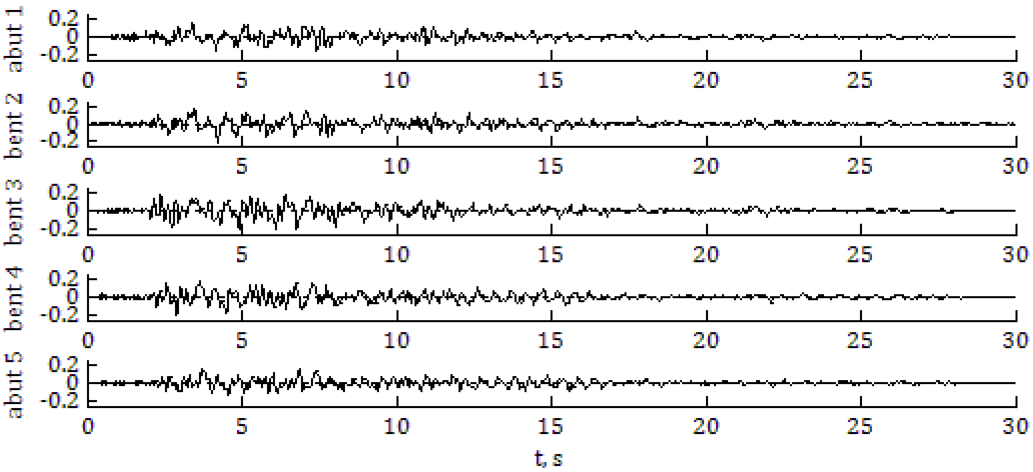

Velocity time-histories (cm/sec)

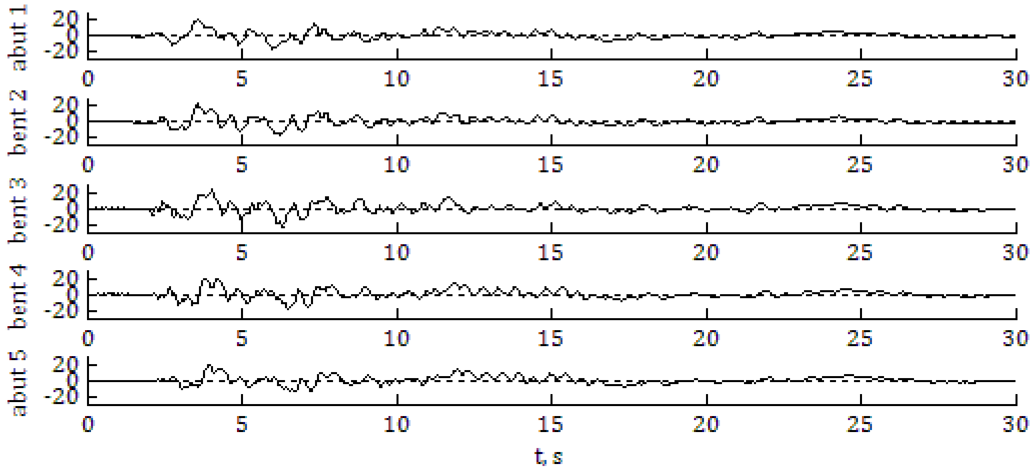

Displacement time-histories (cm)

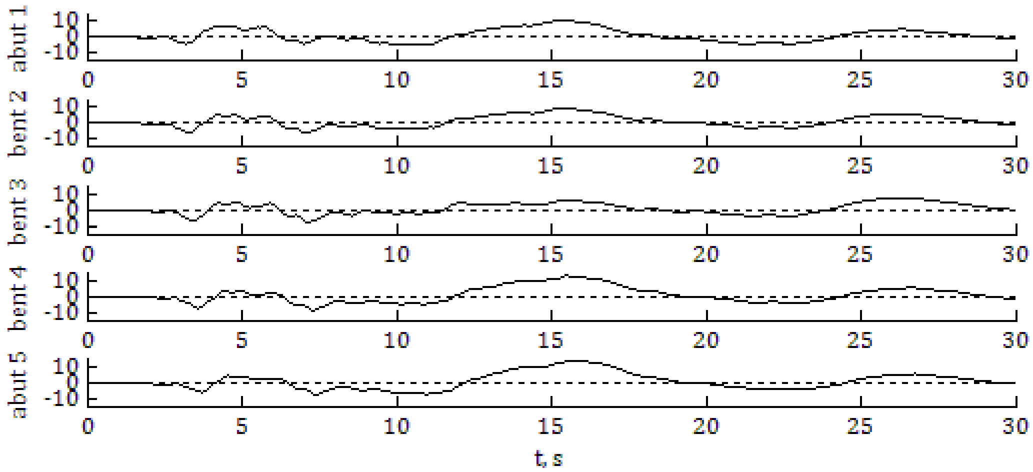

Figure 4.35: Example set of conditioned simulations with initial Butterworth filtering (varying soil conditions: elastic-medium model, only wave passage accounted for in low-frequency component).

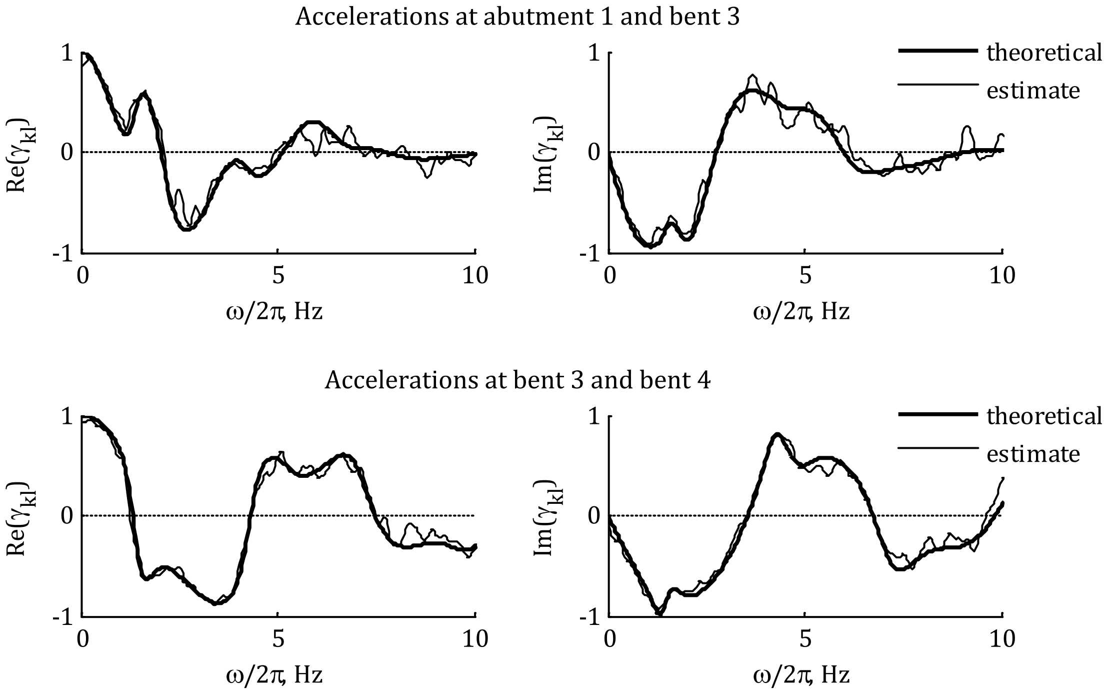
Accelerations at abutment 1 and bent 3

Accelerations at bent 3 and bent 4

Figure 4.36: Acceleration coherency estimates from 20 conditioned simulations with initial Butterworth filtering (varying soil conditions, elastic-medium model, only wave passage accounted for in low-frequency component).

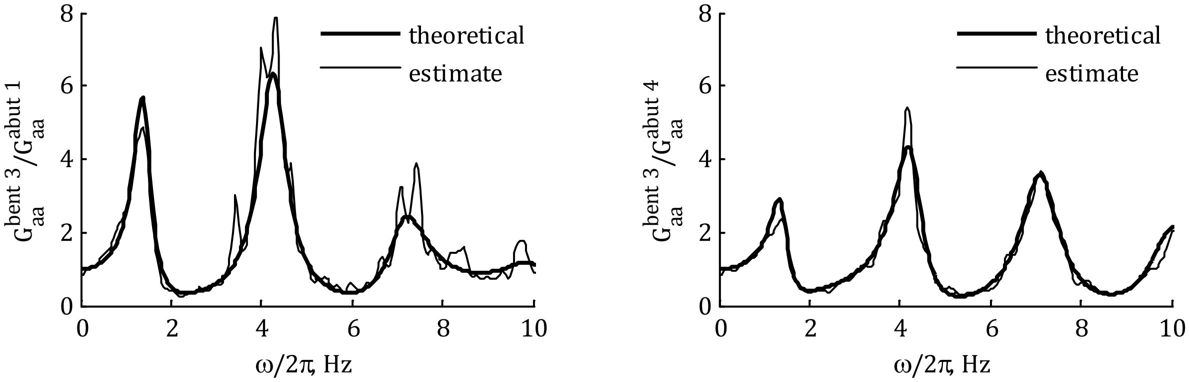

Figure 4.37: Ratios of estimated acceleration auto-PSDs from 20 conditioned simulations with initial Butterworth filtering (varying soil conditions, elastic-medium model, only wave passage accounted for in low-frequency component).

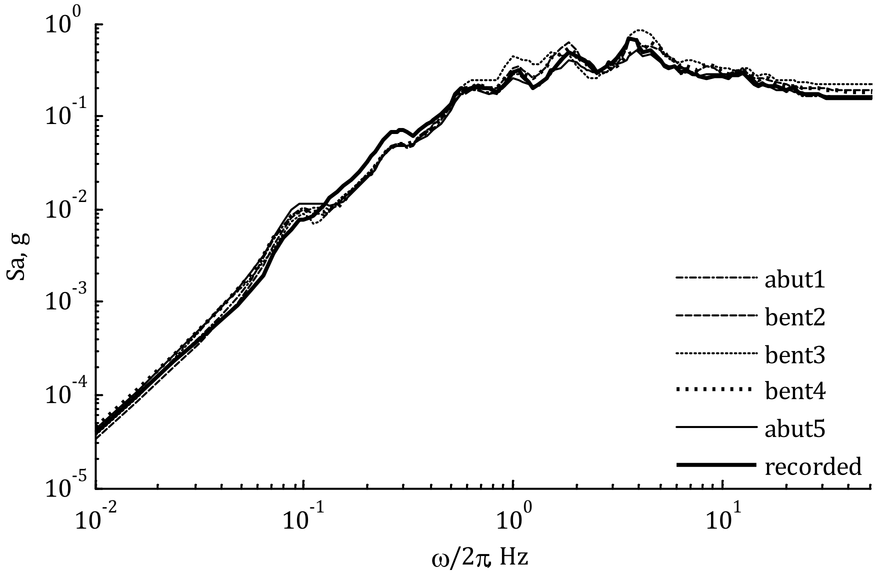

Figure 4.38: Median acceleration response spectra of 20 conditioned simulations with initial Butterworth filtering (varying soil conditions, elastic-medium model, only wave passage accounted for in the low-frequency component).

Chapter 5 - Linear and non-linear time-history analysis using simulated differential support motions and comparison with MSRS estimates

5.1 INTRODUCTION

In Chapter 3, we used the MSRS method to investigate the effect of spatial variability of ground motions on the mean peak linear responses of four real bridge models with vastly different structural characteristics. In this chapter, we investigate responses of the same bridge models under differential support motions using time-history analysis methods. Specifically, we perform linear and non-linear response history analyses (RHA) to evaluate the mean peak responses to ensembles of support motion arrays generated with the unconditioned simulation method described in Chapter 4. The responses examined are pier drifts, which are quantities particularly important in bridge design. We investigate the effect of ground motion spatial variability on the mean peak linear and non-linear drifts, and also on the ratios of non-linear over linear drifts. According to the "equal displacement" rule, for sufficiently flexible systems, these ratios are expected to be close to unity. This rule is commonly used in practice to evaluate the non-linear drift demand from linear analyses. Another objective of this chapter is to assess the accuracy of the MSRS method by comparing mean peak linear responses obtained from RHA with corresponding MSRS estimates.

5.2 DESCRIPTION OF BRIDGE MODELS

In Chapter 3 (Section 3.2), we described the linear models used in MSRS analysis of the four bridges, namely the Auburn Ravine Bridge, the Big Rock Wash Bridge, the South Ingram Slough Bridge, and the Penstock Bridge. In these models, both the piers and the deck were modeled using linear elastic elements. For the piers, we used effective stiffness properties determined through moment-curvature analyses and consistent with the Caltrans specifications (Caltrans SDC, 2004). The same models are used in the linear RHA in this chapter. The models used in the non-linear RHA differ from the corresponding linear ones only in the modeling of the piers.

Similar to the linear models, in the non-linear finite-element models we use three elements along each bridge pier. The elements are force-based with distributed plasticity. For the piers of the Penstock Bridge and the South Ingram Slough Bridge, we define 5 integration points for each element (i.e., a total of 15 integration points along each pier), whereas for the shorter piers of the Big Rock Wash Bridge and the Auburn Ravine Bridge we define 3 integration points for each element (i.e., a total of 9 integration points along pier). For all four bridges, the pier elements are modeled as having fiber sections with 12 subdivisions in the circumferential direction and 8 and 4 subdivisions in the radial direction for the core and the cover, respectively. The reinforcing steel bars are specified as additional layers. The properties of the unconfined concrete and the reinforcing steel are selected as the expected material properties defined in Caltrans SDC, whereas the properties of the confined concrete are determined according to Mander's model (Mander et al., 1988). See Section 3.2 in Chapter 3 for information on the steel reinforcement and the type of material in the piers of each bridge. The fiber model of the pier section accounts for interaction between axial force and bending moment. The shear and torsional behaviors are described by aggregated uniaxial models (OpenSees manual, accessed in April 2011). The yield force for the shear model is determined from Caltrans specifications, whereas the yield force for the torsional model is evaluated according to the theory of strength of materials (e.g. Hjelmstad, 2005) .

Pier ductility

Ductility characterizes the ability of structural components to undergo several cycles of inelastic deformation without significant degradation of strength or stiffness. The ductility capacity of structural elements is quantified through the ductility factor, defined as the ratio of maximum deformation (e.g. strain, displacement, rotation, curvature) over the deformation at yield.

The notion of ductility is fundamental in the displacement-based design, which focuses on evaluating the displacement demands imposed by the earthquake excitation. In Caltrans design, of main interest is the displacement ductility capacity of bridge piers. In this study, we evaluate the displacement ductility ratios of the bridge piers as the ratios of maximum pier drifts obtained from non-linear time-history analysis over pier drifts at yield. Following Caltrans' specifications, the yield drifts are obtained by double integration of the curvature along the pier height, assuming that the section with the largest curvature (i.e., with the largest bending moment) has just yielded. The yield curvature is determined from moment-curvature analysis at the section level. However, determining the yield point in a moment-curvature relationship involves some subjectivity. Furthermore, the yield drift evaluated by exact integration over the pier height may differ slightly from the yield drift evaluated with the numerical integration method used in the non-linear analysis. Thus, in determining the yield curvature, we check to make sure that displacement ductility factors close to 1.0 correspond to similar values of the strain ductility factors for the most critical fiber. For the bridges examined in this study, all piers of the bridge have identical diameter and reinforcement and thus, identical yield curvature. For each bridge, the yield curvature and the corresponding yield displacements of the piers are listed in Table 5.1-Table 5.4.

Damping

In the RHA analysis, we use Rayleigh damping with the parameters adjusted so that the damping ratios of the lower modes are close to 5%. The corresponding damping values for the first three modes of each bridge are listed in Table 5.5.

5.3 GROUND MOTION INPUT

The support excitations used for the subsequent time-history analyses are synthetic ground motions generated with the unconditioned simulation method (non-stationary case) described in Section 4.5.1. As we pointed out in Chapter 4, the arrays of motions generated with this method exhibit similar variability at all support points and, thus, are appropriate as input in statistical analyses of bridge response. This simulation method requires specification of a seed accelerogram, a coherency function that describes the spatial variability of the ground motion random field, and in the case of varying soil conditions, additionally, the FRFs of the soil columns underneath the supports. In this section, we simulate ensembles of ground motion arrays for the four bridge models considering two seed accelerograms and several cases of spatial variability, as described next.

The two seed accelerograms are the fault-normal components of the Hollister South & Pine (HSP) record from the 1989 Loma Prieta earthquake and the Pacoima Dam (PUL) record from the 1971 San Fernando earthquake. Figure 5.1 and Figure 5.2 show the corresponding acceleration time histories and the evolving integral measures of the variance, the predominant frequency and the bandwidth, denoted p_1, p_2 and p_3, respectively (see Section 4.5 for more details). The vertical dashed lines demarcate the nearly stationary segments of the accelerograms.

To model the ground motion spatial variability, we use the coherency function in Eqn. (2.18) with its components given by Eqns. (2.19)-(2.21) in Chapter 2. To describe variations in the soil conditions, we employ the SDOF idealization of the soil-columns and use the FRF in Eqn. (2.23). In all cases, we assume waves propagate in the direction from abutment 1 to the abutment at the other end of the deck. We consider four cases of spatial variability as listed in Table 5.6: Case 1 is uniform support excitations. Cases 2 and 3 include the effects of incoherence and wave passage and represent two different levels of incoherence. Case 4 is case 2 plus spatially varying site effects. In all cases, the values of the shear wave velocity and the apparent wave velocity are taken to be $v_s = 600$ m/s and $v_{app} = 400$ m/s, respectively. The same values of v_s and v_{app} were used in the parametric analyses in Chapter 3. However, the values of the incoherence parameter considered here ($\alpha = 0.2, 0.4$) are smaller than the value used in Chapter 3 ($\alpha = 1$). Smaller values of the incoherence parameter represent a slower decay of the incoherence component, i.e. more coherent motions. Analyses of recorded arrays of motions (e.g. Harichandran and Vanmarcke, 1986;, Abrahamson et al., 1991) have shown that the rate of decay of the incoherence component can vary significantly between different arrays. (See Chapter 6 for more details on this subject.)

For the Penstock Bridge, the support excitations in case 1 are the ground motion at bent 3 for case 2. For the South Ingram Slough Bridge, the support excitations in case 1 are the ground motion at bent 2 for case 2. For the Big Rock Wash Bridge, the support excitations in case 1 are the ground motion at bent 2 for case 2. For the Auburn Ravine Bridge, the support excitations in case 1 are the ground motion at bent 4 for case 2.

The case of varying soil conditions, i.e. case 4, is investigated only for the HSP record as seed. To determine the frequency and damping ratio of the FRF model idealizing the soil-column at the site of the record, we use the method described in Section 2.2.4 and employed in Section 4.6.2, i.e., we assume white-noise excitation at the bedrock level and fit the theoretical PSD of the acceleration at the ground surface to the smoothed periodogram of the record. Non-linear least-squares minimization with MATLAB gives $\omega_1/2\pi \approx 1.19$ Hz and $\zeta_1 \approx 0.6$, when the periodogram of the record is smoothed with a 101-point Hamming window. (For this specific accelerogram, the level of smoothing only slightly affects these least-squares estimates.) These values represent the characteristics of the soil at abutment 1. Comparison between the acceleration PSD estimate of the recorded motion and the fitted theoretical model is shown in Figure 5.3. For case 4, we consider three soil types with idealized SDOF frequencies and damping ratios as listed in Table 5.7. Soil type 1 represents the site of the record, as described above. For each bridge, the assumed variation of soil conditions in case 4 is given in Table 5.8.

We now present samples of simulated support motion arrays from the generated ensembles used in the subsequent time-history analyses. (In all simulations, we have used the non-smoothed periodograms and a corner frequency of $f_c = 0.15$ Hz for the post-processing filter.) Figure 5.4 shows a sample set of acceleration, velocity and displacement time histories simulated for the Penstock Bridge, using the PUL record as seed and for case 2 of spatial variability (only incoherence and wave-passage effects). For the same case of spatial variability but for the HSP record as seed, Figure 5.5 shows a sample set of acceleration, velocity and displacement time histories for the South Ingram Slough Bridge. Figure 5.6 shows similar time histories simulated for the Big Rock Wash Bridge, using the HSP record as seed and for case 4 of spatial variability (site effect in addition to incoherence and wave-passage effects). In this figure, we note the differences in the frequency contents of the motions at locations with different soil conditions. These differences are more apparent in the acceleration time histories, which are richer in high–frequency contents. Finally, Figure 5.7 shows a sample set of acceleration, velocity and displacement time-histories simulated for the Auburn Ravine Bridge, using the HSP record as seed and for case 3 of spatial variability (higher level of incoherence than in case 2 and wave-passage effect). We note that all velocity and displacement time-histories have zero or nearly-zero residual values after the high-pass filtering.

For each bridge and each case of ground motion spatial variability described above (see Table 5.6), we now validate the simulations of support motions by examining the corresponding response spectra and coherency estimates for samples of 20 simulated arrays. In Figure 5.8-Figure 5.11, we present the median 5% damped pseudo-acceleration response spectra. Each of these figures shows the median response spectra at each support of the relevant bridge and also, the response spectrum of the original seed record. The median spectra of the simulated motions are a smoother version of the spectrum of the corresponding recorded seed motion. Differences between the spectra of the simulated motions and the recorded motions also arise from the segmentation and post-processing of the simulation procedure. We note that the median response spectra at support points with similar soil conditions are nearly identical, i.e. spectra at all support points in Figure 5.8, Figure 5.9 and Figure 5.11, and spectra at abutments 1 and 4 in Figure 5.10. These observations indicate that the simulated motions are realistic. In Figure 5.12-Figure 5.15, we compare coherency estimates of the simulated support motions with the corresponding target models. One example support pair for each bridge model is examined. The real and imaginary parts of the coherency function are shown in the left and right charts, respectively. The figures demonstrate excellent agreement between the estimated and theoretical coherency, which further validates the simulations.

We note that for the Auburn Ravine Bridge, which has relatively short spans, the Cholesky decomposition of the correlation matrix (required in the simulation algorithm, see Section 4.4.1), was problematic for the lower frequencies at which the motions are nearly coherent. (MATLAB returned the message that the correlation matrix is not positive definite). To overcome this problem, which arises from numerical instability due to a near-singular covariance matrix at low frequencies, we considered the support motions perfectly coherent at the first 2 or 3 frequency points in each segment (depending on the case), and at these frequencies, we used the Fourier coefficients simulated at location $k = 1$ for all support points. As indicated by the coherency estimates in Figure 5.15, this approximation is justified. (Similar good agreement between the estimates and the target coherency model justified the approximation for other cases, not shown here.)

5.4 ANALYSIS OF BRGDE RESPONSE

In this section, we investigate the mean peak responses of the bridge models described in Section 5.2 to the ensembles of simulated support motions described in Section 5.3. Specifically, we consider cases 1-4 using the HSP record as seed and cases 1-2 using the PUL record as seed. For each case of spatial variability, each ensemble consists of 20 simulated support motion arrays. To achieve non-linear behavior, the motions simulated using the HSP record as seed are scaled with a factor of 1.5. (No scaling is applied to the motions simulated using the stronger PUL record as seed.) The support excitations are applied in the transverse direction. Software OpenSees is used to perform linear and non-linear RHA of the corresponding bridge models. The response quantities of interest are the transverse pier drifts. First, we investigate the effect of ground motion spatial variability on their mean peak values for both the linear and the non-linear models. Additionally, we examine how the ratios of non-linear over linear drifts vary for each bridge model and case of spatial variability. The latter analysis aims to assess the “equivalent displacement” rule, commonly used in engineering practice to approximately evaluate non-linear drifts from linear analysis for sufficiently flexible systems. Finally, we assess the accuracy of the MSRS rule by comparisons between the mean peak responses evaluated with the MSRS method and those obtained from linear RHA.

For each type of analysis, we present the results by ordering the bridges according to their fundamental periods. We start with the more flexible Penstock Bridge ($T = 2.38$ s), followed by the South Ingram Slough Bridge ($T = 1.24$ s), then the Big Rock Wash Bridge ($T = 0.61$ s) and, finally, the Auburn Ravine Bridge ($T = 0.59$ s). We note that for all bridge models, the first mode is largely transverse displacement.

5.4.1 Effect of ground motion spatial variability on peak linear and non-linear pier drifts

In this section, for each bridge model, we examine the effect of spatial variability on the peak linear and non-linear drifts and on the displacement ductilities of the piers. Drifts are specified as percent ratios of the pier heights. The displacement ductility is calculated as the ratio of the peak non-linear drift over the corresponding yield drift. The latter are listed in Table 5.1-Table 5.4.

First, we consider the Penstock Bridge. Table 5.9 and Table 5.10 list the means and standard deviations of the peak linear and non-linear pier drifts, respectively. Table 5.11 lists the means and standard deviations of the displacement ductilities. Let us first examine the results for the HSP record as seed. Comparing cases 2 and 3 with case 1, we note that the presence of wave passage and incoherence may increase or decrease pier drifts of the linear model, but tends to decrease pier drifts of the non-linear model. Comparing cases 2 and 3, increasing level of incoherence may increase or decrease pier drifts of the linear model, but increases all pier drifts of the non-linear model. When the site-effect is also included, i.e. in case 4, pier drifts are the largest among all cases for both the linear and the non-linear models. With the exception of pier 4 (the stiffest among the three piers) in case 1, non-linear drifts are smaller than the corresponding linear ones. For motions simulated using the PUL record as seed, trends are similar to those observed with the HSP record as seed in cases 1 and 2. Ductilities follow similar trends with non-linear drifts and their means are in the range 1.44-1.99 for the HSP record (cases 1-4) and in the range 1.39-1.81 for the PUL record (cases 1-2).

Next, we examine the South Ingram Slough Bridge. Table 5.12 and Table 5.13 list the means and standard deviations of peak linear and non-linear pier drifts, respectively. Table 5.14 lists the means and standard deviations of the displacement ductilities. First, we examine the results for the HSP record as seed. For both the linear and the non-linear models, mean peak drifts under spatially varying ground motions (cases 2, 3 and 4) are smaller than those under uniform support motions (case 1). For both models, increasing level of incoherence (compare cases 2 and 3) or the additional differential-site effect (compare cases 2 and 4) decrease pier drifts. In all cases, the mean peak non-linear response is slightly smaller than the linear response. Results for the PUL record follow similar trends as for the HSP record for the corresponding cases, but are slightly larger. We note that, overall, the effect of spatial variability on pier drifts of the South Ingram Slough Bridge is mild. Ductilities follow similar trends with non-linear drifts and their means are in the range 1.87-2.06 for the HSP record (cases 1-4) and in the range 2.43-2.56 for the PUL record (cases 1-2).

Let us now examine Big Rock Wash Bridge. Table 5.15 and Table 5.16 list the means and standard deviations of peak linear and non-linear pier drifts, respectively. Table 5.17 lists the means and standard deviations of the displacement ductilities. First, we examine the results for the HSP record as seed. We note that in case 4, there was one set of motions (in the ensemble of 20 sets) for which convergence in the non-linear time-history analysis with Opensees was not achieved. This set of motions was not considered in the statistics presented herein i.e., the results for case 4 are from 19 simulations. For both the linear and the non-linear models, mean peak drifts under spatially varying ground motions (cases 2, 3 and 4) are significantly smaller than those under uniform support motions (case 1), particularly for the piers of bent 2, which are shorter and thus, stiffer. For both models, increasing level of incoherence (compare cases 2 and 3) increases pier drifts, but the effect is mild. For both models, the additional differential-site effect (compare cases 2 and 4) decreases pier drifts, but again, the effect is mild. Looking at the results for the PUL record as seed, spatial variability significantly decreases linear and non-linear pier drifts in bent 2, but has a relatively mild effect on pier drifts in bent 3. Mean peak non-linear drifts can be smaller or larger than mean peak linear drifts, depending on the seed record, the case of spatial variability and the location of the pier. Ductilities follow similar trends with non-linear drifts. Their means are in the range 1.90-3.81 for the HSP record (cases 1-4) and in the range 2.67-3.92

for the PUL record (cases 1-2), i.e. larger than the ductilities of the two bridges examined earlier.

Finally, we examine the responses of the Auburn Ravine Bridge. Table 5.18 and Table 5.19 list the means and standard deviations of peak linear and non-linear pier drifts, respectively. Table 5.20 lists the means and standard deviations of the displacement ductilities. First, we examine the results for the HSP record as seed. Again, in case 4, there was one set of motions for which convergence in the non-linear time-history analysis was not achieved, and the statistics for this case are from 19 simulations. For both the linear and the non-linear models, mean peak drifts under spatially varying ground motions (cases 2, 3 and 4) are smaller than those under uniform support motions (case 1) for all piers. The differences are more pronounced for the piers in bents 3, 4 and 5 that are located further away from the abutments. For both models, increasing level of incoherence (compare cases 2 and 3) increases all pier drifts, but the effect is relatively mild. The additional differential-site effect (compare cases 2 and 4) may decrease or increase pier drifts. Looking at the results for the PUL record as seed, spatial variability significantly decreases linear and non-linear pier drifts for bents 3, 4 and 5, but tends to slightly increase pier drifts for other bents. Mean peak non-linear drifts are always smaller than mean peak linear drifts. Ductility ratios follow trends similar to the non-linear drifts. Their means are in the range 0.74-2.13 for the HSP record (cases 1-4) and in the range 1.09-2.75 for the PUL record (cases 1-2).

Summarizing the above results, the effect of spatial variability is found to be more pronounced for the two stiffer bridges, i.e., the Big Rock Wash Bridge and the Auburn Ravine Bridge. In all cases for the Big Rock Wash Bridge and in almost all cases for the Auburn Ravine Bridge, spatial variability decreased pier drifts. For certain cases and piers, the reductions were very significant. Over all bridges and cases examined, whenever spatial variability increased pier drifts, the increase was relatively mild. These trends are true for both the linear and the non-linear models and are consistent with the results of the MSRS analysis reported in Chapter 3.

For the linear models, we further interpret the above results by considering the decomposition of the total response into dynamic and pseudo-static components (the latter are zero in the case of uniform excitation), and the decomposition of the dynamic response into modal responses. For the cases with uniform soil conditions, the spatial variability of ground motion generally induces pseudo-static responses; however, for transverse pier drifts, these have small contributions to the total response. For the bridge models considered, the dynamic responses of the pier drifts are mainly contributed by the first two transverse modes (see Section 3.2 for the modes of the four bridges). Under differential support motions, the contribution of the second transverse mode becomes larger. For the two more flexible bridges (Penstock and South Ingram Slough) and for both records used as seed, the displacement spectral values for the first two transverse modes do not differ significantly. As a result, the effect of spatial variability on the corresponding pier drifts is relatively mild. For the two stiffer bridges and for both records used as seed, displacement spectral values decrease fast with increasing modal frequency. As a result, spatial variability results in significant reductions of the dynamic component and, consequently, of the total responses. The additional effect from differential site-response tends to increase pseudo-static responses, whereas the effect on the dynamic responses depends on the differences between the spectral amplitudes for different soils at the modal frequencies of the bridge (see Figure 5.10). Thus, the total response may increase or decrease.

A detailed comparison of non-linear and linear responses is performed in the following section.

5.4.2 Investigation of the “equal displacement” rule

In Caltrans design practice, the displacement demands of a bridge with fundamental period within the range 0.7s and 3s are estimated from linear elastic response spectrum analysis using the effective element stiffnesses of the bridge. Estimating inelastic displacements with elastic analysis is based on the observation that the inelastic displacement of an SDOF oscillator with a bilinear force-deformation relationship is approximately equal to the displacement of a corresponding linear oscillator, provided that the period of the system is larger than the predominant site period (Veletsos and Newmark. 1960). The applicability of the “equal displacement” rule has been investigated by several researchers, including Rahnama and Krawinkler, 1993; Miranda and Bertero, 1994; Vidic et al., 1994; Gupta and Krawinkler, 2000; and Miranda, 2000. These studies have demonstrated that the equal displacement rule is a reasonable approximation for structures on firm sites, with fundamental periods in the medium (velocity-controlled) or long (displacement-controlled) period range, with relatively stable and full hysteretic loops. In general, a slightly conservative estimate of the mean value of the inelastic displacement may be obtained under these conditions. (According to Gupta and Krawinkler, the mean inelastic to elastic displacement ratio is around 0.85.) Miranda (2000) investigated the dispersion of the results and found that the coefficient of variation is below 0.3 for a ductility factor of 3 and that it tends to increase as the inelastic deformation increases. The transition period below which the “equal displacement” rule is unconservative depends on the frequency content of the ground motion and the ductility factor. It tends to increase (decrease) with increasing (decreasing) ductility factor (Vivic et al. , 1994; Miranda, 2000).

In this section, we examine the applicability of the equivalent displacement rule to bridges under spatially varying ground motions. Adopting Caltrans’ notation, in the following analysis, we denote the ratio of non-linear over linear drifts as C_μ.

Table 5.21 lists the means and standard deviations of the ratio C_μ for each pier of the Penstock Bridge. For the HSP record as seed, the means vary in the range 0.87-1.06 in case 1, and in the range 0.82-0.93 in cases 2-4. For the PUL record as seed, the means vary in the range 0.87-1.07 in case 1, and in the range 0.78-0.90 in case 2. In all cases, spatial variability reduces the mean C_μ values and slightly deteriorates the approximation of the equal displacement rule, but on the conservative side. The effect of spatial variability is more pronounced for pier 4, which is the stiffest among the three piers. Comparing cases 2 and 4, we note that under varying soil conditions, mean C_μ values are slightly larger. For each case in

Table 5.21, Figure 5.16-Figure 5.17 show plots of C_μ versus the ductility for each of the 20 simulations. Note that the ductility ratios for individual simulations exceed 3 in many cases and reach as high as 4 when spatially varying site effects are included (e.g., see case 4 in Figure 5.16).

Table 5.22 lists the means and standard deviations of C_μ for each pier of the South Ingram Slough Bridge. In all cases, the means for the two piers are the same: For the HSP record, they are equal to 0.92 in cases 1-3 and 0.94 in case 4. For the PUL record, they are equal to 0.97 in case 1 and 0.98 in case 2. Thus, in all cases, the approximation of the "equal displacement" rule is very good and the effect of spatial variability is negligible. For the cases in Table 5.22, Figure 5.18-Figure 5.19 show plots of C_μ versus the ductility for each of the 20 simulations. Note again that the ductility is higher than 3 in many cases and reaches as high as 4 or 5 for the HSP or the PUL record as seed, respectively.

Table 5.23 lists the means and standard deviations of C_μ for each pier of the Big Rock Wash Bridge. For the HSP record as seed, the means vary in the range 1.13-1.15 in case 1 (slightly on the unconservative side), and in the range 0.94-1.00 in cases 2-4. For the PUL record as seed, the means vary in the range 1.04-1.05 in case 1, and in the range 0.91-1.04 in case 2. Spatial variability reduces the mean C_μ values, and in all cases of spatial variability the approximation of the "equal displacement" rule is fairly good. Comparing cases 2 and 4, we note that under varying soil conditions, mean C_μ values are slightly larger. For each case in Table 5.23, Figure 5.20-Figure 5.21 show plots of C_μ versus the ductility ratio for each simulation (19 simulations for case 4 in Figure 5.20 and 20 simulations in other cases). Under uniform support motions (case 1), ductility reaches as high as 6 for the HSP record as seed and as high as 8 for the PUL record as seed. Spatial variability of ground motions significantly reduces ductility ratios.

Table 5.24 lists the means and standard deviations of C_μ for each pier of the Auburn Ravine Bridge. For the HSP record as seed, the means vary in the range 0.72-0.82 in case 1, and in the range 0.61-0.92 in cases 2-4. For the PUL record as seed, the means vary in the range 0.79-0.94 in case 1, and in the range 0.82-0.93 in case 2. Let us first consider uniform soil conditions, i.e., cases 1-3. For bents 2 and 6, which are located further away from the abutments, the effect of spatial variability is mild. For other bents, spatial variability always decreases mean C_μ values, and this effect is more pronounced for the HSP record. In general, for the PUL record as seed, the approximation of the "equivalent" displacement rule is better for both cases 1 and 2. Now, Comparing cases 2 and 4 (for the HSP record as seed), under varying soil conditions, mean C_μ values are larger, particularly for bents 3 and 5 which are located on softer soils. For each case in Table 5.24, Figure 5.22-Figure 5.23 show plots of C_μ versus the ductility ratio for each simulation (19 simulations for case 4 in Figure 5.20 and 20 simulations in other cases). Ductility reaches as high as 4 for the HSP record as seed, and in some cases exceeds 4 for the PUL record as seed.

In assessing the above results, we note that the two more flexible bridges, i.e., the Penstock Bridge and the South Ingram Slough Bridge, have fundamental periods ($T = 2.38$ s and

$T = 1.24$ s, respectively) within the range 0.7s-3.0s, in which the "equal displacement" rule is employed by Caltrans. For these bridges, under uniform excitation, the equal displacement approximation is fairly good, mostly on the conservative side. The two stiffer bridges i.e. the Big Rock Wash Bridge and the Auburn Ravine Bridge, have fundamental periods ($T = 0.61$ s and $T = 0.59$ s, respectively) slightly lower than the lower bound considered by Caltrans. These periods are smaller than the predominant period of the site of the HSP record (≈ 0.84 s), but larger than the predominant period of the site of the PUL record (≈ 0.40 s). For the HSP record, under uniform excitation, the "equal displacement" rule is slightly unconservative for the Big Rock Wash Bridge, with corresponding ductility factors in the range of 3.54-3.81, but significantly conservative for the Auburn Ravine Bridge, with ductility factors in the range of 1.12-2.13. For the PUL record, under uniform excitation, the equal displacement rule gives fairly good approximations, particularly for the Big Rock Wash Bridge, which experienced larger ductilities. These results are consistent with findings by Vivic et al. (1994) and Miranda (2000) that, in the short period range, C_μ values depend on the frequency content of the ground motion and the ductility factor. Under uniform soil conditions, spatial variability decreases mean C_μ values in almost all cases. Comparing cases 2 and 4, which differ only in the site conditions, locating piers on softer sites increases C_μ values for all bridges. Finally, the dispersion of the results is consistent with the finding by Miranda (2000): The coefficient of variation of C_μ tends to increase with increasing ductility factor, and is below 0.3 for ductility factors smaller than 3. This can be verified by examining the ratio of the standard deviation to mean of C_μ in Table 5.21-Table 5.24.

5.4.3 Assessment of the MSRS rule by comparisons with RHA results

In this section, we assess the accuracy of the MSRS method by comparing MSRS estimates with the corresponding mean peak responses obtained from linear RHA. For a fair evaluation of the MSRS method, we compare mean peak responses from MSRS analysis using Eqn. 2.12 with mean peak responses from linear RHA using the decomposition formula in Eqn. 2.9, by employing the same integration method for the evaluation of the ith modal time-history response, $s_{ki}(t)$, as the ith-mode spectral value, $D_k(\omega_i, \zeta_i)$. We note that OpenSees does not use the decomposition approach in RHA, but performs integration of the system of equations in matrix form.

We consider the ensembles of simulations described in Section 5.3 for cases 1 and 3 and for the HSP record as seed. In our MSRS analysis, the mean response spectra are obtained by averaging 5% damped spectra for all simulations in case 1, and for all simulations and all support points in case 3. (In case 3, we average over all support points because, under uniform soil conditions, the response spectra at all support points should be the same. Indeed, in Section 5.3, we saw that the median response spectra at support points with similar soil conditions were in good agreement). Response spectra values for damping ratios other than 5% are evaluated by adjusting the 5% damped spectral values according to Caltrans specifications (Caltrans SDC, 2004). We note that in case 1 the MSRS rule reduces to the square-root of the quadruple-sum term (see Eqn. (2.12)) representing the dynamic component of the response. This has the same form as the well known CQC rule (Der Kiureghian, 1981), but with a more accurate approximation of the cross-modal correlation coefficients. (Evaluation of the modal cross-correlation coefficient in the MSRS rule employs the response-spectrum-compatible power spectral density shape, whereas in the CQC rule it employs a white-noise idealization.)

Preliminary analysis has indicated that, for pier drifts, considering the first 4 modes in the analysis is sufficient for the four bridges examined. Table 5.25-Table 5.28 list the mean peak values of pier drifts of the four bridge models (absolute values, not drift ratios) from RHA with OpenSees, RHA with Eqn. 2.9 considering the first 4 modes, MSRS analysis with the first 4 modes, and the percent errors of the MSRS results relative to the results of RHA with Eqn. 2.9. The results from RHA with OpenSees are the same as those in Section 5.4.1 for the linear models and the corresponding cases, but now given in absolute values, not ratios. In all cases, the differences between the two RHA results are small, which validates our analyses. Note that the two RHA analysis methods are vastly different, the one with OpenSees involving integration of matrix equations with Rayleigh damping, while the one with Eqn. 2.9 involving modal superposition considering only the first 4 modes.

Considering the absolute values of the MSRS errors, the maximum error observed is 8.5% in case 1 (Auburn Ravine Bridge, bent 2: pier 2) and 12.5% in case 3 (Auburn Ravine Bridge, bent 4: pier 1). Recall that the MSRS method is intended for use in conjunction with smooth response spectra that represent broadband excitations and a smooth coherency function. In our analysis, jagged response spectra from a relatively narrowband excitation were used. Furthermore, the smooth coherency function used for evaluation of the correlation coefficients in the MSRS analysis differs from the actual coherency values for pairs of simulated support motions, which can exhibit large fluctuations around the theoretical model. Thus, considering these difference, the results of the MSRS analysis are found to be remarkably accurate.

5.5 SUMMARY

In this chapter, we performed linear and non-linear analyses of four bridge models with vastly different structural characteristics to several ensembles of support motion arrays simulated with the unconditioned method introduced in Chapter 4, for different cases of spatial variability of ground motions. For each ensemble of motions, we evaluated the means and standard deviations of the peak linear and non-linear drifts, the ductility values and the ratios of non-linear over linear drifts. The effects of spatial variability on the linear and non-linear mean peak drifts followed similar trends. These effects were more pronounced for the stiffer bridges. For these bridges, spatial variability reduced pier drifts. The approximation based on the “equivalent displacement” rule was found to perform fairly well for the more flexible bridges. For the stiffer bridges, the results were sensitive to the frequency content of the support motions and the ductility factors. When the predominant period of the site was smaller than the fundamental period of the bridge, the approximations were again fairly good; otherwise, the “equivalent displacement” rule was slightly non-conservative for large ductility rations, or overly conservative for small ductility ratios. Finally, we performed comparisons of the mean peak linear drifts with results from consistent MSRS analysis. The good agreement between the two methods validates that MSRS method provides an accurate analysis tool for the analysis of bridges under differential support motions.

Table 5.1: Yield drifts of the piers of Penstock Bridge.

yield curvature at section level = 0.0035			
	bent 2	bent 3	bent 4
yield drift (m)	0.263	0.260	0.210

Table 5.2: Yield drifts of the piers of South Ingram Slough Bridge.

yield curvature at section level = 0.0031		
	bent 2	
	pier 1	pier 2
yield drift (m)	0.146	0.149

Table 5.3: Yield drifts of the piers of Big Rock Wash Bridge.

yield curvature at section level = 0.0024				
	bent 2		bent 3	
	middle pier	side pier	middle pier	side pier
yield drift (m)	0.031	0.029	0.033	0.031

Table 5.4: Yield drifts of the piers of Auburn Ravine Bridge.

yield curvature at section level = 0.0035										
yield drift (m)	bent 2		bent 3		bent 4		bent 5		bent 6	
	pier 1	pier 2	pier 1	pier 2	pier 1	pier 2	pier 1	pier 2	pier 1	pier 2
	0.037	0.039	0.038	0.040	0.043	0.045	0.051	0.053	0.046	0.048

Table 5.5: Modal damping ratios (%) for the first 3 modes.

	bridge name			
mode number	Penstock	South Ingram Slough	Big Rock Wash	Auburn Ravine
1	5.0	5.0	5.0	5.0
2	3.8	4.3	4.6	4.9
3	3.4	3.5	4.6	4.9

Table 5.6: Considered cases of ground motions spatial variability.

	Description of support motions variability
case 1	uniform motions
case 2	variable motions with incoherence ($\alpha = 0.2$) and wave passage
case 3	variable motions with strong incoherence ($\alpha = 0.4$) and wave passage
case 4	variable motions with incoherence ($\alpha = 0.2$), wave passage and site effect

Table 5.7: Variation of soil-column properties for each soil-type.

soil type	1	2	3
$\omega_k/2\pi$, Hz	1.19	1.03	0.80
ζ_k	0.60	0.50	0.40

Table 5.8: Variation of soil types underneath supports in case 4.

Penstock Bridge

support	abutment 1	bent 2	bent 3	bent 4	abutment 5
soil type	1	2	3	2	1

South Ingram Slough Bridge

support	abutment 1	bent 2	abutment 3
soil type	1	3	1

Big Rock Wash Bridge

support	abutment 1	bent 2	bent 3	abutment 4
soil type	1	2	3	1

Auburn Ravine Bridge

support	abutment 1	bent 2	bent 3	bent 4	bent 5	bent 6	abutment 7
soil type	1	2	3	2	3	2	1

Table 5.9: Penstock Bridge: Mean (standard deviation) peak linear drifts as % of pier height.

	bent 2	bent 3	bent 4
HSP record, scaling factor = 1.5			
case 1	2.33 (0.63)	2.18 (0.57)	1.95 (0.51)
case 2	2.17 (0.61)	2.05 (0.55)	2.48 (0.74)
case 3	2.38 (0.93)	2.17 (0.83)	2.43 (0.76)
case 4	2.50 (0.99)	2.39 (0.91)	2.55 (0.77)
PUL record, scaling factor =1.0			
case 1	2.24 (0.89)	2.08 (0.83)	1.89 (0.69)
case 2	2.20 (0.86)	1.98 (0.74)	2.42 (0.90)

Table 5.10: Penstock Bridge: Mean (standard deviation) peak non-linear drifts as % of pier height.

	bent 2	bent 3	bent 4
HSP record, scaling factor = 1.5			
case 1	2.01 (0.55)	2.04 (0.55)	2.04 (0.50)
case 2	1.78 (0.45)	1.88 (0.49)	1.98 (0.53)
case 3	1.98 (0.79)	2.00 (0.75)	2.04 (0.71)
case 4	2.09 (0.84)	2.22 (0.86)	2.20 (0.79)
PUL record, scaling factor =1.0			
case 1	1.95 (0.83)	1.99 (0.82)	2.00 (0.75)
case 2	1.72 (0.69)	1.80 (0.76)	2.00 (0.79)

Table 5.11: Penstock Bridge: Mean (standard deviation) ductility ratios.

	bent 2	bent 3	bent 4
HSP record, scaling factor =1.5			
case 1	1.63 (0.44)	1.65 (0.44)	1.84 (0.46)
case 2	1.44 (0.37)	1.53 (0.40)	1.79 (0.48)
case 3	1.59 (0.64)	1.62 (0.61)	1.84 (0.65)
case 4	1.69 (0.68)	1.80 (0.71)	1.99 (0.72)
PUL record, scaling factor =1.0			
case 1	1.58 (0.67)	1.61 (0.67)	1.81 (0.68)
case 2	1.39 (0.55)	1.46 (0.62)	1.81 (0.71)

Table 5.12: South Ingram Slough Bridge: Mean (standard deviation) peak linear pier drifts as % of pier height.

	bent 2: pier 1	bent 2: pier 2
HSP record, scaling factor =1.5		
case 1	1.97 (0.70)	1.95 (0.69)
case 2	1.89 (0.66)	1.88 (0.66)
case 3	1.80 (0.54)	1.79 (0.53)
case 4	1.81 (0.71)	1.79 (0.70)
PUL record, scaling factor =1.0		
case 1	2.34 (0.86)	2.32 (0.85)
case 2	2.25 (0.82)	2.23 (0.81)

Table 5.13: South Ingram Slough Bridge: Mean (standard deviation) peak non-linear pier drifts as % of pier height.

	bent 2: pier 1	bent 2: pier 2
HSP record, scaling factor =1.5		
case 1	1.79 (0.61)	1.77 (0.61)
case 2	1.72 (0.59)	1.70 (0.58)
case 3	1.65 (0.52)	1.64 (0.51)
case 4	1.66 (0.57)	1.65 (0.57)
PUL record, scaling factor =1.0		
case 1	2.22 (0.77)	2.21 (0.77)
case 2	2.15 (0.74)	2.13 (0.74)

Table 5.14: South Ingram Slough Bridge: Mean (standard deviation) ductility ratios.

	bent 2: pier 1	bent 2: pier 2
HSP record, scaling factor =1.5		
case 1	2.06 (0.71)	2.02 (0.69)
case 2	1.98 (0.68)	1.95 (0.66)
case 3	1.90 (0.60)	1.87 (0.59)
case 4	1.92 (0.66)	1.88 (0.65)
PUL record, scaling factor =1.0		
case 1	2.56 (0.89)	2.52 (0.87)
case 2	2.47 (0.86)	2.43 (0.84)

Table 5.15: Big Rock Wash Bridge: Mean (standard deviation) peak linear pier drifts as % of pier height.

	bent 2: middle pier	bent 2: side pier	bent 3: middle pier	bent 3: side pier
HSP record, scaling factor =1.5				
case 1	1.55 (0.46)	1.60 (0.48)	1.68 (0.55)	1.72 (0.57)
case 2	1.06 (0.24)	1.09 (0.24)	1.43 (0.35)	1.47 (0.36)
case 3	1.16 (0.29)	1.19 (0.29)	1.52 (0.38)	1.56 (0.39)
case 4	0.96 (0.24)	0.99 (0.25)	1.33 (0.35)	1.36 (0.36)
PUL record, scaling factor =1.0				
case 1	1.86 (0.67)	1.91 (0.69)	1.95 (0.74)	2.00 (0.76)
case 2	1.28 (0.33)	1.32 (0.34)	1.97 (0.76)	2.02 (0.79)

Table 5.16: Big Rock Wash Bridge: Mean (standard deviation) peak non-linear pier drifts as % of pier height.

	bent 2: middle pier	bent 2: side pier	bent 3: middle pier	bent 3: side pier
HSP record, scaling factor =1.5				
case 1	1.75 (0.53)	1.81 (0.55)	1.84 (0.53)	1.89 (0.55)
case 2	1.02 (0.25)	1.05 (0.26)	1.36 (0.34)	1.40 (0.35)
case 3	1.08 (0.28)	1.11 (0.29)	1.44 (0.33)	1.49 (0.34)
case 4	0.94 (0.28)	0.97 (0.29)	1.34 (0.42)	1.38 (0.43)
PUL record, scaling factor =1.0				
case 1	1.83 (0.82)	1.89 (0.84)	1.88 (0.84)	1.93 (0.86)
case 2	1.32 (0.36)	1.36 (0.37)	1.67 (0.42)	1.72 (0.43)

Table 5.17: Big Rock Wash Bridge: Mean (standard deviation) ductility ratios.

	bent 2: middle pier	bent 2: side pier	bent 3: middle pier	bent 3: side pier
HSP record, scaling factor =1.5				
case 1	3.54 (1.07)	3.75 (1.14)	3.60 (1.04)	3.81 (1.10)
case 2	2.06 (0.50)	2.19 (0.53)	2.67 (0.63)	2.82 (0.71)
case 3	2.17 (0.57)	2.30 (0.61)	2.83 (0.65)	2.99 (0.69)
case 4	1.90 (0.57)	2.02 (0.60)	2.62 (0.82)	2.77 (0.87)
PUL record, scaling factor =1.0				
case 1	3.70 (1.65)	3.92 (1.75)	3.67 (1.64)	3.88 (1.73)
case 2	2.67 (0.73)	2.83 (0.78)	3.26 (0.82)	3.46 (0.87)

Table 5.18: Auburn Ravine Bridge: Mean (standard deviation) peak linear pier drifts as % of pier height.

HSP record, scaling factor =1.5				
	case 1	case 2	case 3	case 4
bent 2: pier 1	1.12 (0.29)	0.95 (0.27)	0.96 (0.17)	1.00 (0.26)
bent 2: pier 2	1.05 (0.27)	0.93 (0.27)	0.94 (0.18)	0.98 (0.26)
bent 3: pier 1	1.57 (0.42)	0.86 (0.16)	0.99 (0.22)	1.25 (0.32)
bent 3: pier 2	1.48 (0.40)	0.80 (0.16)	0.92 (0.21)	1.18 (0.30)
bent 4: pier 1	1.85 (0.53)	0.90 (0.25)	1.10 (0.29)	0.87 (0.16)
bent 4: pier 2	1.78 (0.51)	0.85 (0.22)	1.04 (0.25)	0.88 (0.18)
bent 5: pier 1	1.89 (0.56)	1.14 (0.32)	1.26 (0.32)	1.09 (0.20)
bent 5: pier 2	1.84 (0.54)	1.06 (0.30)	1.19 (0.32)	0.98 (0.19)
bent 6: pier 1	1.92 (0.56)	1.53 (0.40)	1.57 (0.47)	1.15 (0.29)
bent 6: pier 2	1.90 (0.55)	1.46 (0.37)	1.50 (0.45)	1.12 (0.27)

PUL record, scaling factor =1.0		
	case 1	case 2
bent 2: pier 1	1.45 (0.53)	1.62 (0.75)
bent 2: pier 2	1.39 (0.51)	1.63 (0.74)
bent 3: pier 1	1.88 (0.73)	1.32 (0.50)
bent 3: pier 2	1.79 (0.69)	1.28 (0.51)
bent 4: pier 1	2.13 (0.85)	1.01 (0.27)
bent 4: pier 2	2.06 (0.82)	0.99 (0.27)
bent 5: pier 1	2.02 (0.79)	1.11 (0.44)
bent 5: pier 2	1.99 (0.78)	1.03 (0.39)
bent 6: pier 1	1.94 (0.74)	1.95 (0.81)
bent 6: pier 2	1.91 (0.72)	1.78 (0.76)

Table 5.19: Auburn Ravine Bridge: Mean (standard deviation) peak non-linear pier drifts as % of pier height.

HSP record, scaling factor =1.5				
	case 1	case 2	case 3	case 4
bent 2: pier 1	0.80 (0.20)	0.69 (0.20)	0.71 (0.13)	0.75 (0.21)
bent 2: pier 2	0.75 (0.19)	0.67 (0.20)	0.69 (0.15)	0.74 (0.20)
bent 3: pier 1	1.17 (0.35)	0.54 (0.13)	0.59 (0.11)	1.15 (0.42)
bent 3: pier 2	1.10 (0.32)	0.50 (0.12)	0.55 (0.10)	1.08 (0.40)
bent 4: pier 1	1.46 (0.48)	0.58 (0.17)	0.69 (0.18)	0.70 (0.15)
bent 4: pier 2	1.39 (0.45)	0.53 (0.15)	0.63 (0.16)	0.70 (0.14)
bent 5: pier 1	1.52 (0.49)	0.73 (0.21)	0.87 (0.29)	1.01 (0.30)
bent 5: pier 2	1.48 (0.48)	0.66 (0.18)	0.81 (0.28)	0.90 (0.27)
bent 6: pier 1	1.56 (0.47)	1.07 (0.33)	1.22 (0.38)	0.84 (0.24)
bent 6: pier 2	1.54 (0.47)	1.00 (0.30)	1.14 (0.35)	0.81 (0.23)
PUL record, scaling factor =1.0				
	case 1	case 2		
bent 2: pier 1	1.30 (0.37)	1.40 (0.37)		
bent 2: pier 2	1.24 (0.35)	1.36 (0.35)		
bent 3: pier 1	1.73 (0.59)	1.18 (0.36)		
bent 3: pier 2	1.64 (0.56)	1.13 (0.35)		
bent 4: pier 1	1.95 (0.66)	0.83 (0.26)		
bent 4: pier 2	1.89 (0.65)	0.79 (0.23)		
bent 5: pier 1	1.70 (0.58)	0.95 (0.42)		
bent 5: pier 2	1.70 (0.58)	0.87 (0.36)		
bent 6: pier 1	1.45 (0.41)	1.70 (0.68)		
bent 6: pier 2	1.46 (0.43)	1.55 (0.63)		

Table 5.20: Auburn Ravine Bridge: Mean (standard deviation) ductility ratios.

HSP record, scaling factor =1.5				
	case 1	case 2	case 3	case 4
bent 2: pier 1	1.22 (0.31)	1.06 (0.30)	1.08 (0.20)	1.15 (0.32)
bent 2: pier 2	1.12 (0.28)	1.00 (0.30)	1.03 (0.22)	1.10 (0.30)
bent 3: pier 1	1.76 (0.53)	0.80 (0.19)	0.89 (0.16)	1.74 (0.64)
bent 3: pier 2	1.61 (0.48)	0.74 (0.18)	0.80 (0.15)	1.59 (0.59)
bent 4: pier 1	2.05 (0.67)	0.82 (0.24)	0.98 (0.25)	0.98 (0.21)
bent 4: pier 2	1.92 (0.63)	0.74 (0.20)	0.87 (0.22)	0.97 (0.20)
bent 5: pier 1	1.98 (0.64)	0.95 (0.27)	1.14 (0.37)	1.32 (0.39)
bent 5: pier 2	1.89 (0.62)	0.84 (0.23)	1.03 (0.35)	1.15 (0.34)
bent 6: pier 1	2.13 (0.64)	1.47 (0.45)	1.67 (0.52)	1.15 (0.33)
bent 6: pier 2	2.06 (0.63)	1.34 (0.40)	1.52 (0.47)	1.09 (0.31)
PUL record, scaling factor =1.0				
	case 1	case 2		
bent 2: pier 1	1.99 (0.57)	2.14 (0.57)		
bent 2: pier 2	1.85 (0.52)	2.03 (0.52)		
bent 3: pier 1	2.60 (0.89)	1.78 (0.54)		
bent 3: pier 2	2.41 (0.82)	1.66 (0.51)		
bent 4: pier 1	2.75 (0.93)	1.16 (0.36)		
bent 4: pier 2	2.60 (0.89)	1.09 (0.32)		
bent 5: pier 1	2.22 (0.75)	1.23 (0.55)		
bent 5: pier 2	2.17 (0.73)	1.11 (0.46)		
bent 6: pier 1	1.98 (0.56)	2.32 (0.93)		
bent 6: pier 2	1.95 (0.57)	2.07 (0.84)		

Table 5.21: Penstock Bridge: Mean (standard deviation) values of C_μ ratios.

	bent 2	bent 3	bent 4
HSP record, scaling factor =1.5			
case 1	0.87 (0.09)	0.94 (0.10)	1.06 (0.13)
case 2	0.83 (0.12)	0.92 (0.10)	0.82 (0.15)
case 3	0.84 (0.12)	0.93 (0.13)	0.85 (0.16)
case 4	0.85 (0.09)	0.93 (0.11)	0.86 (0.16)
PUL record, scaling factor =1.0			
case 1	0.87 (0.14)	0.96 (0.14)	1.07 (0.17)
case 2	0.78 (0.13)	0.90 (0.14)	0.83 (0.19)

Table 5.22: South Ingram Slough Bridge: Mean (standard deviation) values of C_μ ratios.

	bent 2: pier 1	bent 2: pier 2
HSP record, scaling factor =1.5		
case 1	0.92 (0.11)	0.92 (0.11)
case 2	0.92 (0.11)	0.92 (0.11)
case 3	0.92 (0.10)	0.92 (0.10)
case 4	0.94 (0.14)	0.94 (0.14)
PUL record, scaling factor =1.0		
case 1	0.97 (0.15)	0.97 (0.15)
case 2	0.98 (0.14)	0.98 (0.14)

Table 5.23: Big Rock Wash Bridge: Mean (standard deviation) values of C_μ ratios.

	bent 2: middle pier	bent 2: side pier	bent 3: middle pier	bent 3: side pier
HSP record, scaling factor =1.5				
case 1	1.15 (0.26)	1.15 (0.26)	1.13 (0.26)	1.13 (0.26)
case 2	0.97 (0.14)	0.97 (0.14)	0.96 (0.12)	0.96 (0.12)
case 3	0.94 (0.17)	0.94 (0.17)	0.96 (0.14)	0.96 (0.14)
case 4	0.98 (0.13)	0.98 (0.13)	1.00 (0.14)	1.00 (0.14)
PUL record, scaling factor =1.0				
case 1	1.05 (0.54)	1.05 (0.54)	1.04 (0.53)	1.04 (0.53)
case 2	1.04 (0.19)	1.04 (0.19)	0.91 (0.24)	0.91 (0.24)

Table 5.24: Auburn Ravine Bridge: Mean (standard deviation) values of C_μ ratios.

HSP record, scaling factor =1.5				
	case 1	case 2	case 3	case 4
bent 2: pier 1	0.72 (0.10)	0.74 (0.16)	0.74 (0.11)	0.76 (0.13)
bent 2: pier 2	0.72 (0.10)	0.73 (0.16)	0.74 (0.08)	0.76 (0.12)
bent 3: pier 1	0.75 (0.11)	0.63 (0.11)	0.61 (0.09)	0.92 (0.13)
bent 3: pier 2	0.74 (0.11)	0.63 (0.13)	0.61 (0.11)	0.91 (0.13)
bent 4: pier 1	0.79 (0.13)	0.66 (0.14)	0.64 (0.08)	0.81 (0.13)
bent 4: pier 2	0.79 (0.13)	0.64 (0.15)	0.61 (0.09)	0.81 (0.13)
bent 5: pier 1	0.81 (0.12)	0.65 (0.12)	0.69 (0.11)	0.92 (0.16)
bent 5: pier 2	0.81 (0.12)	0.63 (0.13)	0.67 (0.11)	0.92 (0.16)
bent 6: pier 1	0.82 (0.11)	0.70 (0.11)	0.79 (0.13)	0.74 (0.09)
bent 6: pier 2	0.82 (0.11)	0.69 (0.11)	0.76 (0.13)	0.73 (0.09)
PUL record, scaling factor =1.0				
	case 1	case 2		
bent 2: pier 1	0.92 (0.14)	0.92 (0.17)		
bent 2: pier 2	0.92 (0.15)	0.89 (0.16)		
bent 3: pier 1	0.94 (0.12)	0.93 (0.14)		
bent 3: pier 2	0.94 (0.12)	0.92 (0.15)		
bent 4: pier 1	0.94 (0.13)	0.83 (0.17)		
bent 4: pier 2	0.94 (0.12)	0.82 (0.16)		
bent 5: pier 1	0.87 (0.13)	0.85 (0.11)		
bent 5: pier 2	0.88 (0.13)	0.85 (0.11)		
bent 6: pier 1	0.79 (0.15)	0.88 (0.09)		
bent 6: pier 2	0.80 (0.14)	0.88 (0.09)		

Table 5.25: Penstock Bridge: Comparison of RHA and MSRS mean peak pier drift estimates.

case 1				
location	RHA with OpenSees (m)	RHA witEqn. (2.9) (m)	MSRS (m)	error (%)
bent 2	0.494	0.484	0.482	−0.4
bent 3	0.460	0.452	0.444	−1.8
bent 4	0.370	0.362	0.345	−4.7
case 3				
location	RHA with OpenSees (m)	RHA witEqn. (2.9) (m)	MSRS (m)	error (%)
bent 2	0.505	0.487	0.480	−1.4
bent 3	0.459	0.449	0.452	0.7
bent 4	0.460	0.442	0.410	−7.2

Table 5.26: South Ingram Slough Bridge: Comparison of RHA and MSRS mean peak pier drift estimates.

case 1				
location	RHA with OpenSees (m)	RHA witEqn. (2.9) (m)	MSRS (m)	error (%)
bent 2: pier 1	0.331	0.325	0.325	0.0
bent 2: pier 2	0.331	0.325	0.325	0.0
case 3				
location	RHA with OpenSees (m)	RHA witEqn. (2.9) (m)	MSRS (m)	error (%)
bent 2: pier 1	0.303	0.295	0.294	−0.3
bent 2: pier 2	0.303	0.295	0.294	−0.3

Table 5.27: Big Rock Wash Bridge: Comparison of RHA and MSRS mean peak pier drift estimates .

case 1				
location	RHA with OpenSees (m)	RHA witEqn. (2.9) (m)	MSRS (m)	error (%)
bent 2: middle	0.096	0.094	0.092	−2.1
bent 2: side	0.096	0.094	0.092	−2.1
bent 3: middle	0.107	0.105	0.106	1.0
bent 3: side	0.107	0.105	0.106	1.0
case 3				
location	RHA with OpenSees (m)	RHA witEqn. (2.9) (m)	MSRS (m)	error (%)
bent 2: middle	0.072	0.067	0.063	−6.0
bent 2: side	0.072	0.067	0.063	−6.0
bent 3: middle	0.097	0.093	0.088	−5.4
bent 3: side	0.097	0.093	0.088	−5.4

Table 5.28: Auburn Ravine Bridge: Comparison of RHA and MSRS mean peak pier drift estimates.

case 1				
location	RHA with OpenSees (m)	RHA with Eqn. (2.9) (m)	MSRS (m)	error (%)
bent 2: pier 1	0.063	0.062	0.057	−8.1
bent 2: pier 2	0.061	0.059	0.054	−8.5
bent 3: pier 1	0.089	0.088	0.085	−3.4
bent 3: pier 2	0.087	0.086	0.082	−4.7
bent 4: pier 1	0.113	0.111	0.110	−0.9
bent 4: pier 2	0.111	0.109	0.108	−0.9
bent 5: pier 1	0.124	0.121	0.122	0.8
bent 5: pier 2	0.124	0.121	0.122	0.8
bent 6: pier 1	0.120	0.116	0.117	0.9
bent 6: pier 2	0.122	0.117	0.119	1.7
case 3				
	RHA with OpenSees (m)	RHA witEqn. (2.9) (m)	MSRS (m)	error (%)
bent 2: pier 1	0.054	0.050	0.049	−2.0
bent 2: pier 2	0.054	0.050	0.049	−2.0
bent 3: pier 1	0.057	0.052	0.046	−11.5
bent 3: pier 2	0.054	0.050	0.045	−10.0
bent 4: pier 1	0.067	0.064	0.056	−12.5
bent 4: pier 2	0.065	0.061	0.054	−11.5
bent 5: pier 1	0.083	0.078	0.071	−9.0
bent 5: pier 2	0.080	0.077	0.069	−10.4
bent 6: pier 1	0.098	0.093	0.086	−7.5
bent 6: pier 2	0.096	0.092	0.084	−8.7

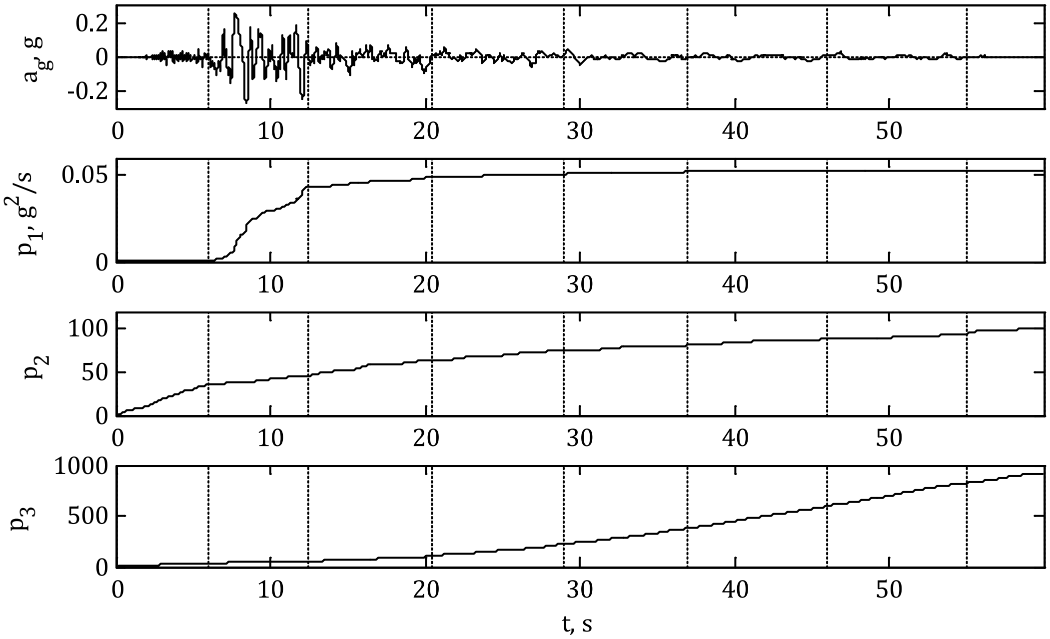

Figure 5.1: "Stationary" segments of the HSP accelerogram selected based on integral measures of evolving cumulative energy, predominant frequency and bandwidth.

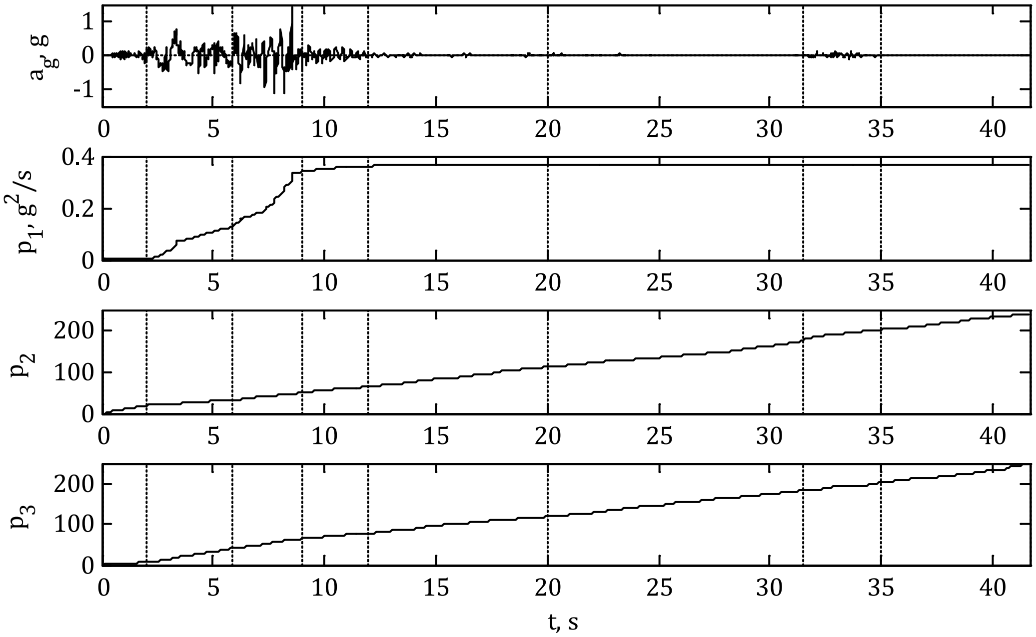

Figure 5.2: Stationary" segments of the PUL accelerogram selected based on integral measures of evolving cumulative energy, predominant frequency and bandwidth.

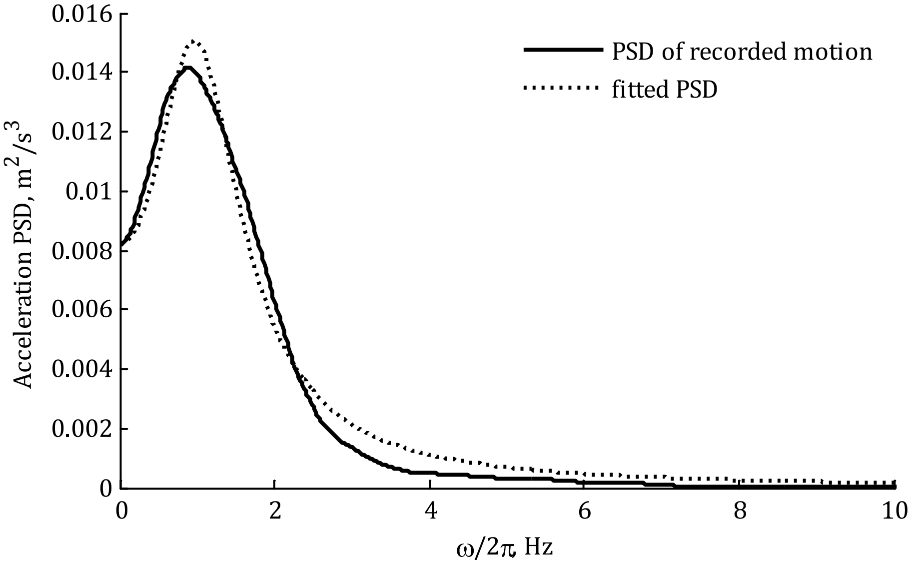

Figure 5.3: Comparison of estimated and fitted theoretical PSD for the HSP record.

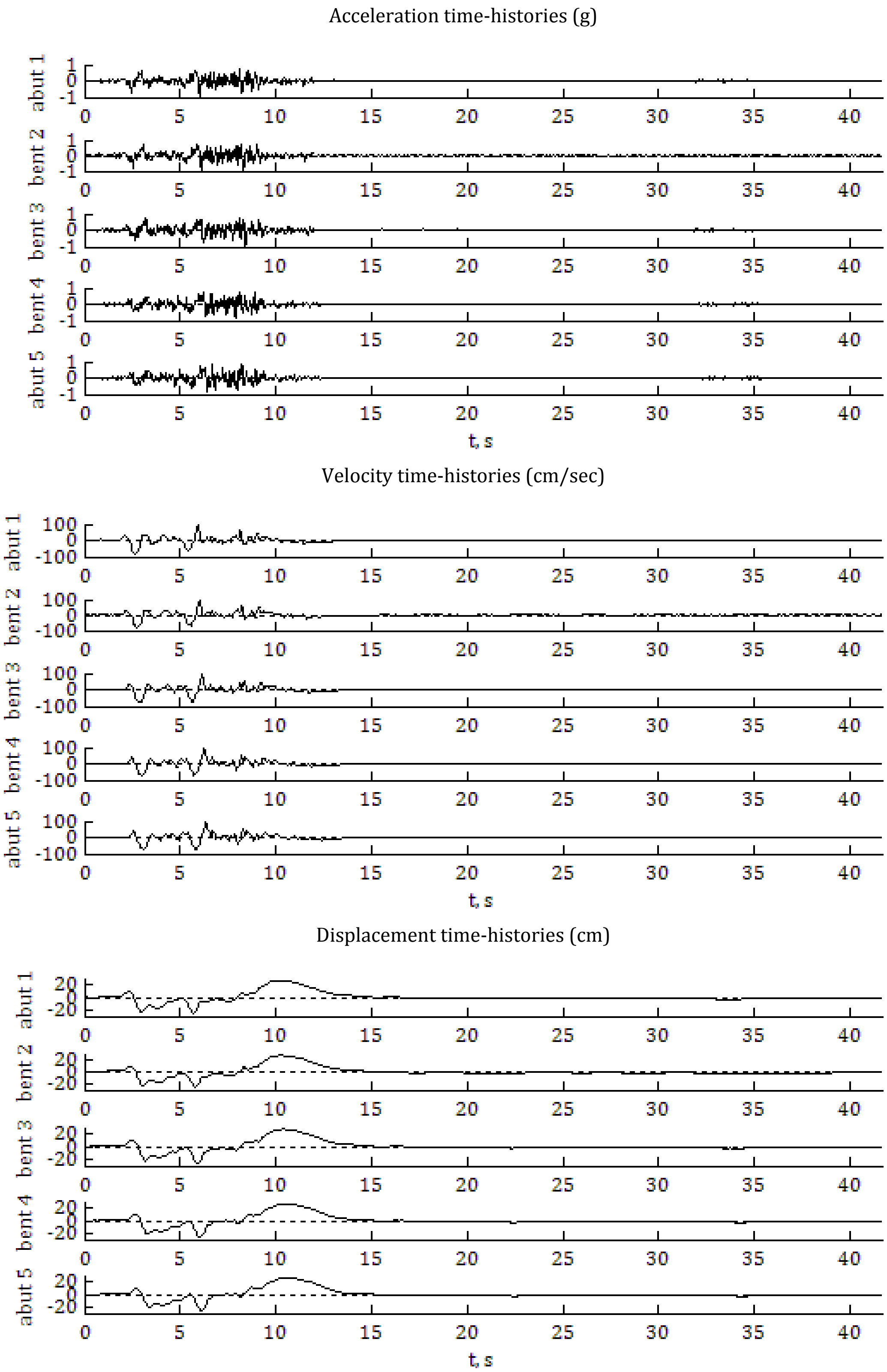

Figure 5.4: Example set of simulated support motions for Penstock Bridge (PUL record as seed, case 2).

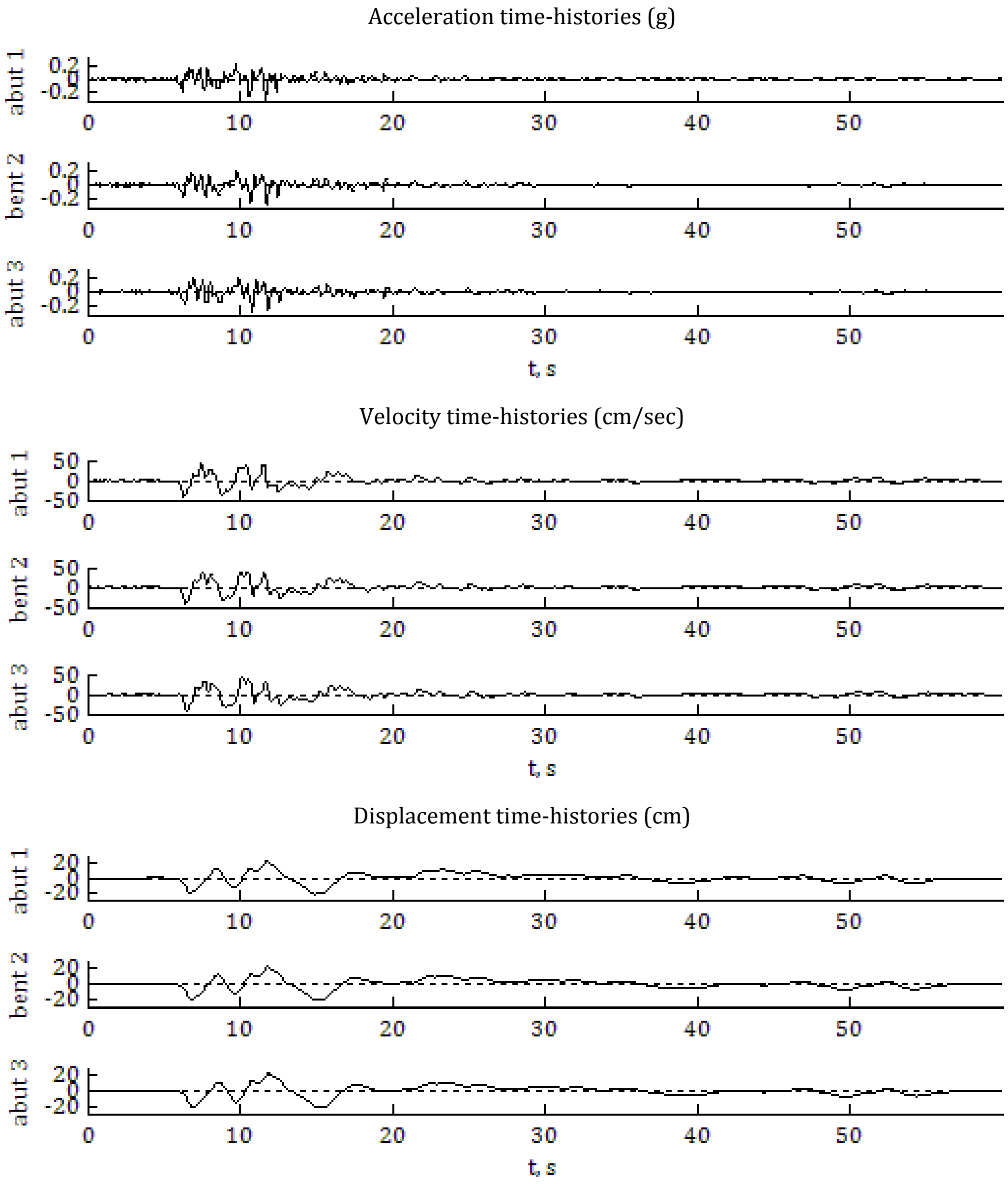

Acceleration time-histories (g)

Velocity time-histories (cm/sec)

Displacement time-histories (cm)

Figure 5.5: Example set of simulated support motions for South Ingram Slough Bridge (HSP record as seed, case 2).

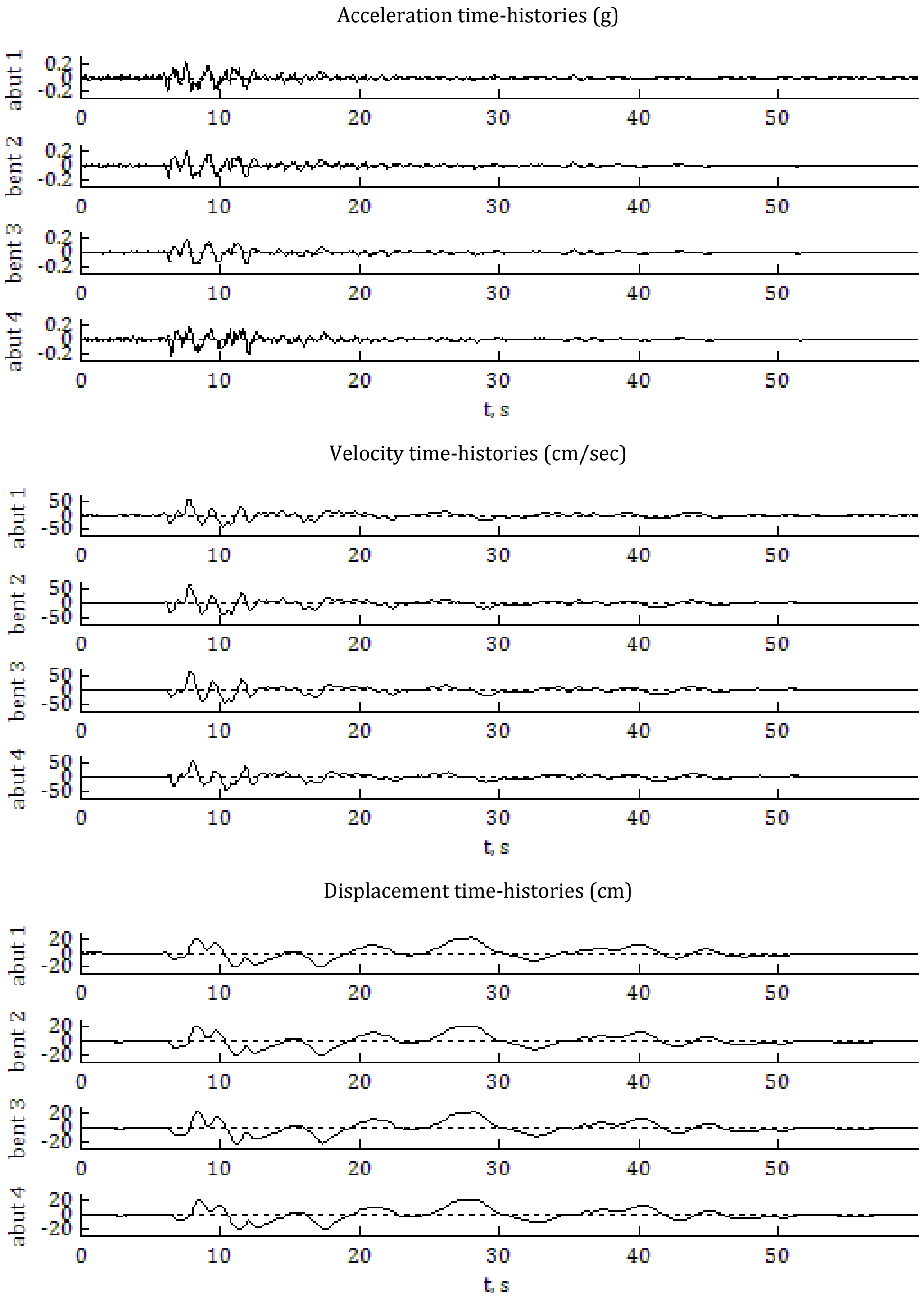
Acceleration time-histories (g)

Velocity time-histories (cm/sec)

Displacement time-histories (cm)

Figure 5.6: Example set of simulated support motions for Big Rock Wash bridge (HSP record as seed, case 4).

Acceleration time-histories (g)

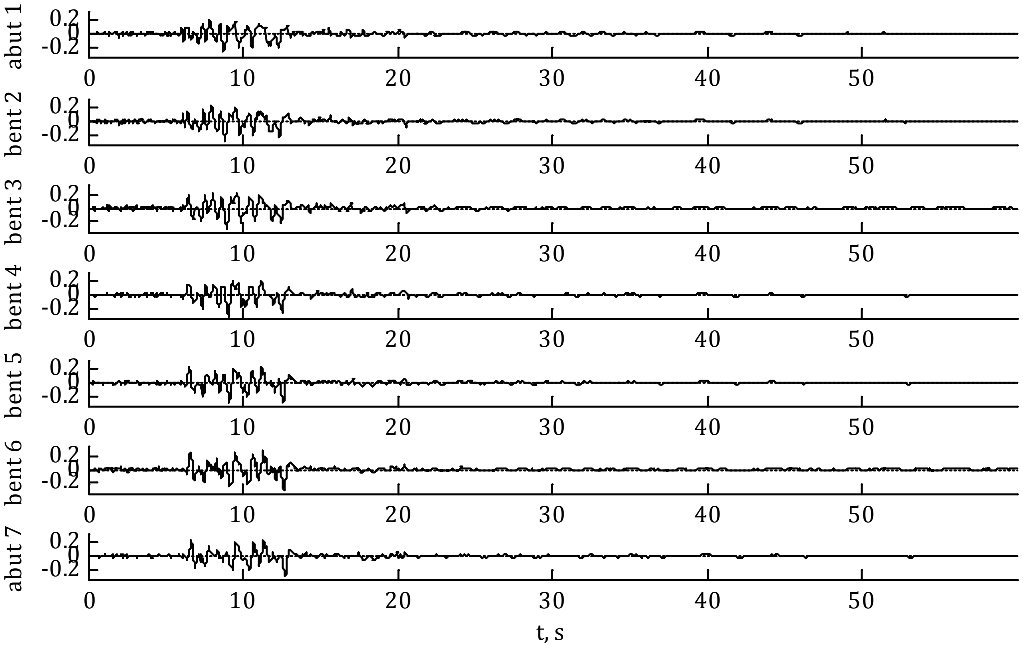

Velocity time-histories (cm/sec)

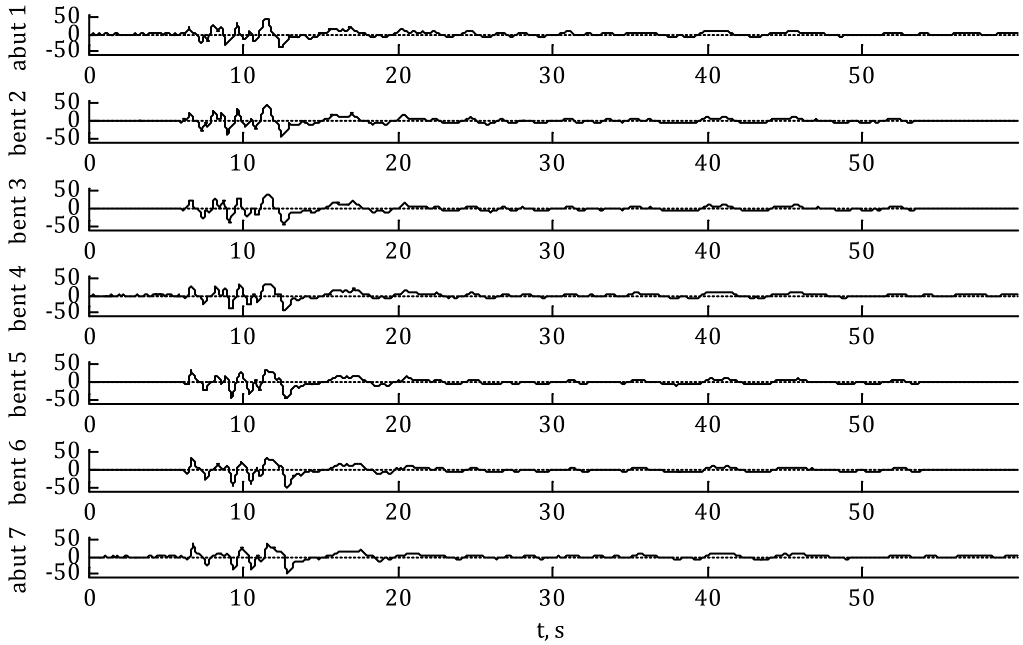

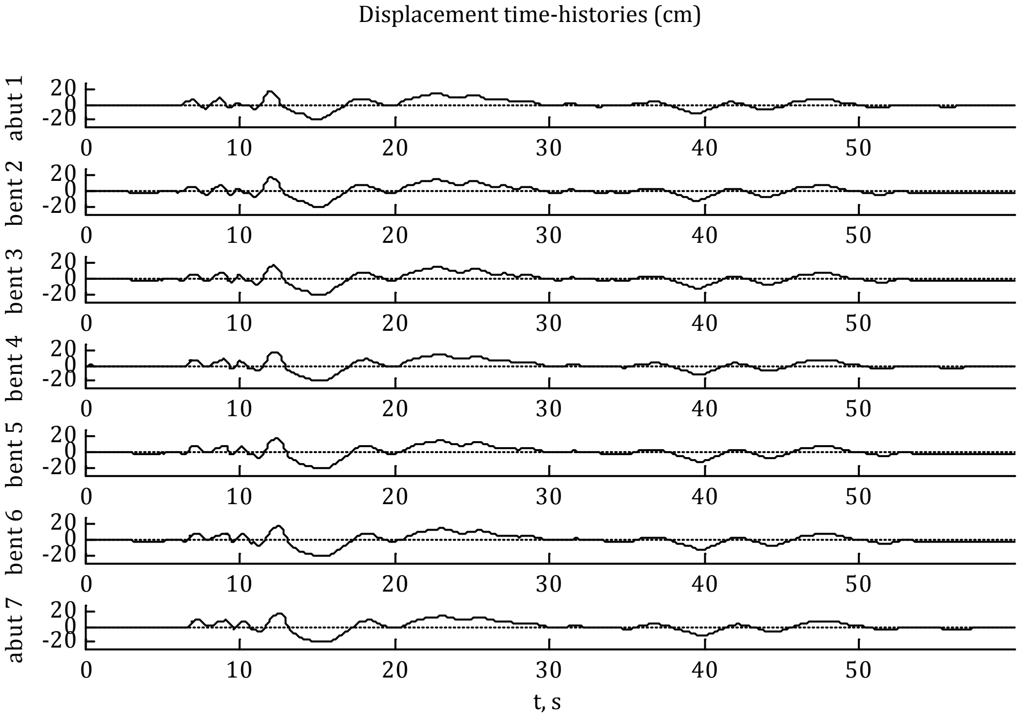

Figure 5.7: Example set of simulated support motions for Auburn Ravine bridge (HSP record as seed, case 3).

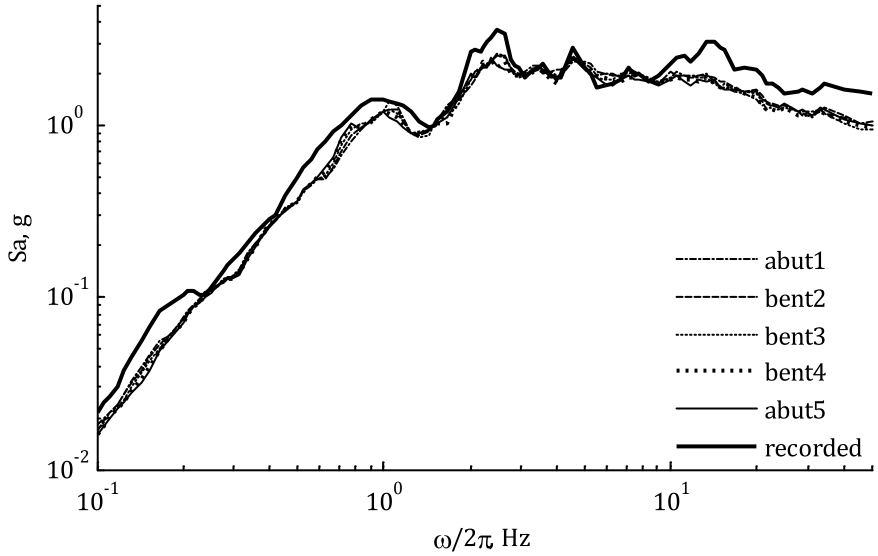

Figure 5.8: Median acceleration response spectra for support motions of Penstock Bridge (PUL record as seed, case 2).

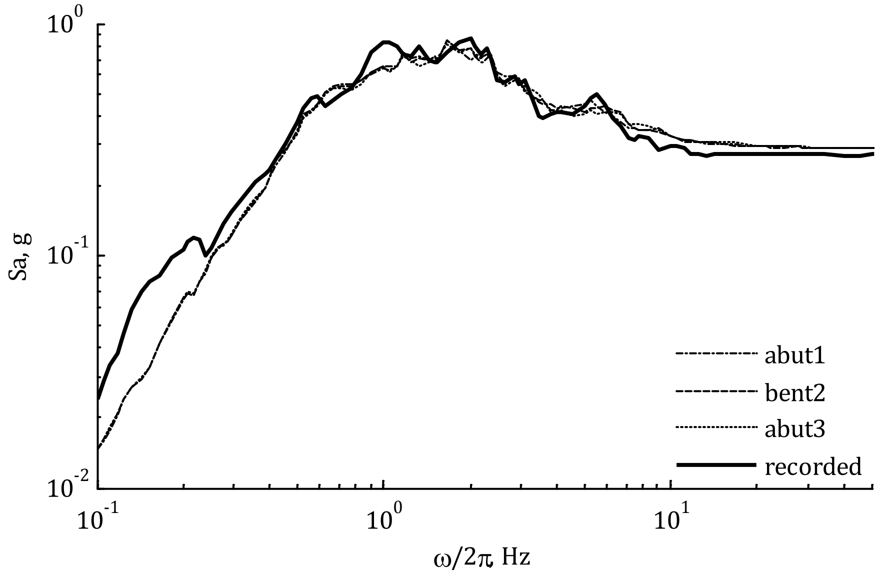

Figure 5.9: Median acceleration response spectra for support motions of South Ingram Slough Bridge (HSP record as seed, case 2).

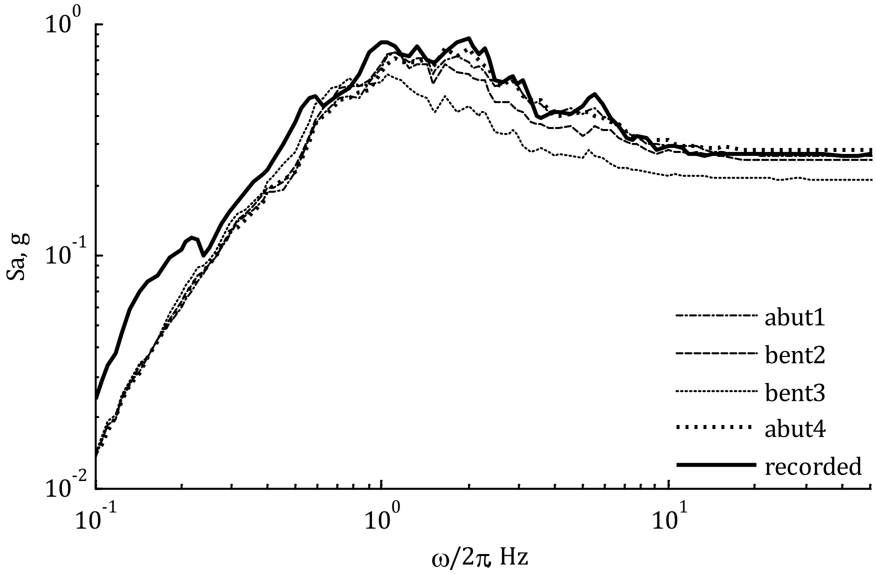

Figure 5.10: Median acceleration response spectra for support motions of Big Rock Wash bridge (HSP record as seed, case 4).

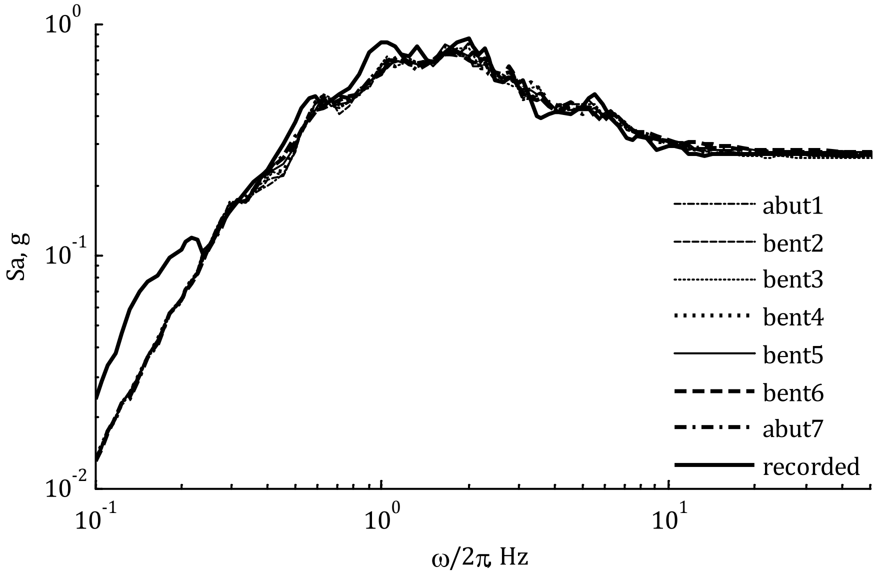

Figure 5.11: Median acceleration response spectra for support motions of Auburn Ravine bridge (HSP record as seed, case 3).

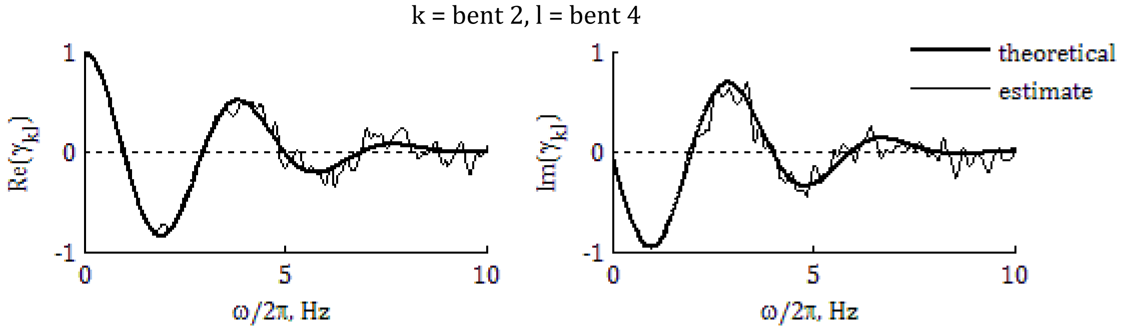

Figure 5.12: Coherency estimates for support motions of Penstock Bridge (PUL record as seed, case 2).

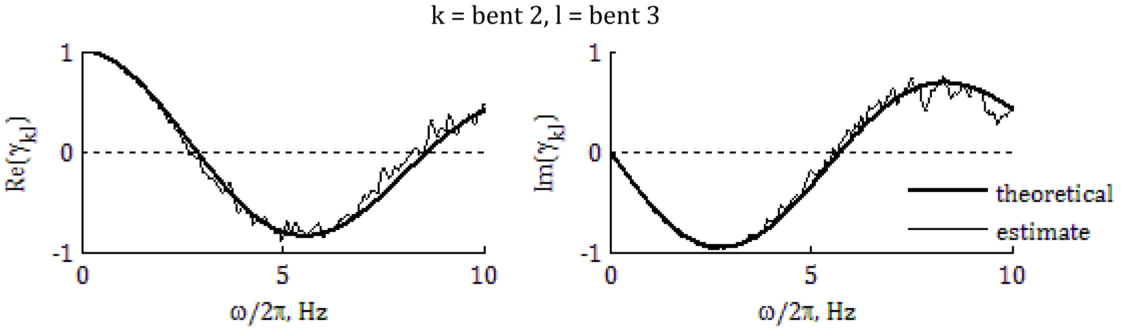

Figure 5.13: Coherency estimates for support motions of South Ingram Slough Bridge (HSP record as seed, case 2).

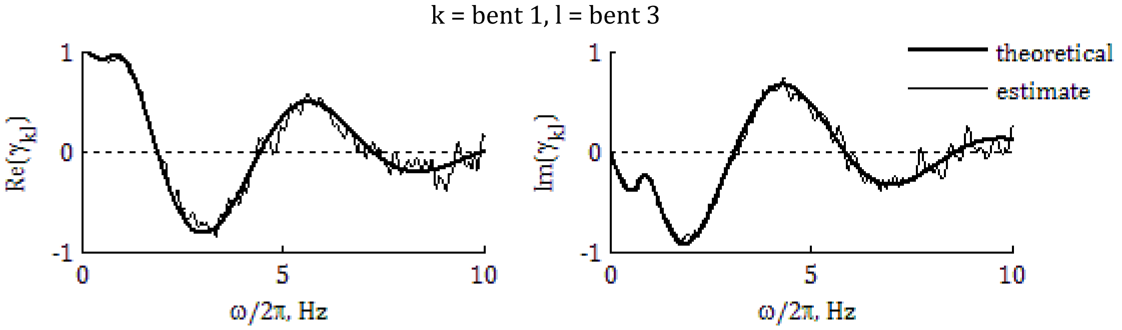

Figure 5.14: Coherency estimates for support motions of Big Rock Wash bridge (HSP record as seed, case 4).

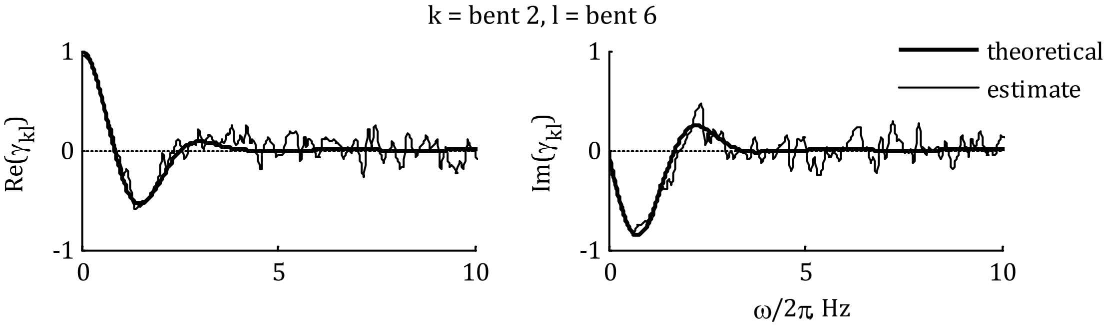

Figure 5.15: Coherency estimates for support motions of Auburn Ravine bridge (HSP record as seed, case 3).

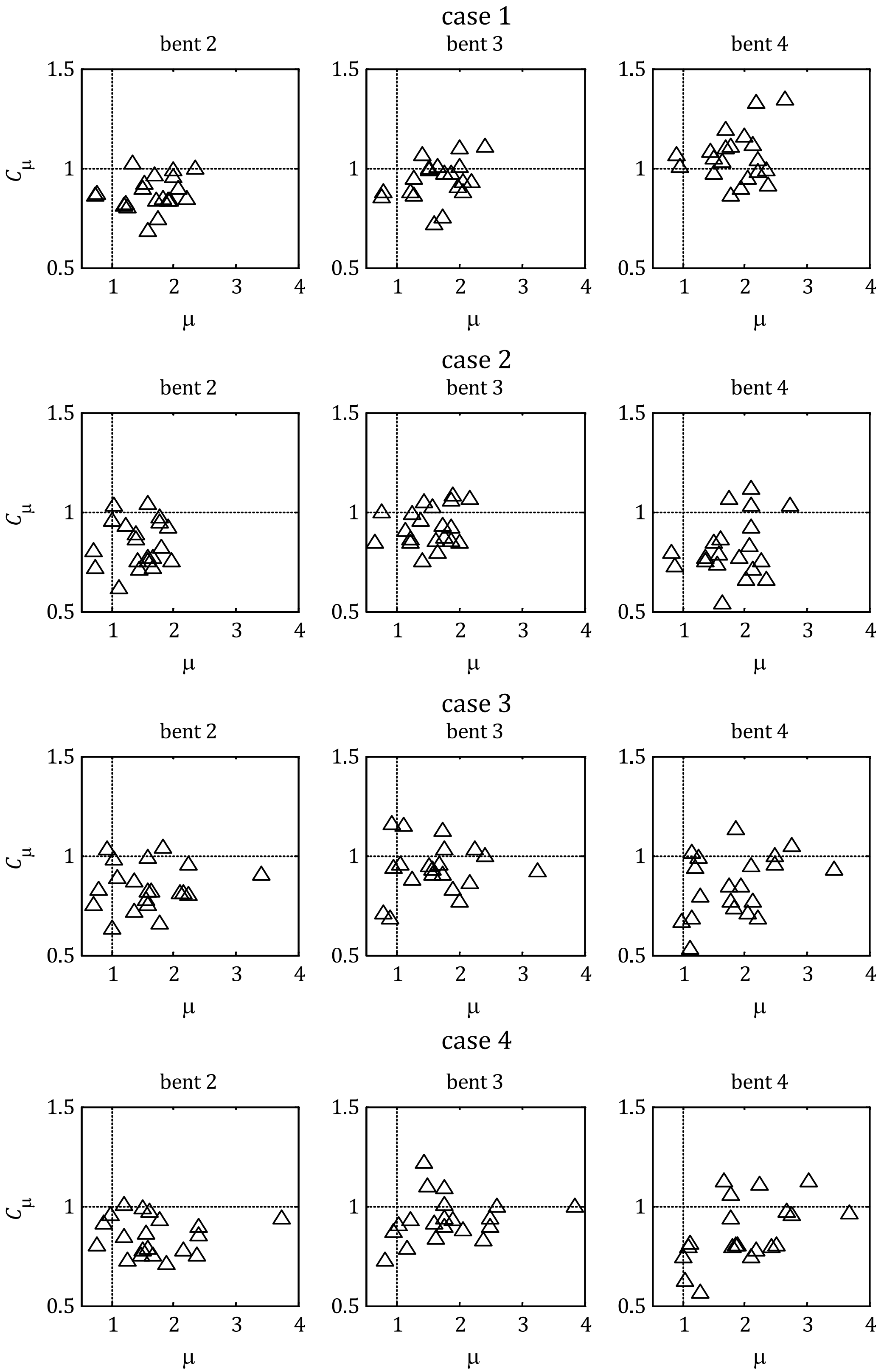

Figure 5.16: C_μ ratio versus ductility for Penstock Bridge (HSP record as seed, scaling factor = 1.5).

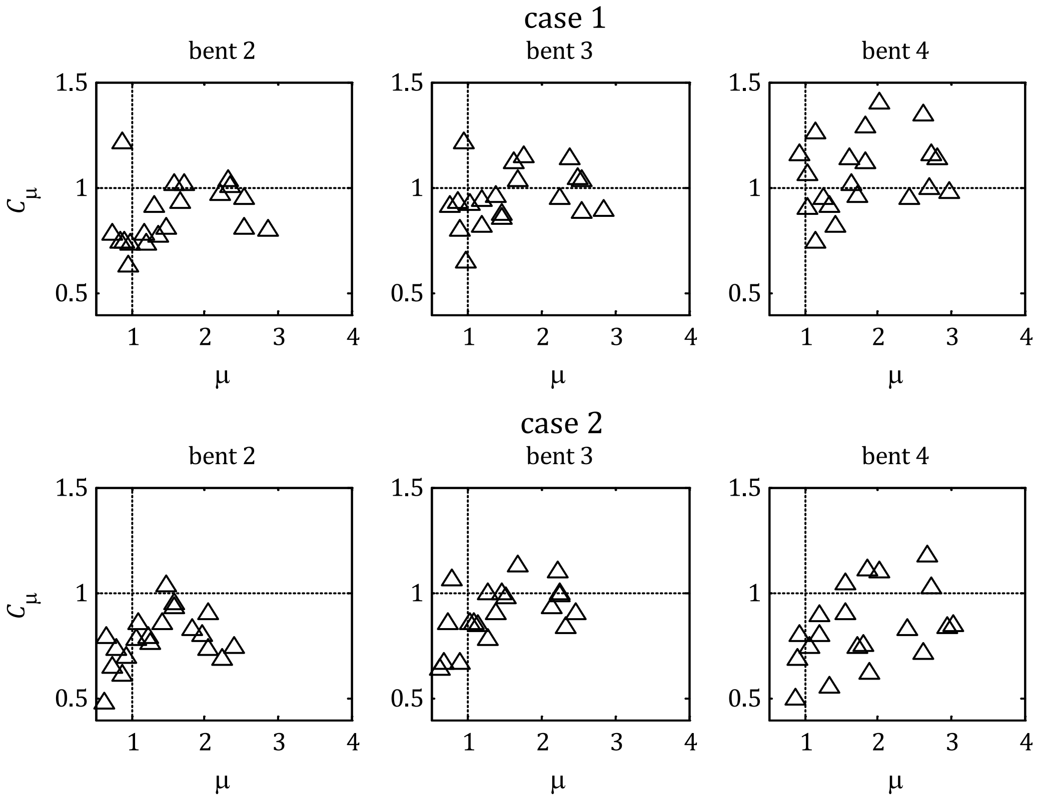

Figure 5.17: C_μ ratio versus ductility for Penstock Bridge (PUL record as seed, scaling factor = 1.0).

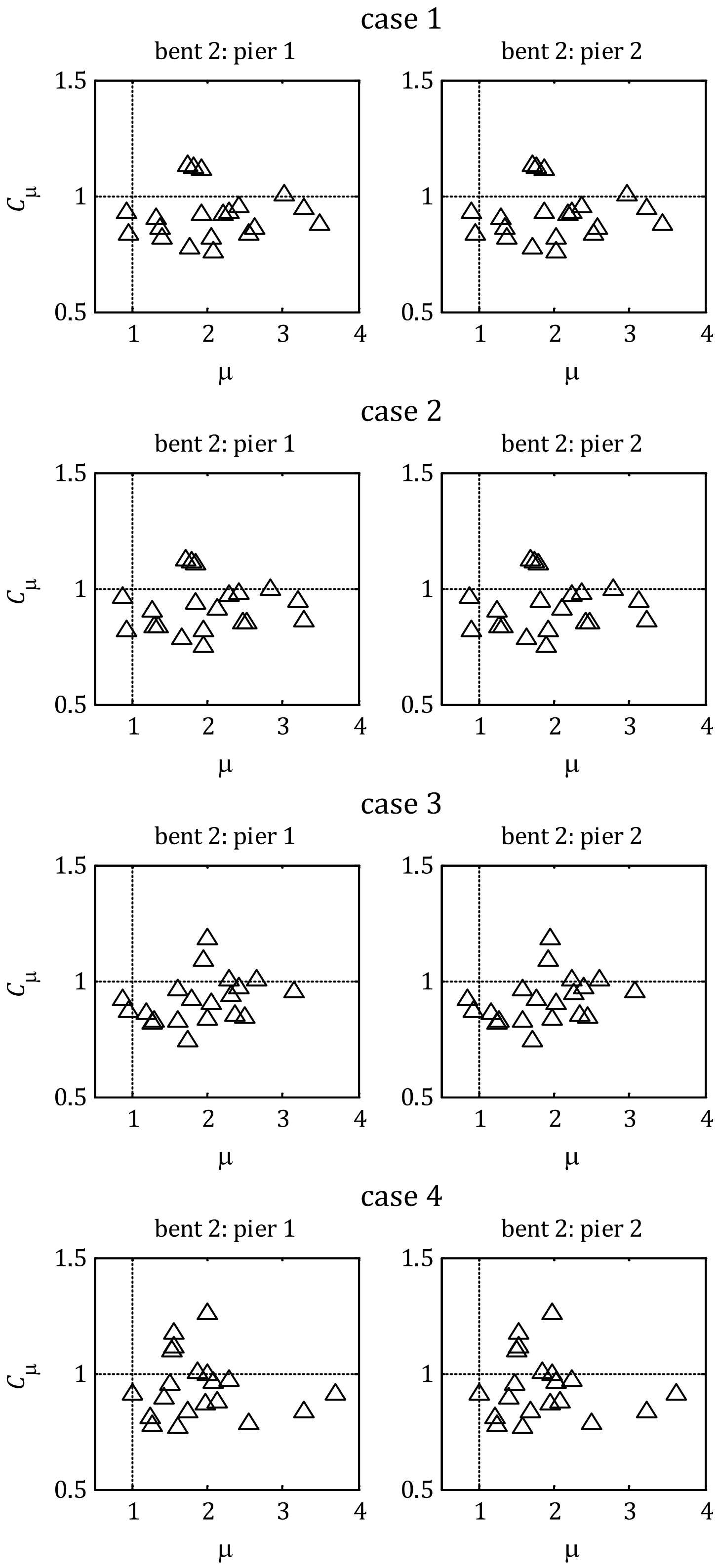

Figure 5.18: C_μ ratio versus ductility for South Ingram Slough Bridge (HSP record as seed, scaling factor = 1.5).

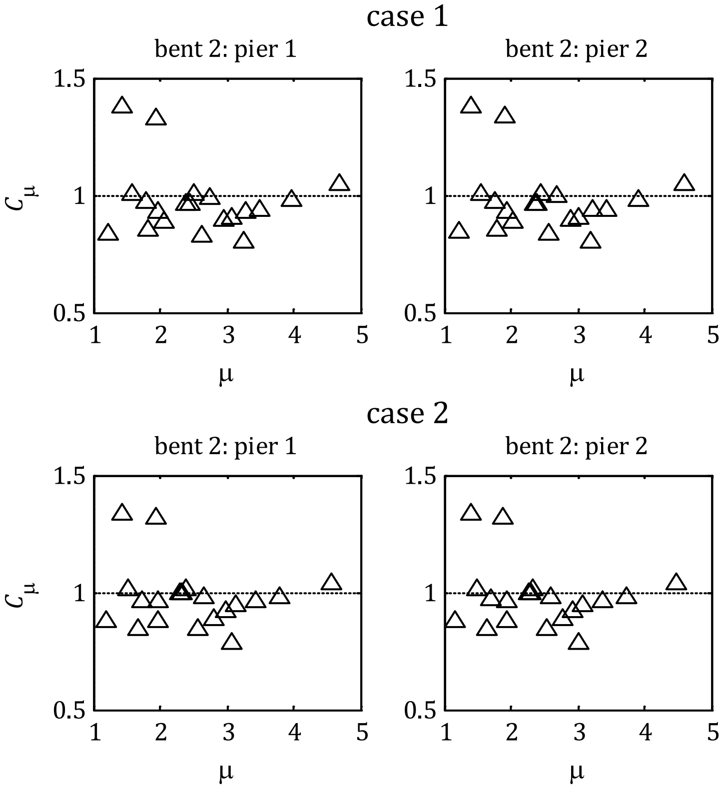

Figure 5.19: C_μ ratio versus ductility for South Ingram Slough Bridge (PUL record as seed, scaling factor = 1.0).

case 1

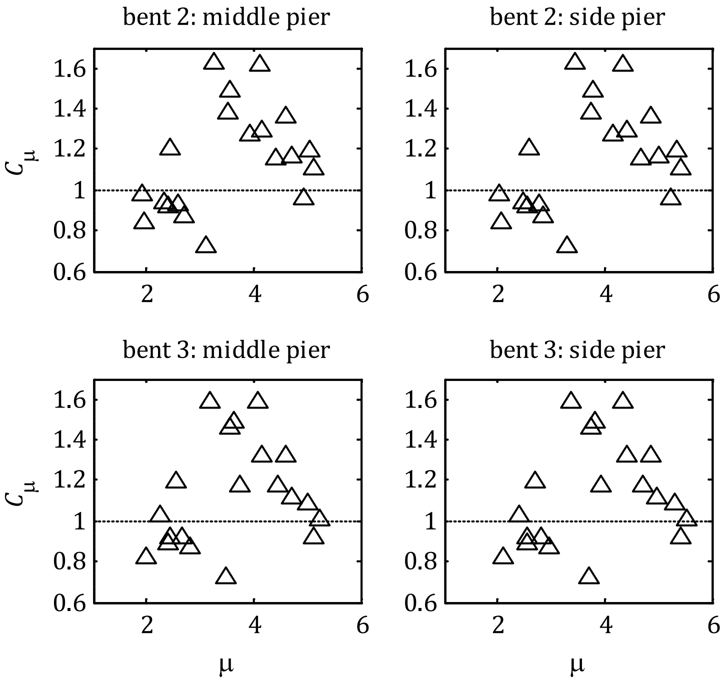
bent 2: middle pier
bent 2: side pier
bent 3: middle pier
bent 3: side pier
C_μ
μ
1.6
1.4
1.2
1
0.8
0.6
2
4
6

case 2

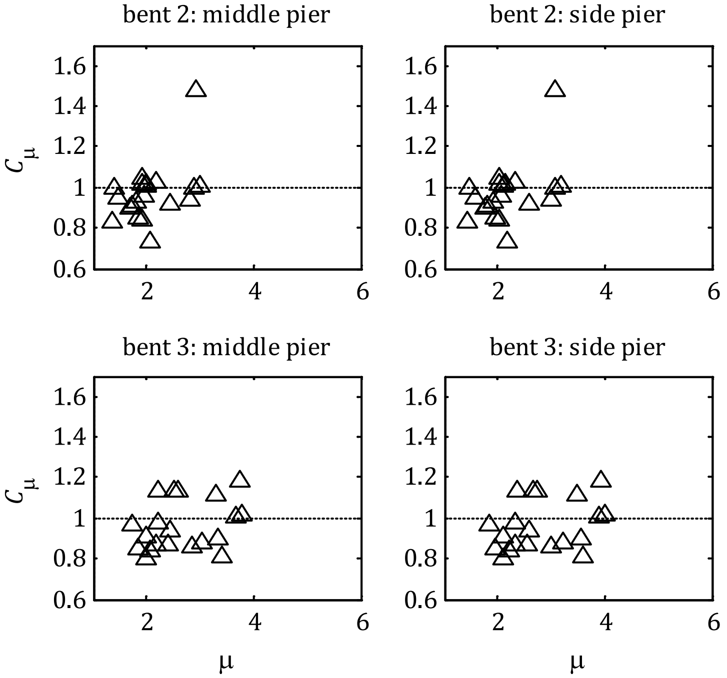
bent 2: middle pier
bent 2: side pier
bent 3: middle pier
bent 3: side pier
C_μ
μ
1.6
1.4
1.2
1
0.8
0.6
2
4
6

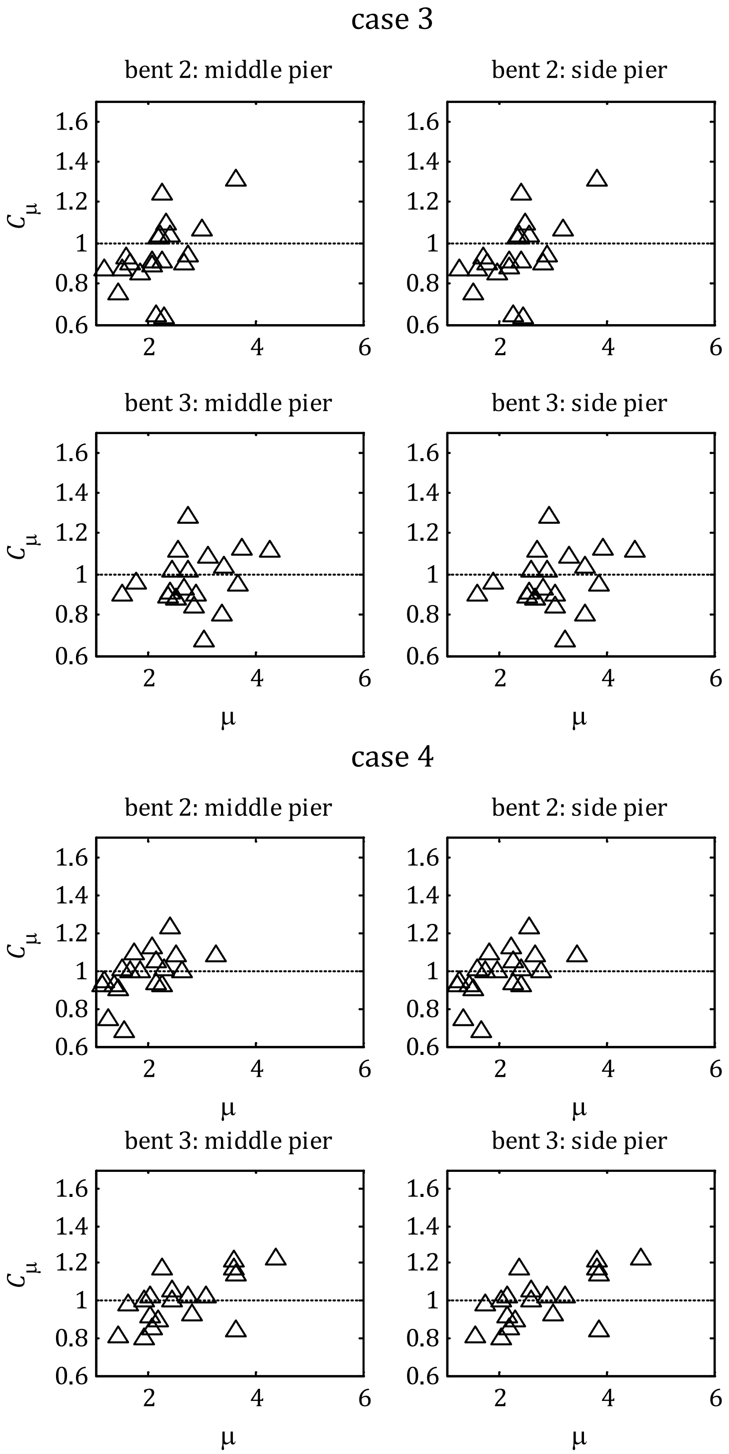

Figure 5.20: C_μ ratio versus ductility for Big Rock Wash Bridge (HSP record as seed, scaling factor = 1.5).

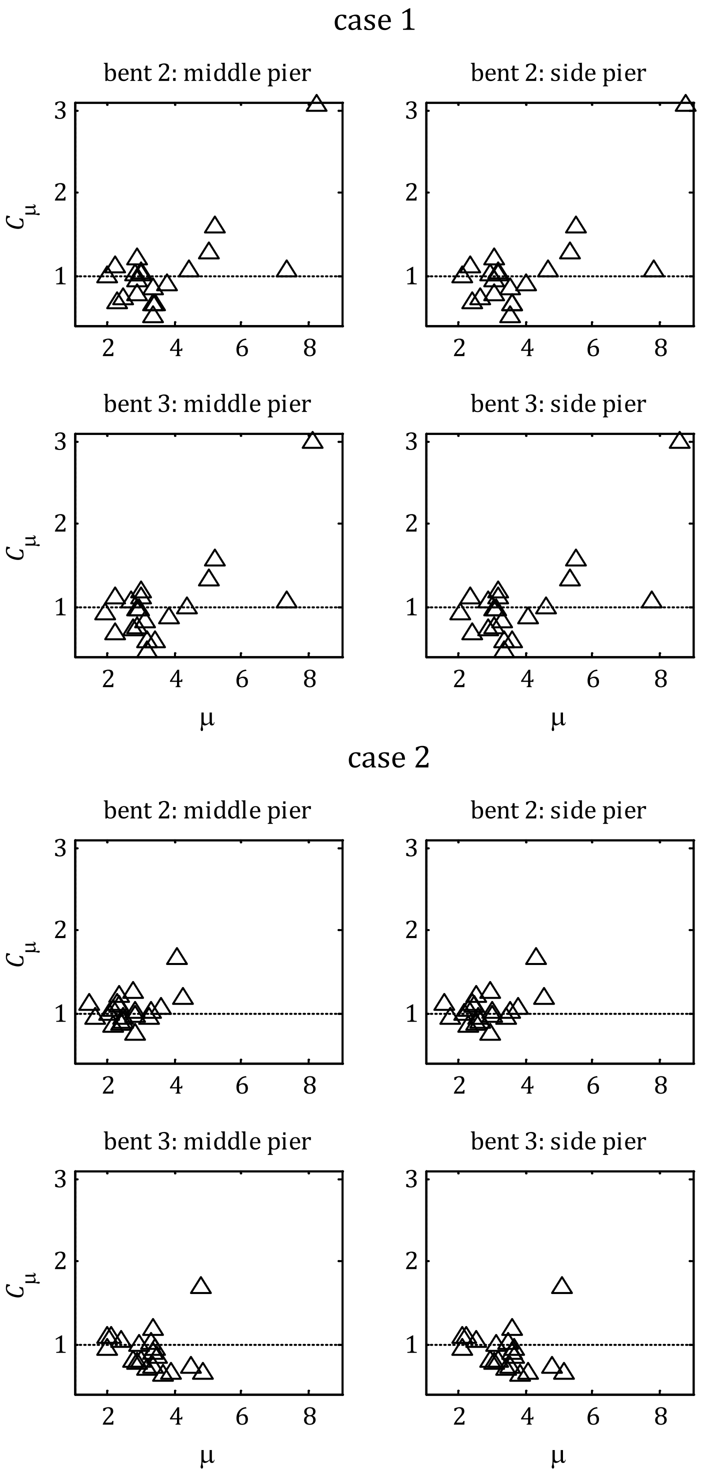

Figure 5.21: C_μ ratio versus ductility for Big Rock Wash Bridge (PUL record as seed, scaling factor = 1.0).

case 1

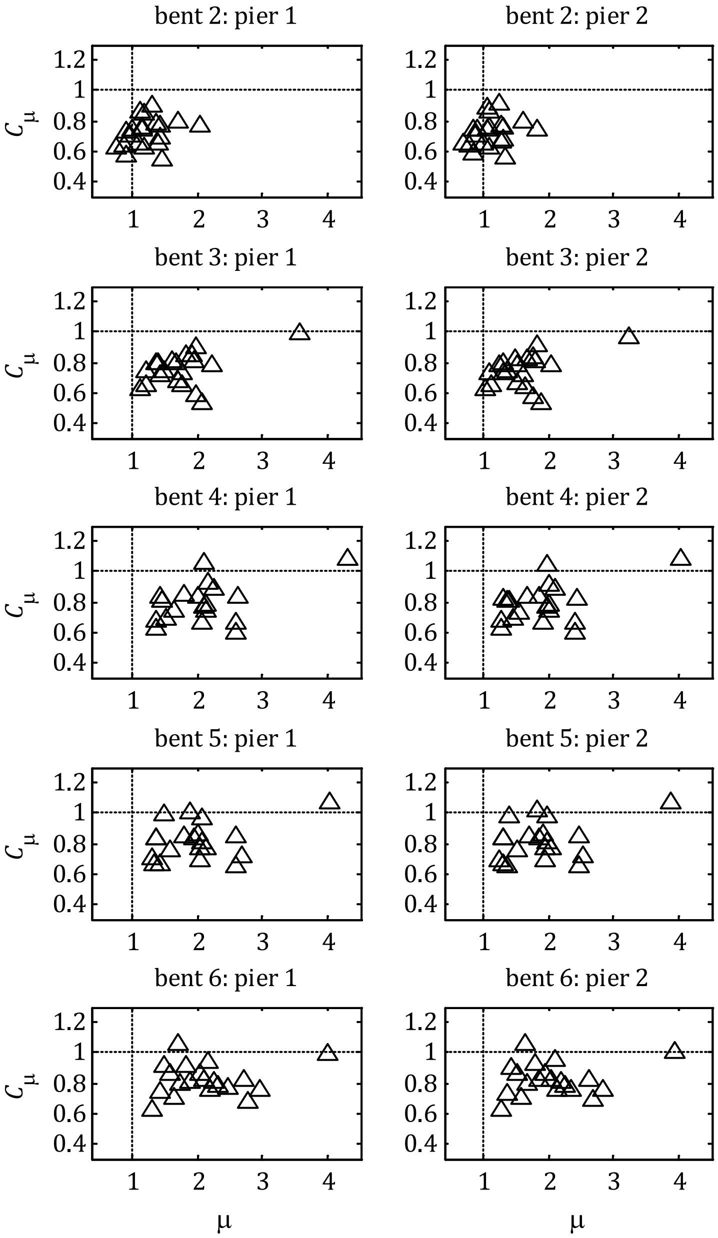
bent 2: pier 1
bent 2: pier 2
bent 3: pier 1
bent 3: pier 2
bent 4: pier 1
bent 4: pier 2
bent 5: pier 1
bent 5: pier 2
bent 6: pier 1
bent 6: pier 2
C_μ
1.2
1
0.8
0.6
0.4
1
2
3
4
μ

case 2

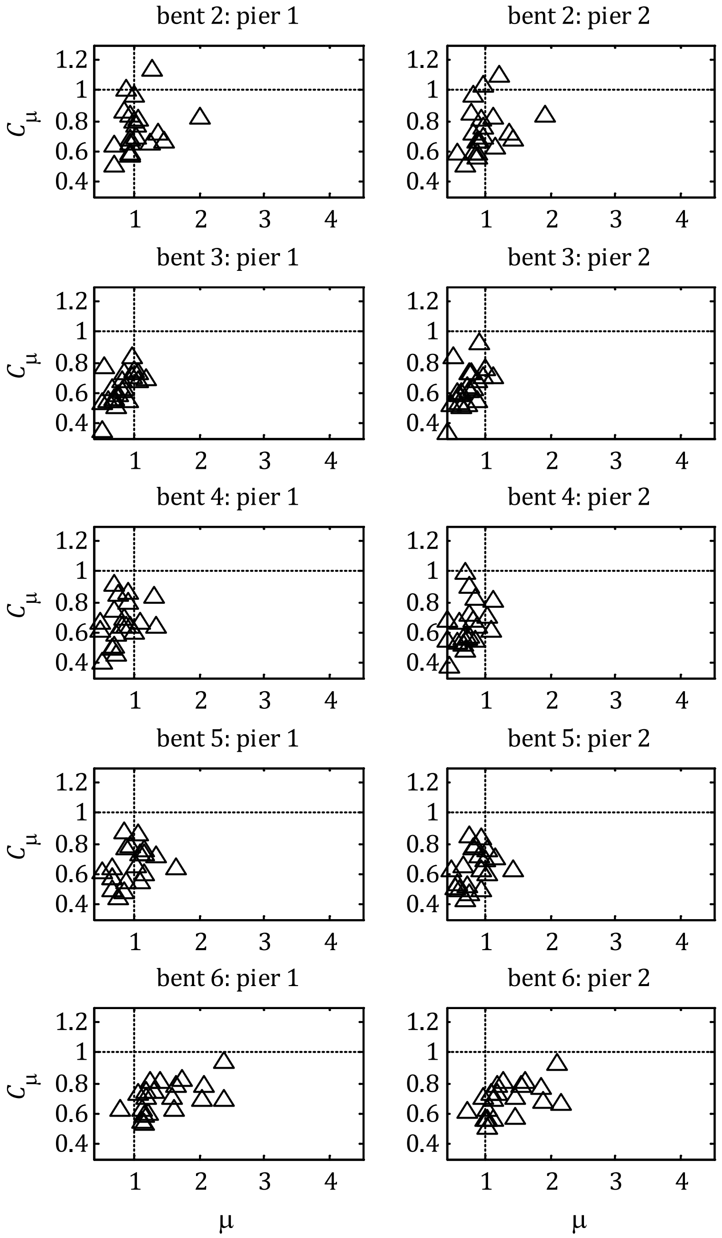
bent 2: pier 1
bent 2: pier 2
bent 3: pier 1
bent 3: pier 2
bent 4: pier 1
bent 4: pier 2
bent 5: pier 1
bent 5: pier 2
bent 6: pier 1
bent 6: pier 2
C_μ
1.2
1
0.8
0.6
0.4
1
2
3
4
μ

case 3

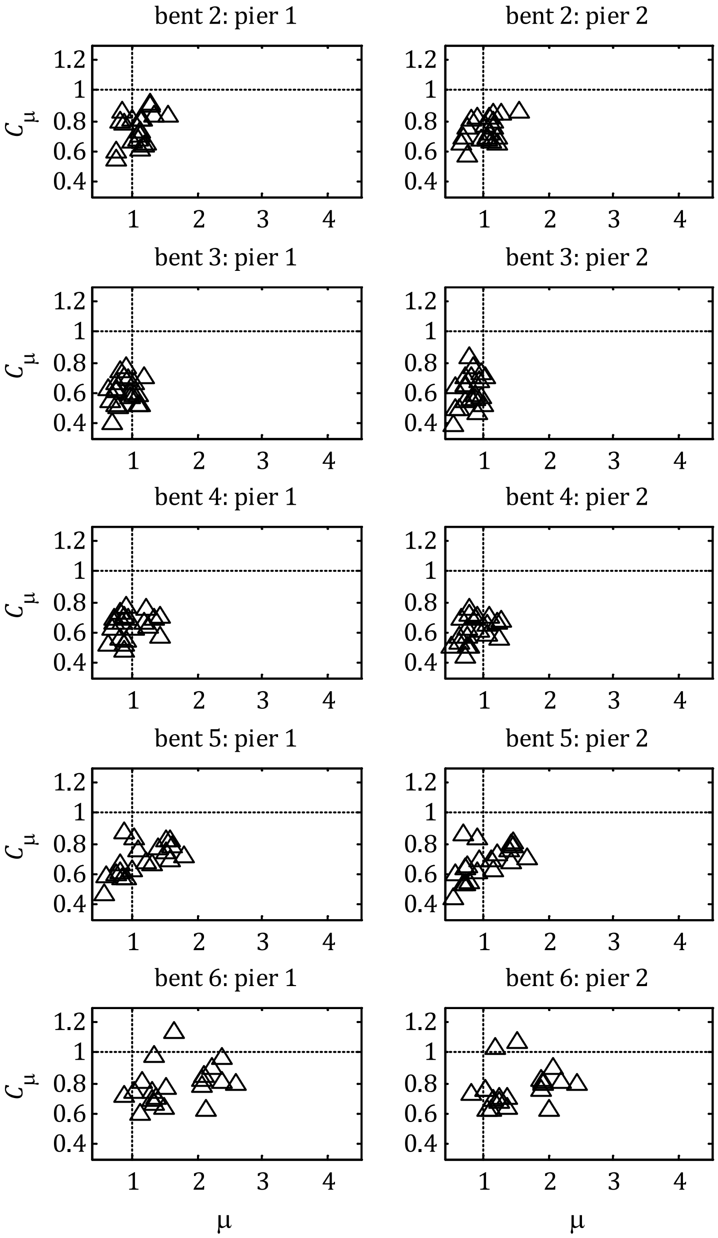
bent 2: pier 1
bent 2: pier 2
bent 3: pier 1
bent 3: pier 2
bent 4: pier 1
bent 4: pier 2
bent 5: pier 1
bent 5: pier 2
bent 6: pier 1
bent 6: pier 2
C_μ
1.2
1
0.8
0.6
0.4
1
2
3
4
μ

case 4

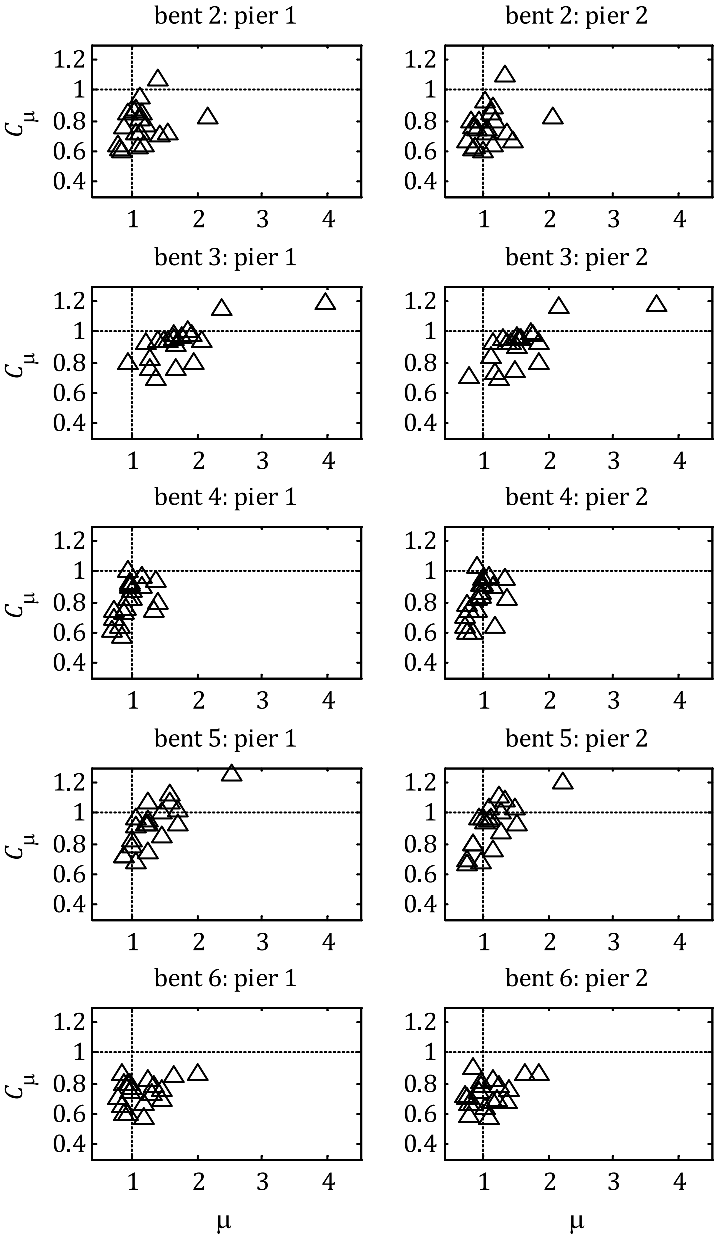

Figure 5.22: C_μ ratio versus ductility for Auburn Ravine Bridge (HSP record as seed, scaling factor = 1.5).

case 1

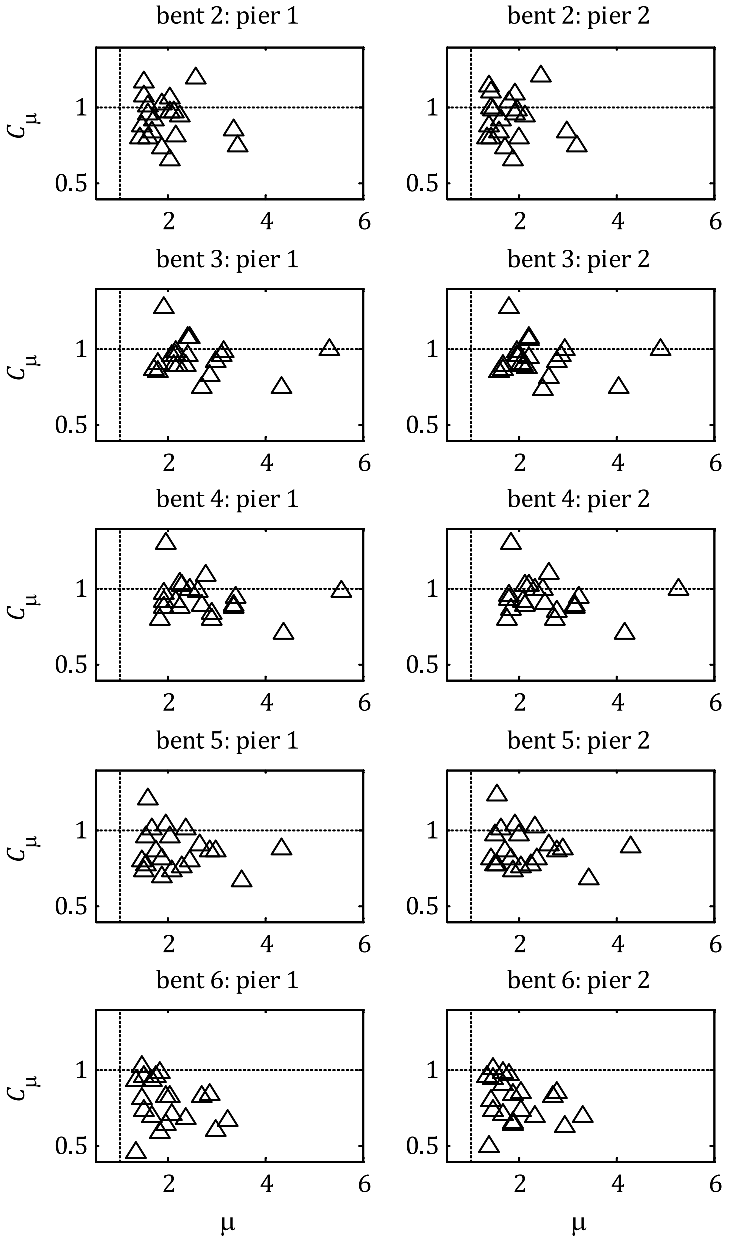
bent 2: pier 1
bent 2: pier 2
bent 3: pier 1
bent 3: pier 2
bent 4: pier 1
bent 4: pier 2
bent 5: pier 1
bent 5: pier 2
bent 6: pier 1
bent 6: pier 2
C_μ
1
0.5
2
4
6
μ

case 2

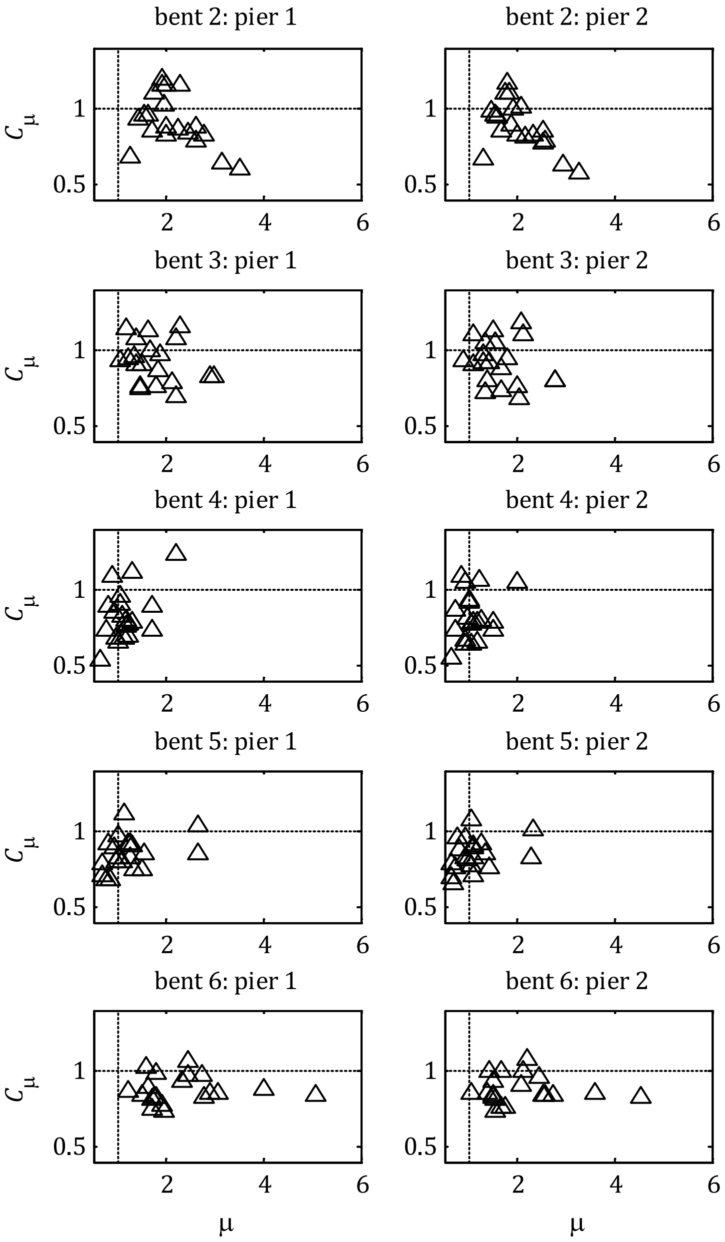

Figure 5.23: C_μ ratio versus ductility for Auburn Ravine Bridge (PUL record as seed, scaling factor = 1.0).

Chapter 6 - Coherency analysis of accelerations recorded by the UPSAR array

6.1 INTRODUCTION

In previous chapters, we used the notion of coherency function to evaluate the cross-correlation coefficients required in response spectrum analysis of multiply supported structures (Chapters 2 and 3). We also used the coherency function to determine distributions of Fourier coefficients in simulating arrays of spatially varying ground motions (Chapter 4). The complex valued coherency function was defined in Chapter 2 and models that describe its components, i.e. the incoherence, wave-passage and site-response effects, were introduced. We saw that the modulus of the coherency function represents the incoherence component, whereas the phase angle is associated with the wave-passage and site-response effects. The phase angle caused by wave-passage is evaluated in terms of the projected algebraic inter-station distance in the direction of propagation of waves and the apparent wave velocity. The phase angle caused by differential site-response is determined in terms of the frequency response functions (FRFs) of soil columns under certain simplifying assumption of upward propagating of waves. However, due to the completely random nature of the incoherence effect, it is not possible to determine a specific form for the modulus of the coherency function.

One approach to model the incoherence component is to use a theoretical model employing parameters that can be determined through statistical inference. A general form for such a theoretical model has been derived by Der Kiureghian (1996) by using a probabilistic approach. A special case is the model by Luco and Wong (1986), which we have adopted in our analysis so far. This model is based on the theory of wave propagation and describes the incoherence component in terms of the inter-station distance, the shear-wave velocity and an incoherence parameter. The incoherence parameter is estimated empirically (Luco and Wong, 1986) or determined in terms of the soil properties and depth of soil layers (Zerva and Harada, 1984). Another approach to model the incoherence component is to develop empirical models using data from recorded acceleration arrays (e.g. Harichandran and Vanmarcke, 1986; Abrahamson et al., 1991). Empirical models account for the complex phenomena that occur during wave propagation and are not captured by simplified mathematical models, but characterize only the specific rupture mechanisms and soil topographies.

In this chapter, we examine spatial variations observed during the 2004 Parkfield (California) earthquake using the UPSAR array of closely spaced acceleration records (Fletcher et al., 2006; Kim and Dreger, 2008) and compare coherency estimates from these data with existing theoretical and empirical models. The recording sites are at approximately 12km from the fault rupture, which is a shorter distance than those for most arrays used in previous studies (see, e.g., Harichandran and Vanmarcke, 1986; Abrahamson et al. 1991). Therefore, one objective of this study is to determine if there is a substantial difference in the coherency characteristics of these near-fault records relative the existing models. It is noted that, though near-fault, the records used in this study do not exhibit directivity pulses.

6.2 DESCRIPTION OF DATA

The data analyzed in this chapter consist of the acceleration time-histories recorded at 12 stations of the UPSAR array during the 2004 Parkfield earthquake of magnitude $M_w = 6.0$ (Fletcher et al., 2006; Kim and Dreger, 2008). The array is located approximately 12 km away from the fault rupture. The geometry of the station locations is shown in Figure 6.1, where each station is identified by the letter S followed by a number in the range 1-12. The horizontal and vertical axes indicate the E-W and N-S orientations, respectively. The earthquake source is located to the east of the recording sites. For the coherency analysis, station 5 is selected as the point with zero coordinates. This choice does not affect the results since we are only interested in relative station distances. The inter-station distances of all 66 station pairs vary in the range 25.0-951.9m. In the following analysis, we only consider inter-station distances in the range 0-500m and separate those in ten 50m bins. Table 6.1 lists the number of station pairs and the mean inter-station distance for each bin.

For each station, recordings of the acceleration components in the N-S, the E-W and the vertical directions are available. Each acceleration time history has a total duration of 200s and is sampled at $N = 40{,}000$ points with a time step of $\Delta t = 0.005$s. The acceleration time histories for the first 20s, which include the strong shaking phase, are shown in Figure 6.2 and Figure 6.3 for the N-S and E-W components, respectively, and in Figure 6.4 for the vertical components. A common scale for the vertical axis is selected for all horizontal components and another for all vertical components to facilitate comparison of the intensities. The peak ground accelerations (PGAs) for all components and stations are listed in Table 6.2.

6.3 POWER SPECTRAL DENSITY ESTIMATES

The acceleration time-histories in Figure 6.2 to Figure 6.4 indicate spatial variations in both intensities and frequency contents. To gain insight, we plot the acceleration PSD estimates of the N-S and E-W components in Figure 6.5 and Figure 6.6, respectively, and the PSD estimates of the vertical components in Figure 6.7. These estimates are obtained by smoothing the corresponding periodograms (see Eqn. (4.5) in Chapter 4) with a Hamming window of 0.5Hz width. Note that a common scale for the vertical axis is used for all horizontal components and another for all vertical components. In general, vertical accelerations are characterized by smaller intensities than the horizontal ones.

The PSD of surface ground acceleration at a site is influenced by the characteristics of the local soil layers. For stiffer soils, the acceleration PSD tends to be broader and richer in high-frequency components, whereas for softer soils, it tends to be narrow-band and richer in low-frequency content, sometimes exhibiting a predominant resonant frequency. Comparing Figure 6.4 with Figure 6.2, and Figure 6.4 with Figure 6.3, it appears that the vertical accelerations are more broad-band processes than the horizontal ones, suggesting that the soil is stiffer in the vertical direction. Several of the stations show predominant peaks, which may be due to local soil effects or topology. These effects are naturally included in the coherency estimates described below.

6.4 COHERENCY ESTIMATES

In this section, we present coherency estimates from the accelerograms recorded by the UPSAR array. Specifically, we examine estimates of the modulus of the coherency function, $|\gamma_{kl}|$, its real and imaginary parts, $\mathrm{Re}(\gamma_{kl})$ and $\mathrm{Im}(\gamma_{kl})$, respectively, and the coherency phase angle, θ_{kl}. See Section 2.2.3 for the definitions of these quantities. Estimates of these coherency measures are obtained as functions of frequency for each inter-station distance bin and for the horizontal and vertical components separately. In estimating the coherency of the horizontal components, we do not account for any directional dependence, i.e., we combine the results for the N-S and E-W components.

The steps involved in estimating each of the above functions for a given inter-station distance bin and pair of acceleration components (or horizontal or vertical) are the following:

1. For each pair of accelerograms in the inter-station distance bin and for the component direction considered:
    a. Evaluate the real and imaginary parts of the cross-periodogram using Eqns. (4.6) (in Chapter 4) and smooth them using a Hamming window of a selected width. This represents an estimate of the cross-PSD of the pair of accelerograms.
    b. Evaluate the periodogram for each component of the pair and smooth it using a Hamming window having the same width as that used in step 1a. This represents an estimate of the auto-PSD of the accelerogram.
    c. Use the estimates of the auto- and cross-PSDs to evaluate $\mathrm{Re}(\gamma_{kl})$ and $\mathrm{Im}(\gamma_{kl})$, where γ_{kl} is defined as in Eqn. (2.17) of Chapter 2.
    d. Use the estimates of $\mathrm{Re}(\gamma_{kl})$ and $\mathrm{Im}(\gamma_{kl})$ from step 1c to evaluate $|\gamma_{kl}| = \left\{[\mathrm{Re}(\gamma_{kl})]^2 + [\mathrm{Im}(\gamma_{kl})]^2\right\}^{1/2}$ and $\theta_{kl} = \tan^{-1}[\mathrm{Im}(\gamma_{kl})/\mathrm{Re}(\gamma_{kl})]$.
2. For each of the functions $\mathrm{Re}(\gamma_{kl})$, $\mathrm{Im}(\gamma_{kl})$, $|\gamma_{kl}|$ and θ_{kl}, we average the estimates obtained in steps 1c-1d for all pairs in the bin for the considered component. For the horizontal components, we average the estimates in both N-S and E-W directions. We note that each considered pair consists of records in the same direction.

Estimation of auto- and cross-PSDs through the cross-periodograms and periodograms is valid for stationary processes, but is applied here under the assumption that the strong-motion segment of the accelerograms, which accounts for most of the power in the frequency domain, is nearly stationary. The results of the analysis are shown in Figure 6.8 to Figure 6.15. In these figures, each inter-station distance bin is represented by the middle point of the corresponding range and is denoted as d_{kl}.

Figure 6.8 and Figure 6.9 show estimates of the modulus of the coherency function, $|\gamma_{kl}|$, for the horizontal and vertical components, respectively, and for three levels of smoothing corresponding to Hamming-window widths of 0.25 Hz, 0.50 Hz and 1 Hz. We note that, for a given window width, the smoothness of the coherency estimate varies depending on the number of station pairs in the inter-station distance bin. As expected, both the vertical and horizontal estimates for bin 7 (inter-station distances 300-350m) are smoothest because that bin has the largest number of records (13), see Table 6.1.

Consider the estimates in Figure 6.8 and Figure 6.9 for the horizontal and vertical components, respectively, which are produced for three levels of the Hamming window widths. In general, the wider the smoothing window, the more biased the coherency estimates is. As a result, for the higher level of smoothing considered, i.e. for the 1Hz window width, estimates of the modulus of coherency deviate from the theoretical unity value at zero frequency. On the other hand, for the lower level of smoothing considered, i.e. for the 0.25Hz window width, the estimates are too jagged, which makes it difficult to interpret the results and identify trends. Thus, we select the 0.50Hz Hamming window width as the most appropriate for our analysis. In the following, we only examine coherency estimates for this level of smoothing.

Figure 6.8 and Figure 6.9 indicate decay of the modulus of the coherency function with increasing frequency and increasing inter-station distance. We note a slightly faster decay of the coherency modulus for the vertical components relative to that of the horizontal components, except for the 1st bin. At high frequencies, the estimate of the coherency modulus does not approach zero, even for large distance bins. The value approached represents the coherency of the random noise in the recorded motions.

Figure 6.10 and Figure 6.11 show estimates of the real part of the coherency function, $\mathrm{Re}(\gamma_{kl})$, for the horizontal and vertical components, respectively. In the absence of wave passage and for similar soil conditions, $|\gamma_{kl}|$ and $\mathrm{Re}(\gamma_{kl})$ are identical. Thus, the differences between the estimates in Figure 6.8 and Figure 6.10 and between the estimates in Figure 6.9 and Figure 6.11 are indicative of the wave-passage and site-response effects. These differences are greater when the actual coherency approaches zero. In these regions, the estimates of the real parts tend to be scattered on either side of zero, whereas the estimates of the coherency modulus are always positive. Thus, smoothing with a wider window would result in nearly zero estimates for the real parts, but not for the modulus.

Figure 6.12 and Figure 6.13 show estimates of the imaginary part of the coherency function, $\mathrm{Im}(\gamma_{kl})$, for the horizontal and vertical components, respectively. These figures are rather hard to interpret because of the small values of the imaginary parts of the coherency function and the large scatter due to noise when the actual coherency is small. However, for each bin, we can identify the frequency ranges dominated by noise by comparison with the corresponding graphs in Figure 6.8 and Figure 6.9, in which these ranges are more apparent.

Figure 6.14 and Figure 6.15 show estimates of the coherency phase angle function, θ_{kl}, which is wrapped within the interval $-1 \leq \theta_{kl}/\pi \leq 1$, for the horizontal and vertical components, respectively. Again, we can identify the frequency ranges that are dominated by noise by comparing with the graphs in Figure 6.8 and Figure 6.9, respectively. For other frequencies, phase angles tend to increase with increasing frequency and separation distance.

6.5 COMPARISON OF COHERENCY ESTIMATES WITH EXISTING MODELS

6.5.1 Comparison with theoretical model

In this section, we examine how the coherency estimates from the UPSAR recordings compare with the theoretical model by Luco and Wong (1986). This model was introduced in Chapter 2 (see Eqn. (2.19)) and describes the incoherence component in terms of the inter-station distance, d_{kl}, the shear-wave velocity, v_s, and a single incoherence parameter, α. Luco and Wong suggested that typical values of the ratio α/v_s are in the range $(2-3) \times 10^{-4}$. In the following, we determine values of the ratio α/v_s that fit the estimates of the modulus of the coherency function obtained for the UPSAR data.

First consider the coherency estimates of the horizontal components. We apply the MATLAB non-linear least-squares minimization algorithm on the variance-stabilizing transformation of the coherency modulus, $\tanh^{-1}|\gamma_{kl}|$ (Brillinger, 2001). Estimates of $\tanh^{-1}|\gamma_{kl}|$ are obtained by applying the procedure described in Section 6.4, but for $\tanh^{-1}|\gamma_{kl}|$ instead of $|\gamma_{kl}|$ in step 1d. In Section 6.4, we saw that for large frequencies, the coherency estimates tend to be dominated by noise. This is not captured by the Luco and Wong model which gives asymptotically zero values for large frequencies. Thus, we expect that the range of frequencies considered in the least-squares minimization process may affect the results. In Table 6.3, for each inter-station distance bin, we list the values of α/v_s obtained by fitting in the range of frequencies $(0, \omega_{end})$, with $\omega_{end}/2\pi$ taking the values 2, 4 and 8Hz. We note that, with the exception of the first bin, the results are not affected or are only slightly affected by the choice of ω_{end}. Figure 6.16 compares the estimates of $\tanh^{-1}|\gamma_{kl}|$ with the fitted Luco and Wong model for the α/v_s values obtained when $\omega_{end}/2\pi = 4$Hz. For the same values of α/v_s, Figure 6.17 compares the estimated and fitted curves for $|\gamma_{kl}|$.

A similar analysis is repeated for the coherency of the vertical components. Table 6.4 shows the values of α/v_s obtained by fitting in the same ranges of frequencies considered for the horizontal components. We note that the choice of ω_{end} affects the results in the first three bins. Figure 6.18 compares the estimates of $\tanh^{-1}|\gamma_{kl}|$ with the fitted Luco and Wong model for the α/v_s values obtained when $\omega_{end}/2\pi = 4$Hz. For the same values of α/v_s, Figure 6.19 compares the estimated and fitted curves for $|\gamma_{kl}|$.

We note that if we were to fit $|\gamma_{kl}|$ instead of $\tanh^{-1}|\gamma_{kl}|$, the results would be largely affected by the choice of ω_{end}, which should be carefully selected so that the region dominated by noise is excluded. This would obviously involve more subjectivity. It is also noted that the estimated values of α/v_s in Table 6.3 and Table 6.4 are somewhat larger than the range suggested by Luco and Wong (1986). This could be due the topology of the recording sites, or due to the near-source nature of the recordings. Comparing Table 6.3 and Table 6.4, it is clear that the decay of coherency with frequency is faster for the vertical components than the horizontal components.

6.5.2 Comparison with empirical models

In this section, we compare the estimates of the coherency modulus from the UPSAR data with two well-known empirical models: the model by Harichandran and Vanmarcke (1986) and the model by Abrahamson et al. (1991).

Harichandran and Vanmarcke developed a coherency model using horizontal recordings from SMART 1 array in Taiwan, which is characterized by a minimum station spacing of 100m. This model is based on data from one far-field event and describes the modulus of coherency as

$$|\gamma_{kl}| = A \exp\left[-\frac{2\nu}{\alpha\,\theta(\omega)}(1 - A + \alpha A)\right] + (1 - A)\exp\left[-\frac{2\nu}{\theta(\omega)}(1 - A + \alpha A)\right] \tag{6.1}$$

where $\theta(\omega) = k\left[1 + (\omega/\omega_0)^b\right]^{-1/2}$, $A = 0.736$, $\alpha = 0.147$, $k = 5210$, $\omega_0 = 1.09/2\pi$ and $b = 2.78$. Abrahamson et al. used data from fifteen earthquakes recorded by the Lotung LSST array, which is a dense array located within the SMART 1 array. The set of data includes both near-fault and far-field records. The model was derived from analysis of the horizontal components only and for separation distances < 100m. According to this model, $\tanh^{-1}|\gamma_{kl}|$ is given by

$$\tanh^{-1}|\gamma_{kl}| = (2.54 - 0.012d_{kl})\{\exp[(-0.115 - 0.00084d_{kl})f] + (1/3)f^{-0.878}\}+0.35 \tag{6.2}$$

where $f = \omega/2\pi$.

In Figure 6.20, we compare the estimates of the coherency modulus from the horizontal UPSAR accelerograms with the model by Harichandran and Vanmarcke for distances > 100m, i.e. for the inter-station distance bins 3-10. The coherency estimates from the UPSAR data differ significantly from the coherency described by this model. We note that for frequencies close to zero, the model by Harichandran and Vanmarcke gives values smaller than unity, which is not reasonable. Earlier, we saw that the estimated coherency for zero values depends on the level of smoothing (see Figure 6.8 and Figure 6.9). But, on physical grounds, the modulus of coherency function must approach 1 at zero frequency since waves of infinite wavelength are perfectly coherent. Figure 6.20 shows that for small frequencies, the coherency of the UPSAR accelerograms decays at a much faster rate than the coherency described by the Harichandran and Vanmarcke model. However, for larger frequencies, when noise is dominant, the model by Harichandran and Vanmarcke gives smaller coherency values.

In Figure 6.21, we compare the estimates of $\tanh^{-1}|\gamma_{kl}|$ from the horizontal UPSAR accelerograms with the model of Abrahamson et al. for distances < 100m, i.e. for the first two inter-station distance bins. In Figure 6.22, we plot the corresponding curves for the modulus of coherency, $|\gamma_{kl}|$. In contrast with the model by Harichandran and Vanmarcke, the model of Abrahamson et al. describes perfectly coherent motions at zero frequency. However, in the range of frequencies of interest (when noise is not dominant), the coherency of the UPSAR accelerograms decays at a much slower rate than the coherency represented by the Abrahamson et al. model. This empirical model also corrects for the effect of noise on the coherency at large frequencies.

6.6 SUMMARY

In this chapter, we investigated spatial variations in the accelerograms recorded by the UPSAR array during the 2004 Parkfield earthquake. The recordings indicate significant variations in the acceleration intensities and frequency contents. The coherency estimates obtained from these recordings were fitted to the theoretical model by Luco and Wong (1986) compared with commonly used empirical models by Harichandran and Vanmarcke (1986) for distances > 100m, and by Abrahamson et al. (1991) for distances < 100m. The coherency modulus estimated from the UPSAR array diverged significantly from those given by both empirical models in the range of frequencies of interest. The model by Harichandran and Vanmarcke described a slower decay of the coherency modulus than that estimated from the UPSAR array, whereas the model by Abrahamson et al. described a much faster decay. The theoretical model by Luco and Wong (1986), when fitted to the estimated modulus of coherency provided a fairly good approximation of the incoherence component of the UPSAR recordings, but for larger values of the incoherence parameter α/v_s than recommended values. This can be attributed to the particularly anomalous topography of the site of the UPSAR array, or to near-source effects. Further analysis with near-source array recordings need to be conducted to determine if this phenomenon is indeed a near-source effect. Finally, the UPSAR recordings suggest a faster decay of coherency with frequency for vertical components than for horizontal components

Table 6.1: Distance bins for station pairs.

Bin number	Distance range (m)	Number of station pairs	Mean distance (m)
1	0-50	3	31.1
2	50-100	1	88.7
3	100-150	5	129.8
4	150-200	3	183.7
5	200-250	5	222.7
6	250-300	4	274.8
7	300-350	13	334.4
8	350-400	4	377.6
9	400-450	4	422.3
10	450-500	5	478.2

Table 6.2: PGA (in units of g) for each component and station.

Component	Station number											
	1	2	3	4	5	6	7	8	9	10	11	12
N-S	0.14	0.17	0.15	0.24	0.23	0.38	0.18	0.20	0.28	0.36	0.25	0.23
E-W	0.18	0.31	0.25	0.37	0.25	0.33	0.26	0.28	0.31	0.47	0.22	0.30
Vertical	0.09	0.09	0.11	0.18	0.11	0.19	0.13	0.14	0.17	0.24	0.11	0.16

Table 6.3: Estimated values of $(\alpha/v_s)*10^{-4}$ for horizontal components.

$\omega_{end}/2\pi$ (Hz)	d_{kl} (m)									
	25	75	125	175	225	275	325	375	425	475
2	8	8	5	5	4	4	4	4	3	3
4	11	6	4	4	3	3	3	4	3	3
8	9	5	3	3	3	3	3	4	3	3

Table 6.4: Estimated values of $(\alpha/v_s)*10^{-4}$ for vertical components.

$\omega_{end}/2\pi$ (Hz)	d_{kl} (m)									
	25	75	125	175	225	275	325	375	425	475
2	11	10	6	5	5	6	5	5	5	5
4	10	10	5	4	5	5	5	5	5	5
8	9	9	4	4	5	5	5	5	5	5

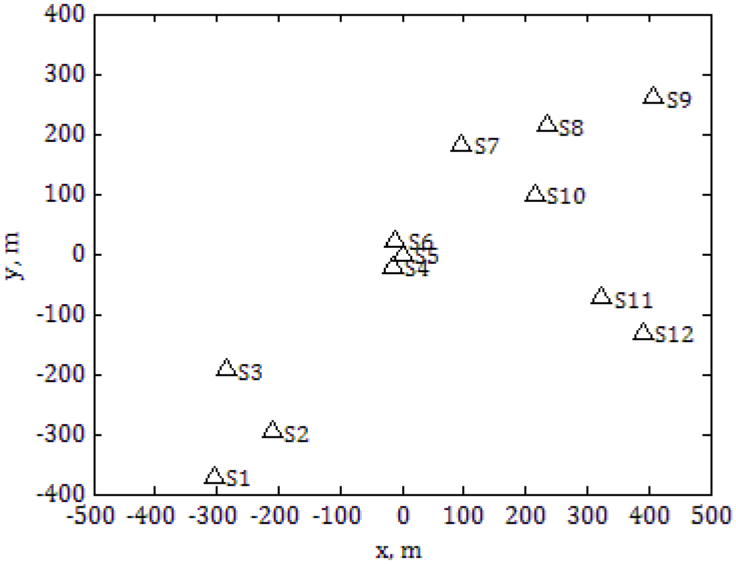

Figure 6.1: Geometry of UPSAR array.

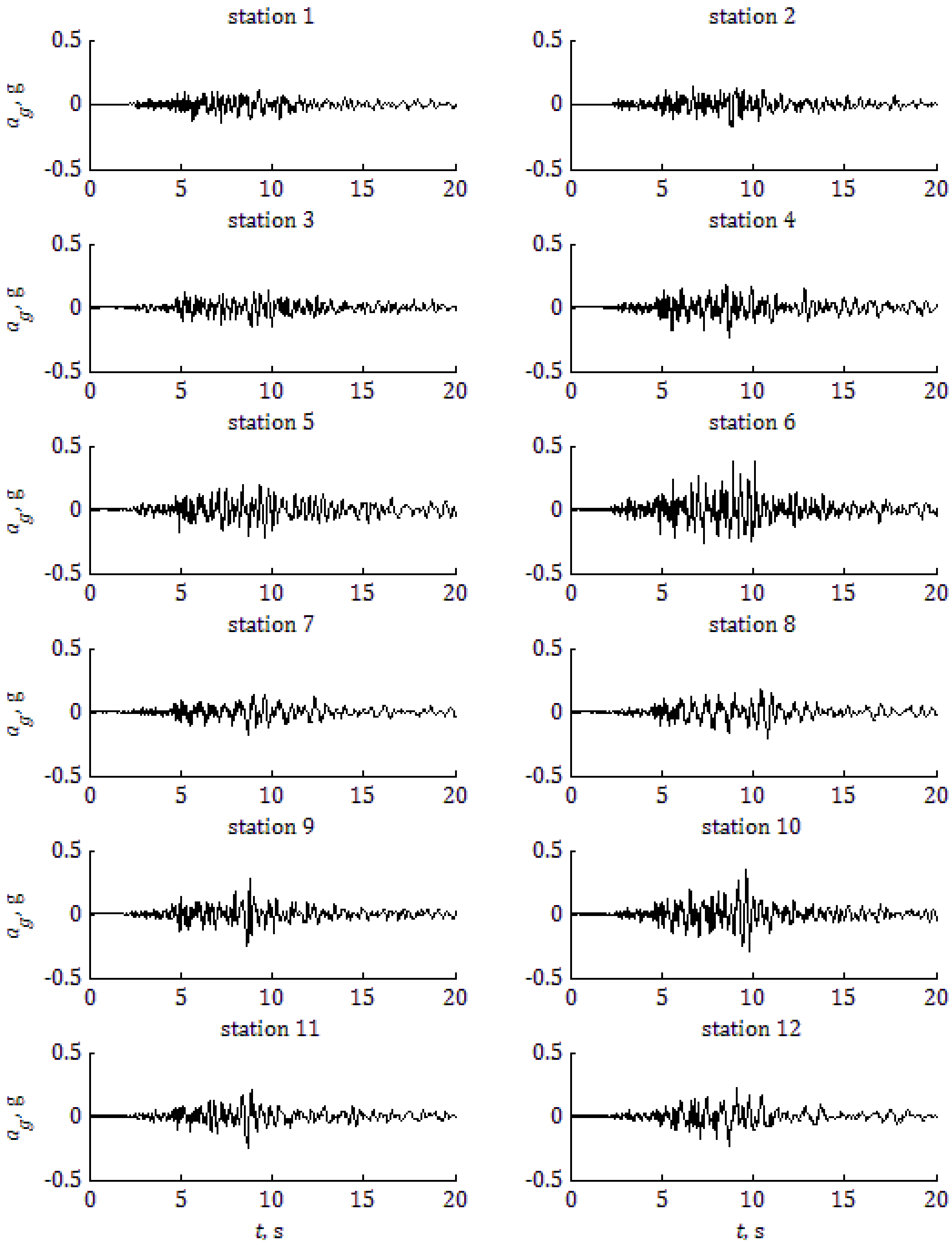

Figure 6.2: Acceleration time histories of the N-S components.

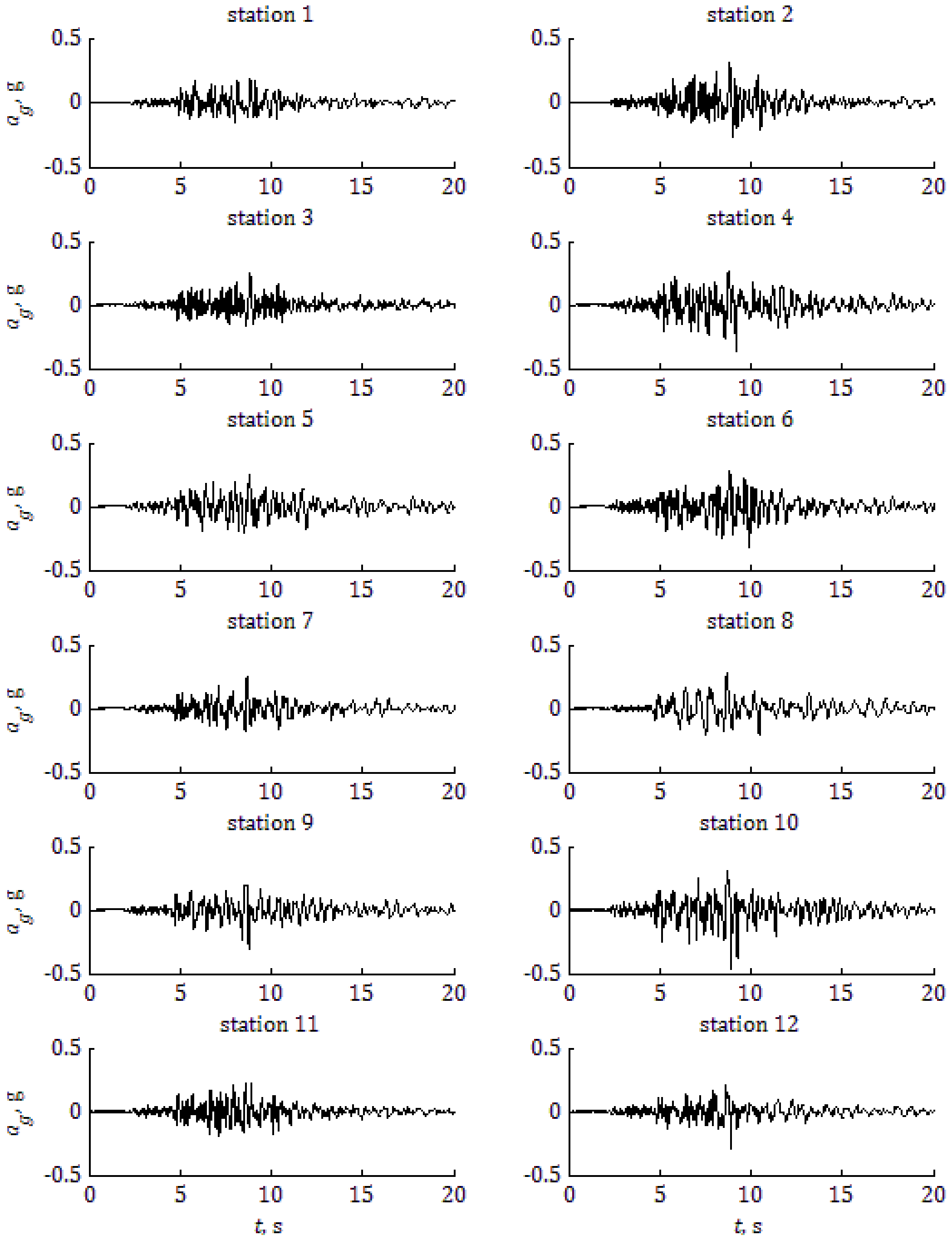

Figure 6.3: Acceleration time histories of the E-W components.

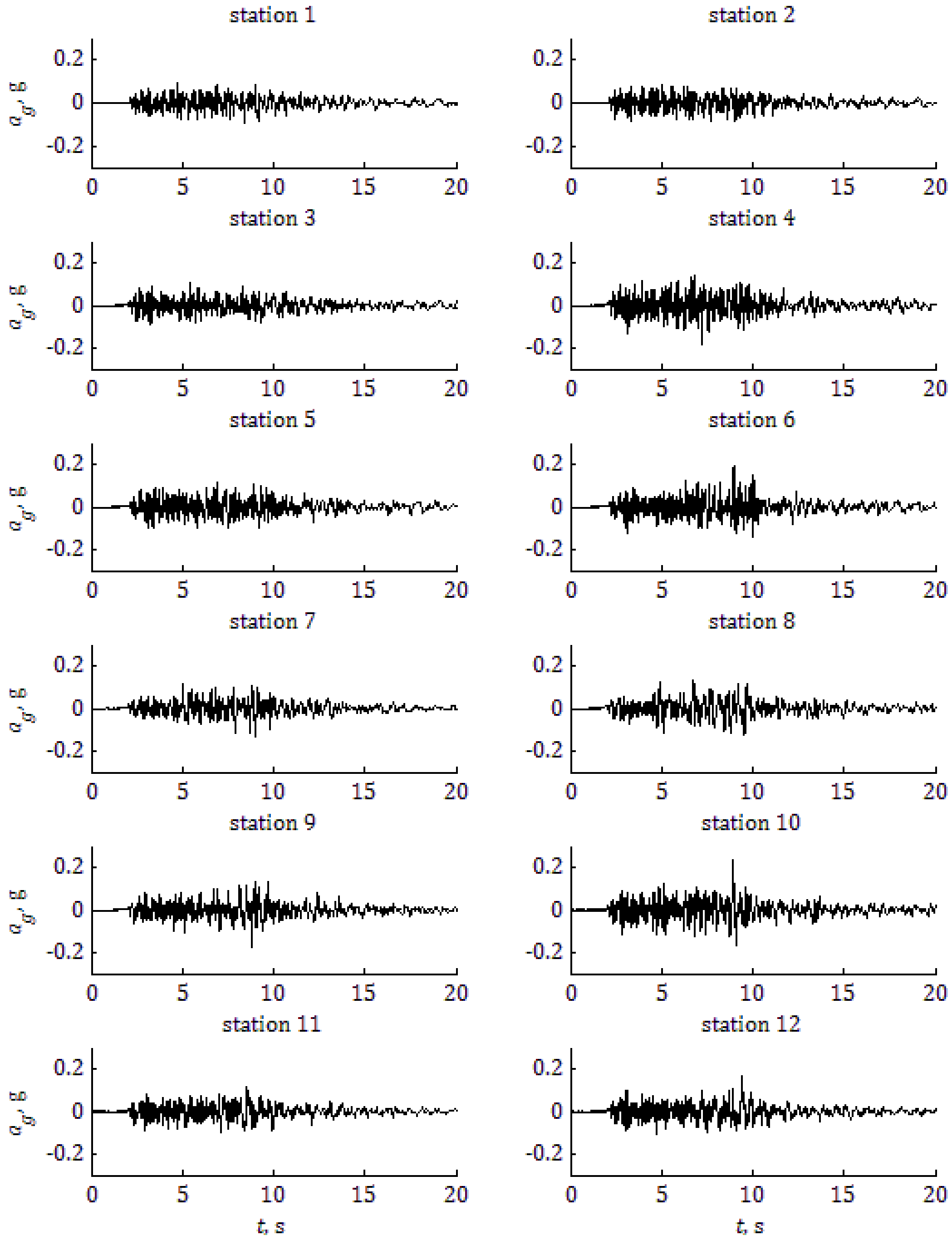

Figure 6.4: Acceleration time histories of the vertical components.

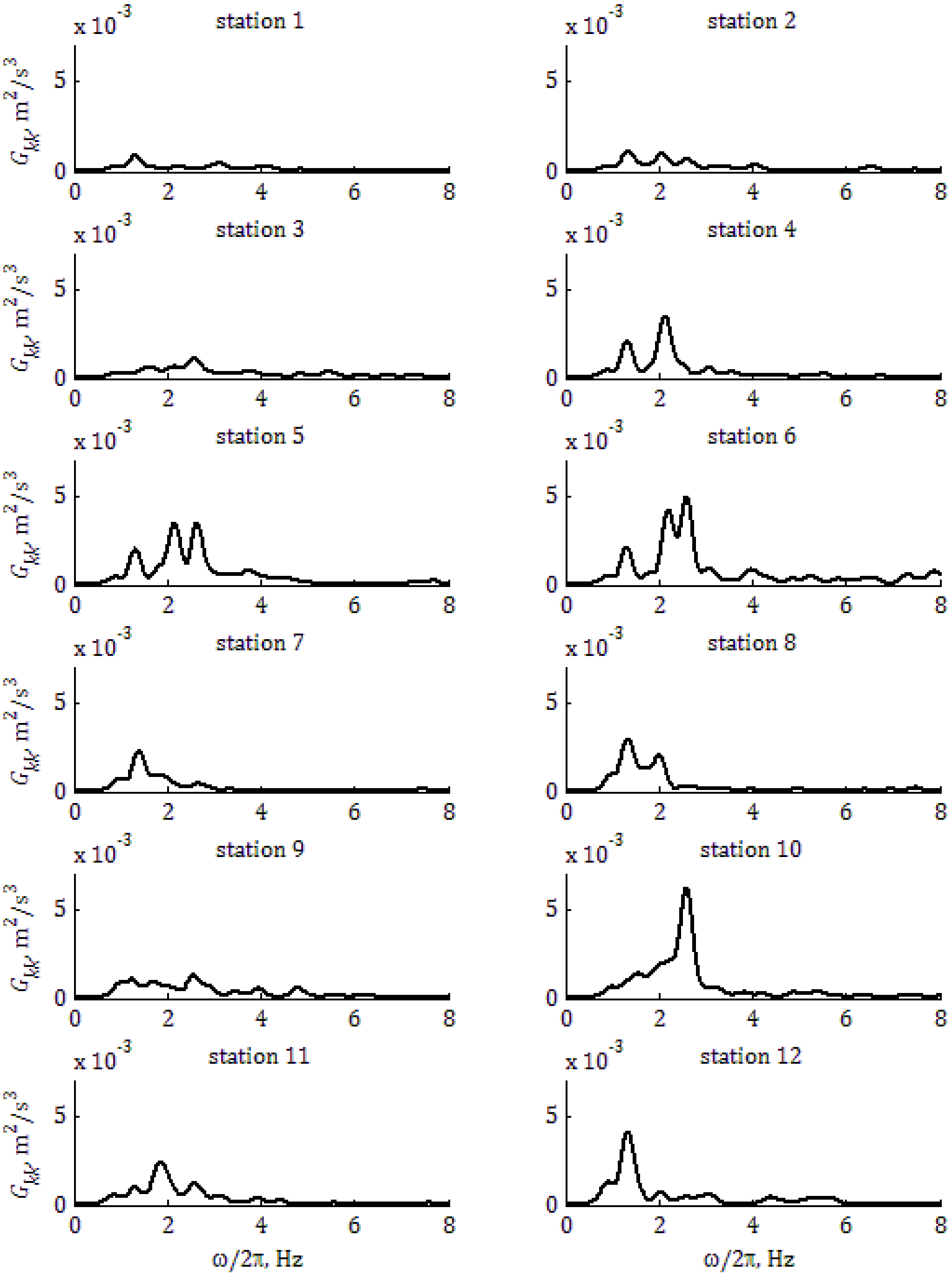

Figure 6.5: Estimated acceleration PSDs of N-S components.

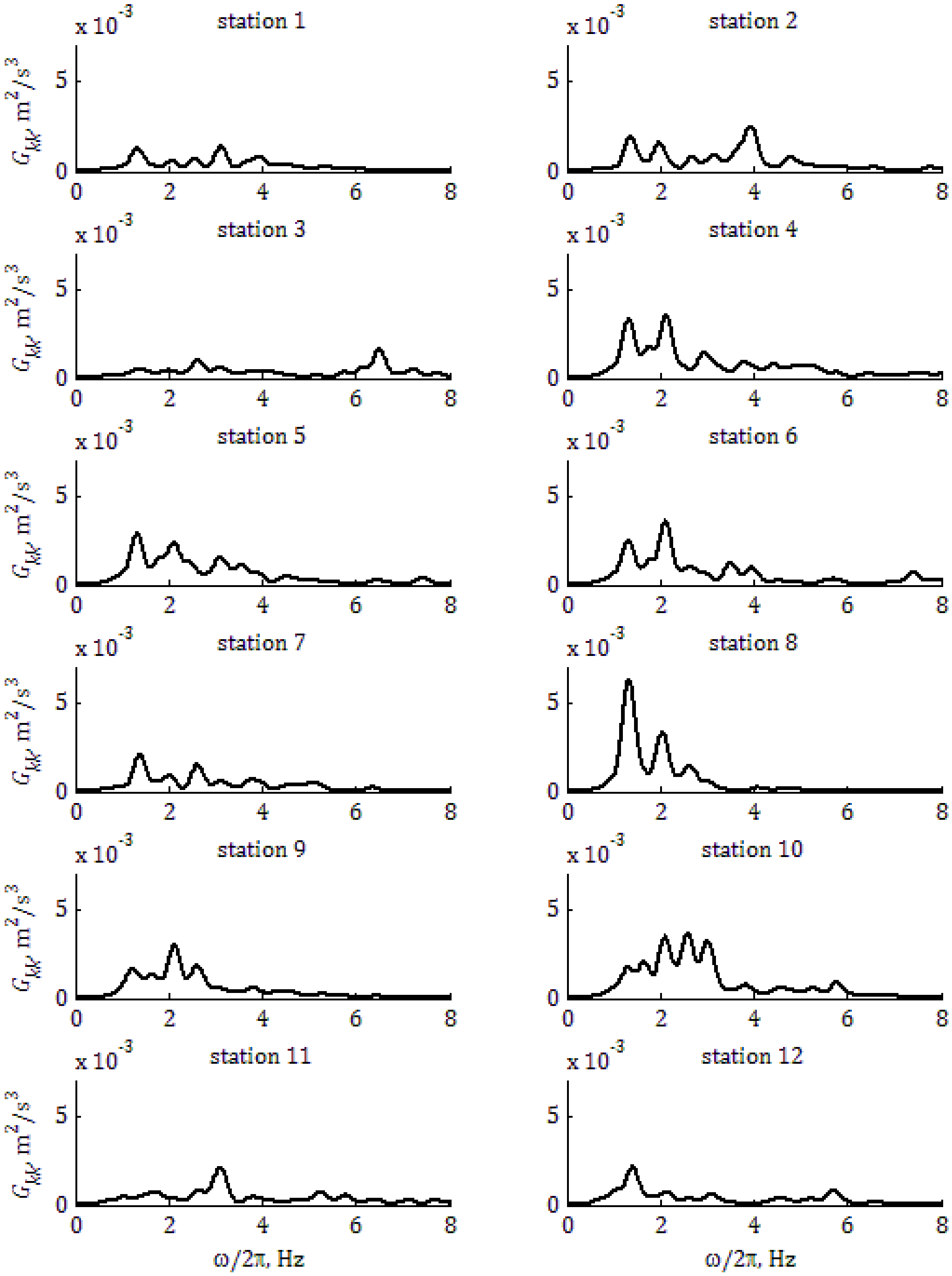

Figure 6.6: Estimated acceleration PSDs of E-W components.

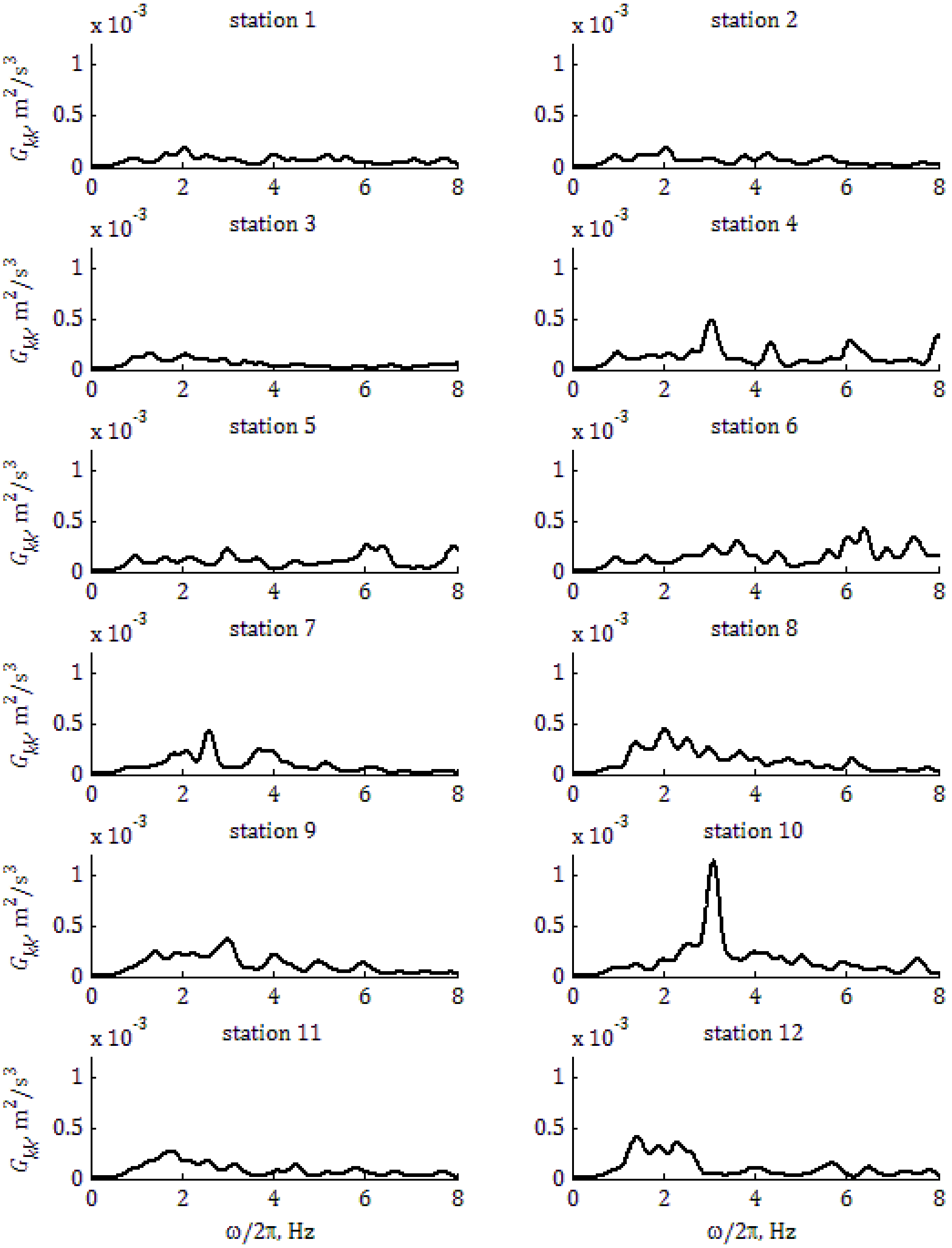

Figure 6.7: Estimated acceleration PSDs of vertical components.

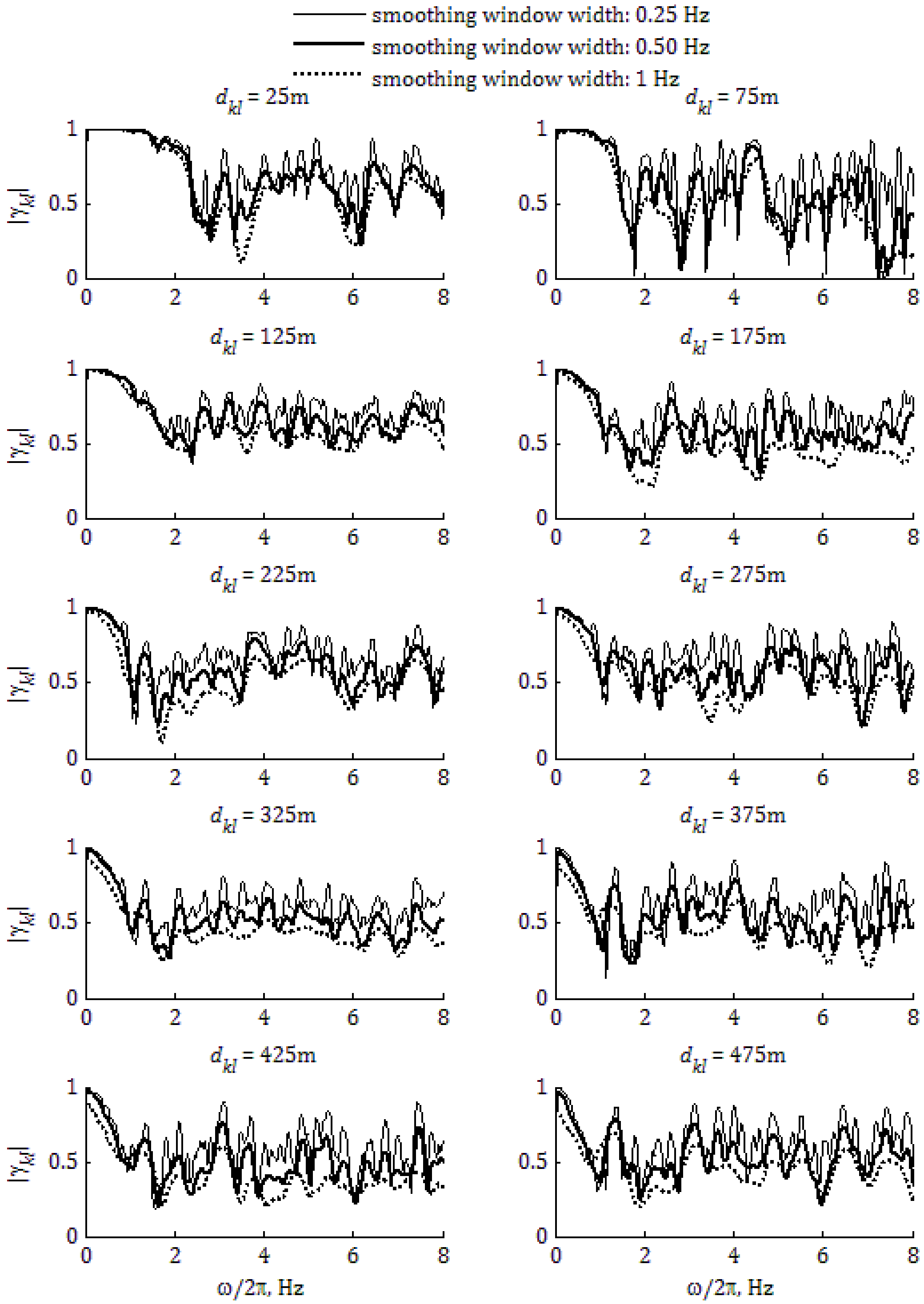

Figure 6.8: Estimates of coherency modulus for the horizontal components for 3 levels of smoothing.

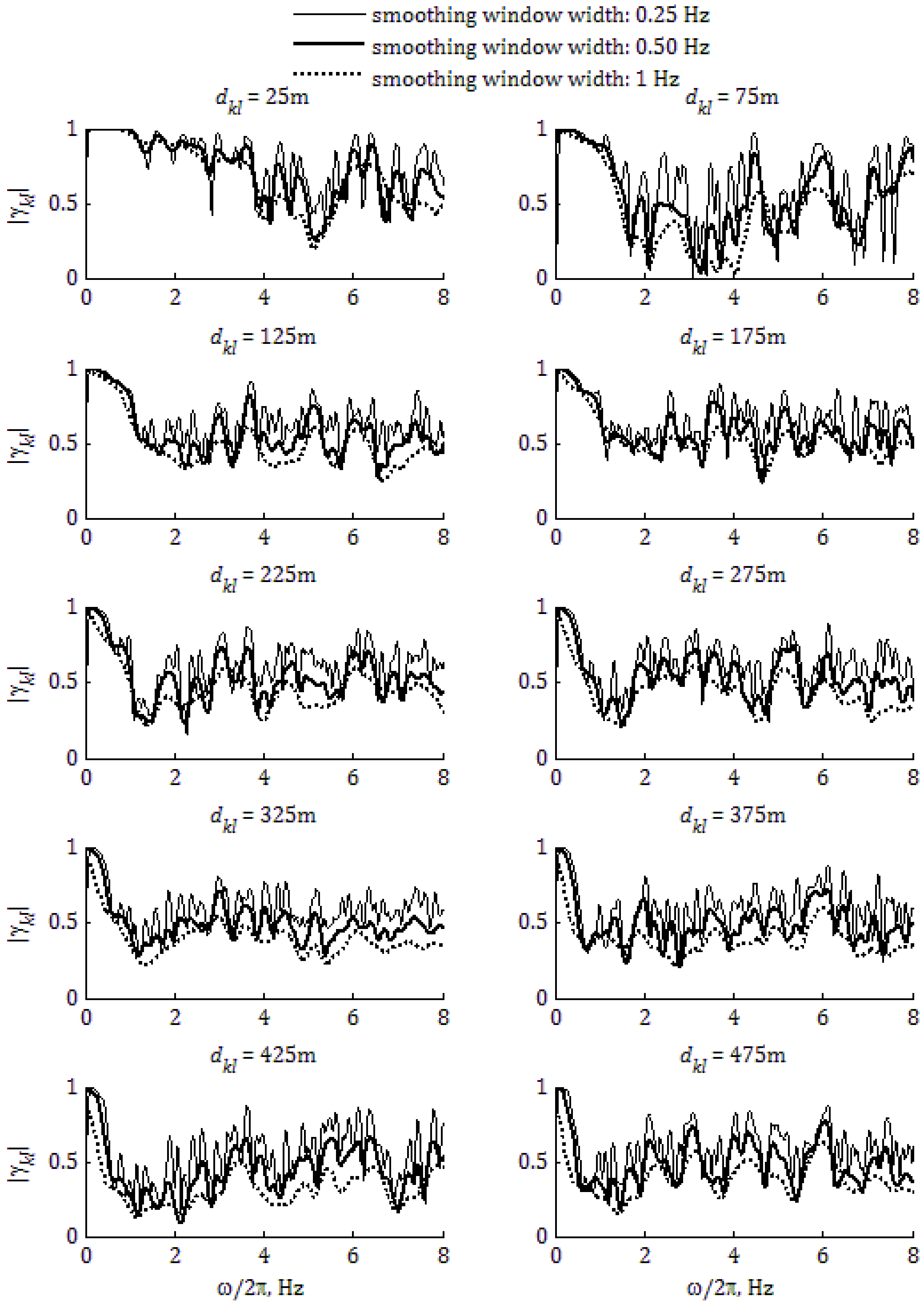

Figure 6.9: Estimates of coherency modulus for the vertical components for 3 levels of smoothing.

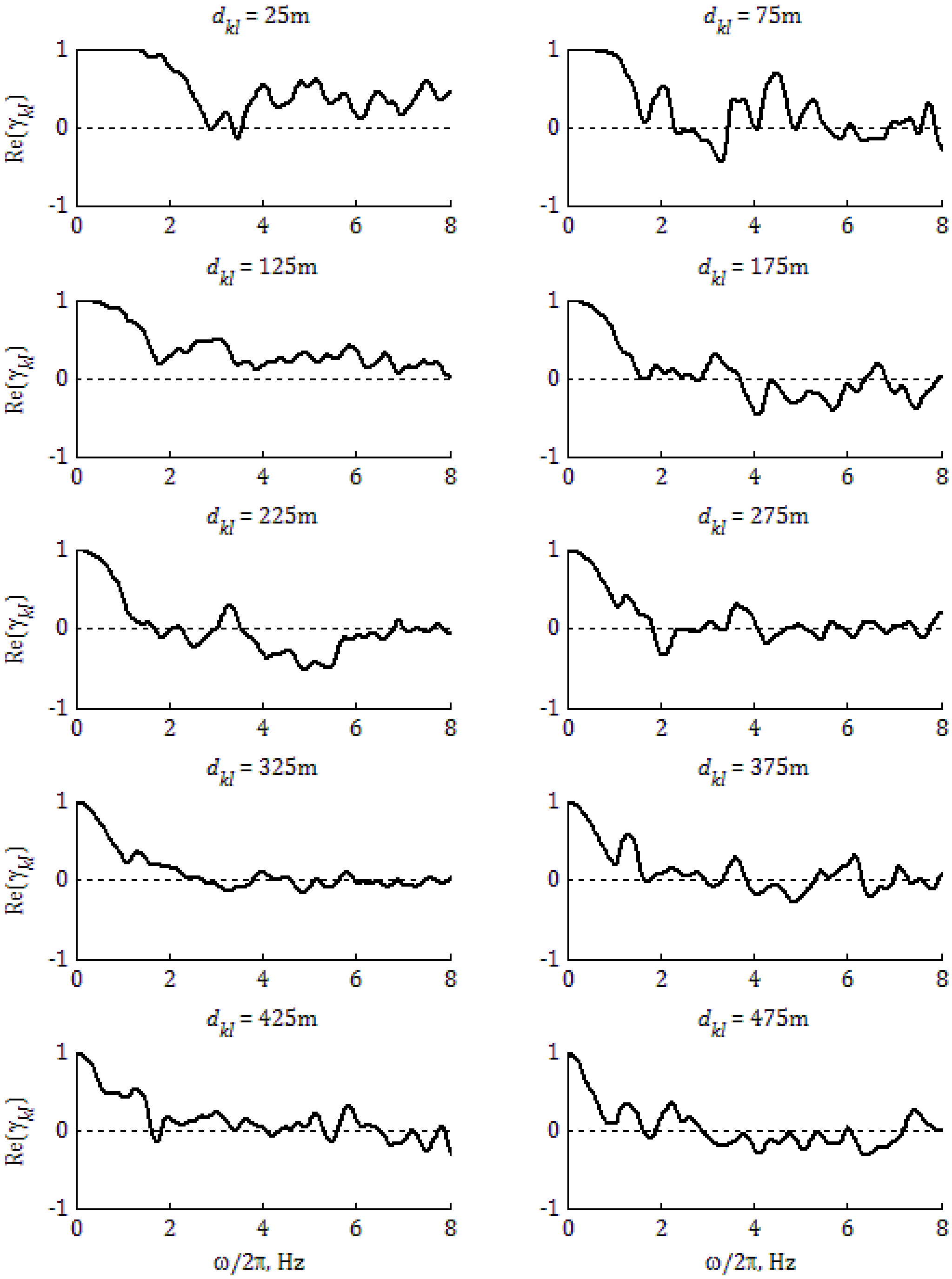

Figure 6.10: Estimates of the real part of coherency for horizontal components.

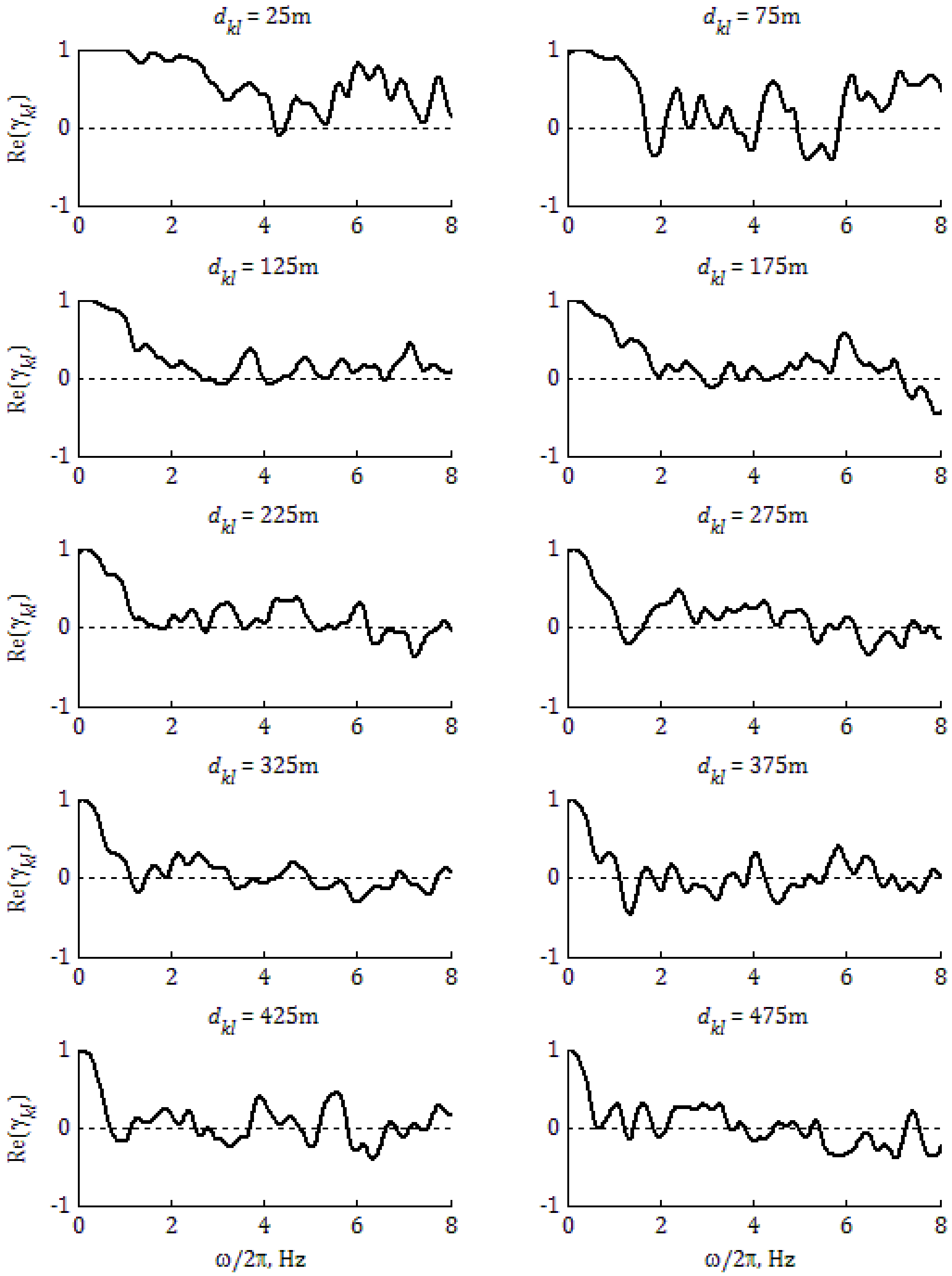

Figure 6.11: Estimates of the real part of coherency for vertical components.

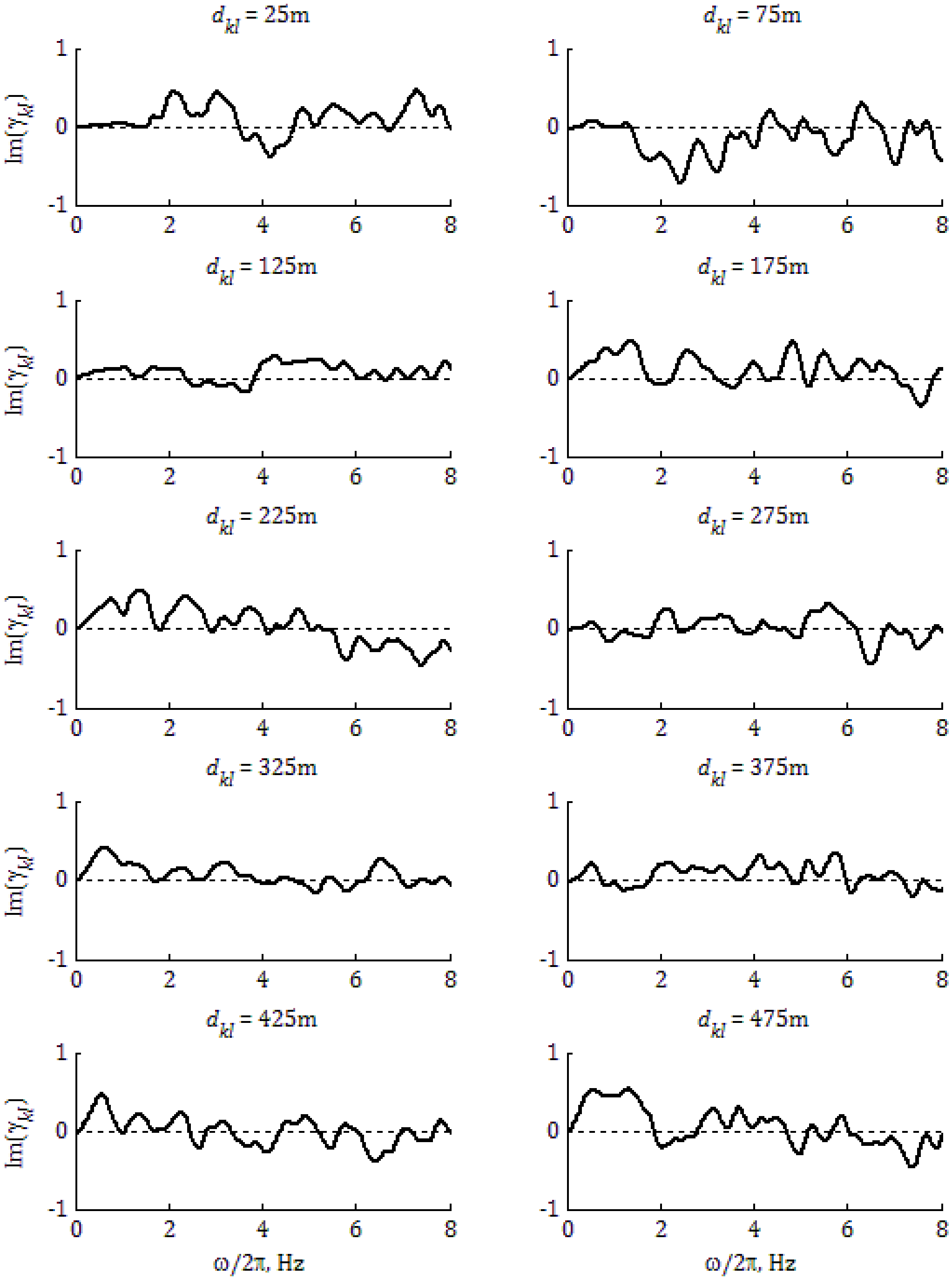

Figure 6.12 Estimates of the imaginary part of coherency for horizontal components.

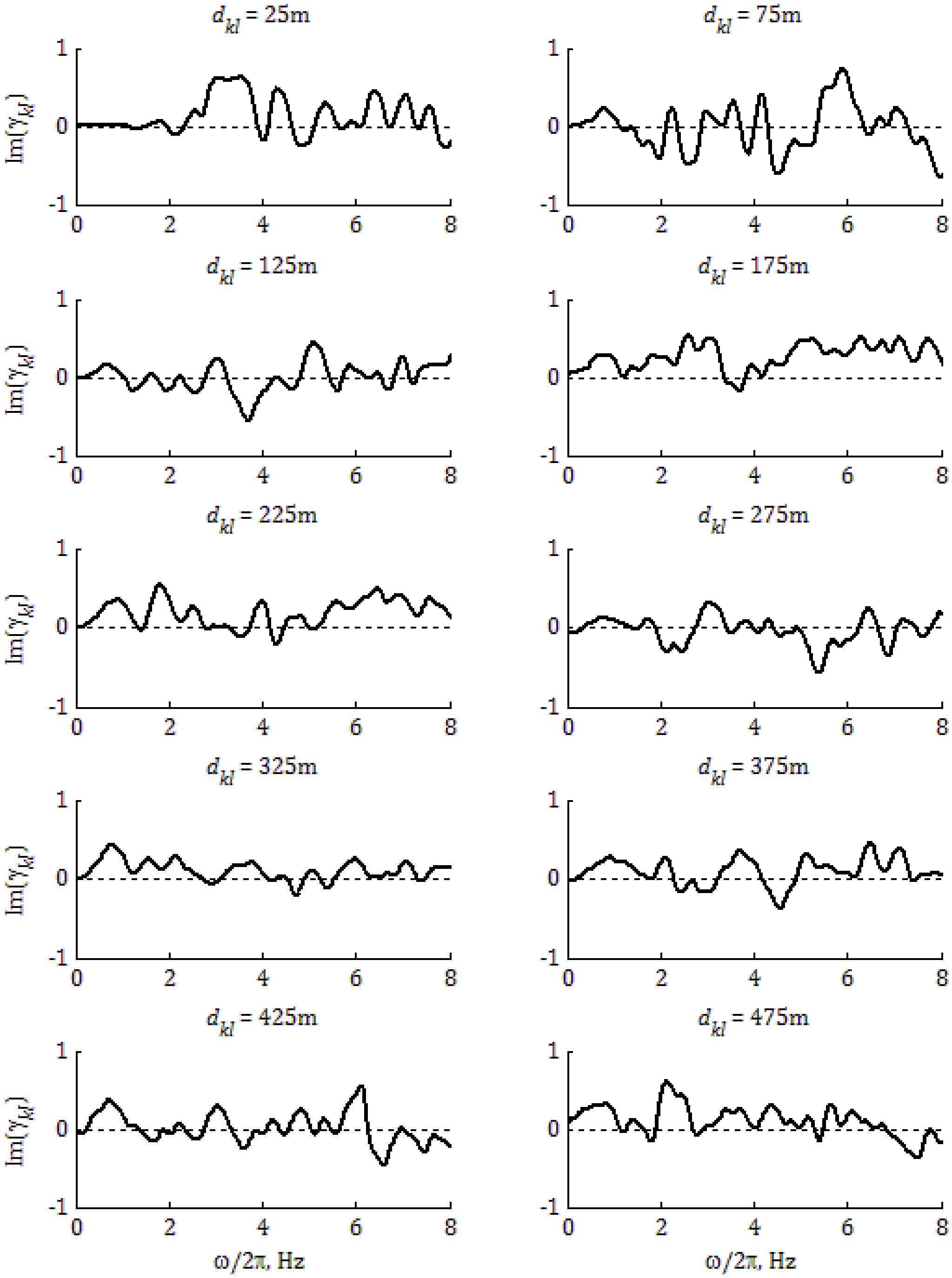

Figure 6.13: Estimates of the imaginary part of coherency for vertical components.

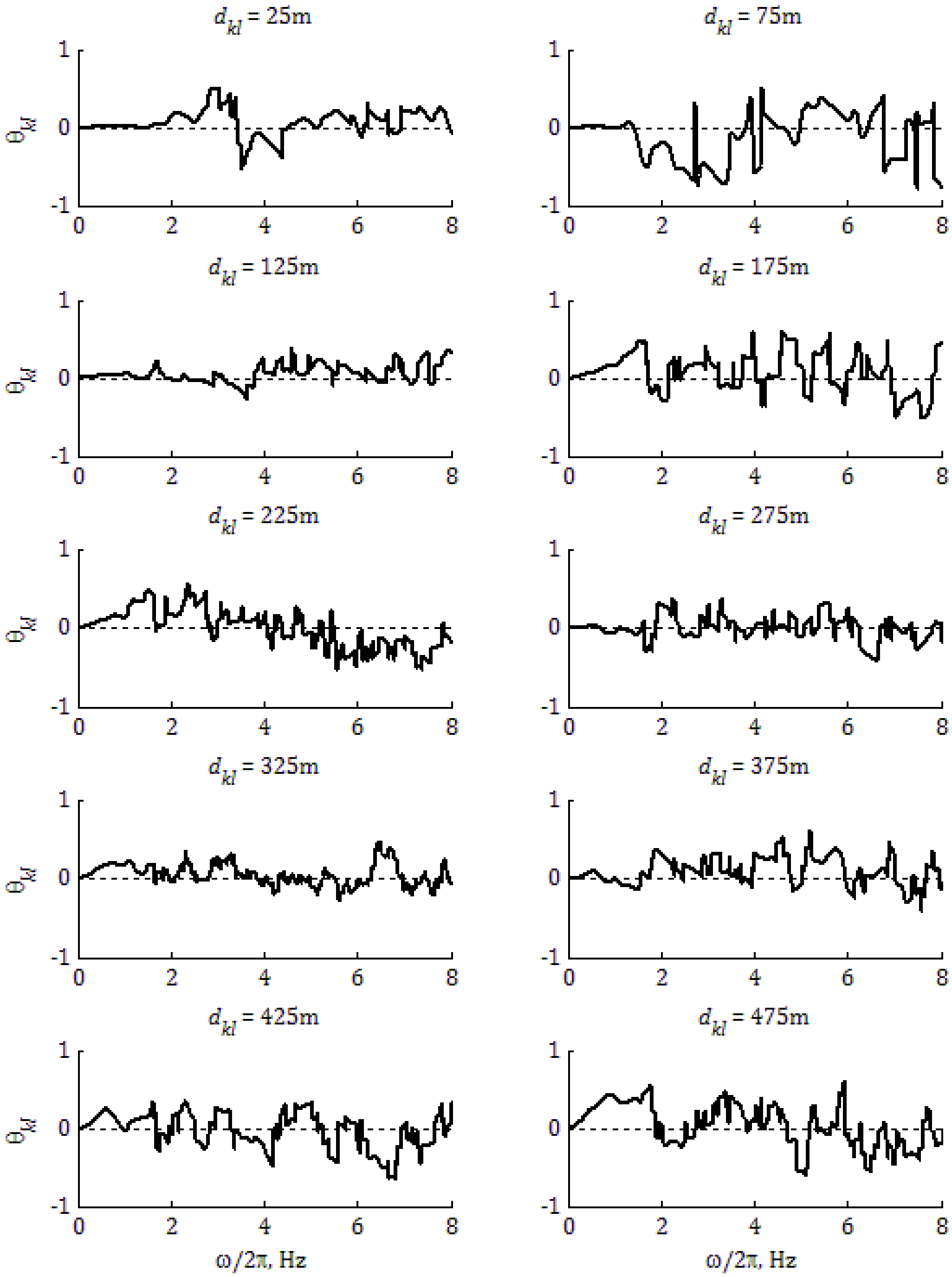

Figure 6.14: : Estimates of coherency phase angle for the horizontal components.

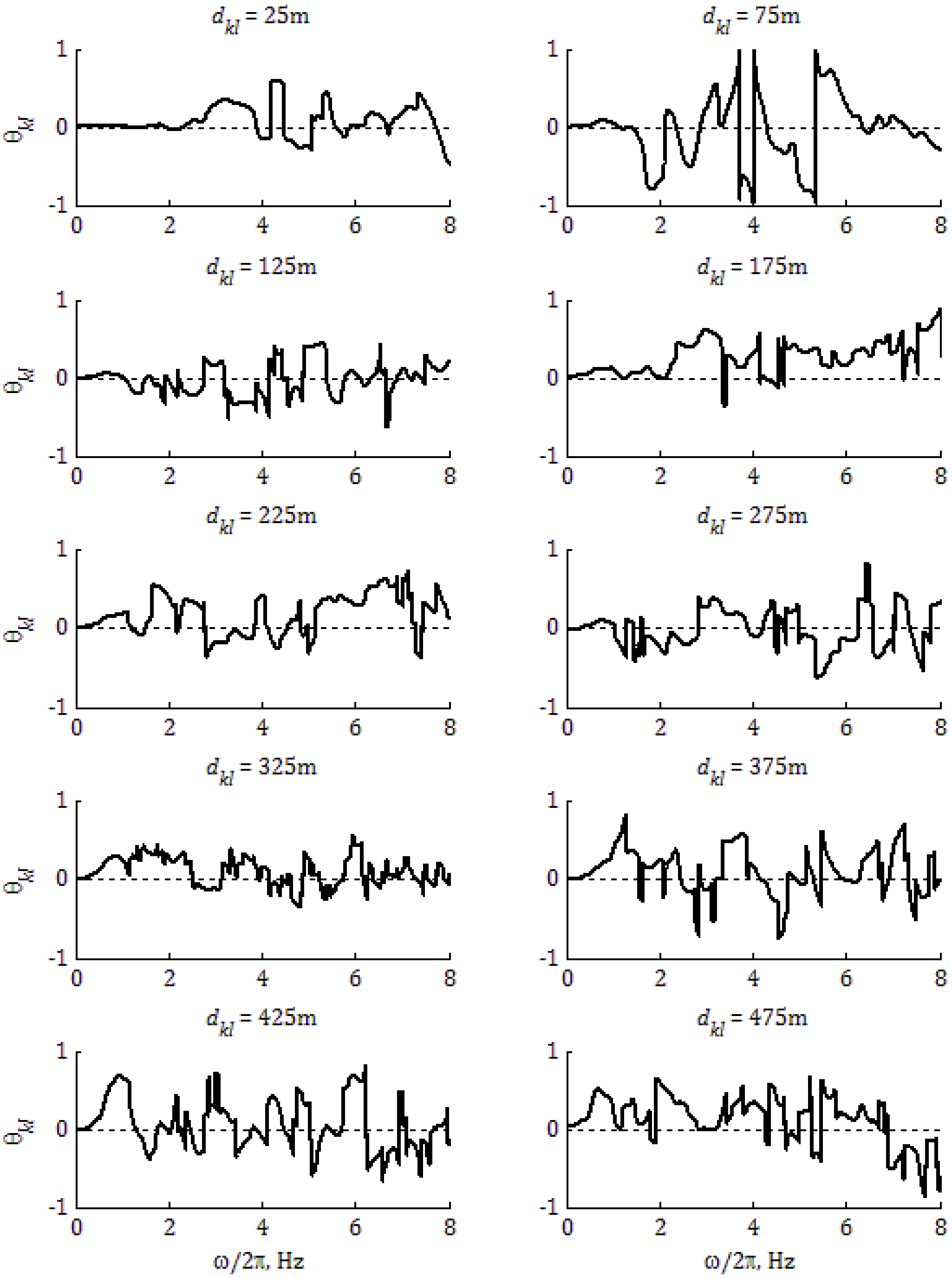

Figure 6.15: Estimates of coherency phase angle for the vertical components.

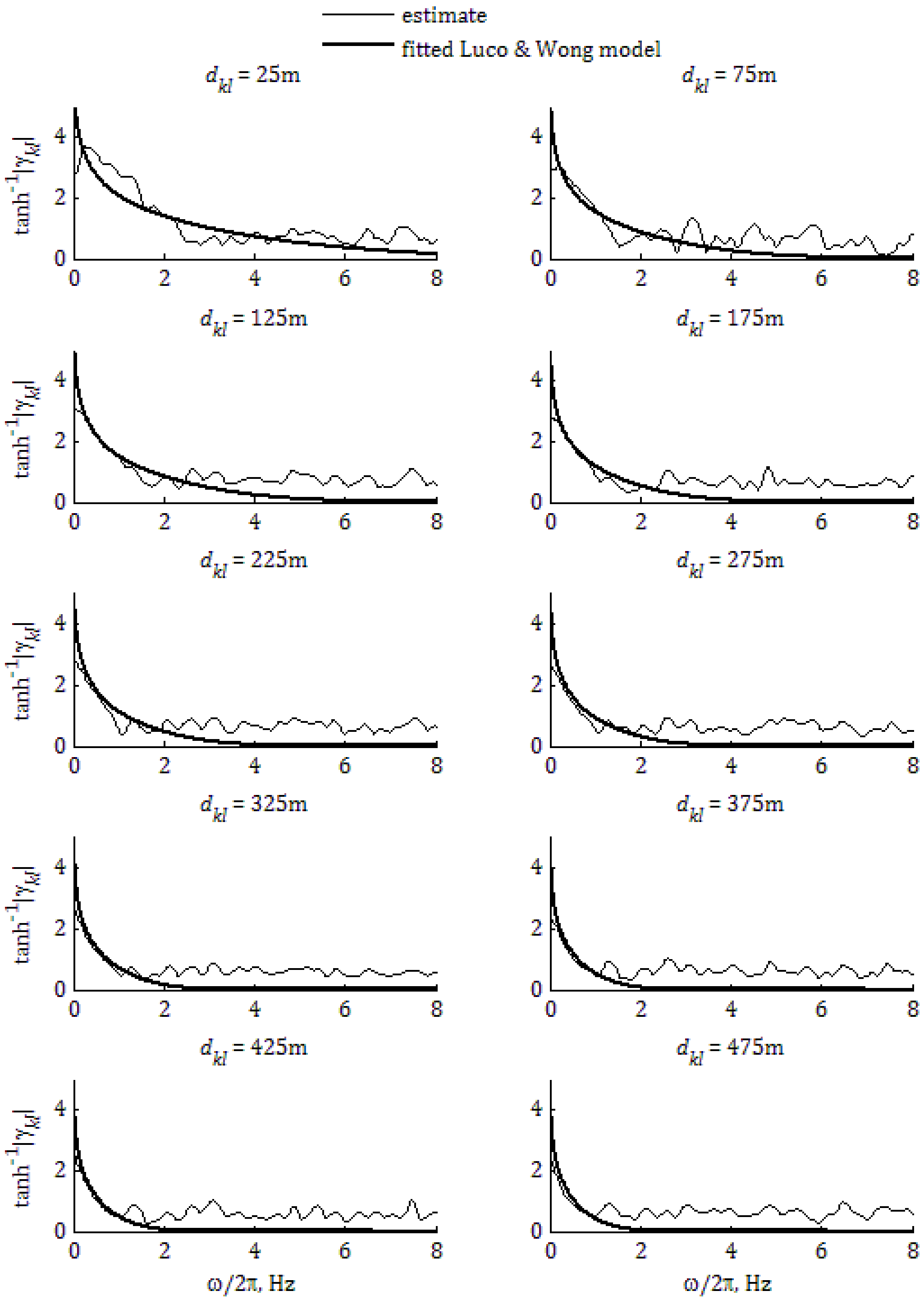

Figure 6.16: Comparison of horizontal coherency estimates ($\tanh^{-1}|\gamma_{kl}|$) with fitted Luco & Wong model.

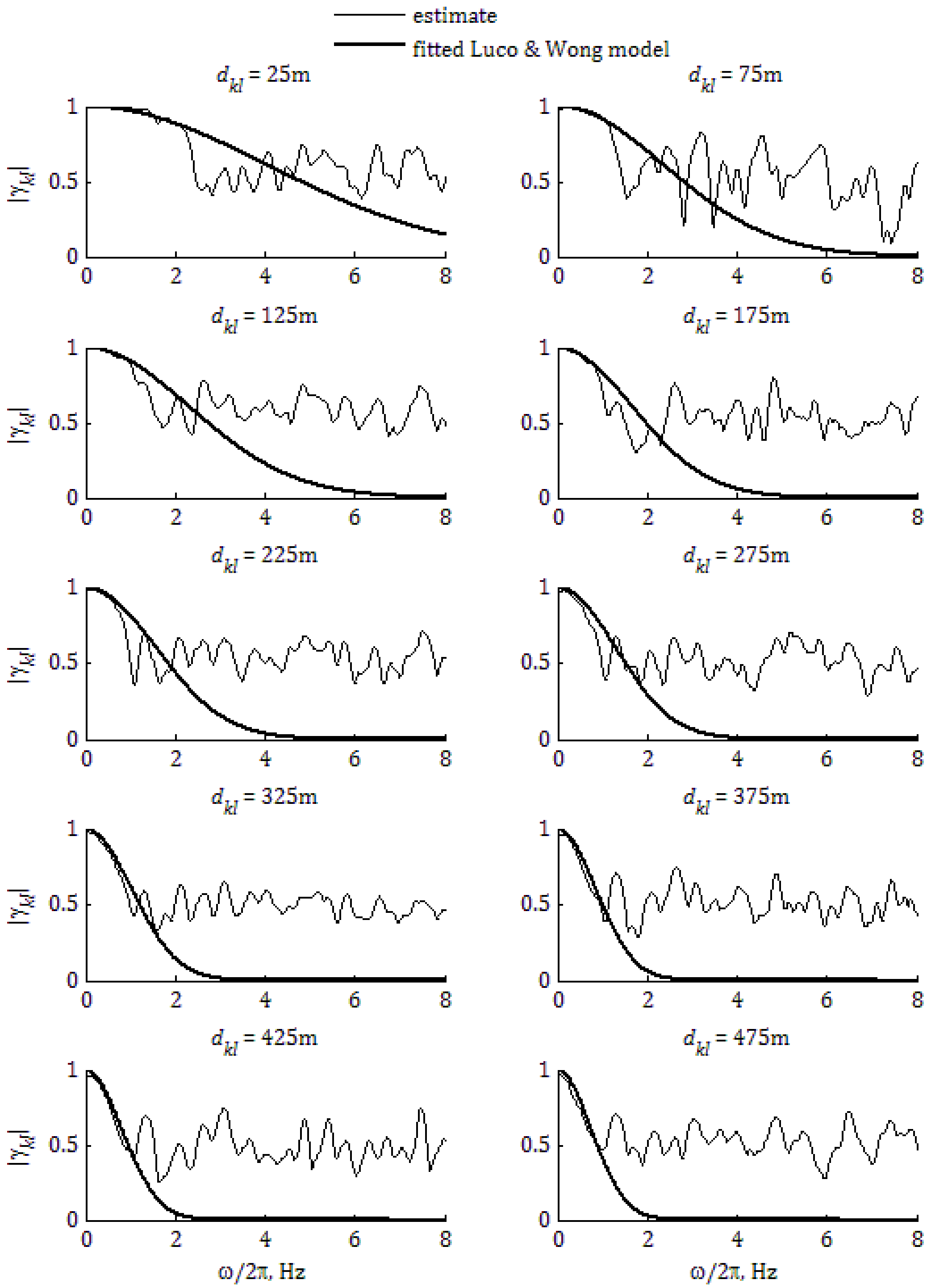

Figure 6.17: Comparison of horizontal coherency estimates ($|\gamma_{kl}|$) with fitted Luco & Wong model.

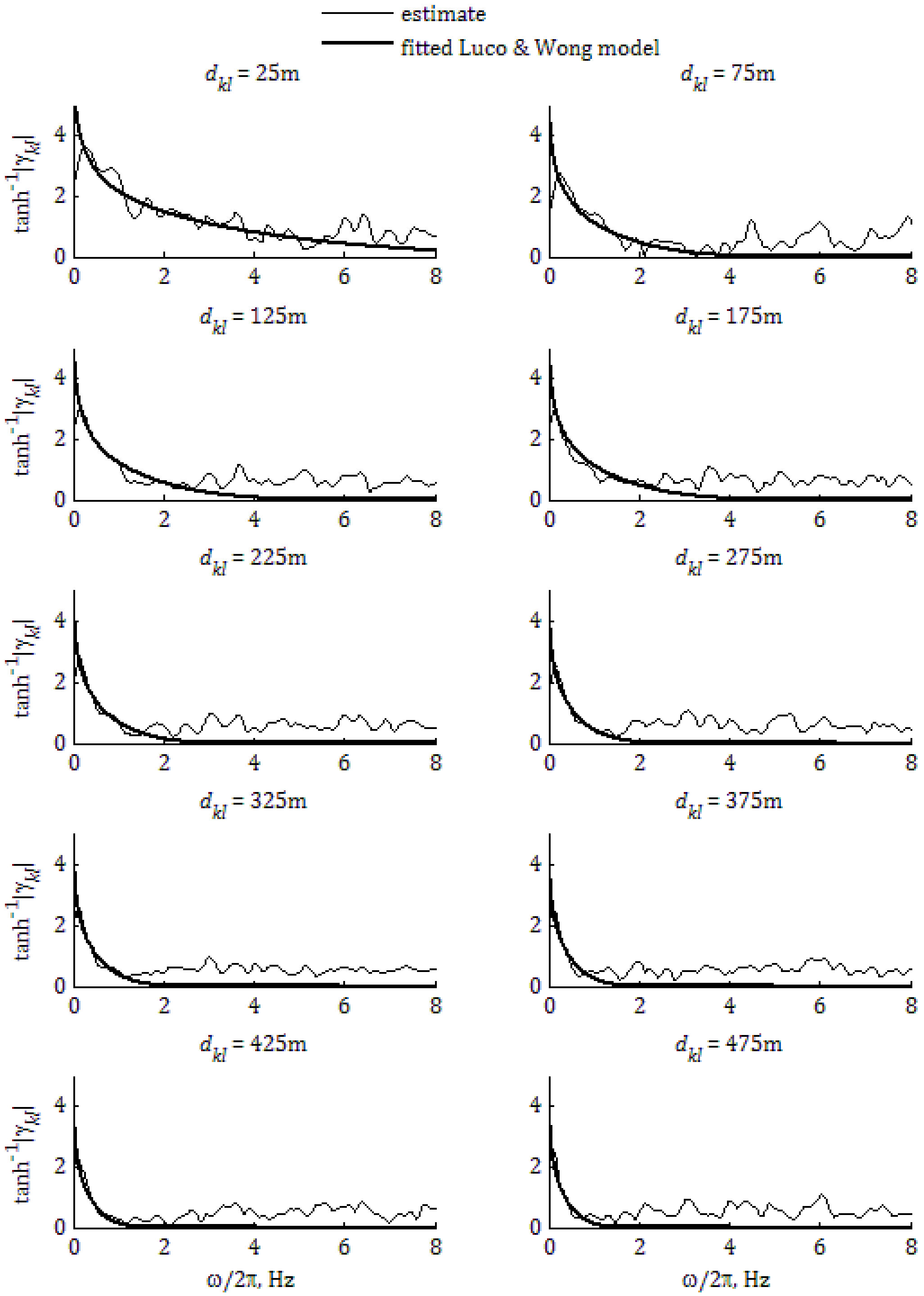

Figure 6.18: Comparison of vertical coherency estimates ($\tanh^{-1}|\gamma_{kl}|$) with fitted Luco & Wong model.

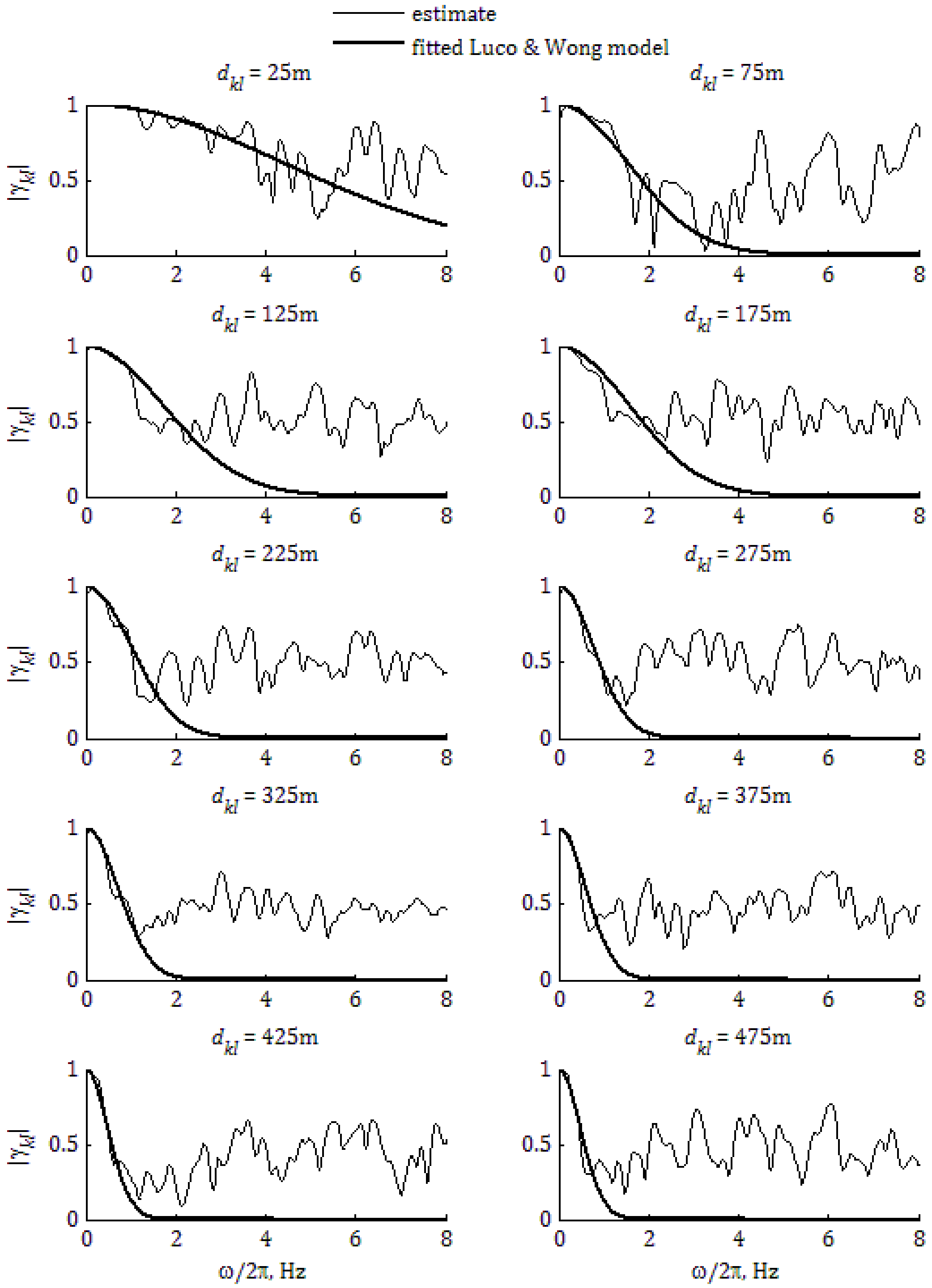

Figure 6.19: Comparison of vertical coherency estimates ($|\gamma_{kl}|$) with fitted Luco & Wong model.

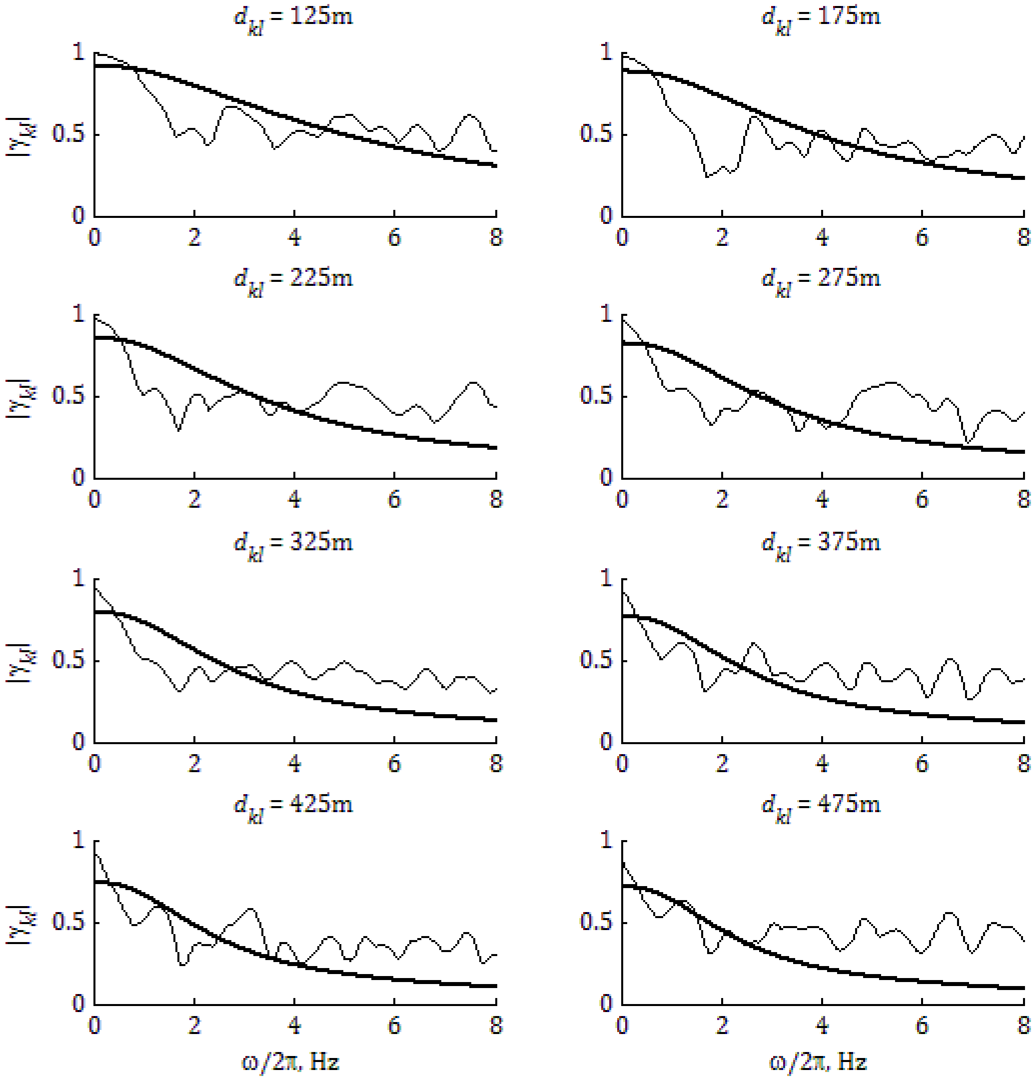

Figure 6.20: Comparison of horizontal coherency estimates ($|\gamma_{kl}|$) with Harichandran and Vanmarcke model.

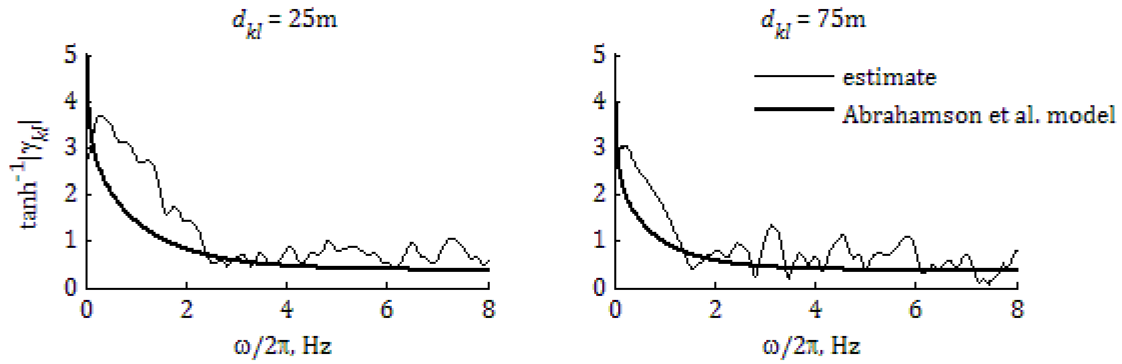

Figure 6.21: Comparison of horizontal coherency estimates ($\tanh^{-1}|\gamma_{kl}|$) with with Abrahamson et al. model.

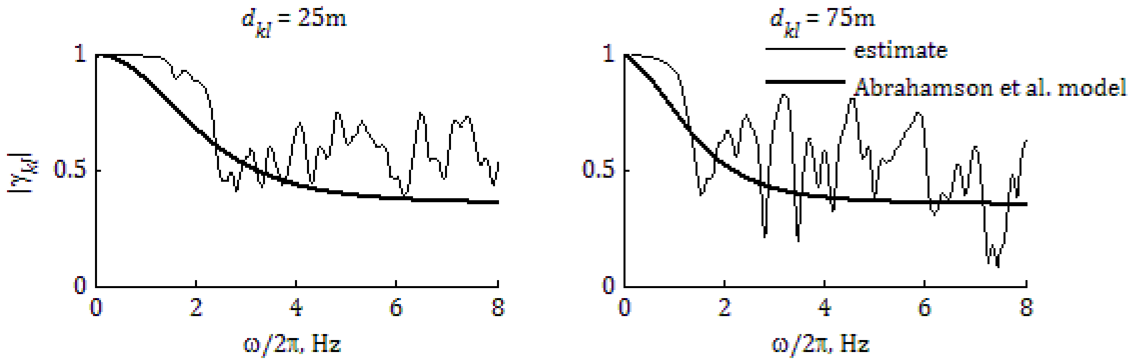

Figure 6.22: Comparison of horizontal coherency estimates ($|\gamma_{kl}|$) with Abrahamson et al. model.

Chapter 7 - Summary, conclusions and further studies

7.1 MAJOR DEVELOPMENTS AND FINDINGS

In this dissertation, we investigated the response of bridges under differential support excitations employing response spectrum and time-history analysis methods. Spatial variability of ground motions due to incoherence, wave-passage and site-response effects was considered. New analysis tools were developed and comprehensive parametric studies of real bridge models under varying conditions were performed. The main developments and findings of the study are summarized below:

- The MSRS method was generalized to account for response quantities that depend on the support DOF, e.g., bridge pier drifts, element forces when rotational DOF are condensed out.

- The MSRS method was extended to account for quasi-static contributions of truncated high-frequency modes. A parametric analysis of the newly introduced cross-correlation coefficients identified cases in which these terms are important.

- The generalized and extended MSRS method was implemented in an efficient computer code. For the computation of the correlation coefficients, a fast and accurate numerical integration method was developed by accounting for the properties of the specific integrand quantities. Another advantage of this code is that it computes the required structural properties using an algorithm that is applicable to any ‘black-box’ structural analysis software.

- MSRS analysis of four real bridge models with vastly different structural characteristics indicated that spatial variability can significantly influence bridge response, even under uniform soil conditions. Among the four bridges, the effect of spatial variability was more pronounced for stiffer bridges, and between bridges with similar fundamental periods the effect was more pronounced in longer bridges. In general, the effect of spatial variability was found to be more significant on element forces along the deck and to be relatively mild on pier drifts. For pier drifts, in most cases, spatial variability reduced the response. For the stiffer bridges, additional variation of support soil properties caused large amplifications of many pseudo-static responses and, consequently, of the respective total responses. When soil conditions rapidly vary in space, the effect of differential site-response on the bridge performance can be more significant than the effect of incoherence and wave passage.

- Comparisons between the original and the extended MSRS methods indicated that when high-frequency truncated modes have significant contributions to the response, the extended rule provides improved approximations with small additional computational effort.

- Methods for simulation of arrays of non-stationary spatially varying ground motions were developed. These methods generate arrays of motions that are consistent with a prescribed coherency model and inherit temporal and spectral characteristics of a specified reference record. The simulation methods account for all three effects of incoherence, wave passage and differential site response. Two approaches were considered:
  a. In the conditional approach, the variability of the motions increases with increasing distance from the location of the specified record. A method that preserves the low-frequency content and thus the displacement waveform of the reference record was investigated.
  b. In the unconditional approach, the arrays of motions are characterized by uniform variability with distance and, thus, are appropriate as input for statistical analysis of bridge response through Monte Carlo simulation analysis.

  Example simulated arrays for both approaches and for both cases of uniform and varying soil conditions were presented. For the case of varying soil conditions, two different methods of modeling the varying soil profiles were considered. The simulation methods were validated by examining the physical compliance of individual time histories, and also by examining median response spectra, coherency characteristics, and PSDs of ensembles of simulated arrays.

- Time-history analyses of the same four bridge models used in the MSRS analysis were performed using as input ensembles of support motion arrays simulated with the unconditional approach. Mean peak pier drifts from linear and non-linear analyses were examined for several cases of spatial variability. For both linear and non-linear responses, the effect of spatial variability was more pronounced for the stiffer bridges. For these bridges, spatial variability reduced pier drifts. These trends are consistent with the results from the MSRS analysis.

- The effect of spatial variability on the "equal displacement" rule was investigated by examining the means and standard deviations of the ratios of peak non-linear over peak linear drifts from time-history analyses. It was shown that under uniform soil conditions, spatial variability tends to decrease these ratios. The effect was more pronounced for stiffer bridges and smaller ductility ratios. When softer soils were considered, these ratios were increased. Similar to the case of uniform support excitations, the "equivalent displacement" rule gave fairly good approximations of the non-linear pier drifts for cases when the fundamental period of the bridge was larger than the predominant period of the site. Otherwise, the results depended on the ductility. For small ductility ratios, the "equal displacement" rule was conservative.

- Comparisons between mean peak responses from linear time-history analyses and the corresponding MSRS estimates demonstrated that the MSRS method is an accurate tool for the analysis of bridges under differential support excitations. This rule is ideal for parametric studies required in the design stage.

- Coherency analysis of the UPSAR array of near-fault motions recorded during the 2004 Parkfield earthquake was performed and estimates of the incoherence components were compared with commonly used models. First, the model by Luco and Wong (1986) was considered. This model is based on the physics of wave propagation, but includes a parameter that must be empirically estimated. Fitting the model to estimates from the UPSAR array yielded smaller values of the incoherence parameter than those previously recommended. The commonly used empirical models by Harichandran and Vanmarcke (1986) and by Abrahamson et al. (1991), which are based on recordings from earthquakes in Taiwan, did not describe well the incoherence component of the UPSAR array.

7.2 RECOMMENDATIONS FOR FURTHER STUDIES

Recommended topics for future studies in the area of bridge response under differential support excitations are the following:

Implementation of MSRS method in commercial codes

This study has demonstrated the accuracy of the MSRS method and its advantages for response analysis of multiply-supported structures subjected to spatially varying ground motions, particularly in the design stage where parametric analysis is often needed. For this method to be adopted in practice, it is necessary that it be implemented in commercial codes, such as SAP2000. The material in Chapter 2 provides all the details that are needed for such implementation.

Extension of the MSRS method to account for spatially correlated orthogonal components

Studies dealing with spatial variability of ground motions, including this dissertation, assume that the components of ground motion in orthogonal directions are statistically independent. This assumption is based on the work of Penzien and Watabe (1975), who investigated correlations between orthogonal components at a single point. However, considering the propagation pattern of surface waves, it is possible that orthogonal components of ground motions at separate locations are correlated. These correlations may influence structural response and, thus, their presence and effects need to be investigated to fully account for the effect of spatial variability of ground motion on multiply-supported structures. Thus, we recommend investigation of the cross-correlation between orthogonal components of ground motion at different locations and extension of the MSRS method to account for this effect, if it is found to be significant.

Extension of the MSRS method to account for directional dependencies

In this dissertation, we examined pier drifts in the longitudinal and transverse directions of each bridge. However, the actual displacement demand on a pier is the vectorial sum of the drifts in two orthogonal directions. For the case of uniform support motions, a response spectrum method for evaluation of vectorial response quantities was developed by Menum and Der Kiureghian (2000). This method needs to be extended for application in the case of differential support motions.

Investigation of the influence of the direction of propagation of seismic waves

In the parametric studies of bridge responses in Chapters 3 and 5, a single direction of propagation of seismic waves was considered. However, preliminary studies have indicated that the direction of wave propagation can have an important influence on bridge response. Further studies on the influence of this phenomenon are recommended.

Development of analysis tools for bridges in the near-fault regions

Near-fault ground motions often include strong directivity pulses that can have significant influence on the bridge response. Such motions are strongly non-stationary and narrow-band and, thus, violate the fundamental assumptions behind the MSRS method and the simulation methods developed in Chapter 4. Investigation of possible modifications of the MSRS method to incorporate near-fault effects is recommended. Simulating arrays of near-fault ground motions requires examination of the spatial variability of the directivity pulse.

Incorporation of the effect of soil-structure interaction

The MSRS method does not explicitly account for the effect of soil-structure interaction. An approximate method to account for this effect for multiply-supported structures, applicable to linear/linearized systems, was developed by Keshishian and DerKiureghian (2001) employing the sub-structuring technique. Further investigations of the issue are recommended.

References

Abrahamson NA, Schneider JF, Stepp JC. Empirical spatial coherency functions for application to soil-structure interaction analyses. *Earthquake Spectra* 1991; **7**:1-28.

Anderson TW. *The Statistical Analysis of Time Series*. Wiley: New York, 1971.

Baker JW. Quantitative classification of near-fault ground motions using wavelet analysis. *Bulletin of the Seismological Society of America* 2007; **97**:1486-1501.

Berrah M, Kausel E. Response spectrum analysis of structures subjected to spatially varying motions. *Earthquake Engineering and Structural Dynamics* 1992; **21**:461-470.

Boore DM, Stephens CD, Joyner WB. Comments on baseline correction of digital strong-motion data: examples from the 1999 Hector Mine, California Earthquake. *Bulletin of the Seismological Society of America* 2002; **92**:1543-1560.

Bozorgnia Y Campbell KW. The vertical-to-horizontal response spectral ratio and tentative procedures for developing simplified V/H and vertical design spectra. *Journal of Earthquake Engineering* 2004; **8**:175-208.

Brillinger RD. *Time Series: Data Analysis and Theory*. Society for Industrial and Applied Mathematics, 2001.

Caltrans Seismic Design Criteria (version 1.3). California Department of Transportation: Sacramento, CA, 2004.

Chatfield C. *The Analysis of Time Series: An Introduction* (6th edition). CRC Press LLC, 2004.

Chopra AK. *Dynamics of Structures: Theory and Applications to Earthquake Engineering* (2nd edition). Prentice-Hall: New Jersey, 2001.

Clough RW, Penzien J. *Dynamics of Structures* (2nd edition). McGraw-Hill: New York, 1993.

Deodatis G. Non-stationary stochastic vector processes: Seismic ground motion applications. *Probabilistic Engineering Mechanics* 1996; **11**:149-167.

Der Kiureghian A. Structural response to stationary excitation. *Journal of the Engineering Mechanics Division* 1980; **106**:1195-1213.

Der Kiureghian A. A response spectrum method for random vibration analysis of MDF systems. *Earthquake Engineering and Structural Dynamics* 1981; **9**: 419-435.

Der Kiureghian A. A coherency model for spatially varying ground motions. *Earthquake Engineering and Structural Dynamics* 1996; **25**:99-111.

Der Kiureghian A, Keshishian P, Hakobian A. Multiple-support response spectrum analysis of bridges including the site-response effect and the MSRS code. *Report No. UCB/EERC-97/02*, Earthquake Engineering Research Center, University of California, Berkeley, 1997.

Der Kiureghian A, Nakamura Y. CQC modal combination rule for high-frequency modes. *Earthquake Engineering and Structural Dynamics* 1993; **22**:943-956.

Der Kiureghian A, Neuenhofer A. Response spectrum method for multiple-support seismic excitation. *Earthquake Engineering and Structural Dynamics* 1992; **21**:713-740.

Dumanogluid A, Soyluk K. A stochastic analysis of long span structures subjected to spatially varying ground motions including the site-response effect. *Engineering Structures* 2003; **25**:1301-1310.

Fletcher JB, Spudich P, Baker LM. Rupture propagation of the 2004 Parkfield, California, earthquake from observations at the UPSAR. *Bulletin of the Seismological Society of America* 2006; **96**:129-142.

Gupta A, Krawinkler H. Estimation of seismic drift demands for frame structures. *Earthquake Engineering and Structural Dynamics* 2000; **29**: 1287-1306.

Hao H. A parametric study of the required seating length for bridge decks during earthquake. *Earthquake Engineering and Structural Dynamics* 2000; **27**: 91-103.

Hao H, Oliveira CS, Penzien J. Multiple-station ground motion processing and simulation based on SMART-1 array data. *Nuclear Engineering and Design* 1989; **111**:293–310.

Harichandran RS, Vanmarcke EH. Stochastic variation of earthquake ground motion in space and time. *Journal of Engineering Mechanics* 1986; **112**:154-174.

Heredia-Zavoni E, Vanmarcke EH. Seismic random-vibration analysis of multisupport-structural systems. *Journal of Engineering Mechanics* 1994; **120**: 1107-1128.

Hjelmstad KD. *Fundamentals of structural mechanics* (2nd edition). Springer Science+Business Media, Inc: New York, 2005.

Kahan M, Gibert RJ, Bard PY. Influence of seismic waves spatial variability on bridges: a sensitivity analysis. *Earthquake Engineering and Structural Dynamics* 1996; **25**:795-814.

Kameda H, Morikawa H. An interpolating stochastic process for simulation of conditional random fields. *Probabilistic Engineering Mechanics* 1992; **7**:243-254.

Kim A, Dreger D. Rupture process of the 2004 Parkfield earthquake from near-fault seismic waveform and geodetic records. *Journal of Geophysical Research* 2008; **113**:B07308.

Kim SH, Feng MQ. Fragility analysis of bridges under ground motion with spatial variation. *International Journal of Non-Linear Mechanics* 2003; **5**:705-721.

Leger P, Wilson EL. Modal summation method for structural dynamic computations. *Earthquake Engineering and Structural Dynamics* 1988; **16**:23-27.

Liao S, Zerva A. Physically compliant, conditionally simulated spatially variable seismic ground motions for performance-based design. *Earthquake Engineering and Structural Dynamics* 2006; **35**:891-919.

Loh CH, Ku BD. An efficient analysis of structural response for multiple-support seismic excitations. *Engineering Structures* 1995; **17**:15-26.

Lou L, Zerva A. Effects of spatially variable ground motions on the seismic response of a skewed, multi-span, RC highway bridge. *Soil Dynamics and Earthquake Engineering* 2005; **25**: 729-740.

Luco JE, Wong HL. Response of a rigid foundation to a spatially random ground motion. *Earthquake Engineering and Structural Dynamics* 1986; **14**:891-908.

Lupoi A, Franchin P, Pinto PE, Monti G. Seismic design of bridges accounting for spatial variability of ground motion. *Earthquake Engineering and Structural Dynamics* 2005; **34**:327-348.

Mander JB, Priestley MJN, Park R. Theoretical stress-strain model for confined concrete. *Journal of Structural Engineering* 1988; **114**:1804-1826.

Menum C, Der Kiureghian A. A replacement for the 30%, 40%, and SRSS rules for multicomponent seismic analysis. *Earthquake Spectra* 2000; **14**:153-163.

Miranda E. Inelastic displacement ratios for displacement-based earthquake resistant design. *Proceedings of the 12th World Conference on Earthquake Engineering*, Auckland, CD-ROM, Paper 1096, New Zealand Society for Earthquake Engineering, 2000.

Miranda E, Bertero V. Evaluation of strength reduction factors for earthquake resistant design. *Earthquake Spectra* 1994; **10**:357-379.

Moehle JP. Displacement-based design of RC structures subjected to earthquakes. *Earthquake Spectra* 1992; **8**:403-428.

Nakamura Y, Der Kiureghian A, Liu D. Multiple-support response spectrum analysis of the Golden Gate Bridge. *Report No. UCB/EERC-93/05*, Earthquake Engineering Research Center, University of California, Berkeley, 1993.

Newmark N, Hall WJ. Seismic design criteria for nuclear reactor facilities. *Proceedings of the 4th World Conference on Earthquake Engineering*, Santiago, Chile, 1969.

Open System for Earthquake Engineering Simulation. http://opensees.berkeley.edu/ Accessed in April, 2011.

Penzien J, Watabe M. Characteristics of 3-dimensional earthquake ground motion. *Earthquake Engineering and Structural Dynamics* 1975; **3**:365-373.

Price TE., Eberhard MO. Effects of spatially varying ground motions on short bridges. *Journal of Structural Engineering* 1998; **124**:948-955.

Rabiner LR, Gold B. *Theory and application of digital signal processing*. Englewood Cliffs, N.J., Prentice-Hall, 1975.

Rahnama M, Krawinkler H. Effects of soft soil and hysteresis model on seismic demands. *Report No. 108*. The John A. Blume Earthquake Engineering Center. Stanford University, Stanford, CA, 1993.

Rezaeian S, Der Kiureghian A. A stochastic ground motion model with separable temporal and spectral nonstationarities. *Earthquake Engineering and Structural Dynamics* 2008; **37**:1565-1584.

Safak E. Discrete-time analysis of seismic site amplification. *Journal of Engineering Mechanics* 1995; **121**:801-809.

Saxena V, Deodatis G, Shinozuka M, Feng MQ. Development of fragility curves for multi-span reinforced concrete bridges. *Proceedings of the International Conference on Monte Carlo Simulation*, Principality of Monaco, Austria, 2000.

Sextos A, Kappos AJ, Mergos P. Effect of soil-structure interaction and spatial variability of ground motion on irregular bridges: the case of the Krystallopigi Bridge. *Proceedings of the 13th World Conference on Earthquake Engineering*, Paper No. 2298, Vancouver, BC, Canada, 2004.

Singh MP, McCown BE. Mode acceleration-based response spectrum approach for non-classically damped structures. *Soil Dynamics and Earthquake Engineering* 1986; **5**:226-233.

Soyluk K. Comparison of random vibration methods for multi-support seismic excitation analysis of long-span bridges. *Engineering Structures* 2004; **26**:1573–1583.

Vanmarcke EH, Fenton GA. Conditioned simulation of local fields of earthquake ground motion. *Structural Safety* 1991; **10**:247-264.

Veletsos AS, Newmark NM. Effect of inelastic behavior on the response of simple systems to earthquake motions. *Proceedings of the 2nd World Conference on Earthquake Engineering*, Japan, **2**:895-912, 1960.

Vidic T, Fajfar P, Fischinger M. Consistent inelastic design spectra: strength and displacement. *Earthquake Engineering and Structural Dynamics* 1994; **23**:502-521.

Wang J, Chen H. A new spatial coherence model and analytical coefficients for multi-support response spectrum combination. *Earthquake Engineering and Engineering Vibration* 2005, **6**:225-235.

Yu RF, Zhou XY. Response spectrum analysis for non-classically damped linear system with multiple-support excitations. *Bulletin of Earthquake Engineering* 2008; **6**:261–284.

Zanardo G, Hao H, Modena C. Seismic response of multi-span simply supported bridges to a spatially varying earthquake ground motion. *Earthquake Engineering and Structural Dynamics* 2002; **31**:1325-1345.

Zembaty Z, Rutenberg A. Spatial response spectra and site amplification effects. *Engineering Structures* 2002; **24**:1485-1496.

Zerva A. Response of multi-span beams to spatially incoherent seismic ground motions. *Earthquake Engineering and Structural Dynamics* 1990; **19**:819-832.

Zerva A, Harada T. A site-specific model for the spatial incoherence of the seismic ground motions. *Proceedings of the 5th National Conference on Earthquake Engineering*, Chicago, Illinois, 1994.

Zhang YH, Li QS, Lin JH, Williams FW. Random vibration analysis of long-span structures subjected to spatially varying ground motions. *Soil Dynamics and Earthquake Engineering* 2009; **29**:620-629.